Determination of Oxygen Reduction on Platinic and Non-Platinic Electrodes and Sulfur Oxidation Reaction Mechanisms on Pt and Pt_3Co Electrodes using *in situ* X-Ray Absorption Spectroscopy

By Daniel S. Gatewood

B.S. Chemistry, May 2004, University of Florida

A Dissertation Submitted to

The Faculty of Columbian College of Arts and Sciences of
The George Washington University in partial satisfaction of
the requirements for the degree of Doctor of Philosophy

May 17th, 2009

Dissertation directed by

David E. Ramaker
Professor of Chemistry

The Columbian College of Arts and Sciences of The George Washington University certifies that Daniel S. Gatewood has passed the Final Examination for the degree of Doctor of Philosophy as of March 13th, 2009. This is the final and approved form of the dissertation.

Determination of Oxygen Reduction on Platinic and Non-Platinic Electrodes and Sulfur Oxidation Reaction Mechanisms on Pt and Pt_3Co Electrodes using *in situ* X-Ray Absorption Spectroscopy

Daniel S. Gatewood

Dissertation Research Committee:

David Ramaker, Professor of Chemistry, Dissertation Director

Stuart Licht, Professor of Chemistry, Committee Member

Vladislav Sadtchenko, Associate Professor of Chemistry, Committee Member

Dedication

This dissertation is dedicated to my grandfather,

Ray Sadler

1924-1985

Acknowledgements

I am grateful to have had the opportunity to have my graduate career directed by Professor David E. Ramaker. My experience of working with him has been very beneficial due to his scientific intuition, guidance, and extreme patience for times when I would get frustrated. I am grateful for all the times he spent with me explaining complex scientific principles, listening to my perspective on ideas, and his intense proofreading of this thesis. Without his support, the work in this thesis would not have been possible.

In addition to my advisor, I must thank Dr. Karen Swider-Lyons at the Naval Research Laboratory (NRL) for hiring me on as an employee in her research group from my second through fourth year of my graduate career. I am incredibly fortunate for this experience as it allowed me to take on various research projects that make up a majority of this thesis. It also led me to independently collect my own XAS data and gain some experimental experience as well. Her support and financial assistance for the research in Chapters 3, 4, and 6 and for trips up to the National Synchrotron Light Source (NSLS) and Brookhaven National Laboratory (BNL) in Upton, NY are greatly appreciated. Also, I'd like to acknowledge Drs. Olga Baturina and Yannick Garsany of the KSL research group for providing me their knowledge of the electrochemical principles discussed in this work. In conclusion, I feel fortunate that Dr. Swider-Lyons served as a second advisor during my graduate career. I also would like to include a big thanks to Dr. Kotaro Sasaki of BNL for showing me how to collect XAS data.

I had the pleasure of working with Dr. Joseph Ziegelbauer who was a part of the research group at Northeastern University (NU) directed under Dr. Sanjeev Mukerjee. He prepared and collected the data on the Rh samples presented in Chapter 5 and gave me valuable advice on XAS data collection at BNL. Also, not only did we manage to get this project published and presented at many conferences, but also a great friendship resulted in this collaboration.

I would like to acknowledge the institutions for providing financial support for these research projects: The Department of Energy (DOE); The Naval Research Laboratory (NRL);

The Office of Naval Research (ONR); Northeastern University (NU); The Electrochemical Society (ECS) and The George Washington University (GWU).

Thank you to my doctoral committee Professors Stuart Licht, Vladislav Sadtchenko, and Susan Gillmor for participating in my defense. Also, there is much appreciation on my part to Dr. Jeremy Pietron from NRL who served as my outside source.

Finally, I would like to thank Drs. Frances Scott and Maggie Teliska formerly of the Ramaker research group for their friendship and invaluable advice given to me over the years. I thank my current colleagues Badri Shyam, Anna Korovina, and Maryam Farmand for their friendship and sympathy during the more difficult times in graduate school. Outside of the Ramaker group, I'd like to thank Stephanie McCartney, Jen Herdman, Nick Deifel, Ryan Brennan, Eric Fallows, Esra Yönel, and Rick Stroman for their help and friendship. I also would like to thank my friends outside of school: Michael Rogers, Claire Bengur, Nick Otto, Clarke Whitehead, Tatyana Gelman, Genevieve Judge, Pavitra Mohan Ram, Carina Ferreiro, Tricia Ryan, and Chris McChesney.

Finally, I am grateful for my family for their faith in me to complete this work. I'd also like to express my extreme thanks to my sister, Rae Andreano, for listening to me rant and rave during many long phone conversations over the past 5 years.

Abstract

Determination of Oxygen Reduction on Platinic and Non-Platinic Electrodes and Sulfur Oxidation Reaction Mechanisms on Pt and Pt_3Co Electrodes using *in situ* X-Ray Absorption Spectroscopy

X-ray Absorption Spectroscopy (XAS) has been used to examine several active fuel cell catalysts with the objective of extending the applicability of the novel Δμ XANES technique to more complex systems, and to develop a catalyst that is more stable, less prone to poisoning, and less expensive than the current standard Pt nanoparticles supported on carbon. In this work we examined Au nanoparticles supported on SnO_x, ligand-stabilized Pt nanoparticles, sulfur poisoned Pt cathodes, and Rh-based sulfide, Rh_xS_y, in *situ* in an electrochemical cell. Both Extended X-ray Absorption Fine Structure (EXAFS) analysis, as well as the novel difference technique utilizing the X-ray Absorption Near Edge Structure (Δμ-XANES) were utilized.

The XAS data, taken at the National Synchrotron Light Source at Brookhaven National Laboratory, were measured *in situ* to acquire information on the oxygen reduction reaction (ORR) mechanism on the indicated electrocatalyts. Particle modeling and EXAFS data were used to estimate catalysts nanoparticle size and morphologies. Full multiple scattering calculations were performed on small atomic models representing the catalysts to interpret the XANES Δμ signatures. The geometric binding sites and relative coverage of simple H, OH, and O species to more complicated organic ligands and various sulfur species adsorbed on the electrocatalysts were determined at different applied electrochemical potentials. The results aided in improving our understanding of how the ORR reaction occurs on different catalysts such as Rh_xS_y, Au-SnO_2, ligand stabilized Pt, and S poisoned Pt.

Au nanoparticles supported on tin-oxide (Au-SnO_x) and mixed with Vulcan carbon (VC) are active electrocatalysts for the ORR, while Au/VC by itself is inactive. These results indicate that the SnO_x support either enhances the ORR activity of the Au, or participates directly in the

reaction. Results obtained from the Δμ XANES and EXAFS show that a bifunctional mechanism plays the dominant role in the ORR reaction. O_2 adsorbs and dissociates on the nearby SnO_x surface with apparent simultaneous electron transfer from the Au, and then ultimate reduction to water.

XAS data were also acquired on Pt nanoparticles stabilized by triphenyl phosphine triphosphonate (TPPTP) ligands attached to the Pt particles. Δμ analysis shows the Pt particles in the Pt/TPPTP catalyst are complexed via the P (i.e., Pt-P<tp) with about 0.3 ML of TPPTP (where the tp indicates the triphenyl groups); these species exist on the surface along with a dramatically reduced OH coverage. The reduction in OH coverage enhances the surface specific ORR rate relative to the same sized Pt particles on carbon, but is not sufficient to increase the mass specific ORR rate.

A broad range of experimental tools were used to study Rh_xS_y/C. These tools include X-ray diffraction (XRD), high-resolution transmission electron microscopy (TEM), micro-analysis and electrochemical investigations, along with the XAS. The adsorption of water, OH, and O as a function of overpotential is reported. Heating of the Rh_xS_y catalysts causes Rh segregation and the formation of Rh metal particles, and immersion in TFMSA causes S dissolution and the formation of a Rh skin on the Rh_xS_y samples. It is shown that some Rh-Rh interactions are needed to carry out the ORR.

Finally XAS data were collected and analyzed using a modified Δμ XANES technique to distinguish the adsorption of O and SO_x species on Pt and Pt_3Co electrocatalysts. This modified Δμ technique enabled the direct observation of O coverage and SO_x oxidation state, and the results were correlated with previous electrochemical data and theory to assign oxidation and reduction potential regions. The data reveal why S oxidation and ultimate removal from Pt_3Co are much more efficient than that which occurs when S interacts with Pt. SO_2 to $SO_{3/4}$ oxidation occurs concurrently with OH and O adsorption on Pt_3Co, while on Pt the potential apparently has

to be cycled to higher potentials to oxidize the SO_2 in the presence of O/Pt, and then back down to lower potentials to remove the $SO_{3/4}$ in the presence of OH/Pt.

Table of Contents

Dedication iii
Acknowledgements iv
Abstract vi
Table of Contents ix
List of Figures xiii
List of Tables xv

Chapter 1: Introduction

1.1 Introduction 1
1.2 History of Pt electrodes as fuel cell material 2
1.3 Electrode reactions 3
1.4 Adsorbate-electrode interactions considered in this thesis 6
    1.4.1 Improving oxygen adsorption on Pt Electrocatalysts 7
    1.4.2 Oxygen Adsorption on Au Electrocatalysts 9
    1.4.3 Rh Chalcogenides electrocatalysts 11
    1.4.4 Sulfur Poisoning on Pt and Pt Alloys 12
1.5 Use of X-Ray Absorption Spectroscopy 13
1.6 References 17

Chapter 2: Experimental and Theoretical Techniques

2.1 Introduction 20
2.2 The XAS spectrum 20
2.3 XAFS Theory 21
2.4 EXAFS and XANES Analysis 30
    2.4.1 EXAFS analysis 31
    2.4.2 Isolation of XANES features 34
2.5 Theoretical Calculations 36
    2.5.1 FEFF 8.0 36
    2.5.2 ATOMS code 37
2.6 Rotating Disk Electrode Cyclic Voltammetry 40
2.7 XAS Data Collection 41
    2.7.1 Synchrotron Radiation 41
    2.7.2 Experimental Setup 42
2.8 References 45

Chapter 3: Support Effects on Water Activation and Oxygen Reduction over Au-SnO_x Electrocatalysts using *in situ* X-ray Absorption Spectroscopy

3.1 Introduction 46
3.2 Experimental 51
    3.2.1 Synthesis of Au-SnO_x/VC 51
    3.2.2 Rotating Disk Electrode (RDE) Cyclic Voltammetry 52
    3.2.3 X-ray Absorption Spectroscopy 53

3.2.4 XANES Analysis 53
3.2.5 EXAFS Analysis 57
3.2.6 FEFF 8.0 Calculations 58
3.3 Results 58
3.3.1 Rotating Disk Electrode (RDE) Cyclic Voltammetry 58
3.3.2 EXAFS Analysis 59
3.3.3 XANES Analysis 59
3.4 Discussion 63
3.4.1 Correlation of EXAFS and Δμ data 63
3.4.2 Effect of Au particle size 69
3.4.3 Electronic Effects vs. a Bifunctional Mechanism 71
3.4.4 Correlation to Gas Sensors and CO oxidation 74
3.4.5 Prospects for improving the performance of Au-SnOx/VC catalysts 75
3.5 Conclusion 76
3.6 References 77

Chapter 4: Characterization of Ligand Effects on Water Activation in Triarylphosphine-Stabilized Pt Nanoparticle Catalysts by X-ray Absorption Spectroscopy

4.1 Introduction 79
4.2 Experimental 83
4.2.1 Catalyst and Electrode Preparation 83
4.2.2 X-Ray Absorption 85
4.2.3 EXAFS and XANES Analysis 86
4.2.4 FEFF 8.0 Calculations 88
4.3 Results 91
4.3.1 EXAFS Analysis 91
4.3.2 Δμ Results 98
4.4 Discussion 109
4.5 Conclusion 114
4.6 References 115

Chapter 5: *In situ* determination of Water Activation and Oxygen Reduction in Rhodium Sulfide based Chalcogenides using X-ray Absorption Spectroscopy

5.1 Introduction 117
5.2 Experimental 121
5.2.1 Synthesis 121
5.2.2 Catalyst Morphology 122
5.2.3 Rotating Disk Electrode Studies 122
5.2.4 XAS Data Collection and Analysis 123
5.3 Results and Discussion 125
5.3.1 Morphology 125
5.3.1.1 X-ray diffraction 125
5.3.1.2 Transmission electron microscopy 128
5.3.2 Electrochemical Kinetics 131
5.3.2.1 Cyclic voltammetry 131

5.3.2.2 RDE studies 133
5.3.3 XAS Analysis 136
5.3.3.1 In situ XANES 136
5.3.3.2 In situ Rh K edge EXAFS 138
5.3.4 Δμ Analysis 149
5.3.4.1 Theoretical signatures 149
5.3.4.2 Δμ spectra for Rh_xS_y/C 151
5.3.4.3 Interpretation of the Δμ signatures 153
5.3.4.4 Correlation of the Δμ spectra with the cyclic voltammetry results 159
5.4. Summary and Conclusions 159
5.4.1 Water Activation and Stability in TFMSA5.5 Experimental Details 159
5.4.2 ORR Activity 160
5.4.3 Summary 161
5.5 Conclusion 161
5.10 References 163

Chapter 6: Elucidation of the Mechanism for Sulfur Oxidation on Pt and Pt_3Co Electrocatalysts using in situ X-ray Absorption Spectroscopy

6.1 Introduction 166
6.1.1 S poisoning 166
6.1.2 S removal 170
6.1.3 This work 173
6.2 Experimental Details 174
6.2.1 Sample Preparation 174
6.2.2 X-ray Absorption experiments 176
6.2.3 XANES analysis 176
6.2.4 EXAFS 177
6.2.5 FEFF 8.0 calculations 178
6.3 Results 178
6.3.1 FEFF 8.0 Calculations 178
6.3.2 XANES analysis 184
6.3.3 EXAFS results 184
6.4 Discussion 190
6.4.1Reaction mechanisms of sulfur species revealed through Δμ amplitudes 190
6.4.1.1 Sulfur oxidation on Pt 190
6.4.1.2 Sulfur oxidation on Pt3Co/VC and the benefits of the ligand effect 197
6.5 Conclusions 203
6.6 References 205

Chapter 7: Summary and Future Directions

7.1 Summary of Current Work 208
7.1.1 Oxygen Reduction on Tin-Oxide Supported Au Electrocatalysts 209
7.1.2 Oxygen Reduction on Ligand-Stabilized Pt nanoparticles. 210
7.1.3 Oxygen Reduction on Rh based Chalcogenides 210
7.1.4 Sulfur Oxidation on Pt and Pt_3Co 211
7.2 Future Directions 212

7.3 References 215

List of Figures

Chapter 1

Figure 1.1 Density of states for the s, p and d orbitals. 4
Figure 1.2 Schematic of a fuel cell. 5

Chapter 2

Figure 2.1 XAS spectrum at the L_3 edge for a Pt foil. 22
Figure 2.2 Illustration of the photoelectric effect. 24
Figure 2.3 Illustration of the events occurring as a result of x-ray absorption. 26
Figure 2.4 Illustration of the constructive and deconstructive phases. 28
Figure 2.5 Illustration of single and multiple scattering paths. 29
Figure 2.6 Isolation of the EXAFS and XANES features. 33
Figure 2.7 M_6 Janin Cluster (M=Pt, Au, or Rh) 38
Figure 2.8 Non-Janin type clusters used for FEFF 8.0 Calculations. 39
Figure 2.9 Illustration of the electrochemical cell for XAS studies 44

Chapter 3

Figure 3.1 Separation of EXAFS and XANES features 50
Figure 3.2 Cyclic voltammetry results 54
Figure 3.3 Fourier Transform fits for Au-SnO_x at Au L_3 and Sn K edges 56
Figure 3.4 Au L_3 absorption spectra, μ, for the Au-SnO_x/VC electrode 60
Figure 3.5 Δμ difference spectra for Au-SnO_x/VC and Au/VC 62
Figure 3.6 Experimental Δμ difference spectra of Au-SnO_x/VC at the Sn K edge 64
Figure 3.7 A comparison of N_{Au-Au} and Δμ amplitudes from Au/VC and Au-SnO_x/VC 66
Figure 3.8 Comparison of N_{Au-Au} and N_{Sn-Sn} in 10% Au, Au-SnO_x/VC 68
Figure 3.9 Comparison of N_{Au-Au} and $\Delta\mu_{mag}$ for10 and 20 wt.% Au, Au-SnO_x/VC 70
Figure 3.10 Electronic effects vs. Bifunctional Mechanism 73

Chapter 4

Figure 4.1 Illustration of TPPTP 82
Figure 4.2 Comparison of the EXAFS signals, kχ(k), for the Pt/C and Pt/TPPTP 89
Figure 4.3 Fourier transform of the EXAFS data for Pt/C and Pt/TPPTP 90
Figure 4.4 Illustration of 13 Pt atom cluster 93
Figure 4.5 Variation of EXAFS spectra with potential for Pt/TPPTP 95
Figure 4.6 Comparison of the EXAFS spectra in the region between 1.0 and 3.5 Å 96
Figure 4.7 Summary of the changes seen in the EXAFS data 97
Figure 4.8 Comparison of changes seen in the *in situ* XAS spectra 99
Figure 4.9 Comparison of Δμ signatures Pt/TPPTP and Pt-O/TPPTP 100
Figure 4.10 Molecular mechanics illustrations of the –O-P<tp and ≡O-P<tp ligands 102
Figure 4.11 Comparison of Δμ in the H region for Pt/TPPTP and Pt-O/TPPTP 103
Figure 4.12 CV curves for the thin-film catalyst layers 105

Figure 4.13 Comparison of Δμ for Pt colloids vs. Pt/VC (E-Tek) 106
Figure 4.14 Comparison of both ligands in the O/OH region 107
Figure 4.15 Plot of Δμ magnitudes for various Pt samples 108
Figure 4.16 Previously reported ORR specific activities 110
Figure 4.17 Previously reported Δμ magnitudes 112

Chapter 5

Figure 5.1 X-ray diffractograms of Rh-S electrodes 126
Figure 5.2 TEM images of Rh–S electrocatalysts 129
Figure 5.3 Room temperature 50 mV s^{-1} cyclic voltammograms of Rh-S electrodes 132
Figure 5.4 RDE results 134
Figure 5.5 In situ Rh K edge XANES signals 137
Figure 5.6 In situ Rh K edge k^2-weighted χ spectra 139
Figure 5.7 Fourier transform in situ spectra 140
Figure 5.8 Model clusters of RhS 141
Figure 5.9 Comparison Fourier transform data for the Rh_3S_4/C preferential phase 143
Figure 5.10 Plot of $\delta N_{Rh\text{-}Rh}$ for Rh/C and Rh_3S_4/C 148
Figure 5.11 Theoretical signatures for Rh_3S_4/C 150
Figure 5.12 Δμ signatures for Rh_xS_y/C in 1M TFMSA 152
Figure 5.13 Δμ signatures for Rh_xS_y/C in 6M TFMSA 154
Figure 5.14 Theoretical and experimental Δμ signatures for Rh_2S_3 and Rh_3S_4 155
Figure 5.15 Theoretical and experimental Δμ signatures for Rh/C 156
Figure 5.16 Linear fits of Δμ amplitudes for Rh-S catalysts 157

Chapter 6

Figure 6.1 Plot of calculated SO_n binding energies 171
Figure 6.2 Cyclic voltammograms of clean and poisoned Pt/VC 172
Figure 6.3 Isolation of XANES and EXAFS features 175
Figure 6.4 Illustration of SO_n adsorption geometries on Pt_6 clusters 179
Figure 6.5 FEFF 8.0 line shapes for S, SO_2, $SO_{3/4}$, 3f-O and H 182
Figure 6.6 The XANES spectra for a Pt/C electrode in 1M $HClO_4$. 183
Figure 6.7 The experimental Δμ spectra of non-poisoned Pt/VC in 1M $HClO_4$ 185
Figure 6.8 The experimental Δμ difference spectra of sulfur-poisoned Pt/VC in 1M $HClO_4$ 186
Figure 6.9 Fourier transforms of S-poisoned Pt and Pt_3Co 187
Figure 6.10 Plot of coordination number vs. potential for clean and poisoned Pt 189
Figure 6.11 Plot of |POS| and |NEG| from the experimental Δμ as a function of potential for clean Pt/VC. 195
Figure 6.12 |NEG| vs. potential for S poisoned Pt/VC 196
Figure 6.13 Comparison of |NEG| data from two different S-poisoned Pt/VC Runs 198
Figure 6.14 Comparison of |NEG| and CV plots for S-poisoned Pt and Pt_3Co 199
Figure 6.15 |NEG| vs. potential for sulfur-poisoned Pt_3Co/VC 201
Figure 6.16 Comparison of |POS| for clean Pt/VC and Pt_3Co/VC (as a function of potential) 202

Chapter 7

None

List of Tables

Chapter 1

Table 1.1 Comparison of various experimental techniques utilized to study catalysts 14

Chapter 2

Table 2.1 X-Ray absorption edges and core level excitations 30
Table 2.2 Summary of crystallographic parameters for Rh catalysts 40

Chapter 3

Table 3.1 Summary of EXAFS Results for 10 wt.% Au/SnO_x/VC at Au L_3 edge 61
Table 3.2 Summary of EXAFS Results for 10 wt.% Au/SnO_x/VC at Sn K edge 61
Table 3.1 Summary of EXAFS Results for 10 wt.% Au/VC at Au L_3 edge 61

Chapter 4

Table 4.1 Parameters of EXAFS fits 87

Chapter 5

Table 5.1 Crystallographic parameters of Rh-S electrodes 127
Table 5.2 Electrochemical Kinetics 135
Table 5.3 First shell EXAFS fit results for Rh_2S_3/C 144
Table 5.4 First shell EXAFS fit results for Rh_3S_4/C 145
Table 5.5 First shell EXAFS fit results for Rh/C 146

Chapter 6

Table 6.1 Parameters from EXAFS fits for a)Pt clean and poisoned and b)Pt_3Co clean and poisoned 191

Chapter 7

none

Chapter 1

Introduction

1.1 Introduction

Research into alternative energy sources has grown in recent years in part because of our need to reduce our dependence on foreign oil. Current research has also been focused on finding a substitute to gasoline-powered internal combustion engines, due to the deleterious effects of gasoline engine exhaust, particularly CO_2, on the environment. According to the Global Carbon Project[1], the United States recently led the world in greenhouse gas emissions until China surpassed us due to its rapidly developing economy.

The biggest contributing factor to the increase in global emissions is the consumption of fossil fuels. The 1850s saw the advent of the Industrial Revolution when CO_2 levels began to increase. CO_2 levels have increased nearly 40% since then from ~280 ppm to ~390 ppm and this is expected to increase with the continued burning of fossil fuels[2]. There are predictions, particularly from the Intergovernmental Panel of Climate Change, that this concentration will increase to a range of ~583 to ~987 ppm by 2100.[3]

The increasing concerns with global CO_2 emissions have stimulated the development of cleaner transportation fuels and overall lower-polluting technologies. Increased attention to fuel cells has been given as an alternative to the fossil fuel burning combustion engines, due in part to their superior fuel efficiency and performance. Fuel cells have efficiencies of nearly ~85-95%, as

opposed to the internal combustion engines which are only around 40% efficient[4]. However, even more importantly, they produce zero hydrocarbon emissions with hydrogen as a fuel[5]. Fuel cells are also attractive because they can be used as power sources in remote areas of the world. They can be utilized anywhere from space missions and military exercises to more routine applications, such as computers and cellular phones[6].

Even though much research has been conducted on fuel cells, and much investment has been made, large scale commercialization has not been realized due to issues involving the overall system complexity[7]. The problems are many and involve numerous variables. The performance of the fuel cell is largely dependent on a critical component: the electrocatalyst. This is an area where there is a surprising lack of detailed atomic level information concerning the most important processes; namely what really happens at the catalyst surface, including the reaction mechanisms for oxygen reduction on different catalysts, as well as mechanisms by which catalyst poisons hinder the fuel cell performance.

1.2 History of Pt-based Electrocatalysts for Fuel Cells

Platinum is the most common catalyst used in fuel cells and was used in the first fuel cell experiment. In 1839, Sir William Robert Grove invented the first fuel cell and was the first to show that a supply of electricity could be produced between two Pt wires via an electrochemical reaction as long as a fuel (hydrogen) and an oxidizer (oxygen) were being fed through the system.

Platinum supported on porous carbon is still the most popular choice for proton exchange membrane fuel cells (PEMFCs). The PEMFC is the the most commercially viable fuel cell to date. The workings of the PEMFC will be defined below. The Pt catalysts are normally highly dispersed with around 3-8 nm sized Pt particles[8]. There are many explanations as to why there is an enhanced activity seen at transition d-metal surfaces, particularly Pt. It is proposed that these metals donate their d-electrons at the surface for bonding with atomic and molecular adsorbates. According to most theories, this is because d-electron metals have low energy electronic states as

well as electron vacancy states that result in hybridization between d and the s,p electrons. These degenerate states can then readily accept or donate electrons to and from absorbed species. The more reactive metal surfaces have higher concentrations of degenerate electronic states, thus making them more reactive towards breaking and creating new bonds[9].

Figure 1.1 illustrates the density of states of Pt in a Pt_6 cluster, where the position of the Fermi level is indicated at -7.529 eV. Because the s, p, and d states of Pt occur above and below the Fermi level, they can contribute to adsorbate bonding quite effectively. Different occupancies in the d-band can also explain changes in adsorbate binding strengths on different metals.

1.3 Electrode Reactions in Fuel Cells

Fuel cells most often utilize the electrochemical reaction between hydrogen and oxygen to produce electricity and water. Hydrogen is fed to the anode side and oxidized while oxygen is fed to the cathode side and reduced. An acid electrolyte is usually incorporated, in the form of a Protron Exchange Membrane (PEM), which conducts protons from oxidized hydrogen to the cathode side to react with oxygen. This reaction, if carried out under optimal fuel cell conditions, will subsequently produce water:

$$\text{Anode:} \quad 2H_2 \rightarrow 4H^+ + 4e^- \qquad 1.1$$

$$\text{Cathode:} \quad O_2 + 4H^+ + 4e^- \rightarrow 2H_2O \qquad 1.2$$

with the overall net reaction:

$$2H_2 + O_2 \rightarrow 2H_2O. \qquad 1.3$$

Figure 1.2 illustrates the operation of a fuel cell, indicating the anode and cathode catalysts, as well as the flow of protons and electrons and their subsequent reactions. The electrolyte or PEM provides a path for protons via hydrophilic channels rich in water. The remaining part of the membrane is hydrophobic and provides the structural framework and barrier to other ion flow. The PEM material most often used is Nafion, a Dupont trademark name for a

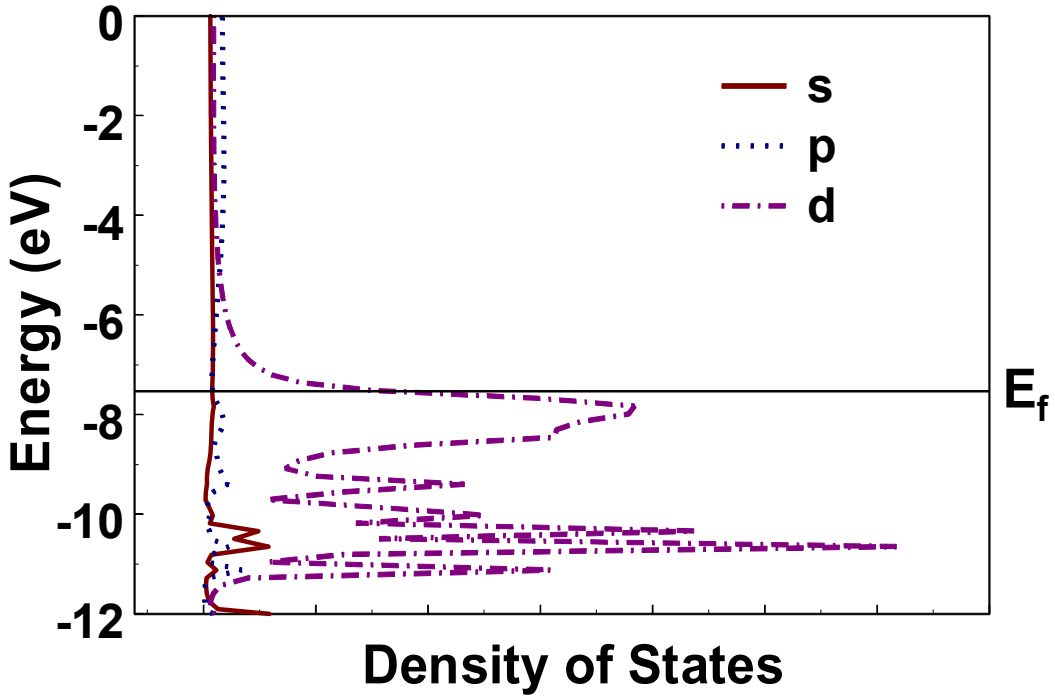

Figure 1.1 Density of states for the s, p, and d orbitals as obtained from a theoretical calculation utilizing quantum mechanics (FEFF 8.0 code)[10] on a Pt_6 cluster pictured in Figure 1.1 The Fermi level is indicated at -7.529 eV.

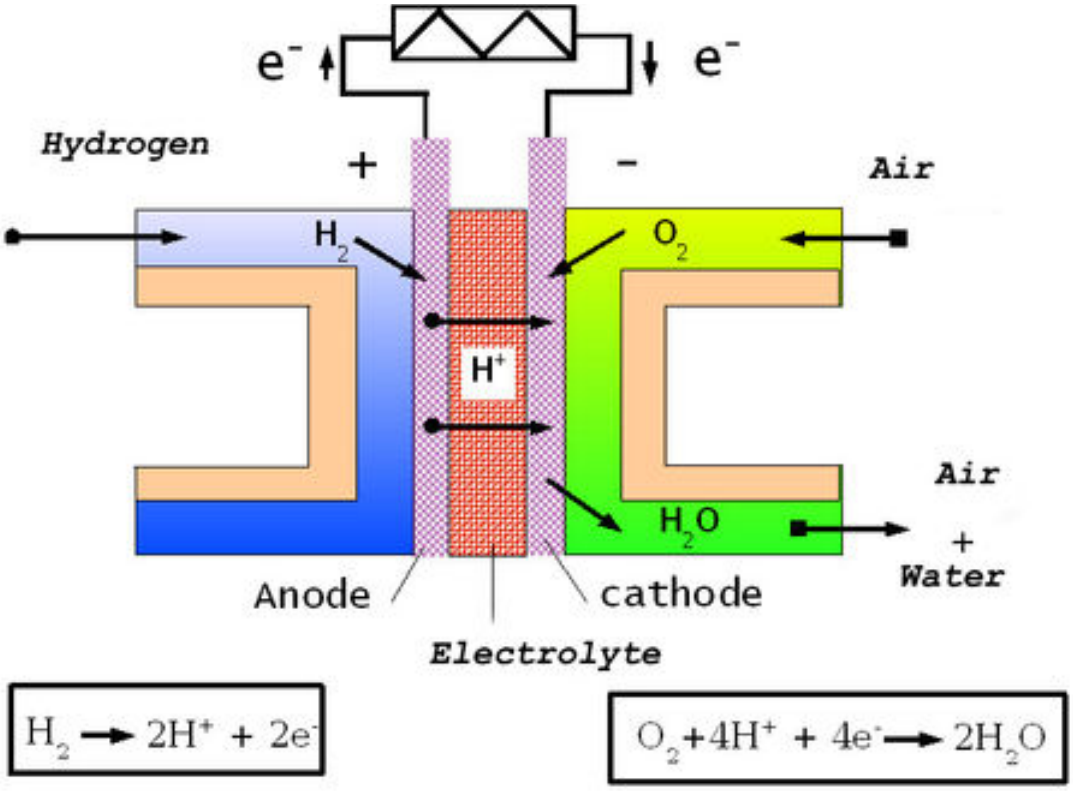

Figure 1.2 Schematic of a fuel cell including the anode and cathode catalysts as well as the flow of protons and electrons and their subsequent reactions. Figure taken from www.efuelcell.biz

trifluoro methyl sulfonic acid based material. The 4-electron cathodic reaction in Eq. 1.3 is vital in fuel cell catalysis. If this reaction does not occur correctly, then a by-product like peroxide may form which will decrease the efficiency of the fuel cell. This will be described in more detail later[11].

1.4 Adsorbate-electrode interactions considered in this thesis

The aim of this thesis is to investigate the chemistry of adsorbate-electrode interactions, support effects, and the fundamental properties of adsorbed species on platinic and non-platinic electrocatalysts and their effect on the ORR. Most commercial electrocatalysts generally consist of metal clusters 3-8 nm in size which are supported on a carbon substrate. The motivation is to obtain an atomic level understanding of the reaction mechanisms from adsorbed species on an electrode interface and the changes that occur to the catalyst under reaction conditions. Metal-support interactions between Au nanoparticles supported on a tin oxide support, using in situ XAS, are studied in Chapter 3. The changes that occur in this catalyst will then be used to explain its effect on the ORR. Chapter 4 describes the analyses of catalysts with incorporated organic ligands, specifically triphenyl phosphate triphosphonate (TPPTP) on Pt nanoparticles. The ligands serve to both stabilize Pt particles through a support/ligand effect, and to make these catalysts more ORR efficient than unmodified Pt nanoparticles. Both of these chapters reveal how altering the chemical environment of the catalyst surface can inhibit OH poisoning and ultimately improve ORR performance.

Non-platinic catalysts are studied in Chapter 5, namely a Rh based chalcogenide of the type Rh_xS_y which possessed a complicated multiphase structure. The relative stability of these phases was studied, and that phase that contributes most to the ORR activity is indicated. Finally, in Chapter 6, a analysis of the sulfur poisoning process on Pt and Pt_3Co alloys provides a more detailed understanding of which sulfur species exist at certain potentials.

The topics from each chapter are briefly introduced below in separate subsections. These studies reveal reaction mechanisms that occur in an electrochemical environment and how

these mechanisms contribute to the overall performance of the catalyst. Many details and intricacies are revealed at an atomic scale level using x-ray absorption spectroscopy (XAS), which is introduced below, with full details given in Chapter 2.

Knowledge of the reaction mechanisms that are responsible for the oxidation and reduction of adsorbates on catalyst surfaces are important because such knowledge can provide direction for improved design and development of better catalysts. Current flow in a fuel cell is dependent on a variety of parameters ranging from the crystal orientation of the electrode surface to the adsorbate's affinity and binding site on the electrode surface[12] . Identification of an adsorbate and determination of its orientation on the catalyst surface from the start of the electrochemical fuel cell process to the end is crucial to fully understanding the mechanistic details of electrocatalysis.

One major goal of fuel cell research includes an understanding of deleterious effects of poisons on Pt during electrochemical operation. Although Pt and Pt alloys are very popular in fuel cell catalysis, they are susceptible to poisoning and are also very expensive [69] . Attempts at using other platinic metals such as Rh and Au have been investigated. There have also been studies on depositing noble metals on activating supports to enhance ORR and reduce poisoning. Altering the chemical environment of Pt catalysts by incorporating ligands has also been studied. These methods have all been incorporated in order to reduce poisoning, lower the loading of the catalysts, and reduce costs. *In situ* spectroscopic techniques can provide a more detailed look at the adsorption processes; however, the electrochemical environment often adds interferences from the bulk electrolyte. As a result, determination of the adsorption sites *in situ* under operating circumstances have traditionally been difficult.

1.4.1 Improving Oxygen Adsorption on Pt Electrocatalysts

The oxygen reduction reaction on Pt is a vital reaction in electrocatalysis that occurs at the cathode, eq. (1.2). The adsorption of molecular oxygen, its dissociation, and formation of subsurface oxide under operation in an electrode make the ORR a very complicated reaction.

Water activation leading to OH or O adsorption on Pt and even oxidation of Pt in electrolyte occurs simultaneously with O_2 reduction:[13,14,15]

$$Pt + H_2O \rightarrow PtOH + H^+ + e- \quad 1.6$$

$$PtOH \rightarrow PtO + H^+ + e^- \quad 1.7$$

$$PtO + H_2O \rightarrow PtO_2 + 2H^+ + 2e^- \quad 1.8$$

This process poisons the Pt surface for O_2 reduction; however, the exact details of this mechanism remain unclear and are the subject of various studies.

At very high O coverage, it is observed that a surface oxide layer is formed on platinum. The evidence for this Pt-OH place-exchange reaction comes in part from the roughening of the Pt surface at high coverage[16,17,18]. The sequence of reactions, eqs. 1.6-1.8, was confirmed recently by Teliska[19], et. al., who found that at low coverage, OH absorbs originally in a 1-fold atop position (eq. 1.6), which takes place on the steps and edges of small Pt clusters. As coverage of O increases, O proceeds to more coordinated positions (eq. 1.7); first in a 2-fold site near edges and corners, then gradually to 3-fold sites on the (111) planes. Eventually Pt-OH place-exchange, eq. 1.8, which occurs at around 0.8V on small clusters, leaves O in 4-fold sites below the surface. This water activation mechanism has been heavily studied because the OH species that form on Pt atoms at potentials above 0.8V poisons the surface by blocking Pt sites required for the ORR. OH formation can occur either because of water activation or from the reaction with O_2 itself. But One reason that a PEM or other concentrated electrolyte such as concentrated phosphoric acid is used in fuel cells is to reduce the amount of water at the Pt surface and thereby reduce water activation.[20]

The electrochemical performance of Pt needs improvement because of the slow kinetics of the ORR. This results in high overpotentials (up to 0.4 volts before significant current flow)[21]

and requires use of Pt loadings that are too high for commercial use[22]. There have been efforts to increase Pt performance by combining Pt with other transition metals[23,24,25,26,27,28,29,30,31,32,33] or to replace it altogether by using other less expensive metals instead of Pt[34,35,36, 37]. One factor contributing to the large overpotential in the ORR is the OH posioning of the Pt surface described above. A strong Pt-O bond makes H_2O removal difficult, and H_2O is the final product in the ORR. Thus a signficant goal is to reduce the Pt-OH bond strength and thereby decrease the ORR overpotential.

A common approach to altering the Pt-O bond strength is through alloying the Pt nanoparticles with a less expensive d-metal[38]. Bimetallic nanoparticles have been shown to enhance the ORR. It has been seen that Pt-Fe and Pt-Cr alloys inhibit OH poisoning the most due to a Pt "skin" on the surface. An electronic effect derived from the Fe and Cr atoms worked best at inhibited OH formation. However, there can be variances in atom distribution and size depending on synthesis procedures which the ORR highly depends on[19,39].

Much attention has been given to incorporating ligands into Pt electrocatalysts to improve the catalyst under study. Ligands can affect the selectivity of metal nanoparticles and also influence the electronic properties of the metal core[40,41,42]. Changes in the electronic properties of the metal core, due to changes in the protecting ligand shell, were observed in $N(alkyl)_4Cl$-stabilized Pd nanoparticles[40,41]. Ligand-stabilized Pt nanoparticles have also been investigated as prospective electrocatalysts due to their ability to delay the onset of OH poisoning[43,44,45]. However, a detailed description of how these novel catalysts work has yet to be provided. Chapter 4 will present XAS results on the use of triphenylphosphine triphosphonate ligands that will provide a unique insight into how this ligand provides enhancement of the ORR on Pt.

1.42 Oxygen Adsorption on Au Electrocatalysts

Gold is usually inactive in the acidic environment of PEMFCs because it does not adsorb molecular oxygen, which is the first step in the ORR[13,14]. Recently, the rate-limiting step of the

ORR on Pt catalysts has been related to the strength of the Pt-O bond, and density functional theory (DFT) studies on Pt (111) crystals in a vacuum have confirmed electrochemical results.[46] As stated previously, the Pt-O bond is relatively strong compared to the Au-O bond; when the 2p orbitals from the oxygen combine with the 5d orbitals of gold, largely occupied antibonding states, these antibonding states are produced making the net Au-O bond strength weak.[47]

It has been found that molecular oxygen does not adsorb on low-index plane single Au crystals in the temperature range from 300 to 500K even at pressures of 1400 Torr.[48] Several investigations were conducted during the 1970s that suggested there was an activated adsorption of oxygen on Au forming a disordered layer on Au (111) between 373 and 873K[49] and a possible surface oxide which was stable up to 1073K.[50] However, these findings are controversial due to the possible formation of surface contamination by calcium and silicon oxides, forming partial layers of their oxides[51,52,53].

Supported gold catalysts have yielded more promising results for ORR. However there has been disagreement in the literature on whether the increased reactivity is due to the smaller particle size or to some interaction involving the support. Early research described a detection of oxygen adsorption[54,55,56]. Some reported a "slight" uptake of oxygen on Au/TiO_2[57,58] and it was found that there was a sufficient amount of oxygen present when Au is supported on various other oxides that were prepared by a deposition-precipitation technique. This allowed coverage estimates to be made by temperature programmed desorption (TPD)[59]. A study on Au/SiO_2 indicated that enough oxygen adsorbed so that Au particle size estimates could be made, although the results were not fully reliable[60]. There has also been spectroscopic evidence[61,62,63] that CO and O can adsorb onto a single Au atom; yielding an intermediate in producing CO_2. Pretreating the supported Au catalysts under oxidizing conditions and the importance of an optimal choice of calcination temperature suggested that the high activity for CO oxidation is related to the mode of oxygen interaction.

In an electrochemical environment, Au has exhibited several instances where it does proceed with the four-electron ORR. In acid, the ORR at Au usually requires very high overpotentials, which make Au a poor choice. ORR reactivity has been reported in base at lower overpotentials[64,65]. Oxygen reduction at Au/VC (Vulcan carbon) in acid, and in base, at high overpotentials usually produces peroxides (Eq. 1.9):

$$O_2 + 2H^+ + 2e^- \rightarrow H_2O_2. \qquad 1.9$$

Some research has been conducted using tin-oxide as a support to enhance the activity of various d-metals like Au and Pt. Pt/SnO_2 was found to be very effective for methanol oxidation[66,67] and oxygen reduction. Baker[68] et. al. found that tin-oxide was sufficiently stable to allow the ORR in a low pH range (0 to 1). Metal oxide supports are favorable in electrochemical catalysis because they are relatively inexpensive, ionically conductive, due to their redox couples which aid in the supply of protons for the ORR, and most are resistive to corrosion; especially tin oxide. However, the effects of incorporating metal oxides as supports for noble metal catalysts to enhance ORR activity has yet to be fully understood. Chapter 3 will present XAS results that confirm that the SnO_2 support exerts a strong ligand effect, but more importantly contributes directly to the ORR reaction at the Au-support interface.

1.4.3 Rhodium Chalcogenides as Electrocatalysts

There have not been many cases of using rhodium in electrocatalysis. It is also highly unlikely that Rh or Rh-based chalcogenides (i.e. RhS) will ever replace Pt in PEMFC or direct methanol fuel cell (DMFC) applications because of their costs. Rh is 5-10 times more costly than Pt[69]. However, despite their cost they are quite useful as industrial catalyts; particularly in automobile catalytic converters and for catalytic carbonylation of methanol to produce acetic acid by the Monsanto process[70,71].

Recently, the most promising alternative to Pt in electrocatalysis have been transition-metal chalcogenides[72,73]. Several of these chalcogenides, particularly RuSe, have exhibited

reasonably high ORR performance[74,75], and seem to be relatively unaffected by poisons that typically poison Pt in methanol[76,77,78] and in the presence of halides[79]. However, due to the toxicity of Se, ReSe catalysts also will most likely not be used in consumer applications[72,80].

The Rh_xS_y/C electrocatalyst produced and patented by De Nora has exhibited the highest ORR performance and stability of the sulfide-based chalcogenide electrocatalysts[81]. The performance and structural characteristics of the Rh_xS_y/C electrocatalyst render it an ideal model compound for investigation of the ORR pathway on a sulfur-based chalcogenide electrocatalysts. Even though this catalyst does not exhibit the high level of methanol tolerance of Ru-based chalcogenides[82], it is well suitable for chlorine gas generation.

Characterization of Rh_xS_y/C has been very difficult using standard methods like X-ray Diffraction (XRD) due to its structural complexity. The catalyst is comprised of three very different phases: Rh_2S_3, Rh_3S_4, and $Rh_{17}S_{15}$[83,84,85]. The big question that has yet to be answered is which phase is active and contributes most to the ORR. Chapter 5 presents results of a study utilizing a combination of XRD, XAS, TEM, and electrochemical measurements, providing an assessment of the relative stability and minimum requirements for the ORR on Ru_xS_y.

1.4.4 Sulfur Poisoning on Pt and Pt-Alloy Electrocatalysts

PEMFCs must maintain high ORR activity over extended periods of time for efficient operation. This activity can be hindered by factors such as the corrosion and poisoning of Pt. Sulfur, often found in either the fuel fed to the anode or the air fed to cathode in Pt fuel cells[86], can be a problem because it can block active sites on Pt and hinder both the H oxidation reaction (HOR) and the ORR.

It has been well documented that as sulfur is cycled in a Pt electrode. It starts out as zero-valent S (S^0) at 0.05V. As the potential increases, it is believed that sulfur becomes oxidized to sulfate (SO_4^{2-}) and then desorbs from the surface[87,88,89,90,91,92,93,94,95,96,97,98]. In situ Fourier Transform (FTIR) spectroscopy showed that SO_2 adsorbed onto the surface at 0.5V oxidizes to

SO_4^{2-} at a potential range from 0.5V to 1.5V. However, coulometric analysis indicated that SO_2 adsorbed onto Pt at 0.65V and oxidized at potentials both higher and lower than 0.65V[99]. As of now, it is very difficult to discern between what species of sulfur are on the electrode surface, especially in the fuel cell operating range (0.6 to 0.8V).

As discussed previously, alloying Pt with another transition metal (e.g. Co) can improve the ORR and inhibit OH poisoning on Pt due to a ligand effect caused by the alloying metal. A recent study has confirmed that initial sulfur coverage is higher on Pt_3Co than Pt, due to decreased surface OH coverage on the alloyed Pt. However, sulfur species are more easily removed from the Pt_3Co surface than Pt; and Pt suffers a higher loss of mass activity[100]. A precise and accurate picture of the type of reaction mechanism which occurs in these catalysts, as well as adsorbate speciation during poisoning has yet to be determined. Chapter 6 presents XAS results which reveal for the first time the changes of S oxidation levels spectroscopically on the surface, why cycling is necessary to remove S from a Pt electrode, and why the cleaning process is greatly enhanced in the case of Pt_3Co.

1.5 Use of X-Ray Absorption Spectroscopy

The development of modern surface science techniques over the past decades has allowed for the investigation of numerous properties of adsorption at the atomic level. These techniques offer information about the electrode surface and the molecular identity of the species adsorbed at the electrode surface. Numerous techniques have been used to study the electrode surface; however, many require a gas phase or *ex situ* environment as summarized in Table 4.1.

X-Ray absorption spectroscopy (XAS) including X-ray absorption Near Edge Spectroscopy (XANES) and Extended X-ray Absorption Spectroscopy (EXAFS) (to be discussed in the next chapter) are *in situ* spectroscopic technique that can provide unique site-specific adsorbate bonding information and particle size information. Further, these techniques do not

Table 1.1 Comparison of various spectroscopic techniques utilized to study catalysts

Technique	Information obtainable	In situ	Disadvantages/advantages
XAS (XANES/EXAFS)	Ads. Binding site Particle size	Yes	Synchrotron required Complex theoretical analysis
XRD	Crystal structure	Yes	Long range order required Complex theoretical analysis
XPS/Auger	Electronic structure	No	UHV required
TPD	Ads. Binding energy	No	UHV required

Vibrational spectroscopies

ATR, IRAS	Binding prop	Yes	Noisy differential/difference techniques Dipole selection rules make 3-fold site vibrations invisible
IR/Raman	Binding prop	Yes	Huge bulk electrolyte adsorption
HREELS	Binding prop	No	UHV required
SHG, SFG SNIFTERS	Binding prop	Yes	Noisy differential/difference techniques Dipole selection rules make 3-fold site vibrations invisible
NIS	Binding prop	No	Huge surfaces areas required because of small cross-section for scattering

suffer from the adsorption by the bulk electrolyte such as occurs in the IR region. X-ray Diffraction (XRD) of course also provides detailed structural properties but it requires long-range order, which is generally not present in real high surface area catalysts. X-ray Photoelectron (XPS) and Auger (AES) electron spectroscopies can provide detailed electronic structure information, unfortunately they require ultrahigh vacuum (UHV). A very powerful technique for providing detailed adsorbate bond strengths is temperature programmed desorption (TPD), unfortunately this also can only be utilized in vacuum.

XAS uses synchrotron radiation, which has wide applications not only in the field of catalysis but in those of chemistry, biology and environmental science to name a few. Synchrotron radiation offers a tunable wavelength which enables certain atoms of interest to be studied. Synchrotron radiation also has higher intensity compared to most conventional light sources and a small spot size which allows for *in situ* determinations.

Vibrational spectroscopy involving infra-red (IR) and Raman absorption are powerful techniques that provide detailed information on different binding sites, and bond stretching frequencies, but they are severely hindered by the large absorption by the bulk water of the electrolyte. Several attempts to eliminate this absorption by taking differences or differentials (such as in the Subtraction and Normalization Fourier Transform Infrared Spectroscopy (SNIFTIRS), Second Harmonic Generation (SHG) and Sum Frequency Generation (SFG) techniques) have been developed, but these often still produce noisy data, and because of dipole selection rules cannot probe vibrations coming from the dominant adsorbate species in the three-fold binding sites. Other vibrational techniques such as High Resolution Electron Energy Loss (HREELS) and Neutron Inelastic Scattering (NIS) enable non-dipole transitions to be observed, but they are not *in situ* techniques. Thus XAS remains as a powerful and unique technique for studying particles under an electrolyte[101,102]

XAS analysis has been limited to providing geometric information on systems with short-range order, i.e. the normal Extended X-Ray Absorption Fine Structure (EXAFS) technique[103]. It

has been reported that the electron scattering producing the Pt L_3 XANES is very sensitive to the adsorption of both O and H.[104] Using a novel analysis technique that isolates this Pt-adsorbate scattering, combined with theoretical calculations, allows for the *in situ* determination of adsorption sites on platinum electrodes utilizing Pt L_3 X-ray Absorption Near Edge Structure (XANES).

One disadvantage of XAS has been the complex theoretical analysis required to obtain information from the data. XANES data can now be interpreted utilizing full multiple-scattering theoretical results from the FEFF8.0 code[105].

1.6 References

[1] Raupach, M.R; Marland, G.; Ciais, P.; Le Quéré, C.; Canadell, J.G.; Klepper, G.; Field, C.B.; *Proc. Nat. Acad. Sci.,* **2007,** *104*, 10288,
[2] Adam, D.; *The Guardian*, May 12, **2008**
[3] Environmental Protection Agency, IPCC, **2007**: Climate Change 2007: The Physical Science Basis. Contribution of Working Group I to the Fourth Assessment Report of the Intergovernmental Panel on Climate Change [Solomon, S., D. Qin, M. Manning (eds.)].
[4] Hydrogen and Fuel Cell Letter January **2003.**
[5] Gottesfeld, S.; in *Handbook of Fuel Cells: Fundamentals, Technology and Applications*, W. Vielstich, A. Lamm, and H.A. Gasteiger Editors, John Wiley & Sons, Ltd. Chichester, England **2003**
[6]Sandstede, G.; Cairns, E.J.; Bagotsky, V.S.;Wiesener, K.; in *Handbook of Fuel Cells: Fundamentals, Technology, and Applications*, W. Vielstich, A. Lamm, and H.A. Gasteiger Editors, john Wiley & Sons, Ltd., Chichester, England **2003**
[7] Ogden, J.M.; in *Handbook of Fuel Cells: Fundamentals, Technology and Applications*, W. Vielstich, A. Lamm and H.A. Gasteiger Editors, John Wiley & Songs. Ltd., Chichester, England **2003**
[8] Christensen, P.; Hammet, A.; *Techniques and Mechanisms in Electrochemistry* 228, Blackie A&P (Imprint of Chapman&Hall) Glasgow, **1994**.
[9] Nørskov, J.K.; *Phys. Rev. B.***1982,** *26*, 2875
[10] Ankudinov, A.L.; Rehr, J.J.; Low, J.; Bare, S.R. *Phys. Rev. Lett.,* 2001, *86(8),* 1642
[11] Wieckowski A.; Vayenas, C.G.; *Catalysis and Electrocatalysis at Nanoparticle Surfaces,* A. Wieckowski, E.R. Savinova, and C.G. Vayenas, Editors, Marcel Dekker, New York **2003**
[12] Tidswell, I.M.; Markovic, N.M.; Ross, P.N. *J. Electroanal. Chem.,* **1994**, *376*, 119
[13] Adzic, R.R.;Lipowski, J.; Ross, P.N.; eds. in *Electrocatalysis*, *197*, Wiley-VCH, Inc., **1998**
[14] Adzic, R.R.; in Electrocatalysis, (J, Lipkowski, P.N. Ross, eds.), *205*, Wiley-VCH, Inc., **1998**
[15] Yeager, E.; Razaq, M.; Gervasio, D.; Razaq, A.; Trick, D.; *J. Serb. Chem. Soc.* **1992**,*51(12),* 819
[16] Wagner, F.T.; Ross, P.N.; *J. Electroanal. Chem.,* **1983,** *150,* 181
[17] You, H.; Zurawski, D.J.; Nagy, Z.; Yonco, R.M.; *J. Phys. Chem.,***1994,** *100(6)*, 4699
[18] You, H.; Nagy, Z.; *Physica B.,***1994,** *198*, 187
[19] Teliska, M.; O'Grady, W.E.; Ramaker, D.E.; *J. Phys. Chem. B.,***2005,** *109*, 8076
[20] Tafel, J.; *Berichte der Deutschen Chem. Ges.,* **1898**, *301*, 285
[21] Bernardi, D.M.; Verbrugge, M.W. *J. Electrochem. Soc.,***1992***, 139*, 2477
[22] Gasteiger, H.A.; Panels, J.E.; Yan, S.G. *J. Power Sources,* **2004,** *127*, 162
[23] Zhang, J.; Vukmirovic, M.B.; Sasaki, K.; Nilekar, A.U.; Mavrikakis, M.; Adzic, R.R.; *J. Am. Chem. Soc.,***2005,** *127*, 12480
[24] Zhang, J.; Vukmirovic, M.B; Xu, Y.; Mavrikakis, M. ; Adzic, R.R; *Angew. Chem. Int. Ed.*, **2005**, *44*, 2132
[25] Zhang, J.; Lima, F.H.B.; Shao, M.H.; Sasaki, K.; Wang, J.X.; Hanson, J.;. Adzic, R.R.*;J. Phys. Chem. B.*, **2005**, *109*, 22701
[26] Marković, N.M.; Schmidt, T.J.; Stamenković, B.; Ross, P.N.; *Fuel Cells*, **2001** *1*, 105
[27] Meng, H.; Shen, P.K.; *J. Phys. Chem. B,* **2005,** *109*, 22705
[28] Anderson, A. B.; Roques, J.; Mukerjee, S; Murthi, V.S; Marković, N.M.;. Stameković, V.; *J. Phys. Chem. B,* **2005**, *109*, 1198
[29] Stameković, V.; Schmidt, T.J.; Ross, P.N.; Marković, N.M.; *J. Phys. Chem. B,* **2002**, *106*, 11970
[30] Gulla, A.F.; Saha, M.S.; Allen, R.J.; Mukerjee, S.; *J. Electrochem. Soc.*,**2006**, *153*, 366

[31] Koffi, R.C.; Countanceau, C.; Garnier, E.; Leger, J.M.; Lamy, C.; *Electrochim. Acta.*, **2005**, *50*, 4117
[32] Sode, A.; Li, W.; Yang, Y.; Wong, P.C.; Gyenge, E.; Mitchell, K.A.R.; Bizzotto, D.; *J. Phys. Chem. B.,***2006***,110,* 8715
[33] Ralph, T.R.; Hogath, M.P.; *Platinum Metals Rev.*, **2002**, *26,* 3
[34] Fernandez, J.L ; Rghuveer, V.; Manthiram A.; Bard, A.J.; *J. Amer. Chem. Soc*, **2005**, *127*, 13100
[35] Raghuveer, V.; Manthiram, A.; Bard, A.J.;*J. Phys. Chem. B,***2005***, 109*, 22909
[36] Fernandez, J.L.; Walsh, D.A.; Bard, A.J.;*J. Am. Chem. Soc.*, **2005**, *127*, 357
[37] Wang, B.J.; *J. Power Sources,* **2005***, 152*, 1
[38] Chan, K.Y. ; Ding, J.; Ren, J.; Cheng, S.; Tsang, K.Y.;*J. Mater. Chem*, **2004,** *14,* 505
[39] Teliska, M.; Murthi, V.S.; Mukerjee, S.; Ramaker, D.E.; *J. Electrochem. Soc.*, **2005**, *152*, A2159
[40] Modrow, H.; Bucher, S.; Hormes, J.; Brinkmann, R.; Bönnemann, H.; *J. Phys. Chem. B*, **2003,** *107*, 3684
[41] Bucher, S.; Hormes, J.; Modrow, H.; Brinkmann, R.; Waldöfner, N. ; Bönnemann, H.; Beuermann, L.; Krischok, S.; Maus-Friedrichs, W.; Kempter, V.; *Surf. Sci.***2002***, 497*, 321
[42] Larsson, J.A.; Nolan, M.; Greer, J.C.; *J. Phys. Chem. B,* **2002**, *106*, 5931
[43] Ye, H.; Crooks, R.M.; *J. Am. Chem. Soc.*, **2005**, *127*, 4930
[44] Zao, M.; Crooks, R.M.; *Adv. Mater.*, **1999**, *11*, 217
[45] Kostelansky, C.N.; Pietron, J.J.; Chen, M.; Dressick, W.J.; Swider-Lyons, K.E.; Ramaker, D.E.; Shroud, R.M.; Klug, C.A.; Zelakiewicz, B.S.; Schull, T.L.; *J. Phys. Chem. B,* **2006***,110*, 21487
[46] Stamenkovic, V.; Mun, B.S.; Mayrhofer, N.M.; Ross, P.N.; Markovic, N.M.; Greeley, J.; Nørskov, J.K.; *Angew. Chem. Int. Ed,* **2006***, 45*, 2897
[47] Zhen-Hua, Z.; Hui-Qiu, D.; Wei-Xue, L.; Wang-Yu, H.; *Acta. Physica Sinica-Chinese Ed.*, **1953**, *55*, 3157
[48] Sault, A.G.; Madix, R.J.; Campbell, C.T.; *Surf. Sci*., **1986**,*169*, 347
[49] Schrader, M.E.; *Surf. Sci.,* **1978**, *78*, L227
[50] Chester, M.A.; Somoraj, G.A.; *Surf. Sci.,* **1975**, *52*, 21
[51] Haruta, M.; *Catal. Today*, **1997**, *36*, 153
[52] Canning, N.D.S.; Outka, D.; Madix, R.J.; *Surf. Sci.*, **1984**, *141*, 240
[53] Huang, L.; Zeppendfeld, P.; Chevrier, J.; Comsa, G.;*Surf. Sci.,***1996,** *352*, 285
[54] Endow, N.; Wood, B.J.; Wise, H.;*J. Catal.,***1969***,15,* 315
[55] Macdonald, W.; Hayes, K.E.; *J.Catal.,* **1970**, *18*, 115
[56] Fukushima, T.; Galvagno, S.; Parravano, G.; *J. Catal.,***1979***, 57*, 177
[57] Lin, S.D.; Bollinger, M.; Vannice, M.A.; *Catal. Lett*., **1999**, *17*, 245
[58] Lin, S.D.; Vannice, M.A.; *Catal. Lett.,* **1991**, *10*, 47
[59] Haruta, M.; Tsubota, S.; Kobayashi, T.; Kageyama, H.; Genet, M.J.; Belmon, L.; *J. Catal*., **1993**, *144*, 175
[60] Yates, D.J.C.; *J. Coll. Interf. Sci.,***1969***, 29*, 194
[61] Haruta, M.; *Catal. Today,* **1997***, 36*, 153
[62] Haruta, M.; *Catal. Surveys Japan*, **1997**, *1*, 61
[63] Boccuzzi, F.; Chiorino, A.; Tsubota, S.; Haruta, M.;*J. Phys. Chem*, **1996**, *100*, 3265; *Catal. Lett.,* **1994,** *29*, 225
[64] Strbac, S.; Adzic, R.R.; *Electrochim. Acta.,* **1996***, 41*, 2908
[65] Strbac, S.; Adzic, R.R.; *J. Electroanal. Chem.,***1996***, 403*, 169
[66] Janssen, M. M. P; Moolhuysen, J.;*Electrochim. Acta* **1976,** *21*, 861.
[67] Watanabe, M.; Venkatesan, S.; Laitinen, H.A.; *J. Electrochem. Soc.* **1983**, *130*, 59.

[68]. Baker, W.S; Pietron, J.J.; Teliska, M.; Bouwman, P.; Ramaker, D.E.; Swider-Lyons, K.E.*J. Electrochem. Soc*. **2006,** *153*, A1702
[69] Johnson-Matthey. The Platinum Metals Report: May 2008. In The Platinum Metals Report; www.platinum.matthey.com, **2008**; Vol. 2008.
[70] George, M.W. "2006 Minerals Yearbook: Platinum-Group Metals". United States Geological Survey USGS.
[71] Shelef, M. ; Graham, G.W.; *Catal. Rev.*, **1994**, *36*, 433
[72] Alonso-Vante, N.;. Novel nanostructured material based on transition-metal compounds for electrocatalysis. In Catalysis and Electrocatalysis at Nanoparticle Surfaces; A. Wieckowski, R.E. Savanova
[73] Vante, N. A. ;Tributsch, H.; *Nature,* **1986**, *323*, 431
[74] González-Huerta, R. G.; Chávez-Carvayar, J. A.; Solorza-Feria, O. J.; *Power Sources,* **2006**, *153,* 11
[75] Shukla, A. K.; Raman, R. K.; *Annu. Rev. Mater. Res.* **2003,** *33,* 155
[76] Reeve, R. W.: Christensen, P. A.; Dickinson, A. J.; Hamnett, A.; Scott, K.; *Electrochim. Acta*.,**2000**,*45***,** 4237
[77] Reeve, R. W.; Christensen, P. A.; Hamnett, A.; Haydock, S. A.; Roy, S. C.; *J. Electrochem. Soc.* **1998,** *145*, 3463
[78] Tributsch, H.; Bron, M.; Hilgendorff, M.; Schulenburg, H.; Dorbandt, I.; Eyert, V.; Bogdanoff, P.; Fiechter, S.; *J. Appl. Electrochem.* **2001**, *31*, 739
[79] Ziegelbauer, J. M.; Gullá, A. F.; O'Laoire, C.; Urgeghe, C.; Allen, R. J.; Mukerjee, S.; *Electrochim. Acta.,***2007***, 52*, 6282
[80] Cao, D.; Wieckowski, A.; Inukai, J.; Alonso-Vante, N.; *J. Electrochem. Soc,*. **2006**, *153***,** A869
[81]Ziegelbauer, J. M.; Gatewood, D.; Gullá, A. F.; Ramaker, D. E.; Mukerjee, S.; *Electrochem. Solid-State Lett.*, **2006,** *9,* A430
[82] Papageorgopoulos, D. C.; Liu, F.; Conrad, O.; *Electrochim. Acta*, **2007**, *52*, 4982
[83] Beck, J.; Hilbert, T.; *Z. Anorg. Allg. Chem.,* **2000**, *626*, 72
[84] Geller, S.; *Acta Cryst.* **1962**, *15,* 1198
[85] Parthe, E.; Hohnke, D. K.; Hulliger, F.; A*cta Cryst.* **1967**, *23*, 832
[86] Chin, D-T.; Howard, P.D.; *ibid*., **1986**, *133*, 845
[87] Swider , K. E.; Rolison, D. R.; *J. Electrochem. Soc.*, **1996**, *143*, 813 .
[88] Swider, K. E.; Rolison, D. R.; *Langmuir,* **1999**, *15*, 3302
[89] Seo, E. T.; Sawyer, D. T.; *Electrochim. Acta,* **1964,** *7*, 184
[90] Seo, E. T.; Sawyer, D. T.; *Electrochim. Acta*, **1965,** *10*, 239
[91] Loucka, T.; *J. Electroanal. Chem. Interfacial Electrochem*., **1971**, *31*, 319
[92] Contractor, A. Q.; Lal, H.; *J. Electrochem. Soc*., **1978,** *93*, 99
[93] Appleby, A. J.; Pichon, B.;*J. Electrochem. Soc*., **1979**, *95,* 59,
[94] Szklarczyk, M.; Czerwinski, A.; Sobkowski, J.;*J. Electroanal. Chem. Interfacial Electrochem.*, **1982**, *132*, 263
[95] Floral, M. J.; Langer, S. H.; *J. Electroanal. Chem. Interfacial Electrochem.*, **1988**, *246*, 193
[96] Spotnitz, R. M.; Colluci, J. A.; Langer, S. H.; *J. Electroanal. Chem. Interfacial Electrochem.*, **1983**, *28*, 1053
[97]Quijada, C.; Rodes, A.; Vazquez, J. L.; Perez, J. M.;Aldaz, A.; *J. Electroanal.Chem.*, **1995**, *394*, 217
[98]Quijada, C.; Rodes, A.; Vazquez, J. L.; Perez, J. M.; Aldaz, A.; *J. Electroanal.Chem.*, **1995**, *398,* 105
[99] Matveeva, E. S.; Shepelin, V. A.; Kasathin, E. V.; *Sov. Electrochem.*, **1982**, *18*, 634
[100] Garsany, Y.; Baturina, O.; Swider-Lyons, K.E.; *J. Electrochem. Soc.,* in submission
[101] Ramaker, D.E.; Koningsberger, D.C.; *Phys. Rev. Lett.,***2002***,89*, 139701

[102] Teliska, M.; O'Grady, W.E.; Ramaker, D.E.; *J. Phys. Chem. B.,***2001**.*108*, 2333
[103] Mukerje e, S.; McBreen, J.; Srinivasan, S.; *Proceedings Electrochemical Society,* **1995**, *38*, 95
[104] Ramaker, D. E.; Koningsberger, D.C.; *Phys. Rev. Lett.,***1981***,128(5),* 956,
[105] Ankudinov, A.L.; Ravel, B.; Rehr, J.J.; *Phys. Rev. B.*, **1998**, *58*, 7565

Chapter 2

Experimental and Theoretical Techniques

2.1 Introduction

This chapter will assess the experimental X-ray absorption (XAS) techniques and methods for analyzing XAS data, and summarize the fundamental theory of X-ray absorption. It will also review the quantum mechanical theoretical methods used to interpret the XAS results, and provide other information such as preferred adsorption sites on various types of catalysts such as Au and metal oxide-supported Au clusters, ligand-stabilized Pt nanoparticles, RhS catalysts, and also adsorption sites of sulfur on Pt clusters. The chapter will also further summarize other experimental techniques used to characterize these catalysts.

2.2 The XAS spectrum

Many surface sensitive analytical techniques are currently available; however, most are not sensitive enough to probe at the atomic level, *in situ* in an electrochemical cell. Synchrotron based *in-situ* XAS is an effective and unique method for determining the metal cluster size

clusters, the electronic structure of the metal, and the short-range atomic order of adsorbates on the surface. XAS can serve as an *in situ* technique since the probe and signal are both x-rays which can penetrate "dilute" or thin samples.

The XAS spectrum is normally divided into two regions, the EXAFS (Extended X-Ray Absorption Fine Structure) and XANES (X-Ray Absorption Near Edge Structure). The physical origins of both XANES and EXAFS are the same, yet they provide complimentary information, and the analysis techniques in these two regions are completely different. Figure 2.1 shows a typical XAS spectrum. The region from 0-50 eV is referred to as the XANES which provides information about the atoms configuration and site symmetry. The region after 50 eV is termed EXAFS which gives more structural and geometric information such as bond length and coordination number.

2.3 XAS Theory

XAS provides a measurement of the x-ray absorption coefficient μ, or the x-ray absorption capacity, of a material as a function of photon energy E, which is above or below the threshold of an absorption edge E_0. The intensity, *I*, of x-ray photons decreases as it passes through a material depending on the absorption coefficient, μ, and the path length that the x-rays have traveled according to the following equation:

$$dI = -\mu(E)\, I dx \qquad 2.1$$

The linear absorption coefficient, μ as a function of energy, E, can then be calculated by the integration of the attenuation in the light intensity from of a sample thickness x which results in Lambert's law

$$I_t = I_o e^{-\mu(E)x} \qquad 2.2$$

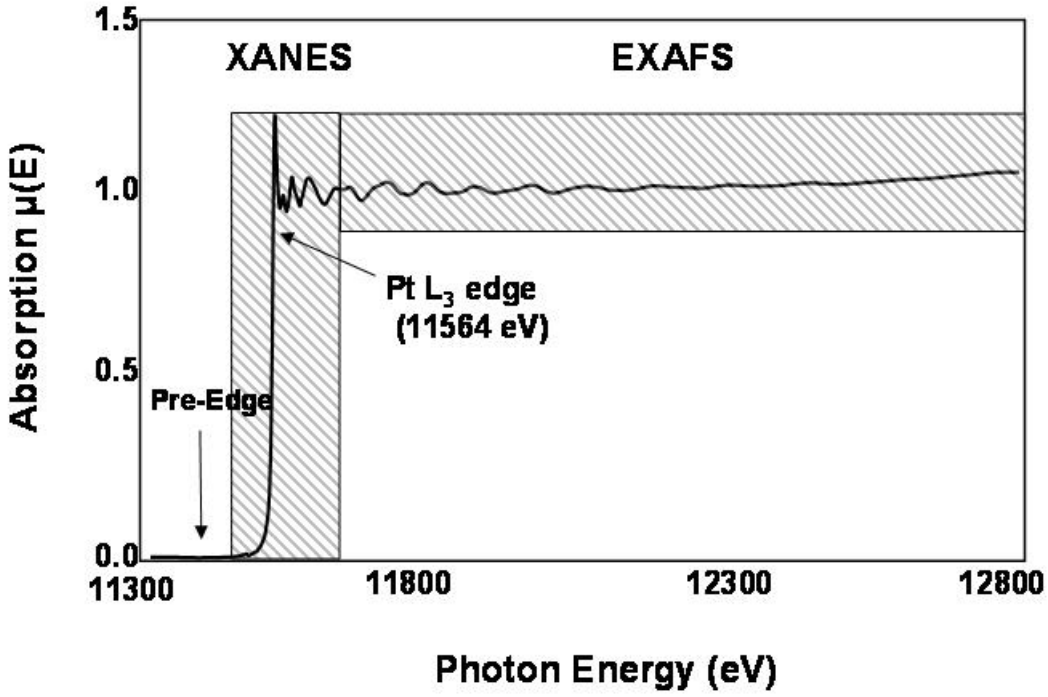

Figure 2.1 XAS spectrum at Pt L_3 edge of a Pt foil. The edge value is indicated where the photoexcitation occurs at 11564 eV. The pre-edge, XANES, and EXAFS regions are also displayed.

The absorption coefficient of an atom depends roughly on the x-ray energy, E, the atomic number Z, the electron density, ρ, and atomic mass, A, according to the following relation:

$$\mu \approx \frac{\rho Z^4}{AE^3} \qquad 2.3$$

If the energy (hv) of the incident photon beam is large enough, an atom absorbs an x-ray of energy E, exciting a core electron with energy E_0, and emitting a photoelectron with a kinetic energy of ($E-E_0$) which is represented by E_b in the equation below. The core state is eventually filled and a fluorescent x-ray or Auger electron is finally ejected. Once the x-ray is large enough to promote an electron into the continuum, a sharp increase in absorption occurs. This increase in absorption is exhibited in the XAS spectrum, as displayed in Figure 2.1 and illustrated in Fig. 2.2. The kinetic energy of the photoelectron E_k is given by the equation:

$$E_k = hv - E_{binding} - \phi \qquad 2.4$$

where: hv is the energy of the incident x-ray, ϕ equals the work function of the metal, and $E_{binding}$ equals the binding energy of the orbital (relative to the Fermi level) from which the photoelectron is excited.

The photoelectron can be expressed in quantum mechanics as a spherical wave with a wavelength, λ, described as:

$$\lambda = \frac{2\pi}{k} \qquad 2.5$$

with the wavevector k:

$$k = \left[\left(\frac{8\pi^2 m}{h^2} \right) (hv - E_o) \right]^{\frac{1}{2}}, \qquad 2.6$$

where m equals the mass of the electron and h is Planck's constant.

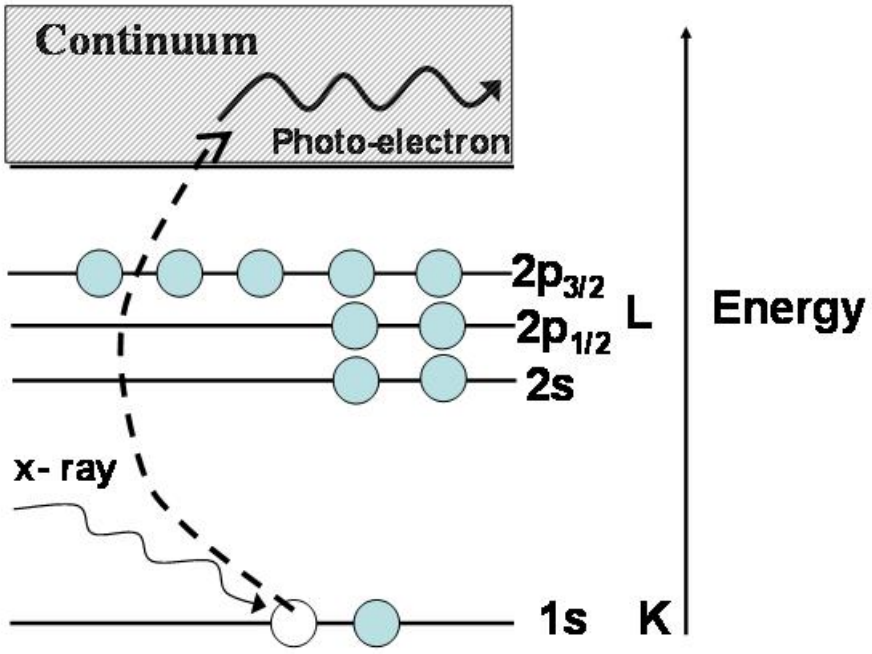

Figure 2.2 Schematic of the photoelectric effect. An x-ray is absorbed by the atom, the energy of the x-ray is transferred to a core level electron (K or L shell) which is ejected from the atom and into the continuum.

The probability for x-ray absorption is given by Fermi's golden rule illustrated in Figure 2.3, where the probability of a dipole mediated transition from a core state, ψ_i to a final unoccupied state ψ_f is given by:

$$\mu(E) = \frac{8\pi e^2 \omega^3 n}{hc^2} \cdot \left| \langle \psi_f | \mathrm{E} \bullet r | \psi_i \rangle \right|^2 \cdot \delta(E_f - E_i - h\nu) \qquad 2.7$$

Here e = electron charge

ω = angular frequency of the incoming photon

c = speed of light

Ψ_f = final state wave function of the bound electrons, core hole and excited photoelectron

Ψ_i = initial state wave function of the bound electrons

E = electron field polarization vector

r = position vector with respect to absorber

δ = density of states at the final energy, and

E_f and E_i = final and initial state energies.

The standard theory of XAFS has historically been based on the approximation of a spherical muffin-tin scattering potential. The potential seen by the photoelectron is composed of non-overlapping, spherically symmetric potentials around each atom and is flat between the different atomic-like potentials.

The propagating electron goes out and consistently returns to the original absorber atom. This backscattered wave can interfere with the original outgoing photoelectron wave. As the photon energy increases, the energy of the photoelectron increases causing the

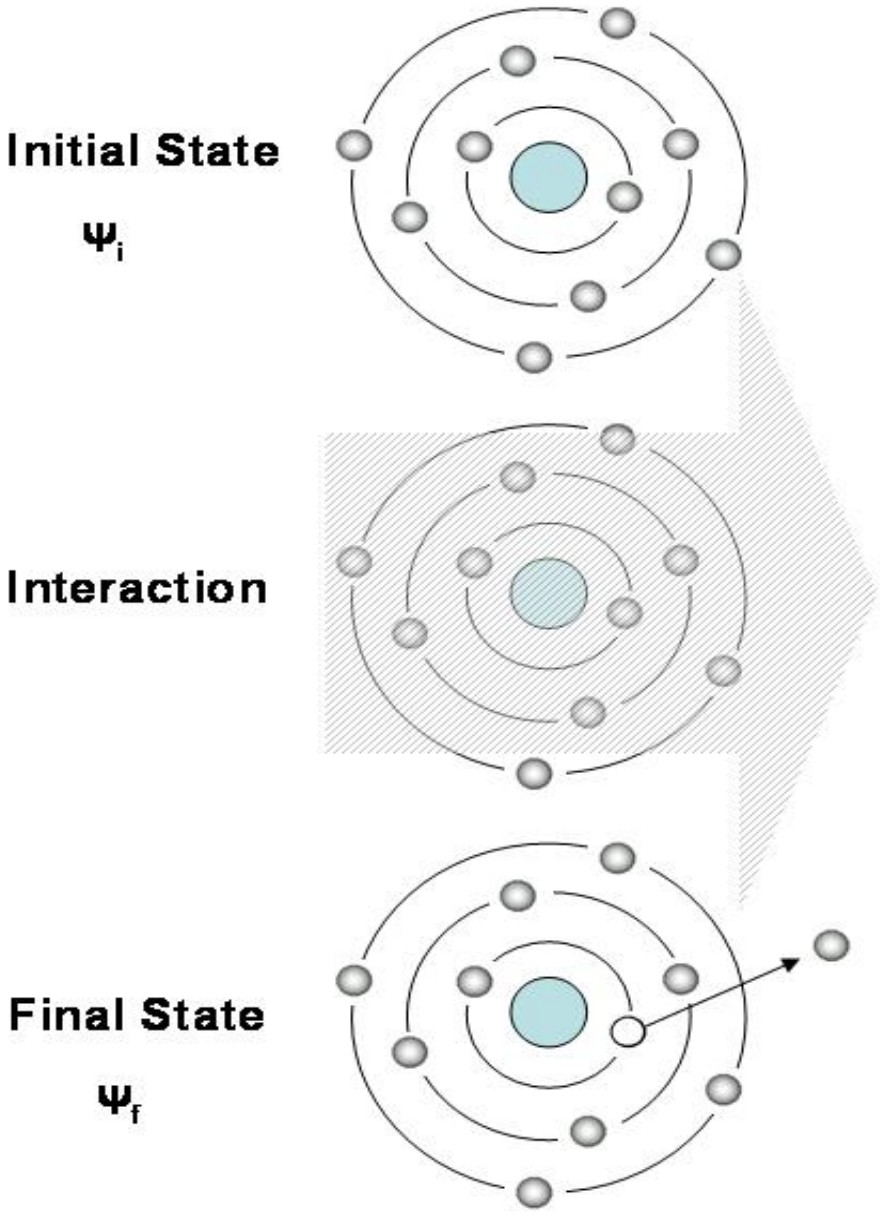

Figure 2.3 Diagram of the sequence of events that occur from x-ray absorption. An ejection of an electron from the ground state or initial state, Ψ_i, to a final unoccupied state, Ψ_f, occurs according to Fermi's golden rule.

wavelength to decrease. This causes the outgoing and backscattered waves to interfere either destructively or constructively depending on the wavelength and path length required to return to the absorber. The initial state is the ground state of the system. In the presence of neighboring atoms, the final state has a core hole along with the photoelectron; the wavefunction describing the photoelectron is given as a sum of the interfering outgoing and backscattered waves. This wave interference gives rise to the oscillations seen in the EXAFS region of the XAS spectra. Figure 2.4 shows the interference patterns of the photoelectron waves.

The multiple scattering (MS) theory, incorporated within the muffin-tin approximation, is based on perturbation theory, and the potential scattering of an electron from atom to atom is often termed a "path" approach. Single scattering and multiple scattering paths are illustrated in Figure 2.5. In multiple scattering, the photoelectron wave is scattered from more than one atom. Photoelectron waves can return to the central atom from many MS paths, but extremely long paths are thought to mostly cancel each other, or at least undergo significant amplitude reductions due to inelastic scattering effects. Thus, the single scattering plane-wave approximation becomes more accurate at higher energy since the multiple scattering is weaker at higher energy.

In the analysis of the EXAFS region, the oscillations will depend on the distance between the absorber atom and the neighboring atoms. Simple EXAFS analysis is based on a single electron, single scattering formalism. It is assumed that the photoelectrons have sufficiently high energies so that only single backscattering is important, which is why only the energy region >50eV is considered in EXAFS analysis. In XANES, the photoelectron has a smaller momentum and a longer mean free path, and consequently the plane-wave and single scattering formalism is no longer valid. Therefore, in this region, the photoelectron wave samples the more immediate environment around the absorber atom many times, and the effects of multiple scattering provide electronic or orbital bonding information.

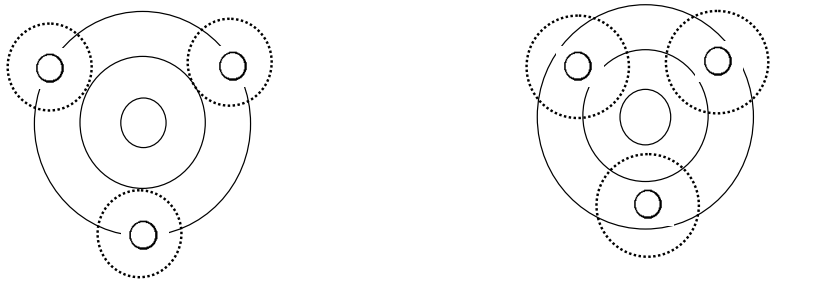

Figure 2.4 Constructive and destructive phases of a backscattered wave which can interfere with the original outgoing photoelectron wave

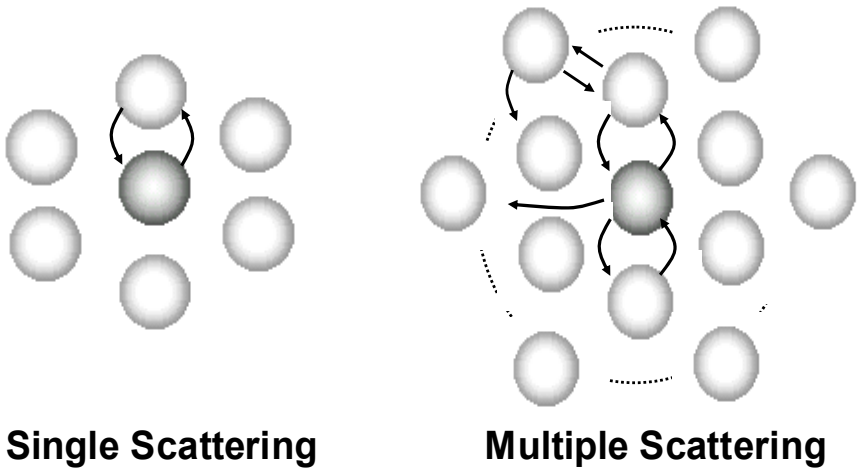

Figure 2.5 Single and multiple scattering paths which an electron can undertake after being ejected from an absorber atom. Single scattering paths dominate in the EXAFS region while both single and multiple scattering paths equally are present in the XANES region

Absorption edges correspond to the threshold for excitation out of core level atomic shells and subshells. For example, an atom of interest could have one K absorption edge, three L edges and five M level edges. Between absorption edges, the absorption coefficient decreases roughly as $1/E^3$ and will decrease in the order of K>L>M. The spectral shape near the edges can give information regarding the effective charge or valence of the absorbing atom since the energy generally correlates with the oxidation state.

In the dipole approximation, the transitions are restricted by the selection rule $\Delta L=\pm 1$ and $\Delta J=\pm 1,0$ where L is the orbital angular momentum quantum number and J is the total angular momentum quantum number. Table 2.1 shows the X-ray absorption edges and the core level excitations. In this thesis, the K edges of Co, Rh, and Sn, and the L_3 edges of Pt and Au, were all studied.

Table 2.1 X-Ray absorption edges and core level excitations

Level	Core-Level Excitation
K edge	$1s \rightarrow p$
L_1 edge	$2s \rightarrow p$
L_{23} edge	$2p_{1/2,3/2} \rightarrow s,d$
M_1 edge	$3s \rightarrow p$
$M_{2,3}$ edge	$3p_{1/2,3/2} \rightarrow s,d$

2.4 EXAFS and XANES Analysis

The Athena code of Ravel and Newville[1], from the IFEFFIT package, was used for both the EXAFS and XANES analysis to subtract the background and normalize the data. The Artemis program in the IFEFFIT package was used for EXAFS analysis, with FEFF 8.0[2] calculated

references. An isolation technique was used and compared with the theoretical calculations for the XANES analysis using the FEFF 8.0 code. The FEFF 8.0 code was developed by John Rehr at the University of Washington over the last 20 years[3]

2.4.1 EXAFS analysis

The absorption coefficient μ is generally expressed as μ_o $(1+\chi)$, where μ_o is the absorption due to the absorber atom itself, and the χ part arises from the photoelectron backscattering and interference as described above. Thus χ provides the geometric information. The well-known and basic EXAFS equation is:

$$\chi(k) = \sum_j \frac{N_j f_j(k) e^{-2k^2\sigma_j^2}}{kR_j^2} \sin[2kR_j + \delta_j(k)] \qquad 2.8$$

It incorporates the scattering interferences and probability for scattering as discussed above. Here *f(k)*, the scattering amplitude, and $\delta_j(k)$, the phase shift, are scattering properties of a neighboring atom, which depend on the atomic number Z of the scattering atom. From this equation the following can be determined:

R: distance to the neighboring atoms

N: number of neighboring atoms, and

σ^2: mean-square displacement of neighboring atoms due to thermal vibration and static disorder.

A fourth parameter, the inner potential E_o, required in the determination of k, eq. 2.6, is also generally required.

The first step required in both EXAFS and XANES data analysis is removal of the pre-edge background. The background is removed by normally fitting a quadratic or linear

polynomial to approximately 50 eV of the data prior to the edge, which is then extrapolated beyond the edge as seen in Fig. 2.6 (1). The pre-edge absorption curve can sometimes contain background noise arising from higher beam harmonics, elastic scattering and other discontinuities in data collecting, producing glitches, spikes or steps in the data that can hinder the background removal process, but usually this is not a problem.

The next step in the analysis is to normalize the data by estimating the edge step, $\Delta\mu(E_o)$. The absorption coefficient $\mu(E)$ can be expressed as $\mu_o(E)(1+\chi(E))$ where $\chi(E)$ is given by eq. 2.8 and contains all of the information of interest, and $\mu_o(E)$ is the atomic absorption coefficient. The effective edge, $E_{0,}$ is selected as the energy with the maximum derivative (i.e. steepest onset) shown in Figure 2.6, and the step height $\Delta\mu$ is normalized to 1 over a large energy above the absorption edge. The absolute photon energy at E_o is the effective binding energy of the core electron.

To extract the desired $\chi(E)$ function, $\mu_o(E)$ must be determined. This is most often done by performing a spline smoothing of $\mu(E)$ which is then subtracted from $\mu(E)$ as shown in Fig. 2.6. The proper removal of $\mu_o(E)$ from $\mu(E)$ is still an "art" that one must acquire, but better criteria have been developed in recent years.[4,]

$$FT(R) = \frac{1}{\sqrt{2\pi}} \int_{k\,\min}^{k\,\max} k^n \chi(k) e^{i2kR} dk \qquad 2.9$$

Once the final $\chi(E)$ function is extracted, the Fourier transform is used to convert the data from k-space to R-space as shown in eq 2.9. The Fourier transform gives peaks at the distances between the absorber atom and its neighbors, albeit slightly shifted from the true value of R. From least-squares fitting procedures utilized in the ARTEMIS code and functions obtained from theoretical calculations for the scattering amplitudes and phases in eq. 2.8, the critical distances Rj, and coordination numbers Nj can be determined.

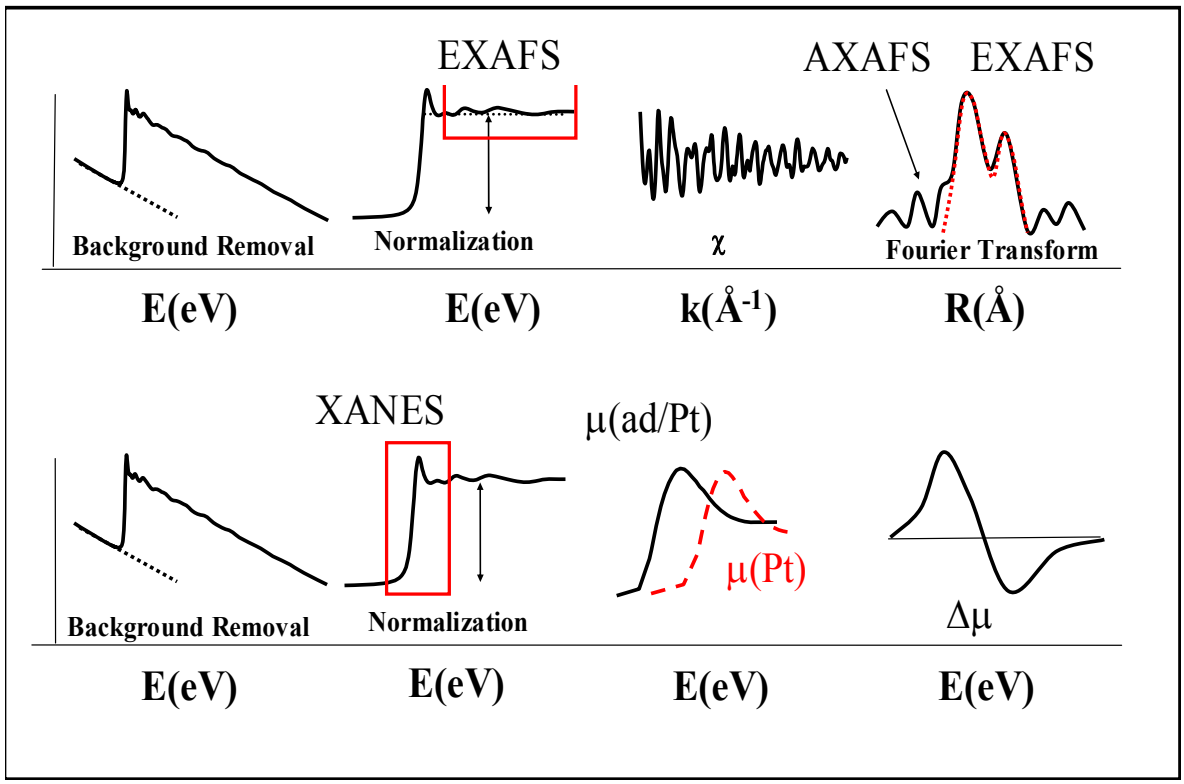

Figure 2.6 Separation of a) EXAFS and b) XANES features. 1) Pre-edge background removal. 2) Normalization range. 3a) Post-edge background removal and conversion to k-space and 4a) Fourier Transform and fitting with FEFF 8.0 references. 3b) Illustration of Pt L_3 line shapes before subtraction and 4b) Segregation of $\Delta\mu$ adsorption signatures.

FEFF 8.0 calculations were used in this work to determine the scattering amplitudes, phases, and other variables in eq. 2.8. These parameters can also be obtained by fitting a model to experimental data from known similar reference materials and then transferring the obtained parameters to the unknown system for structural determination, however this procedure was not used in this work. Using the simple EXAFS model of eq. 2.8, with FEFF 8.0 references, the parameters R, N, σ^2, and E_o are obtained from the least-squares fits with a typical uncertainty in the interatomic distance of ± 0.02 Å, and in the coordination number, N, of about ± 0.5. Here the Debye-Waller factor involving σ^2 is caused by thermal vibration and static disorder, and is particular to each material. Unfortunately, a large linear dependence exists between N and σ^2, so that often σ^2 is fixed to decrease the uncertainty in N. This was generally done in this work, so that just 3 parameters were utilized per shell, with at most two shells (Pt-Pt, Pt-O, Pt-P, Au-Au, Sn-Sn, Sn-O, Rh-Rh, and Rh-S) considered in this work.

2.4.2 Isolation of XANES features

The fine structure features in the XANES arise from transitions of the excited photoelectron into unoccupied states just above the Fermi level. The excited low energy photoelectron has a long mean free path, which allows a significant amount of multiple scattering around the absorbing atom without significant loss of energy. There is no convenient generally used XANES equation like that for EXAFS, therefore a new interpretation technique must be developed. This technique has been used in previous work and applied to H, O, and OH on Pt[5,6], Pt-M (M=Cr, Fe, Co, and Ni) cathodes[7] both in an electrochemical cell, and CO poisoning in PtRu catalysts in a fuel cell[8].

The pre-edge background is removed exactly like that for the EXAFS as described above and shown in Figure 2.6. The effective edge, E_o is chosen as the half height of the absorption edge step and the normalization is now done over a smaller (compared to EXAFS) energy region, typically 0-50eV. Careful energy alignment is needed in order to carry out the analysis to be described below,

and this is done by using the Pt foil spectra always taken simultaneously with that for the Pt sample. This alignment eliminates the slight "wandering" in photon energy that exists in any photon beam coming from a synchrotron. The Pt L_3 foil (or a foil corresponding to the edge being studied) spectra taken simultaneously with each sample run are aligned and then the actual sample spectra are shifted by the exact same energy required to align the foil spectra.

In order to highlight the adsorbate bonding effects, a difference:

$$\Delta\mu = \mu(X/Pt)-\mu(Pt) \qquad 2.10$$

is taken where $\mu(Pt)$ is the spectrum of the "clean" electrode at or near 0.54V used as a reference. Near 0.54 V the Pt electrode lies in the double layer region where there is no adsorbed hydrogen and oxygen expected. Directly adsorbed anions and water may exist on or near the surface in this region, but since these species do not adsorbed in registry on the surface (i.e. they are either somewhat mobile or disordered on the surface), they are found not to contribute significantly to the XANES data.

With $\mu = \mu_o(1+\chi)$ as indicated above, the $\Delta\mu$ of eq. 2.10 can be expressed by the following equation:

$$\Delta\mu = \Delta\mu_o + \Delta\lceil \mu_o \chi_{Pt-Pt} \rceil + \mu_{o,Ads/Pt}\chi_{Pt-Ads} \qquad 2.11$$

where $\Delta\mu_o$ is the change in the atomic XAFS, $\Delta(\mu_o\chi_{Pt\text{-}Pt})$ is the change in the Pt-Pt total scattering induced by the atom adsorption, and $\chi_{Pt\text{-}Ads}$ is the additional scattering arising from the adsorbate. Both the $\chi_{Pt\text{-}Pt}$ (with and without the adsorbate) and the $\chi_{Pt\text{-}Ads}$ include the full scattering (both the single and multiple scattering), which in the XANES region can be dominated by the multiple scattering contributions. In order to fully interpret the $\Delta\mu$ difference spectra, theoretical calculations were used as described below.

2.5 Theoretical Calculations

Theoretical calculations were performed on model clusters in order to interpret the XANES data and understand the results. Real-space full multiple scattering calculations utilizing a muffin-tin potential are performed using the FEFF 8.0 code. These calculations effectively approximate the continuum orbitals, and because of the full multiple scattering, also reasonably approximate the strong antibonding resonances present in this energy region.

2.5.1 FEFF 8.0

The FEFF 8.0 code perfoms ab-initio self-consistent field, real-space, full mutiple scattering calculations. It is known that in the FEFF 8.0 code, the results are somewhat dependent on the potentials used in the code. Previously it was found that the Dirac-Hara potential with an imaginary part of 5 eV was optimal for describing the Pt-Pt and Pt-O scattering.[4,9,10,11] However, the emphasis in that optimization procedure was placed on the 25-150 eV region. Here we are interested in the region below 40 eV. Although a more complete analysis in this energy region is required, the Hedin-Lundquist potential is preferred.

The Pt_6 cluster shown in Figure 2.7 was used for a majority of the FEFF 8.0 calculations presented in this work. This cluster known as the "Janin" cluster is favored due its lower symmetry and it also contains both fcc and hcp sites as indicated. The adsorption sites for atop and bridged are also shown. The theoretical $\Delta\mu$ difference spectra are obtained by taking the difference:

$$\mu(Ads/Pt_6) - \mu(Pt_6), \qquad 2.12$$

which give theoretical results exactly comparable to that obtained experimentally. It is also important to note that throughout this work, the Janin cluster was used for other non-platinic catalysts that were studied such as Au and Rh. Being that these single crystal elements are all fcc lattices, it

can be assumed that they can be incorporated into the Janin cluster.

There were certain circumstances where the Janin cluster could not be incorporated. In Chapter 3, the Cassiterite[12] structure for Sn-O_x support was used in generating theoretical signatures to interpret the experimental results. In Chapter 5, different RhS crystal structures were also incorporated. Figure 2.8 shows the non-Janin type clusters used for theoretical calculations.

2.5.2 ATOMS code

The ATOMS code developed by Bruce Ravel[13] was used to generate Pt clusters of approximately 200 atoms with the Fm3m space group, fcc, a=3.92Å of 8 shells for Chapters 4 and 6. These clusters were used to model the Pt-Pt coordination numbers for comparison with results obtained from the EXAFS analysis. Chapter 3 consisted of generating Au clusters with an Fm3m space group, fcc, a= 4.08 Å and for the SnO_x support a Cassiterite structure for SnO_2 was incorporated with a tetragonal P 4_2/m3m space group, a=4.74 Å and c=3.19 Å. For the catalysts studied in Chapter 5, there were no ATOMS input files in the database for the catalysts studied so XRD parameters obtained from collaborators at Northeastern University (NEU) were used instead. With these parameters, it was possible to generate our own input file in Artemis and then fit the experimental EXAFS data. Table 2.2 shows these parameters for clarity.

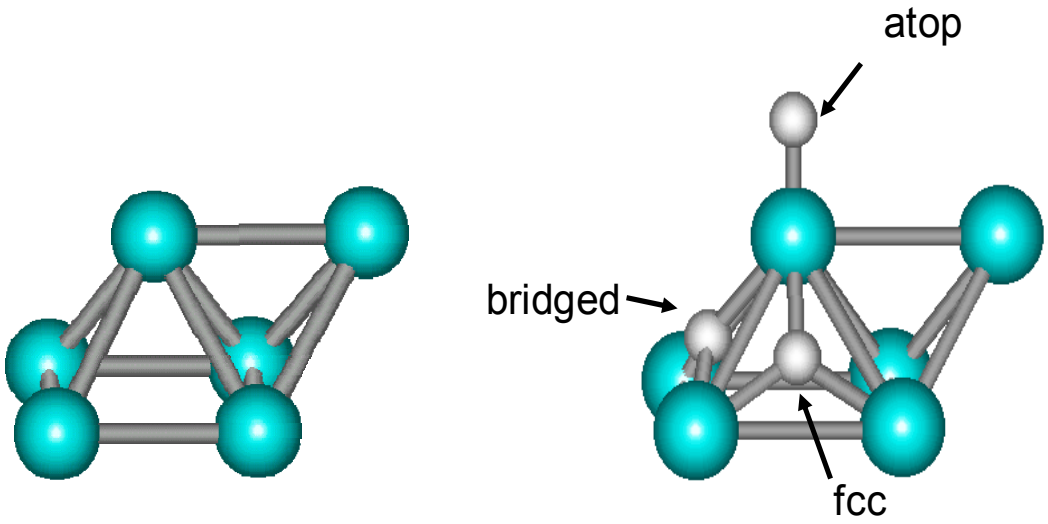

Figure 2.7 M_6 "Janin" Cluster (M=Pt, Au, or Rh) clean (left) and with various adsorbate geometries (right).

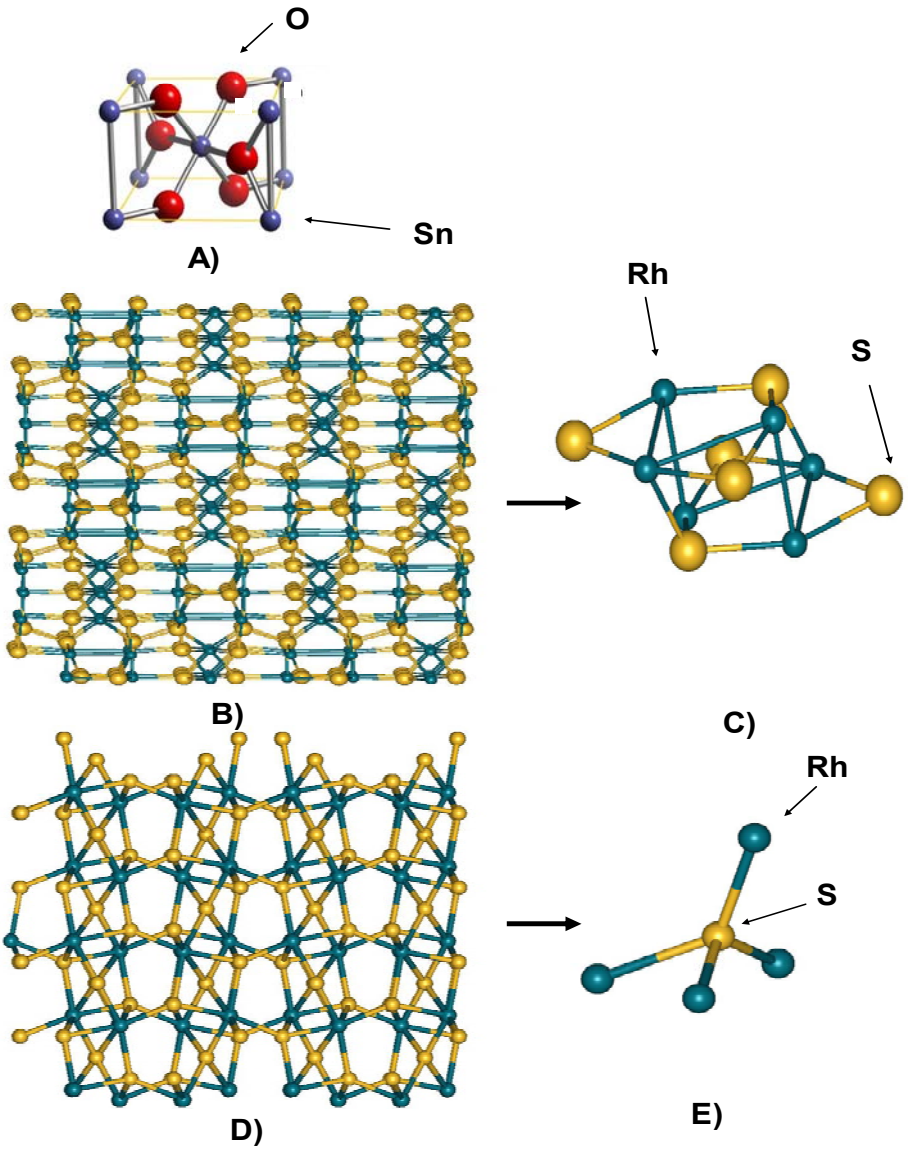

Figure 2.8 Display of non-Janin type clusters used in this thesis. SnO_2 Cassiterite structure (A). Rh_3S_4 full lattice (B) and its fragment (C) used for FEFF 8.0 calculations. Rh_2S_3 full lattice (D) and its fragment (E) also used for FEFF 8.0 calculations

Table 2.2: Summary of Cell Parameters for Catalysts studied in Chapter 5

Catalyst	Symmetry	Space Group	Cell Parameters		
			a/Å	b/Å	c/Å
Rh	cubic	*Fm3m*	3.803	-	-
Rh_2S_3	orthorhombic	*Pbcn*	8.462	5.985	6.138
Rh_3S_4	monoclinic	C*2/m*	10.292	10.671	6.213
$Rh_{17}S_{15}$	cubic	*Pm3m*	9.911	-	-

2.6 Rotating Disk Electrode Cyclic Voltammetry

Before XAS experiments can be conducted, it is imperative to fully characterize the sample and see if it is active for the ORR. The tool needed to study this is Rotating Disk Cyclic Voltammetry also know as RDE. All catalysts studied were supported on Vulcan carbon XC-72 (E-TEK). Thin catalyst films on glassy carbon electrodes were prepared for the voltammetric analysis using a method adapted from the literature[14]. These films are made by making inks of the catalyst by ultrasonically dispersing a certain amount of catalyst that is in the form of a powder into a solution composed of isopropanol (Sigma-Aldrich or ACS grade), deionized water (Nanopure), and a small aliquots of 5 wt. % Nafion® ionomer binder (Sigma-Aldrich or Ionpower Liquion). This mixture is sonicated for around 30 minutes to 1 hour and allowed to mix overnight to maximize overall catalyst dispersion. The inks are then applied onto rotating disk glassy carbon electrodes (Pine Instruments GCE, 5 mm diameter) which are attached to a Pine AFCPRB rotator couple with an Eco Chemie Autolab PG Stat 30 potentiostat. Before testing can begin, it is important to polish the GCE to a mirror finish in 0.05 μm alumina-particle suspension (Buehler) on a moistened polishing cloth. The GCE is coated with a catalyst film and then submerged in a 25°C Ar-saturated cell which is flooded with 0.1M $HClO_4$ (electrolyte used in Chapters 3, 4 and 6) or 1M TFMSA (electrolyte used in Chapter 5). The glass cell is a three-

electrode potentiostatic circuit where a gold mesh is used as a counter electrode. All potentials are measured with respect to a sealed reversible hydrogen electrode (RHE)[15,16]. The catalyst is activated under Argon and cycles by applying potential cycles 20 or 50 mV/s at 1600 rpm. Once activation is achieved, then the cell is saturated with O_2. The electode is rotated at 1600 rpm and voltammetric cycles are performed at 5 mV/s or 20 mV/s.

2.7 XAS Data Collection

XAS requires synchrotron radiation which provides a continuum of photon energies that are 10^3 to 10^6 higher in intensity than conventional x-ray tubes. The synchrotron provides a wide tunable energy range enabling almost all elements to be studied. All of the data obtained and presented in this thesis were obtained on beamline X-11A and B or X-18A at the National Synchrotron Light Source (NSLS) at Brookhaven National Laboratory located in Upton, NY.

2.7.1 Synchrotron Radiation

Synchrotron radiation is produced when charged particles (electrons or positrons) are orbiting at relativistic speeds ($v \approx c$). Synchrotron radiation is created in storage rings where the charged particles circulate for many hours under high vacuum. The electrons are produced in an electron gun, accelerated in a booster, and injected then into the storage ring where they are post accelerated to their nominal kinetic energy. The path of the electrons in the ring is controlled by quadrapole and other bending magnets surrounding the ring. Synchrotron radiation is produced when the bending magnets change the momentum of the electrons giving them a curved trajectory.

Continuous energy x-rays are produced by the synchrotron, but the beam can be made nearly monochromatic using a silicon double-crystal diffraction monochromator. Two parallel crystals diffract the beam according to Bragg's law:

$$n\lambda_{hkl} = 2d_{hkl}\sin\theta_B \qquad 2.13$$

where λ_{hkl}, n, and d_{hkl} are the wavelength of the diffracted x-rays, the harmonic order, and the lattice spacing at that plane at a Bragg angle θ_B from the beam direction. The x-ray wavelength is controlled by a computer system, which rotates the monochromator so that θ_B changes at a constant rate per unit time. Thus measurements over the entire energy region of interest can be investigated.

The XAS spectra obtained in this thesis were obtained in transmission mode. Three gas flow ionization detectors were used to measure the incident and transmitted x-rays as described below.

2.7.2 Experimental Setup

The XAFS data were collected at room temperature in transmission mode on beamline X-11A and X18B of the National Synchrotron Light Source (NSLS) at Brookhaven National Laboratory. The NSLS storage ring is operated at 2.52 GeV beam energy with ring currents between 40 and 200 mA. Three gas flow ionization detectors were used to monitor the intensities of the incident (I_0) and transmitted x-rays (I) through the sample and the reference detector (I_{ref}). A Si(111) double crystal monochromator was detuned by 30% at 200 eV above the Pt and Au L_3 edges (11564 and 11919 eV respectively) and the Rh K edge (23220 eV) to minimize the presence of higher harmonics in the beam. Data was also collected at the Sn K edge (29200 eV) in Chapter 3 which incorporated a Si(311) double crystal monochromator. The energy calibration was achieved by recording the XAFS of a 7 μm thick metal foil simultaneously with the sample. The material of the foil corresponded to which element would be studied.

Figure 2.9 illustrates the cell used in these measurements taken for Chapters 3, 4 and 6, an electrochemical half-cell, which was designed by the Adzic research group at Brookhaven National

Lab[17]. The catalyst powders are mixed with enough 1M $HClO_4$ until the material is a paste. The sample is then applied onto a carbon cloth and assembled into the cell. The cell is a three-electrode cell where the counter electrode is a Pt foil with a wire connected to it for contact, and another Pt foil was used for contact with the working electrode (the catalyst). The data was taken in reference to an Ag/AgCl reference electrode. The cell was then placed in front of the beam between two detectors that collected incident (I_0) and transmitted x-ray (I) beam intensity. An Eco Chemie Autolab PGSTAT-30 potentiostat was used to hold the cell at a desired potential. The cell setup for the material in Chapter 5 had a slightly different design and the sample had been previously hot-pressed onto a carbon cloth then soaked in 1M TFMSA before being assembled into the cell.

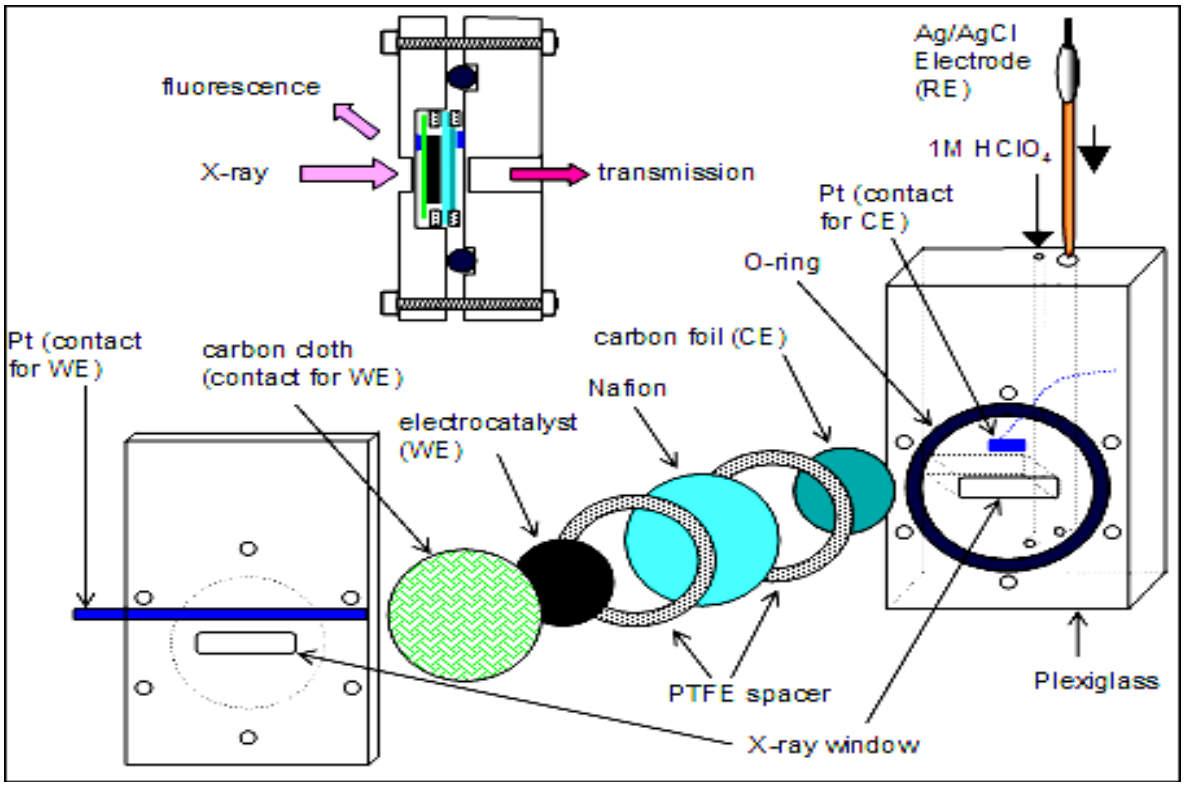

Figure 2.9: Schematic of the experimental setup used in XAS experiments

2.8 References

[1] Ravel, B.; Newville, M.; *J. Synch. Rad.,* **2005**, *12*, 537
[2] Zabinsky, S.I.; Rehr, J.J.; Ankudinov, A.; Albers, R.C.; Eller, M.J.; *Phys. Rev. B: Condens. Matter,* **1995***, 52*, 2995
[3] Ankudinov, A. L.; Rehr, J.J; Low, J.;Bare, S.R.; *Phys. Rev. Lett.,* **2001**, *86*, 1642
[4] van Dorssen, G.E.; Koningsberger, D.C.; Ramaker, D.E. *J. Phys Cond. Matt*. **2002**, 14(49), 13529.
[5] Teliska, M.; O'Grady, W.E.; Ramaker, D.E.;*J. Phys. Chem.B,*, **2004**,*108*, 2333
[6] Teliska, M.; O'Grady, W.E.;Ramaker, D.E.; *J. Phys. Chem. B,* **2005***, 109*, 8076
[7] Teliska, M.; Murthi, V.S.; Mukerjee, S.; Ramaker, D.E.; *J. Electrochem. Soc.,* **2005,** *152*, A2159
[8] Scott, F.J.; Roth, C.; Ramaker, D.E.; *J. Electrochem. Soc.,* **2007,** *111*, 11403
[9] Koningsberger, D.C.; Mojet, B.I.; van Dorssen, G.E.; Ramaker, D.E.; *J. Phys.: Condens. Matter,* **2002**, *14***,** 13529
[10] Ramaker, D.E.; Teliska, M.; Zhang, Y.; Stakheev, A.Y.; Koningsberger, D.C.;*Phys. Chem. Chem. Phys.* **2003**, *5*, 4492
[11] Ramaker, D.E.; Mojet, B.L.; Koningsberger, D.C.; O'Grady, W.E.; *J. Phys.: Condens. Matter*, **1998**,*10*, 8753
[12] Godin T.J.; LaFemina, J.P.; *Phys. Rev. B*. **1993**, *47,* 6518
[13] Ravel, B**.** *J. Synchrotron Rad.* **2001,** 8**,** 314.
[14] Paulus, U.A.; Schmidt, T.J.; Gasteiger, H.A.; Behm, J.; *J. Electroanal. Chem.,***2001***, 495*, 134
[15] Gong, S.; Lu, J.; Yan, H.; *J. Electrochem. Soc.*, **1997**, *436*, 291
[16] Will, F.G.; *J. Electrochem. Soc.*, **1986**,*133*, 154
[17] Sasaki, K.; Wang, J.X.; Balasubramanium, M.; McBreen, J.; Uribe, F.; Adzic, R.R.; *Electrochim. Acta.,* **2001**, *49*, 3873

Chapter 3

Support Effects on Water Activation and Oxygen Reduction over Au-SnO_x Electrocatalysts

3.1 Introduction

This work examines gold as a non-platinum electrocatalyst for the oxygen reduction reaction (ORR). Gold nanoparticles supported on hydrous tin-oxide (Au-SnO_x) and mixed with Vulcan carbon (VC) are active below 0.55 V (vs. the reversible hydrogen electrode, RHE) for the 4-electron ORR (Eq. 1) in acid electrolyte.[1,2] Comparable 1.7-nm Au nanoparticles supported solely on carbon are inactive for the ORR in acid, generating peroxides rather than water (Eq. 3.2) at current thresholds below 0.3 V. These results suggest that the Au reactivity is enhanced by the SnO_x support through a synergistic mechanism or metal/support interaction.

$$O_2 + 4H^+ + 4e^- \rightarrow 2H_2O \quad 1.23\ V \qquad (3.1)$$

$$O_2 + 2H^+ + 2e^- \rightarrow H_2O_2 \quad 0.7\ V \qquad (3.2)$$

Pt and its alloys are the most active electrocatalyst for the ORR, and thus are the favored cathode electrocatalysts for polymer electrolyte membrane (PEM) fuel cells. Platinum, as well as most d-electron transition metals, has a "d-band" just below the Fermi level that results from hybridization between the d and s,p electrons[3]. This band can readily accept or donate electrons to and from adsorbed or absorbed species. The most reactive metal surface has an optimal O_2 binding energy making it efficient at adsorbing O_2 and breaking the O_2 bond (Eq. 3) while keeping the Pt-OH bond sufficiently weak to avoid significant OH poisoning[3]. This poisoning arises from the OH intermediate formed in the ORR, which must be removed in a later step (Eq. 4), as well as from water activation (Eq. 5). Norskov et al[4] have indicated that alloying with other transition metals, such as Co or Ni, lowers (increasing the binding energy) the Pt d-band and decreases the Pt-O bond strength, and thereby decreases the coverage of OH poison and increases its reactivity for ORR.

$$O_2 \rightarrow (O_2)_{ad} \xrightarrow{e^-} (O_2)^-_{ad} \qquad (3.3)$$

$$\text{Pt-OH} \xrightarrow{e^-,H^+} \text{Pt-OH}_2 \xrightarrow{H_2O} \text{Pt}^0 \qquad (3.4)$$

$$Pt + H_2O \rightarrow OH/Pt + H^+ + e^{-+} \qquad (3.5)$$

In bulk Au, the d-band binding energy is almost fully occupied,[4] hence it is inefficient at breaking the O_2 bond and is inactive[5], but some more structurally open Au surfaces can facilitate the ORR. Studies of Au in acid have proven that Au is a poor ORR catalyst because it does not adsorb oxygen nor ORR reaction intermediates, but in base, the Au (100) surface is active for the ORR at low overpotentials due to adsorption of O(H) groups at 4-fold symmetry sites. [6-9]

Nanoscale Au supported on transition metal oxides can also be active heterogeneous catalysts. Gold supported on various oxides is active for catalytic processes such as NO removal, the combustion of volatile organic compounds, hydrotreatment, chemical processing, and in the purification of hydrogen (removal of CO) for fuel cell applications[10]. The latter application is of interest because of the surprisingly high activity for CO oxidation ($2CO + O_2 \rightarrow 2CO_2$) at low

temperatures reported for small (3-5 nm) gold particles supported on various oxides[11]. A multitude of active sites for the O_2 dissociation which carries out the CO oxidation have been proposed including metallic Au, monodisperse, cationic Au, an Au-OH site, and an oxide-Au interface site[10].

Work on CO oxidation over Au has been recently reviewed[12-16]; its relevance to the ORR is clear as both reactions involve either O_2 or H_2O dissociative adsorption. Water activation and/or the presence of OH groups were recently reported to also be involved, or at least enhance, the CO oxidation reaction[17-19]. The nature of the support is clearly very important, with a distinction between "inert" (SiO_2, MgO, Al_2O_3) and active or reducible (TiO_2, Fe_2O_3, CeO_x) oxide supports generally made on the basis of their capability to adsorb little or high amounts of oxygen, respectively[20,21]. For Au nanoparticles on inert oxide supports, the reaction is believed to advance via O_2 dissociative adsorption on the Au particles at either edge or kink sites, which has been enhanced electronically from the bulk. With the active class of oxides, oxygen is assumed to adsorb on the support where it may or may not dissociate before reacting with CO adsorbed on Au[10]. The active oxide materials are believed to act as co-catalysts by providing oxygen via a Mars van Krevelen mechanism, when lattice oxygen is used to oxidize the CO, leaving a defect which is replenished by a separate reaction with oxygen from the gas phase[14].

The utilization of a tin-oxide support to promote the activity of various noble metals such as Au or Pt for the ORR has been studied previously. Pt-SnO_2 is very effective for electrocatalysis with methanol oxidation[23, 24] and oxygen reduction[24]. CO oxidation over Au-SnO_2 has been studied,[25] where it was found that minimizing the Au metal's particle size and/or maximizing the Au metal oxide interface increased the reactivity. In the context of CO oxidation, it is not known whether SnO_x is active or inert, but previous work on O_2 sensors using Au-SnO_x suggest that indeed SnO_x is active in adsorbing O_2 [26, 27].

Tin oxide was chosen as a support for Au in ORR due to several factors including its redox couple, and the requirement that it be resistant to dissolution under the corrosive conditions of the

PEMFC cathode. Baker et al[1] found that SnO_x was sufficiently stable to carry out accurate characterization in the 0 to 1 pH range[1]. Hydrous metal oxide supports generally have a low vulnerability to poisons, are inexpensive to work with, and provide an ionically conductive hydrous surface that provides a ready supply of protons for the ORR, as well as a pathway for shuttling water away from the catalyst. Thus they can make reasonably good supports for the ORR at the cathode. Hydrous metal phosphates and hydrous metal oxide composites have been utilized in earlier work[28,29].

To understand whether metal support interactions play a role in the Au-SnO_x ORR activity, we use X-ray absorption spectroscopy (XAS). XAS is an *in situ* spectroscopic technique that can provide detailed adsorbate information at the atomic level, and has been used successfully to study adsorbate-metal surface interactions and adsorbate binding site geometries on both Pt and Pt alloys[30-36]. X-ray absorption near edge spectroscopy (XANES) analysis can be used to follow the coverage of H, O, OH and CO adsorbates on Pt, and determine the different binding sites i.e. atop, bridged, fcc, or hcp sites in some cases. It is important to note that the XAS experiments are conducted in an inert atmosphere, i.e., the oxygen gas used in the RDE experiments to carry out the ORR (eqs. 1-4) is not applied in the XAS experiments. However, one can still observe O(H) adsorption from water activation (eq. 5), and previous experiments on Pt have shown a direct correlation between O(H)/Pt coverage vs. potential in current-potential curves and ORR rates as determined from O_2 RDE experiments[30-36]. Comparison of XAS results actually conducted under oxygen and those under an inert gas such as Ar or N_2 show that slightly higher O(H) coverages exist to lower potentials under oxygen[37].

Oxygen and/or OH (here indicated as O(H)) coverage can be determined in situ from XAS. This is done by analyzing the XANES region using the $\Delta\mu$ technique[30-32] along with theoretical calculations to determine the adsorbate binding sites. In this technique the difference between two spectra, μ, are taken. The difference $\Delta\mu = \mu(V) - \mu(V_{ref})$ is generally obtained by subtracting the μ at a suitable reference potential, V_{ref}, to highlight an adsorbate signature as shown in Figure 3.1.

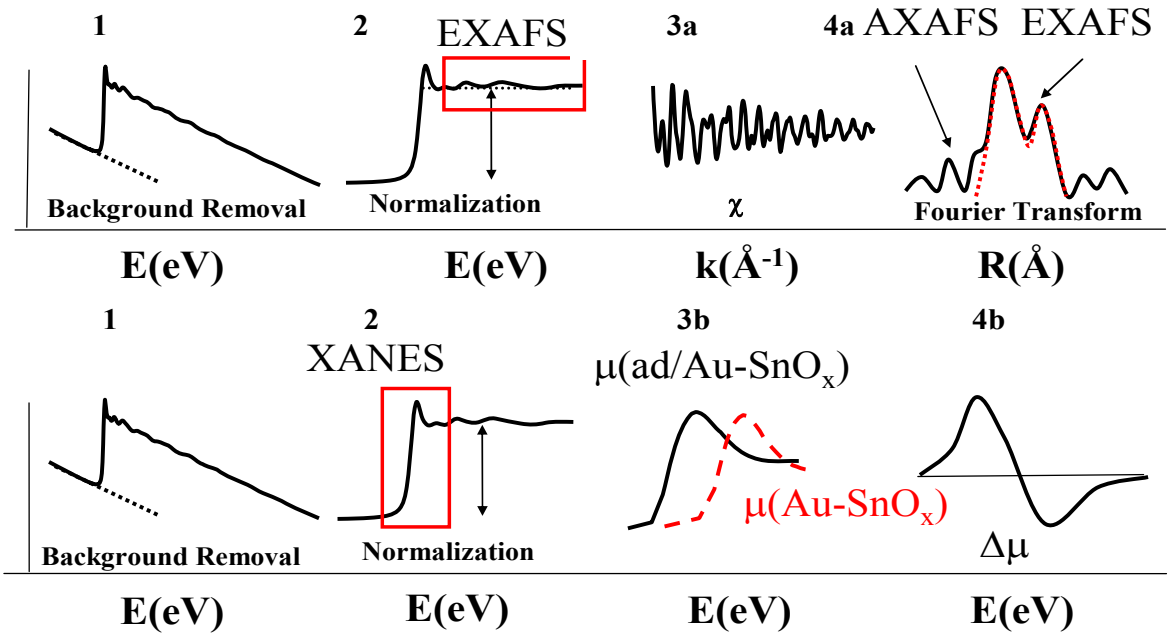

Figure 3.1 Separation of a) EXAFS and b) XANES features. 1) Pre-edge background removal. 2) Normalization range. 3a) Post-edge background removal and conversion to k-space and 4a) Fourier Transform and fitting with FEFF 8.0 references. 3b) Illustration of Au L_3 line shapes before subtraction and 4b) Segregation of Δμ adsorption signatures.

V_{ref} is usually a potential that is relatively free of adsorbates. This technique has also been used on XAS data taken for Pt-M (M=Cr, Fe, Co, and Ni) cathodes[33], and CO and OH adsorption on PtRu electrocatalysts in an electrochemical cell[34].

Extended X-ray Absorption Fine Structure (EXAFS) analysis (also shown in Figure 3.1) is a more established XAS technique that provides further information. At the Au L_3 edge, EXAFS analysis allows an indication of the Au particle sizes as well as particle morphology changes (spherical vs hemispherical) and O adsorption with potential. At the Sn K edge, EXAFS analysis allows an indication of the Sn oxidation state in the SnO_x. Thus the EXAFS and $\Delta\mu$ analyses complement each other to provide some common information, but also each provides its own unique information. These XAS data analysis procedures are used here to explain how the noble metal (Au) interacts with the metal oxide support (SnO_x). Two Au-SnO_x/VC samples with Au weight percentages of 10 and 20% and particles sizes (2.0 and 2.7 nm, respectively) are analyzed to compare particle size differences. The XAS results for Au-SnO_x/VC are also compared to those obtained for Au/VC as a standard.

3.2 Experimental

3.2.1 Synthesis of Au-SnO_x/VC

Full details of the synthetic procedures are described elsewhere[1,38]. Anhydrous $SnCl_2$ (Aldrich, 98%) was dissolved in high-purity H_2O (18 MΩ-cm, NANOpure, Barnstead International) proceeded by drop-wise addition of 1 M NH_4OH (Aldrich, ACS grade) until a white precipitate formed under moderately acidic conditions (pH 2.5), the latter characterized via X-ray diffraction as $Sn_{21}Cl_{16}(OH)_{14}O_6$. This tin-oxy-chloride precipitate was then washed in high-purity water, centrifuged, and the resulting powder was isolated and air-dried. A portion of this powder (1.5 g in 10 mL H_2O) was added to water, suspended by stirring, and impregnated with Au by a drop wise addition of 20 mL $HAuCl_4 \cdot xH_2O$ (49% Au, Alfa Aesar) solution (0.021 M) to

achieve 9.4 wt.% Au and 40 mL to achieve 20 wt.% Au. The previously white tin compound turned brown with the Au^{3+} addition. The resulting catalyst was repeatedly washed, isolated, and then air-dried before being heated to 150 ºC in air for 12 hours. The heat-treated catalyst was later stirred in hot, high-purity H_2O for 1 hour. The final material was isolated by vacuum filtration. The desired product, Au-SnO_x, was mixed with Vulcan carbon (VC) in a 3:1 catalyst:carbon ratio to make Au-SnO_x/VC. Final compositions of the two catalysts were nominally 10 wt. % and 20 wt. % Au. Electrochemical testing using RDE was then conducted on the sample, as described in reference 1, to confirm the materials activity for the ORR. A standard Au/VC of 10 wt% Au was used as received from E-TEK.

3.2.2 Rotating Disk Electrode Cyclic Voltammetry

Electrochemical measurements were conducted with the use of a rotating disk glassy carbon electrode (GCE) (Pine Instruments GCE, 5mm diam). The GCEs were attached to a Pine AFCPRD rotator that was connected to a Brinkmann Instruments Eco Chemie Autolab PG Stat 30 potentiostat utilizing a Ag/AgCl reference electrode or a RHE (all potentials reported relative to RHE).

Catalyst inks were applied to the GCE using a technique adapted from the literature[38]. The ink catalysts were made by grinding a 20mg, ~3:1 mass ratio of Au-SnO_x: Vulcan carbon (VC) (Cabot, XC-72) using a mortar and pestle to improve electronic conductivity of the metal oxides. The ground Au-SnO_x/VC ink was mixed with a 2.0g solution containing 20 mL isopropanol, 80mL deionized H_2O, and 0.4mL of 5 wt.% nafion ionomer. The resulting Au-SnO_x/VC ink was sonicated for 1 hour, stirred overnight and sonicated for an additional 30 minutes to 1 hour. A 12-20 μL aliquot of the ink was administered onto the GCE and dried rapidly under air. This “fast-drying” technique of the GCE was used to improve the quality and uniformity of the film as opposed to letting the GCE dry for several hours. The final coated GCE was submerged in a 25°C cell containing 0.1M $HClO_4$, a Au wire counter electrode, and RHE.

3.2.3 X-Ray Absorption Spectroscopy

In situ X-ray Absorption Spectroscopy (XAS) experiments were conducted at the National Synchrotron Light Source (NSLS) at Brookhaven National Laboratory, Upton, NY. The measurements were taken in an X-ray transparent electrochemical half-cell, which was designed by the Adzic research group at Brookhaven National Lab[39]. Au-SnO_x/VC and Au/VC powders were mixed with enough 1M $HClO_4$ to make a paste. The catalyst paste was then applied to a carbon cloth and assembled in the cell. The cell was placed in front of the beam between two detectors that collected incident (I_o) and sample (I) data. After the cell was cycled, full EXAFS scans were collected at potentials ranging from 0.3 - 1.0V at 0.1V increments for the Sn K edge data, and at these same potentials plus two higher potentials, 1.2 and 1.4V, for the Au L_3 edge data. The cell was cycled to a desired potential and held potentiostatically throughout the duration of the absorption measurement

XAS data were taken at the Au L_3 and Sn K edges for 10 wt. % and 20 wt. % Au, Au-SnO_x/VC catalysts and only at the Au L_3 edge for 10 wt. % Au/VC standard. The Au L_3 edge data were collected on NSLS beamline X-11B with a Si (111) double crystal monochromator and the Sn K edge data collected on X-11A with a Si (311) double crystal monochromator. The NSLS storage ring operated at a beam energy of 2.80 GeV and ring currents between 40 and 200 mA.

3.2.4 XANES Analysis

The absorption coefficient, μ, was obtained from the raw XAS data using the ATHENA code of Ravel and Newville[40]. The contributions of μ arising from any adsorbed O is isolated (as illustrated in Figure 3.1) by taking the difference between a referential μ (stated as Au or SnO_x) and the μ in the presence of adsorbed or desorbed O, given as O/Au or O/SnO_x, hence the Δμ can be presented by Eqs. 6 and 7:

$$\Delta\mu = \mu\,(O/Au) - \mu\,(Au). \qquad (3.6)$$

$$\Delta\mu = \mu\,(SnO_x) - \mu\,(O\text{-}SnO_x) \qquad (3.7)$$

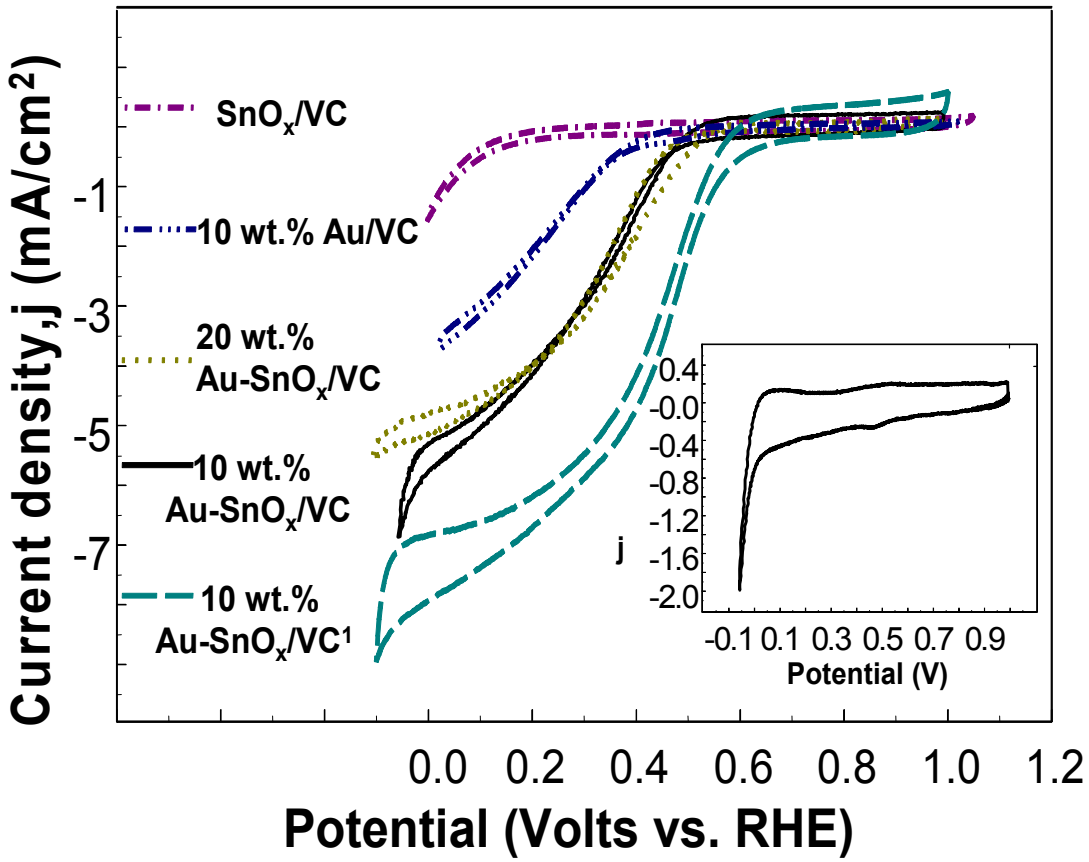

Figure 3.2 Cyclic voltammetry in O_2-saturated 0.1 M $HClO_4$ for 10 and 20 wt.% Au in Au-SnO_x/VC compared to previous results[1] for Au/VC, SnO_x/VC and 10 wt.% Au, Au-SnO_x/VC. Measurements taken at 20 mV/s, 1600 rpm, and 25 °C. Inset shows cyclic voltammogram of 10 wt.% Au, Au-SnO_x/VC under Ar-saturated 0.1M $HClO_4$ at 20mV/s, 1600 rpm, and 25 °C

Note that eq. 6 represents O adsorption onto Au, while eq. 7 represents O desorption from the SnO_x, thus the "reference" states represent a state at a potential where there is a "clean" Au metal particle and a "native" SnO_x surface so that the magnitudes of the $\Delta\mu$ will reflect changes from these reference states. The optimal choice for the "clean" μ(Au) reference is that of the electrode at 0.3V; where there are little or no adsorbed hydrogen ions or ClO_4^- anions on the Au. The Sn K edge data were treated similarly to the Au L_3 data where the μ obtained at 0.3V RHE in $HClO_4$ is also used as the $\mu(SnO_x)$ reference. This choice for the $\mu(SnO_x)$ reference is arbitrary, since we have no other evidence to indicate that the SnO_x surface was more ordered at this potential than at the others (see CV under Argon in Figure 3.2 insert); it was done for consistency with the Au L_3 analysis.

All XANES spectra were energy aligned before calculating the $\Delta\mu$. This alignment procedure is critical to achieve full cancellation of the large atomic contribution in μ, since the $\Delta\mu$ arising from adsorbates is only in the range of 1-3% of the normalized μ step height. Slight shifts in the data may arise from photon beam drift and other possible energy uncertainties arising from the monochromator and/or analyzer. Normally these energy uncertainties are removed by aligning the μ data for reference foils that were taken simultaneously with the sample at each potential. These reference foils are placed between the second and third detector so that $\mu_{ref} = \ln I/I_{ref}$. The energy shifts required to align the reference foils are then applied to the sample spectra.[30, 34]. However, in this work, the Au loading in the Au-SnO_x catalysts are low (10 mg Au /g catalysts) so that in order to achieve a sufficient step height in the Au XANES, rather thick layers of catalyst were required (roughly 7-8 mg/cm^2). This causes significant scattering of the beam, making the analyzer current, 'I', so small that the obtained μ_{ref} is not ideal for alignment.

Therefore an alternate procedure is employed in this work that we have used previously when μ_{ref} was not available[41, 43]. This procedure involves aligning the sample Au-Au EXAFS

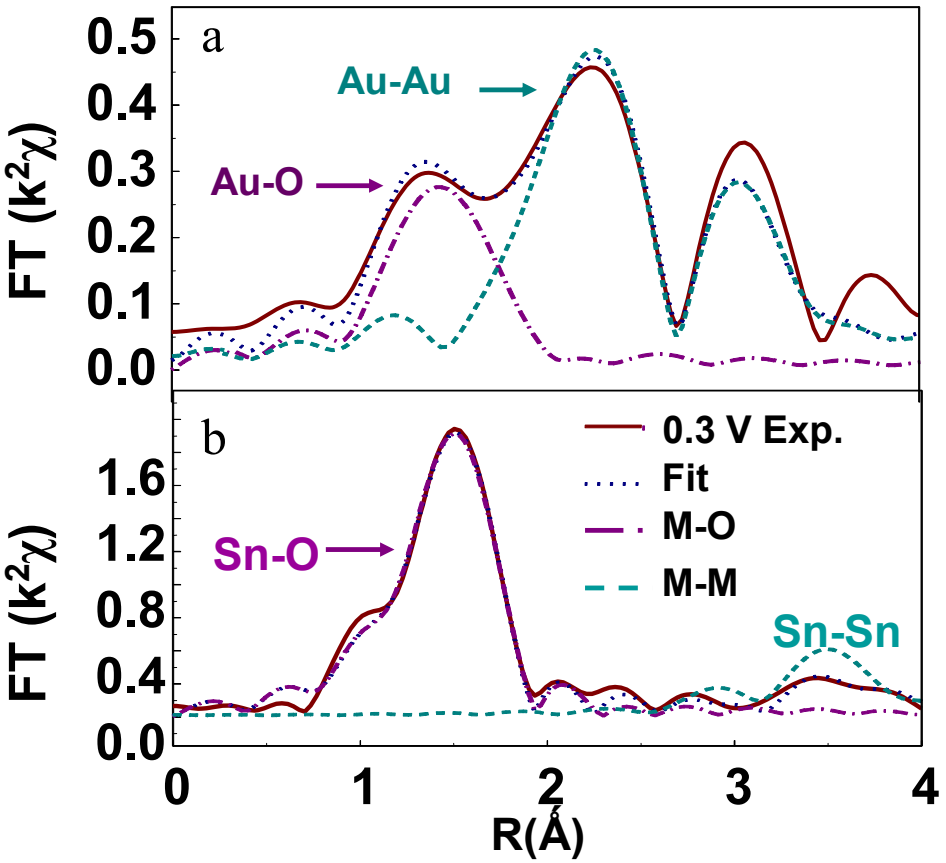

Figure 3.3 (a) Fourier transform of the Au L_3 edge EXAFS data (2.5<k<9.5 $Å^{-1}$, k^2) and two shell (Au-Au and Au-O) fit in R space (1.5<R<3.5Å) at 1.4V in $HClO_4$. The individual Au-Au and Au-O components are also shown. (b) Fourier Transform of the Sn K edge EXAFS data (2<k<10$Å^{-1}$) and two shell (Sn-Sn and Sn-O) fit in R space (0.5 < R < 4Å) at 0.3V in $HClO_4$. The individual Sn-Sn and Sn-O components are also shown.

oscillations in the range of 70-200 eV. Since the Au-O EXAFS scattering contribution is not present at this energy ($\Delta\mu$ is near zero at above 70 eV), it does not interfere with this alignment procedure. Using this procedure the spectra taken at potentials >0.3V were aligned to that at 0.3V.

3.2.5 EXAFS Analysis

The EXAFS analysis was carried out using the ATHENA and ARTEMIS codes[40] from the IFEFFIT software package[45]. The absorption coefficient, μ, was obtained from the Athena program in the same process as described above for the XANES region. The post-edge background was removed using normal spline techniques, and a smoothing criterion that leaves the atomic XAFS in the χ function rather than in the background is used here as described previously in the literature[46-49]. The data were then imported into the ARTEMIS program for EXAFS analysis. The theoretical analysis was based on calculations with the FEFF 8.0 code[50] on a Au_6 "Janin cluster"[51] for the Au L_3 edge data and a cluster with the Cassiterite (SnO_2)[52] crystal structure to be used for the Sn K edge data. The model was used in FEFF8.0 to calculate Au-Au, Au-O, Sn-Sn, and Sn-O scattering paths which were fit to the experimental data taken at the Au L_3 and Sn K edges, allowing determination of coordination numbers and ultimately particle size. The pre-edge background was removed using a linear polynomial, and the many-body S_0^2 factor was set at 0.933 for the Au edge and 0.921 for the Sn edge. The S_0^2 values were also calculated in the FEFF 8.0 code. ARTEMIS calculates a factor labeled as "amp" (for amplitude) for each path used for a fit to the data. This "amp" should technically correspond to the experimental S_0^2, assuming FEFF's model cluster and the experimental cluster are identical. This is not actually true in this case, because the model cluster is in fact much smaller than the experimental cluster. However, the relation

$$S_0^2(\text{FEFF})/N_{\text{theory}}=\text{amp}/N_{\text{exp}}, \qquad (3.8)$$

where N_{theory} is the coordination number of the model (theoretical) cluster, allows the coordination number of the actual experimental cluster to be calculated:

$$N_{exp}=amp*N_{theory}/ S_0^2(FEFF). \quad (3.9)$$

3.2.6 FEFF 8.0 Calculations

FEFF 8.0 calculations were conducted to interpret not only the EXAFS region but also the Δμ spectra obtained from the XANES region, i.e. eqs. 6 and 7. This was done for Au, eq. 6, using the Au_6 "Janin cluster"[51]. The model cluster has been used extensively in previous research conducted on Pt electrocatalysts[30-34]. The geometry for Pt (and now for Au) is preferred because it contains fcc and hcp sites just in case there are different binding sites for O. However, as it will be shown later, atop O(H) is the only geometric binding site prevalent in Au. The Janin cluster also has low symmetry. This is advantageous because a higher symmetry model such as an octahedral cluster produces a state near the Fermi level in the unoccupied density of states (DOS) that complicates the accurate prediction of Δμ signatures by FEFF 8.0[31]. Throughout this work, the Au_6 cluster is used, with the Au-Au distance set at 2.88 Å.

For the Sn K edge data, the crystal structure SnO_2 in Cassiterite form was used to interpret the XANES data. The crystallographic parameters were generated by using the ATOMS database[53]. The structure contains threefold-coordinated oxygen atoms which form distorted octahedra around the tin atoms. In the FEFF 8.0 program, the Sn was then modeled to be further reduced by removing more oxygen atoms as indicated in Eq. 7.

3.3 Results

3.3.1 Rotating Disk Electrode (RDE) Cyclic Voltammetry

Figure 3.2 shows the RDE voltammetry for the 10 wt. % Au-SnO_x/VC and 20 wt. % Au-SnO_x/VC sample that was studied in this work. The RDE results are also shown from a previous study[1] for SnO_x/VC, the 10 wt% Au/VC standard, and 10 wt. % Au, Au-SnO_x/VC. Though the previous 10 wt. % Au-SnO_x/VC sample has higher ORR activity than the sample used in this study, the potential at the onset for ORR for both Au-SnO_x/VC samples occur at a higher

potential than in Au/VC or SnO_x/VC. The RDE data for the Au/VC and SnO_x/VC also do not reach the limiting current for the ORR which is around -6 mA/cm^2 at 1600 rpm. These observations indicate that Au-SnO_x/VC has some ORR activity, although with much higher overpotentials than typically found for Pt/VC.

3.3.2 EXAFS Analysis

The results from the EXAFS analyses of the data at each potential taken in situ are shown in Tables 3.1 (for Au-SnO_x, Au L_3 edge) and 3.2 (for the Sn K edge data). Table 3.3 lists the results for Au/VC. The EXAFS results in Tables 3.1-3.3 were obtained by fixing the Debye-Waller σ^2 parameter at an optimum value for all potentials in order to decrease the number of parameters, and make the resultant relative values of N_{Au-Au} and N_{Sn-Sn} more significant. The large linear dependence between N and σ^2 gives a sizeable disparity in N if σ^2 is allowed to change. Figure 3.3 shows the Fourier Transform of experimental data and representative theoretical fits in R space for Au-SnO_x/VC at the Au L_3 and Sn K edges revealing the overall quality of the fits, using the 3 fit parameters per path (namely N, R, and E_o) as indicated in the Tables. Comparably good fits were obtained in nearly all cases.

Table3.1 shows a gradual decrease in Au-Au coordination, and then a sharp decrease at 1.2V as the cluster is oxidized above this potential. In the case of Sn, N_{Sn-Sn} increases to a maximum at 0.5V then decreases a bit and plateaus. Then, at 0.9V, it increases again. This shows oxidation and reduction of the SnO_x support which affects the reactivity of gold. A correlation between the changes in Au-Au and Sn-Sn coordination numbers with potential will be shown and discussed below, suggesting that the Au and Sn exhibit a metal-support interaction.

3.3.3 XANES Analysis

Figure 3.4 shows the L_3 absorption spectrum, μ, for a Au-SnO_x/VC electrode at several potentials. Similar data were obtained for Au/VC and Sn K edge samples as well. Clear differences in μ

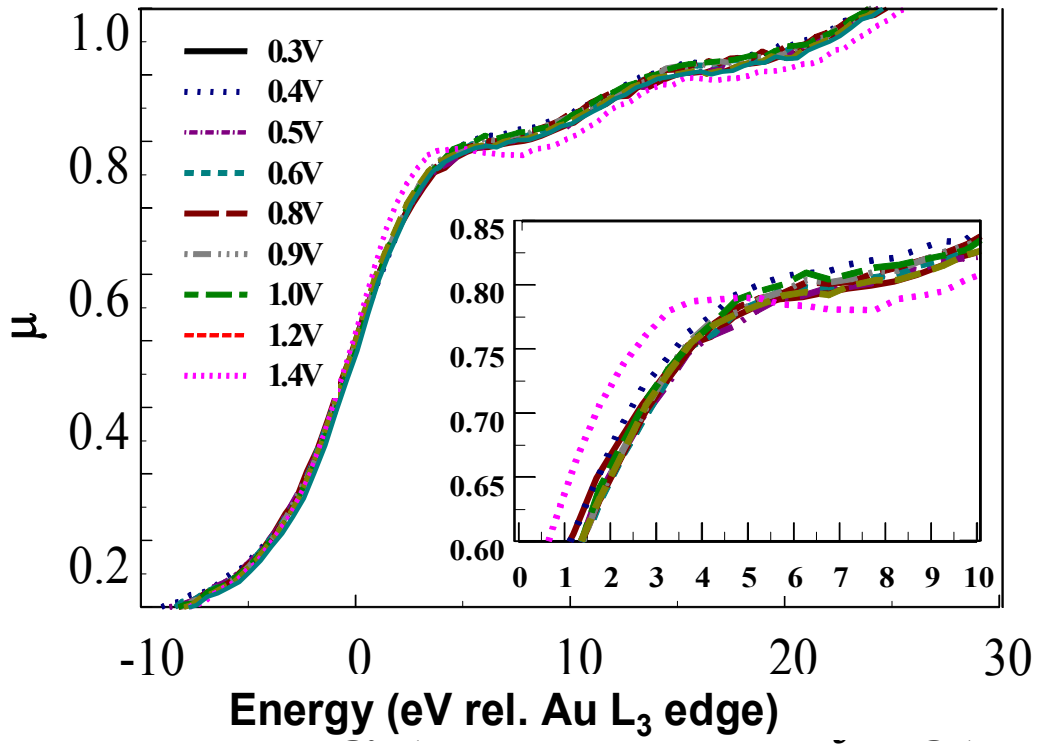

Figure 3.4 Experimental Au L_3 absorption spectra, μ, for the Au-SnO_x/VC electrode at indicated potentials in $HClO_4$.

Table 3.1: Summary of EXAFS Results for 10 wt.% Au/SnOx/VC at Au L_3 edge[a]

Potential (V,RHE)	N_{Au-Au}[b]	R_{Au-Au} ±0.01Å	σ^2 (Å^2)	E_0 (eV) ±1 eV	N_{Au-O}[b]	R_{Au-O} ±0.01Å	σ^2 (Å^2)	E_0 (eV) ±1 eV
0.3	8.93	2.83	0.009	5.07	N/A	N/A	N/A	N/A
0.4	8.88	2.84	0.009	5.76	N/A	N/A	N/A	N/A
0.5	8.66	2.83	0.009	5.05	N/A	N/A	N/A	N/A
0.6	8.52	2.82	0.009	3.43	N/A	N/A	N/A	N/A
0.8	8.48	2.83	0.009	3.50	N/A	N/A	N/A	N/A
0.9	8.22	2.83	0.009	3.66	N/A	N/A	N/A	N/A
1.0	7.97	2.84	0.009	4.06	N/A	N/A	N/A	N/A
1.2	7.65	2.84	0.009	4.27	0.59	2.12	0.003	7.09
1.4	7.20	2.83	0.009	5.71	0.81	1.96	0.003	-0.43

[a] S_0^2 fixed at 0.933 as calculated by FEFF8

Table 3.2: Summary of EXAFS Results for 10 wt.% Au/SnOx/VC at Sn K edge[a]

Potential (V,RHE)	N_{Sn-Sn}[b]	R_{Sn-Sn} ±0.02Å	σ^2 (Å^2)	E_0 (eV) ±1eV	N_{Sn-O}[b]	R_{Sn-O} ±0.02Å	σ^2 (Å^2)	E_0 (eV) ±1 eV
0.30	3.31	3.72	0.0015	6.58	5.97	2.04	0.0032	3.47
0.40	3.48	3.71	0.0015	5.57	5.99	2.03	0.0032	2.75
0.50	3.66	3.73	0.0015	7.62	5.99	2.05	0.0032	4.70
0.60	3.43	3.74	0.0015	7.82	5.90	2.05	0.0032	4.11
0.70	3.37	3.73	0.0015	7.11	5.75	2.05	0.0032	4.44
0.80	3.40	3.72	0.0015	7.82	5.82	2.04	0.0032	4.78
0.90	3.41	3.74	0.0015	8.81	5.61	2.05	0.0032	4.28
1.00	3.60	3.71	0.0015	5.70	5.70	2.04	0.0032	4.02

[a] S_0^2 fixed at 0.921 as calculated by FEFF8

Table 3.3: Summary of EXAFS Results for Au/VC at Au L_3 edge[a]

Potential (V,RHE)	N_{Au-Au}[b]	R_{Au-Au} ±0.01	σ^2 (Å^2)	E_0 (eV) ±1 eV
0.3	8.83	2.84	0.007	3.66
0.4	9.05	2.84	0.007	3.82
0.6	9.02	2.84	0.007	3.66
0.8	9.09	2.84	0.007	3.84
1.0	9.22	2.84	0.007	3.90
1.2	9.03	2.85	0.007	4.34
1.4	8.77	2.85	0.007	4.43

[a] S_0^2 fixed at 0.933 as calculated by FEFF8

[b] Although the absolute errors are of the order of 20%, the changes with potential are expected to be meaningful to 0.1 because of the fixed σ^2

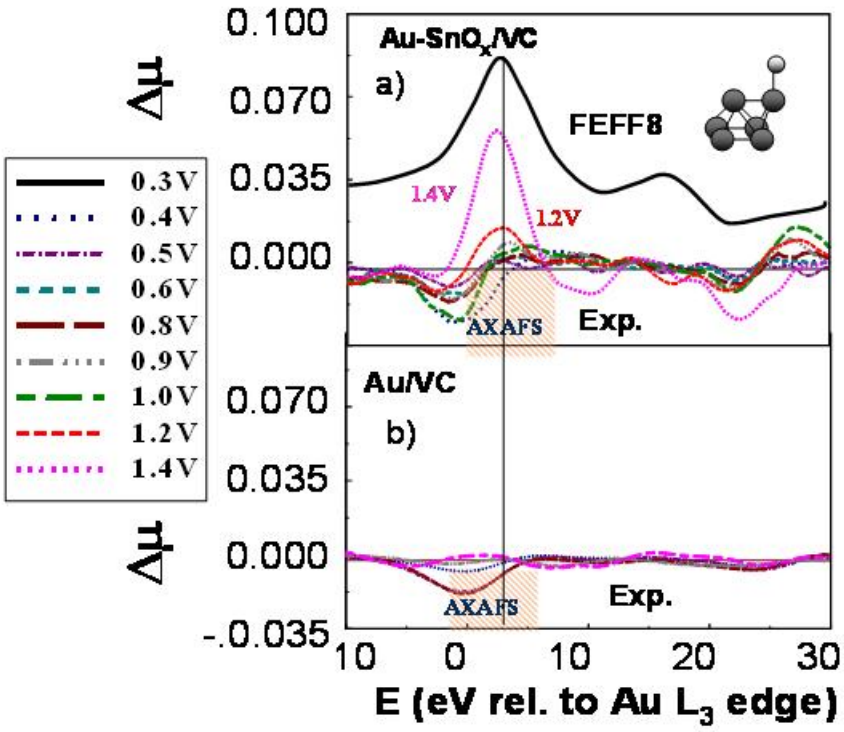

Figure 3.5 Experimental Δμ difference spectra for (a)Au-SnO_x/VC and (b) Au/VC. The theoretical signature for atop O(H) generated by FEFF 8.0 is also shown (solid line). Theory was shifted up for illustration.

well above the noise level, as indicated by the inset, are seen as a function of potential. Figure 3.5 shows the Δμ difference spectra using the 0.3V spectrum as the reference spectrum for both Au/VC and Au-SnO_x/VC at the Au L_3 edge respectively. The FEFF8 calculated theoretical signature for O/Au in an atop binding sight indicative of OH/Au is also shown for comparison. Although a systematic trend is not observed in these spectra at all potentials, the Δμ at 1.2 and 1.4V show a sharp increase in magnitude around 3 eV, revealing a strong similarity in lineshape with the theory for O/Au, while a similar sharp increase is not seen for Au/VC. We will show below that the small negative contributions in Δμ below 1 V are due to EXAFS and possibly AXAFS[53] contributions. Only significant atop O(H) adsorption is seen for Au-SnO_x/VC above 1.0V potential and no two-fold or subsurface oxygen (n-fold) is present (they give significantly different signatures[31]); though at higher potentials this n-fold O adsorption may occur

Figure 3.6 shows the Sn K edge Δμ difference spectra for Au-SnO_x/VC using the 0.3V spectrum as the reference and the FEFF8 calculated Δμ signature for O removal from the cassiterite SiO_2 structure shown. The magnitudes of Δμ at -2 eV will be plotted below showing a correlation in the reduction and reoxidation of the SnO_x surface with increasing potential.

3.4 Discussion

3.4.1 Correlation of EXAFS and Δμ data

Combining EXAFS and Δμ analysis procedures reveals significant new details regarding the effect of the Au-SnO_x metal support interaction. Comparison between the EXAFS and Δμ data can best be made by comparing the magnitude of the Δμ signal and the EXAFS coordination numbers with potential. Figure 3.7 shows such a comparison of the Au L_3 edge data, and Figure 3.8 of the Sn K edge data.

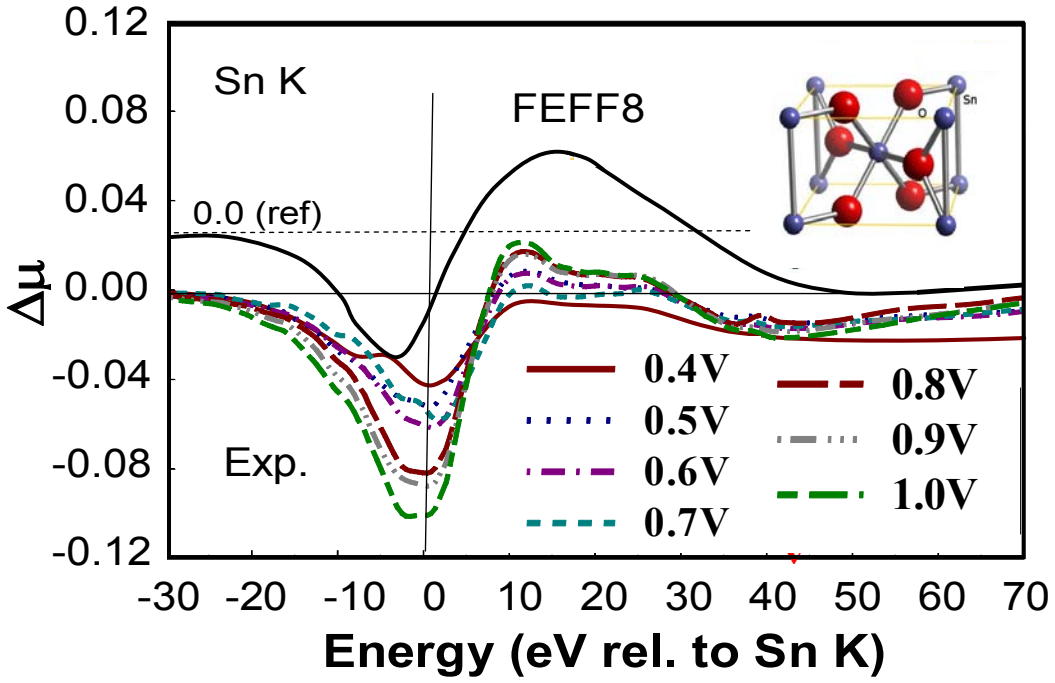

Figure 3.6 Experimental Δμ difference spectra of Au-SnO_x/VC in $HClO_4$ at the Sn K edge with the theoretical signature for oxygen desorption generated by FEFF 8.0. Theory has been shifted up for illustration.

Figure 3.7 compares the N_{Au-Au} and $\Delta\mu$(O/Au) for both the Au/SnO_x/VC and Au/VC catalysts. A sharp decrease in N_{Au-Au} beginning above 0.8 V correlates with an increase in the $\Delta\mu$ for the Au-SnO_x/VC catalysts. The N_{Au-Au} drops because the presence of O decreases the Au-Au scattering making the effective N_{Au-Au} appear smaller. Thus both the EXAFS and $\Delta\mu$ data indicate that OH adsorption is occurring on the Au above 0.8 V. The $\Delta\mu$ data reveals that it is due to OH adsorption, indicated by the good agreement with the theoretical $\Delta\mu$ signature for atop O/Au in Figure 3.4, and the different signature which arises for n-fold bonded O[31]. Note that a similar correlation between N_{Au-Au} and $\Delta\mu$ occurs for Au/VC, but the indicated adsorption of OH now begins nearly 300 mV to higher potential. This reveals a very strong ligand effect by the SnO_x support on these small Au particles, making the Au much more oxophilic.

Au particles are known to be relatively unreactive with water and with O_2 compared to Pt[6-9] which is apparently why the ORR rate for Au/VC is very low as shown in Figure 3.2. OH adsorption via water activation does not occur on Au/VC until above 1.3 V, which is moved down by 300 mV due to the SnO_x support. However, Figure 3.7 reveals a slight drop in N_{Au-Au} already above 0.4 V for Au-SnO_x/VC when the $\Delta\mu$ shows no OH adsorption. The reason for this earlier drop in N_{Au-Au} becomes evident in Figure 3.8, which reveals a change in the SnO_x support is occurring around this potential.

Figure 3.8 compares the Sn K-edge data (both N_{Sn-Sn} and $\Delta\mu$ magnitudes) with the N_{Au-Au} plot from Figure 3.7. An N_{Sn-Sn} of 2 is expected for SnO_2 and 4 for SnO. Figure 3.8 shows that in Au-SnO_x/VC the N_{Sn-Sn} increases from 3.3 to 3.7 between 0.3 and 0.5V, suggesting that the SnO_x/VC is always a mixture of Sn^{2+} and Sn^{4+} (i.e. SnO_2 and SnO), and is most reduced at 0.5V. The dominant peak in the Fourier transform of Figure 3b due to N_{Sn-O} coordination stays essentially constant (as also revealed by Table 3) because Sn is surround by 6 O atoms in both oxidation states. Thus the oxidation state of the Sn is best determined from the Sn-Sn coordination as shown in Figure 3.8. An exact estimate of the amounts of SnO_2 and SnO cannot be made from

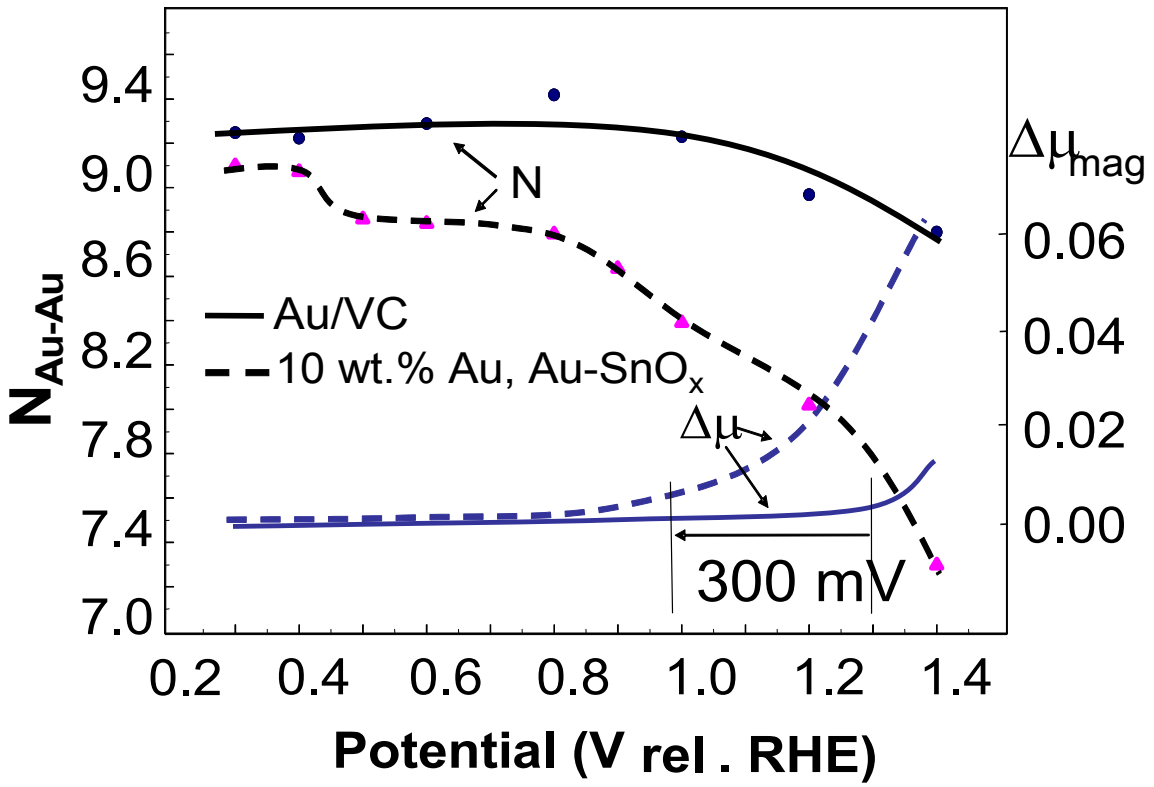

Figure 3.7 A comparison of N_{Au-Au} from Au/VC (solid line) and 10 wt. % Au, Au-SnO_x/VC (long dashed line) from Tables 1 and 2, along with the amplitudes of the Δμ spectra obtained from Figure 3.5.

the N_{Sn-Sn} values obtained, because the values of 2 and 4 indicated above are only expected for infinite bulk crystals, and the finite size of the hydrous SnO_x agglomerates used in this work will reduce the actual N_{Sn-Sn} from the bulk values. The values of 3.3-3.7 found suggest that the oxidation state of the SnO_x is quite close to that of SnO. While Sn-Sn bonds are not found in either SnO_2 or SnO, the compounds both have comparable Sn-Sn lattice distances which are revealed by the EXAFS[55].

The increase in N_{Sn-Sn} and $\Delta\mu$ results between 0.3 and 0.5 V both suggest that O atoms from the SnO_x are being depleted (recall that in the case of SnO_x, Eq. 3.7, the $\Delta\mu$ magnitude indicates O reduction). The small change in N_{Au-Au} mentioned above falls at exactly the same potential as this sharp O depletion of the SnO_x support, revealing that the change in Au particles is brought on by the change in the SnO_x support. We attribute the small decrease in N_{Au-Au} at this potential to a small change in the morphology of the Au particle from more spherical to more hemispherical or oblate. Such a reduction in N_{Pt-Pt} data has been seen previously in EXAFS when Pt particles have changed their shape due to changes in the support from more acidic to basic[56]. The illustrations of the Au clusters near the top of Figure 3.8 reflect these changes in Au clusters from spherical below 0.4 V, to oblate above 0.4 V to finally covered with OH above 1.2 V.

The increasing reduction of the SnO_x support between 0.3 an 0.5 V in this O_2 free solution correlates very well with the ORR active region seen in Figure 3.2. However, as the potential increases past 0.5V and apparently ORR ceases (either from O_2 in the electrolyte or from the SnO_x), the N_{Sn-Sn} decreases again, indicating that the SnO_x becomes more oxidized again. Above 1.0V the N_{Sn-Sn} increases yet again, suggesting that the SnO_x is becoming reduced again. The words Red, Ox and Red in Figure 3.8 help to follow what process is occurring in each potential region. This latter reduction is probably due to the O(H) adsorption on the Au, which has become more oxophilic than the SnO_x above 1.0 V, as indicated by the direct O(H) adsorption seen in the $\Delta\mu$ data at these potentials.

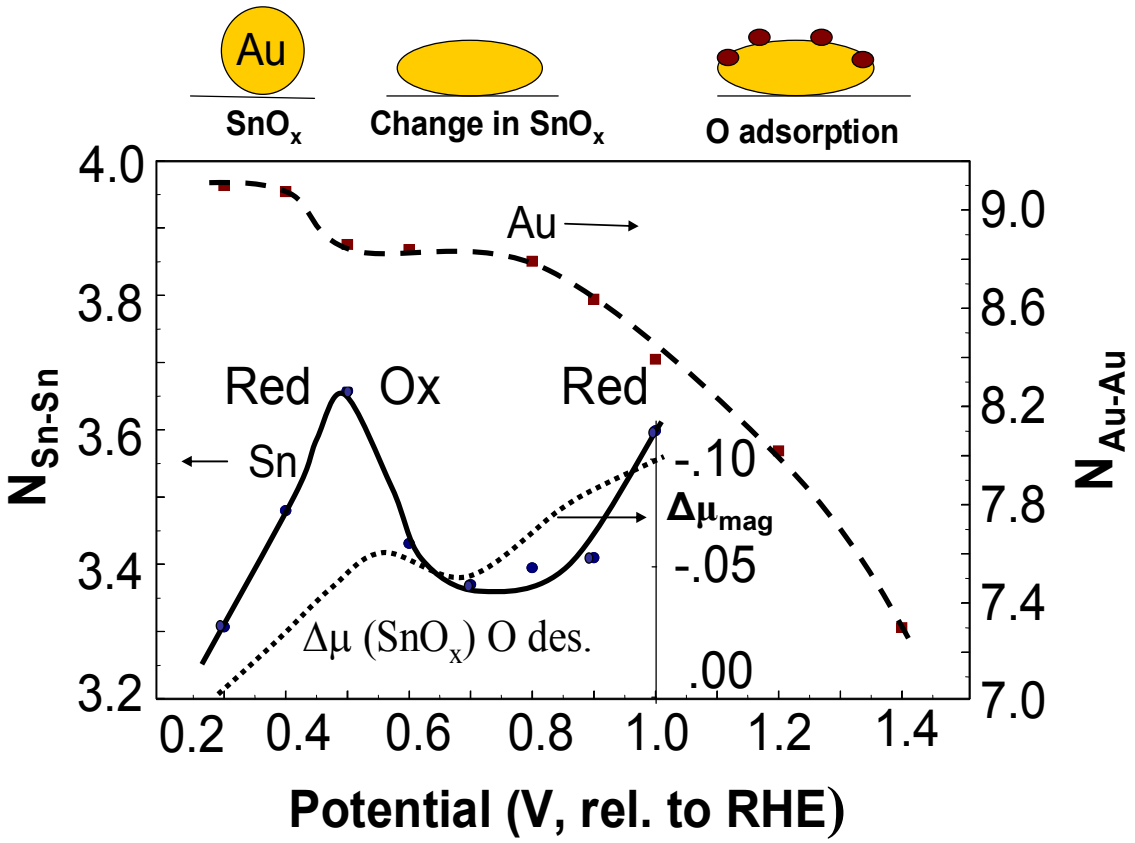

Figure 3.8 A comparison of $N_{Sn\text{-}Sn}$ (solid line, left axis) and $N_{Au\text{-}Au}$ (dashed line, right axis) from Tables 1-3 and Δμ (SnOx) from Figure 6 (dotted line, inset axis) for Au-SnO_x/VC. $N_{Sn\text{-}Sn}$ from 20 wt. % Au, Au-SnO_x/VC are not shown.

The trends in N_{Sn-Sn} in Figure 3.8 also include the Δμ magnitude They both show a general O depletion with increasing potential as indicated above, but the trends are different. Both show a maxima around 0.8 V, but this maximum is must stronger in N_{Sn-Sn}.

Why is the increase of N_{Sn-Sn} between 0.2 and 0.5 V much sharper than that in Δμ? N_{Sn-Sn} is reflecting the change in Sn-Sn coordination of the SnO_x, while Δμ is reflecting the change in Sn-O on the surface. As mentioned above, both SnO_2 and SnO have a N_{Sn-O} coordination number of 6, so N_{Sn-Sn} should change faster than the Δμ magnitude. The change in Δμ is probably reflecting the decrease in SnO_6 octahedra at the surface of the SnO_x agglomerates, where the octahedral are more apt to be disrupted. Thus N_{Sn-Sn} probably more faithfully reflects O depletion than does Δμ.

3.4.2 Effect of Au particle size

All of the data reported in the figures thus far were obtained using the 10 wt % Au-SnO_x/VC. This was done to avoid confusion between the two Au samples. Figure 3.9 now presents comparable N_{Au-Au}, and Δμ(Au) for 10 wt. % and 20 wt % Au-SnO_x/VC. The N_{Sn-Sn} (which is not shown) was remarkably similar in both compounds, which it should be because the Au loading should not significantly affect the SnO_x support. This remarkable similarity increases our confidence that the results reported above reflect the sample and are not artifacts.

The N_{Au-Au} for the 20 wt. %sample in Figure 3.9 shows larger fluctuations through the entire potential region, and does not show the large drop above 1 V as shown in Figure 3.7 for the 10 wt. % sample. The absence of the large drop in N_{Au-Au} magnitude strongly suggests that now OH adsorption is NOT occurring on the Au even up to 1.4 V, reflecting the much lower reactivity of the Au particles in this case. We attribute this to the much larger Au particles in the 20 wt.% Au case, as indicated by the much larger N_{Au-Au} coordination number, 9.6 in the 20 wt.% Au vs. 9.1 in the 10 wt. % Au. Assuming spherical particles this corresponds to particles of about 2.7 nm vs. 2 nm (or about 400 atoms/particle vs 200 atoms/particle) [57]. Larger Au particles are expected to be less reactive[58], and of course the ligand effect facilitated by the SnO_x support will be much

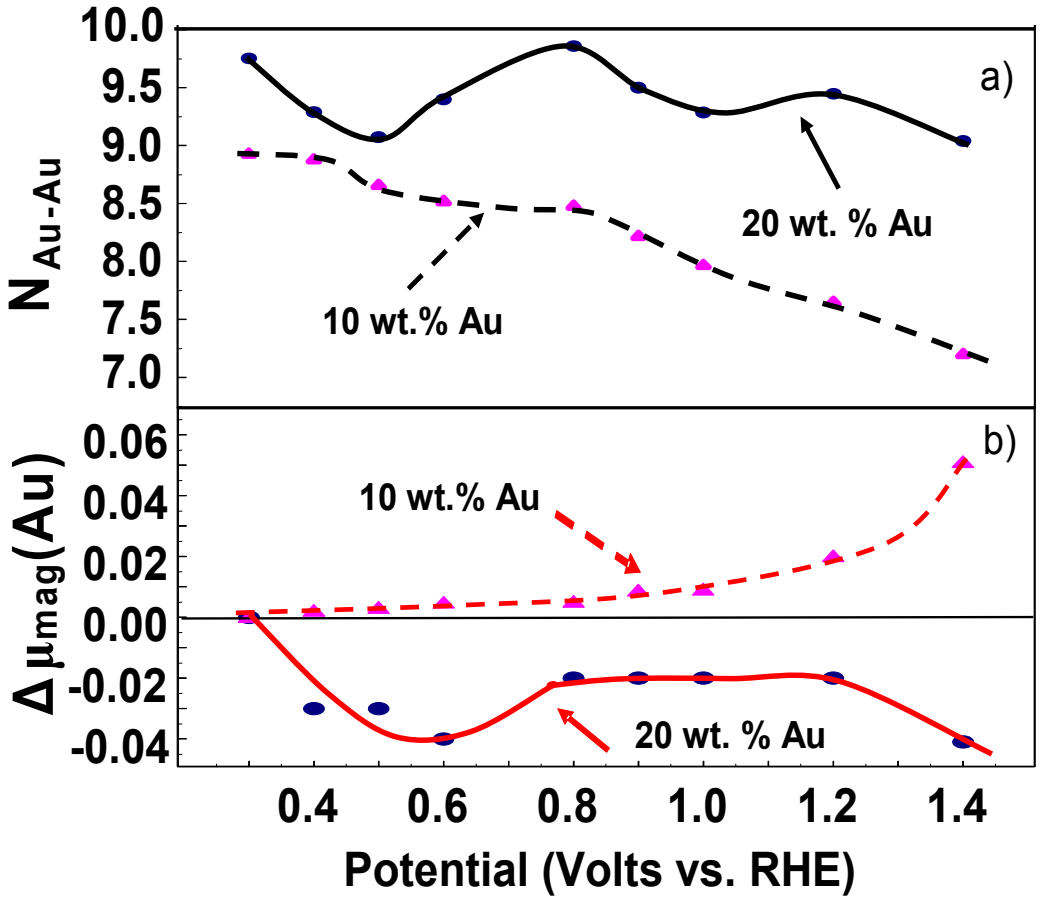

Figure 3.9 Comparison of $N_{Au\text{-}Au}$ (a) and $\Delta\mu_{mag}(Au)$ (b) for10 (2.0nm) and 20 (2.7nm) wt.% Au in Au-SnO_x/VC catalysts.

less effective for larger particles. Therefore, we are not surprised by the lack of significant OH/Au adsorption seen above 1.0 V for the 20% case. Figure 3.9 shows a reasonable correlation between the changes in $\Delta\mu$(Au) and $N_{Au\text{-}Au}$ for the 20wt% sample. This suggests strongly that the changes seen in $\Delta\mu$(Au) are simply reflecting changes in the EXAFS oscillations that are also reflected in $N_{Au\text{-}Au}$. As the SnO_x support is reduced, the bigger Au particles should reveal an even bigger change in $N_{Au\text{-}Au}$ as they change from spherical to more oblate in shape. Bigger particles are expected to undergo larger morphological shape changes with support compared to smaller ones, and in any event such shape change will be magnified in the $N_{Au\text{-}Au}$ for larger particles.

The $\Delta\mu$(Au) amplitudes are all negative for the 20 wt. %, like those seen at lower potential in Figure 3.5, and at no point do the $\Delta\mu$ magnitudes at 0 eV go positive reflecting OH/Au. Thus these data for the bigger Au particles suggest that the negative $\Delta\mu$ contributions at low potentials in Figure 3.5 are also due to small EXAFS changes (as suggested in the Results section above). However in Figure 3.5 they are much smaller because of the smaller Au particles in the 10 wt. % sample. In any event, the $\Delta\mu$(Au) are again consistent with the EXAFS $N_{Au\text{-}Au}$, indicating that no OH/Au is evident for these bigger particles below 1.4 V.

We conclude that all of the morphological shape changes seen in the smaller 10wt % Au-SnO_x/VC sample are magnified in the 20%, but that the larger particles are much less reactive toward water activation.

3.4.3 Electronic Effects vs. a Bifunctional Mechanism

The enhanced ORR rate seen for the Au-SnO_x catalysts compared to the Au/VC arises from a concerted Au-SnO_x mechanism, and two possible mechanisms have been previously given[1,2]. These include an electronic effect or a bifunctional mechanism as illustrated in Figures 3.10a and b. These mechanisms are in many aspects similar to the two summarized above for CO oxidation, one involving an "inert" oxide (which exerts only a ligand effect), and the other the active oxide providing O in a classic Mars van Krevelen like mechanism. The results above

suggest both mechanisms are active (at least for the smaller particles in water activation), but only the latter is apparently playing a role in the ORR.

The more commonly proposed electronic (or ligand) mechanism postulates that the support polarizes the Pt cluster in effect changing the position of the Pt 5d band. This effect can strongly change the Pt-O bond strength as shown previously by DFT calculations[3]. This phenomenon can be seen in our work with Au. This mechanism is indeed enhancing the absorption of OH on the Au via water activation in the Au-SnO_x/VC catalysts above 1.0 V, as clearly indicated by comparison of the $\Delta\mu$ intensities for Au-SnO_x/VC and Au/VC. Consistent with the DFT calculations of Norskov et al., this would suggest that the SnO_x support is moving the Au 5d band up or reducing the binding energy of the 5d electrons. In this mechanism, the upward movement of the 5d band pushes more electrons out of the Au-O antibonding orbital thus increasing the strength of the Au-OH bond. Although this mechanism appears to operate here for the 10 wt % Au-SnO_x/VC catalysts, it is important only above 1.0 V where the ORR is not occurring.

Perhaps the most convincing argument against the importance of the ligand mechanism in ORR reduction is the comparison between the 10 wt % and 20 wt % samples. ORR tests (Figure 3.2) show that they have nearly identical ORR reactivity curves, even though above we showed that the ligand effect from the SnO_x on the bigger Au particles for water activation was nearly negligible compared to that for the smaller particles in the 10 wt. % sample.

The strong O depletion seen in the SnO_x around 0.5 V as exhibited in Figure 3.8, suggests strongly that a bifunctional ORR mechanism is active for the Au-SnO_x/VC catalysts. In this the SnO_x is being reduced by the Au causing the depletion of O. In the presence of O_2, one would imagine that either a) the depleted SnO_x can dissociate the O_2 molecules, with then the O atoms moving toward the Au particle for reduction, or perhaps b) more likely only the interface between the Au particle and the nearby support are active sites for the ORR. When utilizing the Au-SnO_x/VC data shown in Figure3.2, one finds that the Tafel slope is essentially around 120 mV/decade,

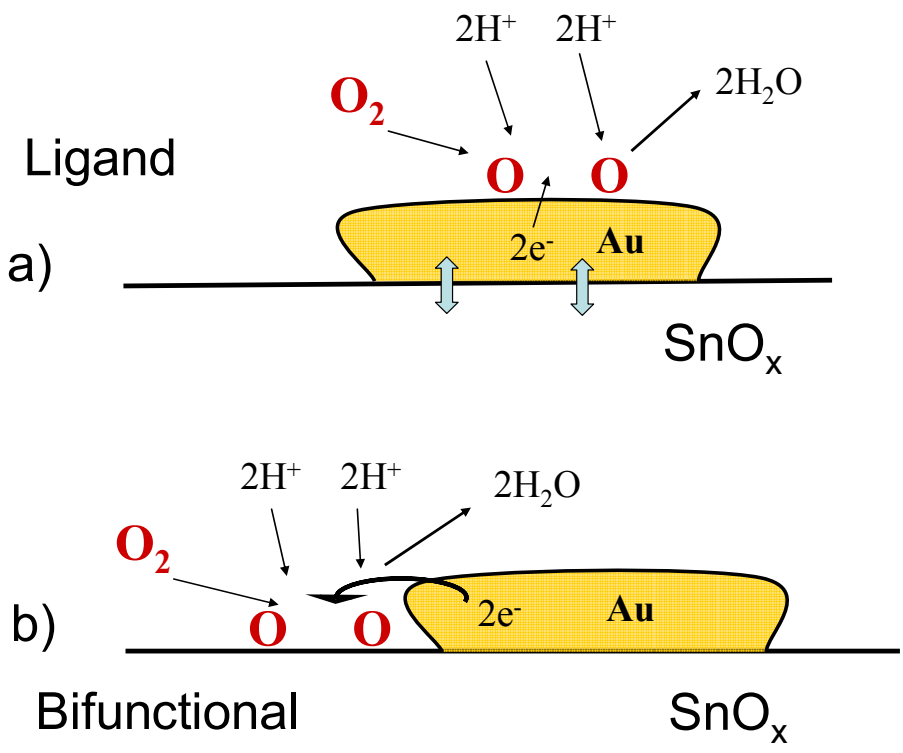

Figure 3.10 Electronic effects (a) vs. Bifunctional Mechanism (b)

just as found in Pt. This indeed suggests that the rate-determining step is the electron transfer to molecular O_2, suggesting step b above rather than step a.

In any event the SnO_x support appears to be directly involved in dissociating the O_2 molecule, with the Au particle doing the reduction; hence the terminology "bifunctional mechanism". Since we find this O depletion the strongest right at 0.5 V where the onset of the ORR begins, this mechanism most definitely appears to be the source of the enhance ORR rate for the Au-SnO_x catalysts.

3.4.4 Correlation to Gas Sensors and CO oxidation

Numerous studies have been previously reported on oxygen adsorption on Au in contact with SnO_2, and its electrical response in tin oxide gas sensors[58, 59]. Electrical conductance and calorimetric tests have shown that the presence of Au in contact with SnO_2 increases the heat of oxygen chemisorption to values larger than on either Au or SnO_2 separately. This strongly suggests that the Au-SnO_x interface is involved as suggested above. These gas sensor papers suggest the following mechanism for the O reduction

$$O_n^- - S_{ox} + S_I + e_M \rightarrow O_n^{2-} - S_I + S_{ox} \qquad \text{(Eq. 3.10)}$$

where O_n is either O or O_2, $-S_{ox}$ is an adsorption site on SnO_2, $-S_I$ is at the Au-SnO_2 interface, and e_M is an electron from the Au metal. Pulkkinen et al[59] have recently shown that below 700 K the ionic adsorbate is primarily O_2^-. Electrical conductance studies on the gas sensors also suggest the presence of space charge depleted SnO_2 areas near the interface, consistent with that suggested by the results in Figure 3.8 in the electrochemical cell.

The results above indicate strongly that SnO_x is indeed an "active" oxide for O_2 adsorption, and probably serves in this capacity also for CO oxidation. Previous studies[25] of CO oxidation over Au-SnO_2 did find that minimizing the Au metal's particle size and/or maximizing the Au metal oxide interface increased the reactivity. Unfortunately the CO oxidation reactivity should increase with decreasing particle size for either mechanism, so this does not rule out the ligand mechanism in this case.

3.4.5 Prospects for improving the performance of Au-SnOx/VC catalysts

Improvements in the electrocatalytic efficiency of Au-SnO_x/VC must be made if they are to become useful catalysts in fuel cells. From the electrochemical results in Figure 3.2, Au-SnO_x/VC becomes active only at 0.55V as compared to Pt/VC which is active at around 0.95V.

Possible improvements to the Au-SnO_x catalysts include:

1) Optimizing the Au and SnO_x interface through control of particle size (i.e. making them smaller). Assuming the bifunctional mechanism, and the active sites at the Au-SnO_x interface, suggest that the extent of this interface region must be increased. Recent results have shown that the reactivity toward O_2 and CO increases significantly with decreasing Au particle size[60]. This would suggest that smaller Au islands on the SnO_x surface would be better; however, the O_2 sensor data also suggest that the O adsorption energy is larger at the interface, and this may require a certain threshold amount of Au to trigger the increased oxygen adsorption energy. The results reported above showed no significant effect on the ORR reactivity for the 10 and 20 wt. % Au-SnO_x/VC catalysts loading so the effects of Au particle size may be small.

2) Improving sample purity: unfortunately chloride, which was present in our precursor, could be poisoning some Au sites. Our $\Delta\mu$ results, which is able to detect Cl on a Au surface did not detect it in this case, but the $\Delta\mu$ signature for Cl and O is similar, so we cannot rule out the presence of all Cl. Thus our catalysts might be improved by eliminating Cl as precursor.

3) Modifying support composition. Many metal oxides have been used as a support for CO oxidation of Au, with some serving as active and others as inactive supports. Evidence has been given to show that different preparation procedures for even the same support, such as calcination temperature and other variables can significantly alter the effectiveness of "active" supports [12-16]. A different oxide support such as tin phosphates instead of SnO_x might possibly be more efficient at adsorbing and dissociating O_2 atoms. Little work has been published in this regard for the

ORR, and of course the oxide must be stable in the highly acidic electrolytes utilized in a fuel cell.

3.5 Conclusion

Analyses of experimental Au L_3 and Sn K XANES and EXAFS data taken in situ on Au/VC and Au-SnO_x/VC electrodes, and evaluation with theoretical FEFF 8.0 calculations provides major new insights into the metal support (Au-SnO_x) interaction. These XAS results are consistent with the previous gas sensor and CO oxidation results for active oxide supports, and show that a bifunctional mechanism plays the dominant role in the ORR reaction on Au-SnO_x. In this mechanism, O_2 adsorbs and dissociates on the SnO_x surface probably in the interface region with the Au, and then the O- is further reduced by the nearby Au either directly or after conversion to O(H) groups. Enhanced O(H) adsorption via water activation occurs above 1. V on the 10 wt. % Au-SnO_x/VC when smaller 2 nm Au particles are present, probably through a metal/support ligand mechanism, but this has no apparent effect on the ORR occurring at much lower potentials. On larger 3 nm Au particles such a metal/support ligand effect was not seen.

3.6 References

[1]Baker,W.S.; Pietron, J.J.; Teliska, M.; Bouwman, P.; Ramaker, D.E.; Swider-Lyons, K.E., *J. Electrochem. Soc.* **2006,** *153*, A1702.

[2] Gatewood, D.; Ramaker, D.E.; Sasaki, K.; Swider-Lyons, K.E.; in *Proton Exchange Membrane Fuel Cells VII*, T. Fuller et.al., Editors, PV 11-1, p. 271, The Electrochemical Society Proceeding Series, Washington, D.C. **2004**

[3] Stamenkovic, V.; Mun, B.S.; Mayrhoffer, K.; Ross, P.; Markovic, N.; Rossmesil, J.; Greeley, J.; Nørskov, J.K.; *J. Angew. Chem. Int. Ed*. **2006**, *45*, 2897

[4] Hammer, B.; Nørskov, J.K; *Nature,* **1995**,*376*, 238

[5] Jansen, M.; Mudring, A.V.;*The Chemistry of Gold Oxides in Gold: "Progress in Chemistry, Biochemistry and Technology"*, Wiley, New York **1999**

[6] Štrbac, S.; Adzic, R.R.; *J. Electroanal. Chem.* **1993***, 362*, 47

[7] Štrbac, S.; Adzic, R.R.; *Electrochim. Acta.,***1996***, 2903*, 41

[8] Štrbac, S.; Adzic, R.R.; *J. Electroanal. Chem.* **1996**,*403*, 169

[9] Blizanac, B.B.; Lucas, C.A.; Gallagher, M.E; Arenz, M.; Ross, P.N.; *J. Phys. Chem. B*. **2004**,*108*, 625

[10] Venezia, A.M.; Pantaleo, J.; Longo, A.; Di Carlo, G.; Casaletto, M.P.; Liotta, F.L.; Deganello, G.; *J. Phys. Chem. B.,* **2005**,*109*, 2821

[11] Haruta, M.; Tsubota, S.; Kobayashi, T.; Kageyama, H.; Genet, M. J.; Delmon, B.;*J. Catal.* **1993,***144*, 175. Haruta, M.; Yamada, N.; Kobayashi, T.; Iijima, S.; *J. Catal.,* **1989***,115*, 301

[12] Bond, G.C.; Louis, C.; Thompson, D.T.;*Catalysis by Gold*, Imperial College Press, London **2006**

[13] Thompson, D.T.; *Topics. Catal.,* **2006***, 38*, 231

[14] Corti, C.W. ; Holliday, R.J.; Thompson, D.T.; *Appl. Catal. A: Gen.,* **2005***, 291*, 253

[15] Hutchings, G.J.; *Catal Today,* **2005**, *100*, 55

[16] Hashmi, A.S.K; *Angew Chem Int Ed,*. **2005**, *44*, 6990

[17] Daté, M.; Haruta, M.; *J. Catal.,***2001,***201*, 221

[18] Sanchez-Castillo, M.A.; Couto, C.; Kim, W.B.; Dumesic, J.A.;*Angew. Chem.-Int'l. Ed.* **2004***, 43***,** 1140

[19] Ketchie, W.C.; Murayama, M.; Davis, R.J.;*Topics in Catal.* **2007**, *44*, 307

[20] Weiher, N.; Bus, E.; Prins, R.; Delannoy, L.; Louis, C.; Ramaker, D.E.; Miller, J.T.; van Bokhoven, J.A. ; *J. Catal.,* **2006**, *240*, 100

[21] Schubert, M.M.; Hackenberg, S.; Van Veen, A.C.; Muhler, M. ; Plzak, V.; Behm, R.J.; *J. Catal*. **2001***,197*, 113

[22] Katayama, A. ; *J. Phys. Chem.* **1980***, 84*, 376

[23] Janssen, M. M. P; Moolhuysen, J.; *Electrochim. Acta,***1976***, 21*, 861

[24] Watanabe, M.; Venkatesan, S.; Laitinen, H.A.; *J. Electrochem. Soc.* **1983**, *130,* 59

[25] Upchurch, B.T.; Schryer, D.R.; Davis, P.P.; Brown, K.G.; Schryer, J.L.; Kielin, E.J; Miller, I.M.; Hoyt, R.F.; *Proceedings of the Third International DRA/NASA Conference on Long-Life CO_2 Laser Technology Proceedings,* D.V. Willetts and M.R. Harris, Editors, DRA/British Crown **1992**

[26] Montmeat, P.; Marchand, J.; Lalauze, R.; Viricelle, J.; Tournier, G.; Pijolat, C.; *Sensors and Actuators B.* **2003**, *95*, 83

[27] Bielansky A.; Haber, J.; *Catal. Rev. Sci. Eng.***1979***, 19*, 1

[28] Bouwman, P.J.; Dmowski, W.; Stanley, J.; Cotten, G.B.; Swider-Lyons, K.E.;*J.Electrochem. Soc.* **2004**,*151*, A1989

[29] Baker, W. S.; Bouwman, P.J.; Teliska, M.E.; Dmowski, W.; Swider-Lyons, K.E.; in *Proton Conducting Membrane Fuel Cells IV*, Editors: J.W. Van Zee, et. al., The Electrochemical Society Proceedings Series, **2004**

[30] Teliska, M.; O'Grady, W.E.; Ramaker, D.E.; *J. Phys. Chem. B.* **2004**, *108*, 2333

[31] Teliska, M.; O'Grady, W.E.; Ramaker, D.E.;*J. Phys. Chem. B.* **2005***,109*, 8076
[32] Ramaker, D.E; Koningsberger, D.; *Phys Rev Lett.* **2002**, *89*, 139701
[33] Teliska, M.; Murthi, V.S; Mukerjee, S.; Ramaker, D.E; *J. Electrochem. Soc.* **2005**, *152*, A2159
[34] Scott, F.J.; Mukerjee, S.; Ramaker, D.E.; *J. Electrochem. Soc.* **2007**,*154,* A392
[35] Scott, F. J.; Roth, C.; Ramaker, D. E.; *J. Phys. Chem. C.,* **2007**,*111*, 11403
[36] Bae, I.T.; Scherson, D.A.; *J. Phys. Chem.* **1996**, *100*, 19215 Bae, I.T.; Scherson, D.A.; *J. Electrochem. Soc.* **1998**, *45*, 80
[37] Arruda, T.M; Shyam, B.; Ziegelbauer, J.M.; Ramaker, D.E ; Mukerjee, S.; to be submitted to *J. Phys. Chem. C.*
[38] Gasteiger, H.A.; Kocha, S.S.; Sompalli, B.; Wagner, F.T.; *Appl. Catal. B,* **2005**, *56,* 9
[39] Sasaki, K.; Wang, J.X.; Balasubramanium, M.; McBreen, J.; Uribe, F.; Adzic, R.R.; *Electrochim. Acta* **2004**, *49*, 3873
[40] Ravel, B.; Newville, M.; *Synchrotron Radiat.* **2005,** *12*, 537
[41] Koningsberger, D.C.; de Graaf, J.; Mojet, B.L.; Ramaker, D.E.; Miller, J.T.; *Appl Catal.* A. **2000**,*191*, 205
[42] Mojet, B.L ; Miller, J.T.; Ramaker, D.E.; Koningsberger, D.C.; *J. Catal.* **1999,** *186*, 373
[43] Ramaker, D.E.; Mojet, B.L.; Oostenbrink, M.T; Miller, J.T.; Koningsberger, D.C.; *Phys. Chem. Chem. Phys.* **1999,** *1,* 2293
[44] Mojet, B.L.; Ramaker, D.E.; Miller, J.T.; Koningsberger, D.C.; *Catal. Lett.***1999**, *62*, 15
[45] Newville, M.; *Synchrotron Radiat.,* **2001,** *8*, 322
[46] Ramaker, D.E.; Mojet, B.L.; Koningsberger, D.C.; O'Grady, W.E.;*J. Phys. Cond. Matt.* **1998,** *10,* 8753
[47] Van Dorssen, G.E.; Koningsberger, D.C.; Ramaker, D.E.; *J. Phys Cond. Matt.* **2003**, *14*, 13529
[48] Ramaker, D.E.; Mojet, B.L.; Miller, J.T.; Koningsberger, D.E.; *Top. Catal*. **2000**, *10,* 157
[49] Koningsberger, D.C.; Mojet, B.L.; Ramaker, D.E.; *J. Synch. Rad.* **1999**, *6,* 135
[50] Newville, M.; Livins, P.; Yacoby, Y.; Rehr, J.J.; Stern, E.A.; *Phys. Rev. B.* **1993**, *47*, 14126
[51] Janin, E.; von. Schenk, M.; Gothelid, M.; Karlsson, U.O.; Svensson, M.; *Phys. Rev. B*. **2000**, *61*, 13144
[52] Godin, T.J.; LaFemina, J.P.; *Phys. Rev. B*. **1993**, *47*, 6518
[53] Ravel, B.;*J. Synchrotron Rad***, 2001**, *8*, 314
[54]. Roth, C; Benker, N.; Buhrmester, T.; Mazurek, M.; Loster, M.; Fuess, H.; Koningsberger, D.C.; Ramaker, D.E; *J. Am. Chem. Soc.* **2005,** *127*, 14607
[55] Shannon, R.D.; Prewitt, C.T.; *Acta. Cryst*. **1969**, *B25*, 925
[56] Zhang, Y.; Yu, A.; Stakheev, A.; Ivanov, V.; Baeva, G.N.; Ramaker, D.E ; Koningsberger, D.C.; J. *Phys. Chem. C.* **2007,** *111*, 3938
[57] Ramaker, D.E. ; Oudenhuijzen, M.K.; Koningsberger, D.C.; *J. Phys. Chem. B.* **2005**, *109*, 5608
[58] El-Deab, M.S. ; Ohsaka, T.; *Electrochim. Acta.* **2002**, *47*, 4255
[59] Pulkkinen, U.; Rantala, T.T.; Rantala, T.S.; Lantto, V.; *Journal of Molecular Catalysis A: Chemical.* **2001**, *166*, 15
[60.] van Bokhoven, J.A; Miller, J.T.; *J. Phys. Chem. C.* **2007**, *111*, 9245

Chapter 4

Characterization of Ligand Effects on Water Activation in Triarylphospine-Stabilized Pt Nanoparticle Catalysts by X-ray Absorption Spectroscopy

4.1 Introduction

One of the major obstacles to increasing the efficiency of proton exchange membrane fuel cells (PEMFCs) is the slow kinetics of the oxygen reduction reaction (ORR, Eq. 4.1) at the cathode.

$$O_2 + 4H^+ + 4e^- \rightarrow 2H_2O \qquad (4.1)$$

For platinum catalysts in aqueous acid electrolytes, it is generally accepted[1-3] that the rate-limiting step of the ORR involves electron transfer to chemisorbed O_2 (Eq. 4.2).

$$O_2 \rightarrow (O_2)_{ad} \xrightarrow{e^-} (O_2)^-_{ad} \qquad (4.2)$$

However, above 0.6 V, OH is adsorbed on the surface. This results in an incomplete byproduct of ORR (Eq. 4.1) directly from water activation

$$Pt + H_2O \rightarrow OH / Pt + H^+ + e^{-+} \qquad (4.3)$$

This adsorbed OH is believed to inhibit the ORR due to site-blocking and a possible detrimental electronic effect. Thus, another important step in the ORR is OH removal from the surface (eq. 4).

$$Pt\text{-}OH \xrightarrow{e^-,H^+} Pt\text{-}OH_2 \xrightarrow{H_2O} Pt^0 \qquad (4.4)$$

The conclusions drawn from eqns. 4.1-4.4 is that electron transfer to chemisorbed oxygen is facilitated by strong bonding between the surface platinum atoms and dioxygen, but removal of surface OH is easier when the Pt-O bond is weaker. This suggests that there is an optimal Pt-O bond energy for faster ORR kinetics. Indeed, Nørskov, et al. calculated that the best electrocatalyst should bind oxygen about 0.2 eV more weakly than does pure platinum.[4] The challenge, then, is how to selectively change the strength of the Pt-O bond.

One of the first and most common approaches to altering catalyst activity is the use of mixed-metal nanoparticles.[5] Bimetallic nanoparticles are known to increase the ORR rate. However, for a given elemental composition, mixed-metal nanoparticles may differ widely in atom distribution and size, depending on the manner of synthesis and activation treatment, and the enhancement is found to depend significantly on this atom distribution.[2, 6] More recently, intricately designed core-shell nanoparticles consisting of Pt atom monolayers on mixed-metal cores have shown remarkable ORR activity.[7] The effect has been interpreted to be the result of a shift of the d-band orbital energy of the surface platinum atoms.[8]

It has previously been shown that organic ligands on the surface of metal nanoparticles can significantly change the catalytic activity of certain reactions, such as the selective hydrogenation of alkynes by palladium clusters modified with 2-butyl-1,10-phenanthroline

ligands.[9] Removal of the butyl group from the phenanthroline, a seemingly small change, had a profound effect on the kinetics and product distribution of the reaction. However, it is not known if the origin of this effect is electronic in nature or due to some other physicochemical effect such as steric hindrance or hydrophobicity.

There are many examples of ligand-stabilized nanoparticles used as electrocatalysts, but in nearly all cases the ligand, typically a carboxylic acid or amine, is exploited only to control nanoparticle formation.[10,11] These ligands are σ-donors which would interact only weakly with platinum primarily through s-band orbitals, if at all. However, dioxygen is known to interact with platinum through d-band orbitals, and it is of interest to know if this bonding can be perturbed by surface ligands which have significant d-orbital interaction.

Organophosphorus compounds have rich transition metal coordination chemistry.[12] They are σ-donors as well as π-acceptors, which can form pπ-dπ phosphorus-metal bonds. There are a handful of examples of metal nanoparticles stabilized by phosphines, [13] although to our knowledge none of these materials have been used as electrocatalysts.

We have previously reported[14,15] the synthesis, characterization, and electrochemistry of Pt nanoparticles (Pt NPs) stabilized with water-soluble phosphine TPPTP (triphenylphosphine triphosphonate, $P(4\text{-}C_6H_4PO_3H_2)_3$, see Figure 4.1). Aqueous solutions of these nanoparticles were used for construction of polyelectrolyte multilayers with poly(allylamine·HCl) that were grafted to glassy carbon electrodes for ORR kinetic studies using rotating disk electrode voltammetry. The Pt-TPPTP catalysts unfortunately had a lower mass activity for Pt vs the standards, making them impractical fuel cell catalysts; however it is still useful to understand what effects change the activity of the available surface area [15]. We observed that the TPPTP ligands increased the Pt surface-specific activity of the ORR vs Pt/C standards.

Herein, we report the *in-situ* x-ray absorption spectroscopy (XAS) of Pt/TPPTP, Pt functionalized with oxidized TPPTP (Pt/ox-TPPTP), and compare the results with the "naked"

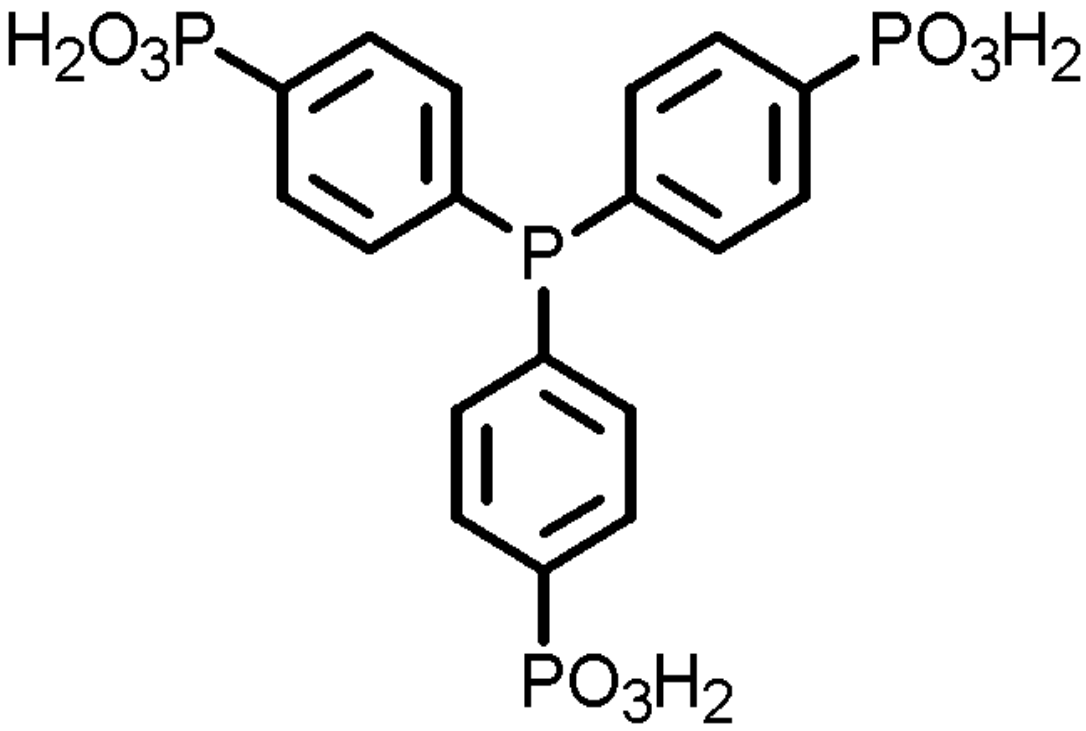

Figure 4.1 Water-soluble phosphine TPPTP (triphenylphosphine triphosphonate) ligand used in this work. An oxidized TPPTP (ox-TPPTP) ligand has an additional =O group bonded to the central P atom.

Pt/C, i.e., without phosphine ligands. The Pt/ox-TPPTP contains a P=O bond and was predicted to have little or no direct P-Pt electronic interactions but nearly identical physical characteristics compared to the unoxidized TPPTP. Analysis of the XANES (near edge) region of the XAS data was carried out using the $\Delta\mu$ technique[17, 18] previously applied to adsorption of H, O, and OH on Pt[18] and Pt-M (M=Cr, Fe, Co, and Ni) cathodes[2] to CO and OH adsorption on Pt-Ru anodes[19] in an electrochemical cell[6], and even to Pt and PtRu anodes in an operating fuel cell with simulated reformate (H_2 and ppm CO)[19] or methanol[20]. The $\Delta\mu$ technique can provide not only adsorbate coverages but even binding site information (e.g., atop, bridged, 3-fold) of adsorbates such as H and O(H) on the Pt nanoparticles and will be utilized in this work to also provide information on the Pt-P linkage with the ligands as a function of potential in an electrochemical cell. The XANES is measure for an in situ half cell containing the various catalysts at potentials from 0 to 1.1 V with utlizilation of the ΔXANES and extended x-ray absorption fine structure (EXAFS) analysis techniques to determine the voltage-dependent behavior of the catalysts for water activation. Potentials of 0.2 V and less are in the hydrogen adsorption region, 0.54 V is the double-layer region where the catalysts should be free of adsorbates, and potentials from 0.7 to 1.1 V are used to study oxygen or hydroxide, O(H), adsorption.

4.2 Experimental and Data Analysis

4.2.1 Catalyst and electrode preparation

Details of the catalysts synthesis and electrode preparation have been given previously [21] Briefly, glycol-stabilized Pt nanoparticles (Pt NPs) were dispersed in deaerated acetone and added to a solution of TPPTP, resulting in a homogenous brown dispersion. This dispersion was mechanically stirred under N_2 for 1 h to allow for partial exchange of the TPPTP ligand at the platinum surface. The solvent mixture was then removed in vacuo and deaerated water was added resulting in a transparent brown Pt colloidal dispersion. Complete exchange of the TPPTP

ligand at the Pt NP surface required several days. The crude material was redispersed in a minimal amount of water and purified by gel filtration chromatography. Elemental analysis by ICP showed a Pt metal content of 48.6% and P content of 6.9%, corresponding to a Pt:TPPTP mole ratio of ~4.5:1 for the sample used here. Pt/ox-TPPTP nanoparticles are produced in tandem as a minority fraction when synthesizing Pt-TPPTP, but are produced in higher relative fraction when adding the ligands to the "bare" Pt nanoparticles at lower pH values. Elemental analysis yielded a Pt metal content of 12.78% and P content of 9.90%, corresponding to a Pt/ox-TPPTP mole ratio of ~0.8:1 (i.e., 60% $Pt_{15}(TPPTP)_{15}$ and a larger component of water and Cl consistent with the greater amount of TPPTP). The Pt/C nanoparticles, prepared as described previously[21], were supported on Vulcan carbon XC-72 (VC). Elemental analysis by ICP revealed that the composite was 7.1 ± 0.2% Pt by weight.

Inks of VC, PDAC, and Pt-TPPTP were made as follows for electrochemical evaluation. Briefly, VC was added to an aqueous solution of PDAC and sonicated for 1 h, resulting in a black suspension with no visibly aggregated carbon. Approximately 2 mg of Pt-TPPTP was added to ~2 mL of the PDAC/VC ink and sonicated for 30 s and then stirred for 1 h. Approximately 8-9 μL aliquots of the ink were added to glassy carbon disk electrodes polished to a mirror finish. The films were dried in air to yield smooth, evenly deposited composite films featuring ~0.020 $mg_{Pt}/cm^2_{geometric}$. Inks made with Pt-TPPTP-oxide required a different formulation, as the Pt/ox-TPPTP particles were only 12.8% Pt by weight (compared to 48.6% for Pt-TPPTP); the higher weight fraction of anionic ligand required a greater amount of the polycationic PDAC in the inks to achieve sufficient excess cationic charge to bind the anionic nanoparticles and ensure good suspension of the VC (vide infra). Otherwise, the procedure was similar, yielding smooth, evenly deposited composite films with ~0.010 $mg_{Pt}/cm^2_{geometric}$. Inks of Pt/VC were made and cast as films on glassy carbon electrodes according to methods described elsewhere[22], producing evenly deposited films featuring 0.020 $mg_{Pt}/cm^2_{geometric}$. Two different Pt/VC samples were utilized, one completely prepared in this work, and a commercial Etek sample used as a standard, so that in

total four different catalysts were utilized. The one prepared in this work will be referred to as Pt/C and the latter always as the Etek sample.

The thin-film catalysts on glass carbon electrodes were characterized by cyclic voltammetry (CV) and rotating disk electrode (RDE) methods, as have been previously described,[14,15,22] vs. a reversible hydrogen electrode (RHE) in 0.1 M $HClO_4$ electrolyte at room temperature. These results were used to determine the specific activity of the platinum in the catalysts for the oxygen reduction reaction at 0.9V, both from the underpotential deposited hydrogen region in the CVs and the kinetic activity from the RDE. [15,22]

4.2.2 X-ray Absorption

In situ X-ray Absorption Spectroscopy (XAS) experiments were conducted at the National Synchrotron Light Source (NSLS) at Brookhaven National Laboratory in Upton, NY. XAS data, simultaneously in transmission and fluorescence mode, were taken at the Pt L_3 edge at beamline X-11B with a Si (111) double crystal monochromator. The monochromator was detuned by 30% at 200 eV above the Pt L_3 edge (11564 eV) to minimize the presence of higher harmonics in the beam. The energy calibration was achieved by recording the XAS of a 7μm thick Pt foil simultaneously with the sample. Reference foil transmission data was collected between the second and a third detector. The fluorescence mode data were utilized in both the EXAFS and ΔXANES analysis. The NSLS storage ring operated at 2.80 GeV beam energy with ring currents between 40 and 200 mA.

The measurements are taken in an electrochemical half-cell, which was designed by the Adzic research group at Brookhaven National Lab[23]. Thick film electrodes on carbon diffusion layers (Etek) were made from the inks described earlier, but were prepared with a higher platinum loading (7 mg Pt cm^2).These were saturated with 0.1 M $HClO_4$ and placed in the cell. The cell was then placed in front of the beam between two detectors that collected incident (I_0) and sample

(I) beam intensity as well as fluorescence intensity. The potential was controlled by an Eco Chemie Autolab PGSTAT-30 potentiostat, and all data presented is with respect to the RHE.

4.2.3 XANES and EXAFS Analysis

A brief summary of the $\Delta\mu$ method is given here for clarity and to highlight slight differences from the previous method.

The absorption coefficient,μ, was obtained from the raw data using the ATHENA code developed by Ravel and Newville[24]. The pre-edge background is removed using the AUTOBK algorithm, described more fully elsewhere[25], followed by normalization over the 50 to 200 eV (relative to the edge) range for XANES analysis. This procedure was carried out for both the sample data (fluorescence) and the simultaneous transmission reference foil data (ln I/I_{ref}). The foil data were then aligned, and the resultant energy differences were transferred to the sample data; i.e., the ΔE determined for the foil at 'x' potential is added to the energy of the data at the same potential. This energy calibration corrects for shifts due to photon beam drift, and other possible effects. This energy calibration is crucial for the success of the $\Delta\mu$ technique to ensure full cancellation of the atomic contribution in the XANES, which dominates the spectrum; i.e. $\Delta\mu$ is typically only about 1-5% of the total μ signal.

The difference $\Delta\mu = \mu(V) - \mu(V_{ref})$ is generally determined by subtracting the μ at an appropriate reference potential, V_{ref}, (usually taken to be that potential at which the electrode is relatively free of most adsorbates) from other potentials to highlight the effect of these adsorbates. However, the choice of reference can change based on the nature of the inquiry, the sample, the adsorption edge, and the operating conditions. In this work, the $\Delta\mu$ signals were obtained using two different types of references:

Table 4.1: Parameters from EXAFS fits					
	Path	**N**	**R(Å)**	**ΔE_o(eV)**	**σ^2(Å^{-2})**
Pt/C	*0.54V (2<k^1<12 1.6<R<3.0)*				
	Pt-Pt	6.4±1	2.72±.02	9±2	0.008
	0.94V (2<k^1<12 1.6<R<3.0)				
	Pt-Pt	5.9±2	2.72±.03	9±1	0.008
	Pt-O	0.5±0.5	2.12±1	19±4	0.005
Pt/C (ETEK)	*0.54V (2<k^2<12 1.6<R<3.0)*				
	Pt-Pt	8.5±0.3	2.74±0.01	8±0.6	0.006
Pt/TPPTP	*0.54V (2<k^1<12 1.8<R<3.0)*				
	Pt-Pt	3.4±1	2.75±0.04	11±5.0	0.006
	Pt-P_s	0.6±0.4	2.4±0.1	19±10	0.005
	0.90V (2<k^1<12 1.4<R<3.7)				
	Pt-Pt	6.4±2.0	2.75±0.02	10±2.0	0.006
	Pt-P_s	0.4±0.5	2.4±0.1	23±9.0	0.005
	Pt-O	0.6±0.3	2.2±0.2	20±5.0	0.003
	Pt-P_l	N_{P-O}	3.2±0.2	27±27	0.004
*Parameters for ox-TPPTP are not reported because an accurate EXAFS fit was unobtainable					

$$\Delta\mu_L(V) = \mu(V,Pt/TPP) - \mu(0.54, Pt/TPP). \quad (4.5)$$

$$\Delta\mu_{cl}(V) = \mu(V) - \mu(0.54, Pt/C). \quad (4.6)$$

Here the notation subscript 'L' is used when the ligand-stabilized catalysts are used as reference and 'cl' when the Pt/C catalyst is used as the reference. As will be shown below, the use of both eqs. 5 and 6 are advantageous for bringing out different features of the adsorbates, Eq. 4.5 highlighting O(H) adsorption in the presence of the ligand, and Eq. 4.6 highlighting the ligand adsorption itself. The $\Delta\mu$ were smoothed to remove random noise using a standard Savitzky – Golay smoothing routine with a 1.5 eV range.

The EXAFS analysis was performed using the Artemis code[24], and several paths were included in the fits for each sample; either Pt-Pt, Pt-P<, and/or Pt-O-P< as indicated. Here the < sign indicates bonding to the tp (triphenyl) groups; however, the tp groups themselves were not included in the FEFF8 calculations since they would have a relatively small effect on the Pt-P scattering. The Debye- Waller factor was held at some fixed value as indicated in Table 4.1 for all fits to reduce scatter in the coordination numbers (CNs), and FEFF8 was used to calculate all of the other needed parameters including the many-body S_o^2 factor.

4.2.4 FEFF 8.0 Calculations

The FEFF 8.0 code was used to model the adsorbate $\Delta\mu_{theo}$ signatures. The $\Delta\mu_{theo}$ was determined by subtracting the μ of a clean "Janin" [26] type Pt_6 cluster" from the μ of a cluster containing an adsorbate molecule in the atop, bridged or n-fold position (as illustrated in Figure 4.9); e.g., $\Delta\mu_{theo}(O) = \mu(O/Pt_6) - \mu(Pt_6)$. The Janin cluster, used in much but not all of our previous work[16-20], was chosen here because it is about the smallest cluster that contains atop, bridged, fcc, and hcp sites. The bond distances used in the clusters were the same as those in our

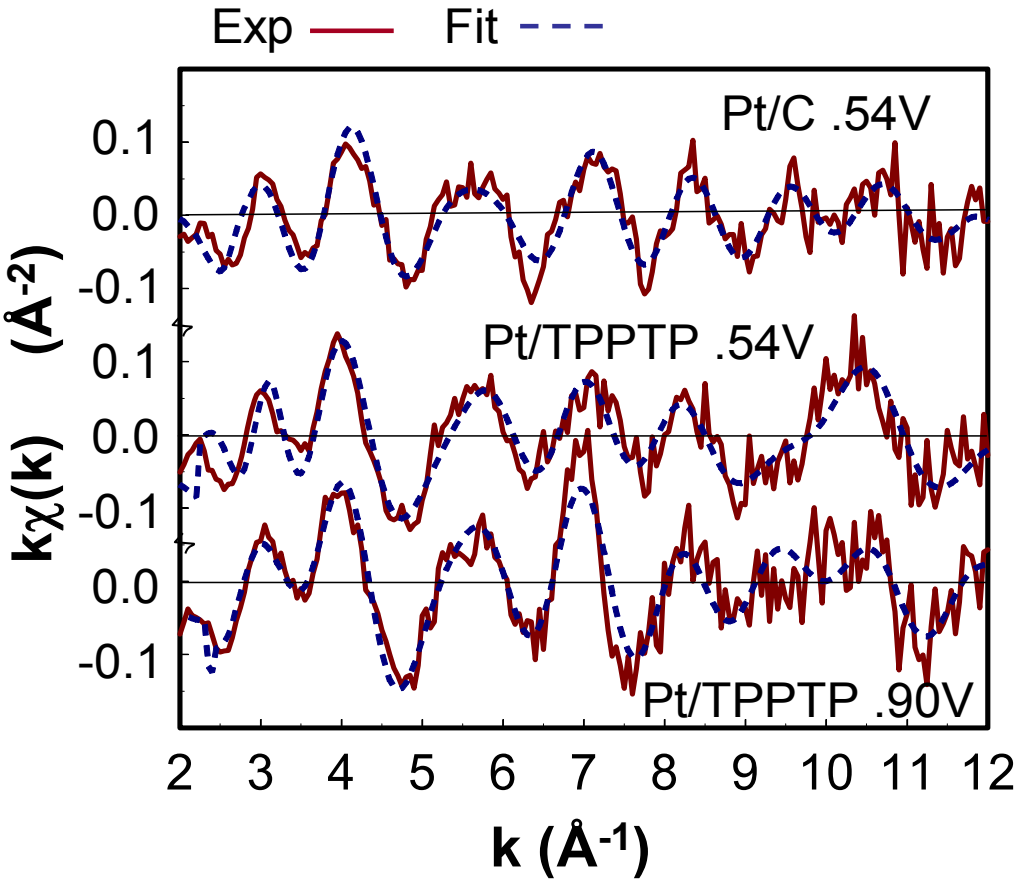

Figure 4.2 Comparison of the experimental EXAFS signal, kχ(k), for the Pt/C and Pt/TPPTP catalysts (at the indicated potentials)

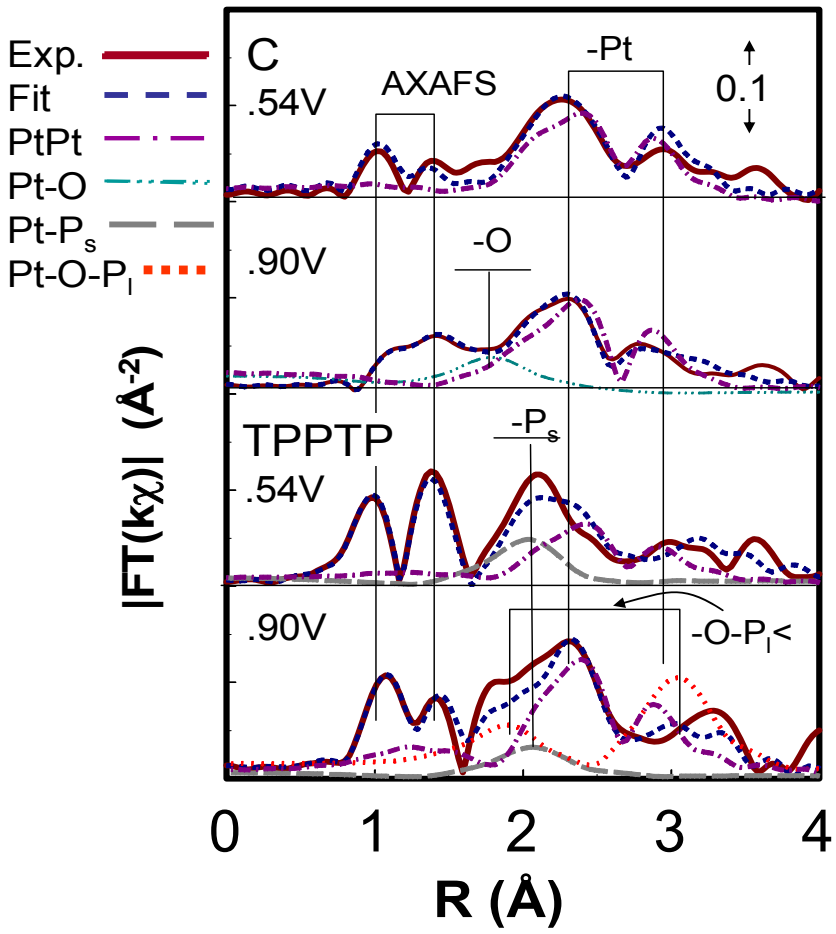

Figure 4.3 Comparison of FT(kχ(k)) for the Pt/C and Pt/TPPTP (at 0.54 and 0.90 V) catalysts along with the fits. Also shown are the individual paths as indicated. The subscripts s and l refer to short and long Pt-P distance. The Pt-O-P_l contribution is actually the sum of the 2 and 3 step multiple scattering paths involving the Pt-O and Pt-O-P_l atoms with the fit parameters as in Table 4.1. Experimental uncertainty in FT estimated to be ±.007.

previous FEFF 8.0 calculations[6,19]. Oxygen in the atop position was treated as OH (since the scattering from H is negligible), while oxygen in an *n*-fold position was treated as O. This is consistent with chemical intuition and density functional theory calculations[27], which show that OH prefers to be singly coordinated, and O doubly or triply.

4.3 Results

4.3.1 EXAFS Results

Figures 4.2 and 4.3 show EXAFS results for Pt/C and Pt/TPPTP at the indicated potentials both in *k*-space and *R*-space (the Fourier transform). These figures reveal the quality of the data and the fits. The relatively large noise level is clearly revealed in Figure 4.2 for $k>6$ and with the signal for $k>14$ dominated by noise. This arises in part because of the low Pt loading (16 mg Pt/g catalyst (TPPTP+PDAC+VC)) in these samples and the relatively small photon flux of the beam. This requires large amounts of sample to be placed in the beam to achieve a Pt step height of about 0.5, and the large amount of support significantly scatters the light beam. Smoothing of the data and comparison to the EXAFS data for Pt/C Etek with larger Pt loadings nevertheless reveals comparability out to about $k \approx 14$. Thus, the high noise level is not expected to significantly alter the fit parameters, but it does lead to relatively large uncertainties in these fit parameters as shown in Table 4.1 (see much smaller uncertainties for the Etek sample). The relatively small Pt particles also introduce relatively large Pt-C contributions due to the carbon support around 1.4Å in Figure 4.2 for the Pt/C sample. In Figures 2 and 3 and others below, a background (an option in the Artemis code) was included in the fits as shown. These background fits account for the relatively large atomic XAFS (AXAFS) peaks seen in these data. The AXAFS features for the Pt/C are very similar to that found previously[16-20] and increase with potential exactly as found previously.[28] That for Pt/TPPTP in Figure 4.3 has the same doublet peak shape but is much larger apparently due to the Pt-TPPTP interaction. An increase in AXAFS with adsorbate coverage or support interaction has been noted previously.[28]

Table 4.1 shows that the Pt-Pt coordination number (CN_{Pt-Pt}) is around 6 for the catalysts prepared in this work, suggesting a particle size of 0.8-1 nm consisting of around 12-15 Pt atoms[29]. Previously these same particles were indicated to be around 1.7 nm as obtained from HRTEM. It is well known that EXAFS generally gives a lower estimate than either HRTEM or XRD Scherrer analysis[30], because EXAFS "sees' all particles apparently weighted toward the smaller ones, while HRTEM and XRD yields sizes weighted toward the larger particles. Thus, the average particle size may be somewhere around 1.3 nm. The CN_{Pt-Pt} of around 3.4 in the Pt/TPPTP catalysts does not necessarily suggest a smaller particle, but rather reduced scattering due to the presence of the phosphine linkage to the Pt cluster. The CN_{Pt-P} of around 0.6 suggest that a 12-15 atom cluster should have around 4-5 TPPTP groups attached to it. Figure 4.4 illustrates such a geometry optimized (molecular mechanics, MM[31]) cluster revealing how the tri-phenyl groups steer clear of each other and still allow significant numbers of free Pt atoms. Atomic analysis also reveals a P/Pt ratio of about 1/4.5 consistent with the EXAFS results.[14,15]

The results in Table 4.1 are consistent with other EXAFS results on Pt catalysts.[2,16-20] For example, the Pt-Pt bond distance around 2.72 Å is considerably shorter than in bulk Pt (2.76 Å) or than in the larger Pt particles in the C(Etek) sample as expected due to the smaller Pt coordination in these small particles. This Pt-Pt distance increases back to 2.75 Å in the Pt/TPPTP and Pt/ox-TPPTP catalysts consistent with relaxation back to the near bulk length due to the complexation with the ligands. The Pt-P_s (short Pt-P distance in direct Pt-P bond) bond length of around 2.4 Å is consistent with that obtained in the molecular mechanics calculations of Figure 4.4. The Debye-Waller factors (σ^2) were not allowed to vary but set at fixed values typical of that seen in small Pt particles. This was to reduce the number of parameters in the fit. Finally the ΔE_o values all appear to be larger (10-20 eV) than normal (e.g. 7-8 in the Etek sample), consistent with a shift of the conduction band minimum to higher binding energy in these small Pt particles as expected.

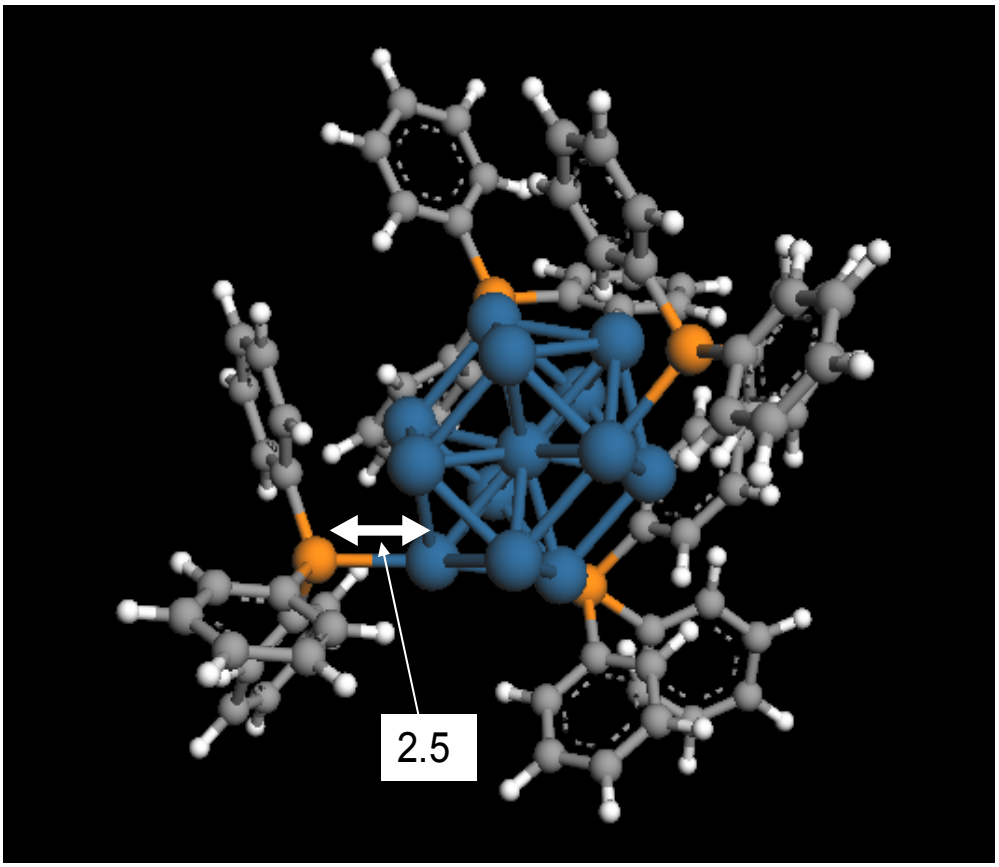

Figure 4.4 Illustration of a 13 atom Pt cluster and 4 TPPTP ligand groups linked through the P atom. (the PO_3H_2(phosphonate) groups attached to the phenyl groups to make the ligands soluble in water are not shown). Figure constructed using the Arguslab software[31] which performs a simple molecular mechanics (MM) calculation to reduce atom-atom repulsions.

Figure 4.5 shows how the $FT(k^2\chi)$ for the Pt/TPPTP catalysts changes with potential. Note that as the potential increases up to 0.9 V, the Pt-O and Pt-Pt peak intensities increase while the Pt-P_s peak decreases. This suggests that the Pt-phosphine linkage breaks with increase in potential as one might expect. However, Figure 4.5 shows that a peak around 3.4 Å also increases with potential suggesting that as O adds to the cluster; the TPPTP groups now link to some of the adsorbed oxygen atoms. The fit in Figure 4.3 already included this Pt-O-P_l scattering path for 0.9 V, and Table 4.1 shows that the Pt-P_l distance (the long Pt-P_l distance because of the intervening O atom) is around 3.2Å. At potentials above 0.9 V, the Pt-Pt intensity decreases again. This is obviously due to oxidation of the Pt (i.e. Pt and O atom displacement and increased subsurface O atoms) as seen with all Pt particles at high potential (e.g the Pt/C as shown in Table 4.1).

Figure 4.6 compares the $FT(k\chi)$ for Pt/C, Pt/TPPTP and Pt/ox-TPPTP at 0.0, 0.54, and 1.0 V. This figure reveals the effects under reducing condition (i.e. 0.0 V) and several important differences between the TPPTP and ox-TPPTP ligands. For Pt/TPPTP at 0.0V, the Pt-P_s peak remains, suggesting that H does not break the Pt-P linkage. The Pt-P_l peak also remains small because of course a Pt-H-P linkage would not occur. The Pt-Pt peak intensity is larger at 0.0 V than at 0.54 V, consistent with a change in the shape of the Pt particle from more oval like to spherical like with H adsorption as seen previously[16-18] and perhaps some weakening (although not breaking) of the Pt-P_s bond. In contrast to the Pt/TPPTP catalysts, the Pt/ox-TPPTP catalyst does not show any breaking of the Pt-P_s bonds with potential, and no sharp increase in the Pt-O-P_l peak at 1.0V. Already at 0.54 V, a significant Pt-O peak is visible. Thus, the Pt-O-P bond remains primarily intact at all potentials in this case. This suggests that the Pt-O-P_l bonds are different in the two cases, and indeed this will be clearly shown by examining the $\Delta\mu$ spectra below. All of these EXAFS results are summarized in Figure 4.7.

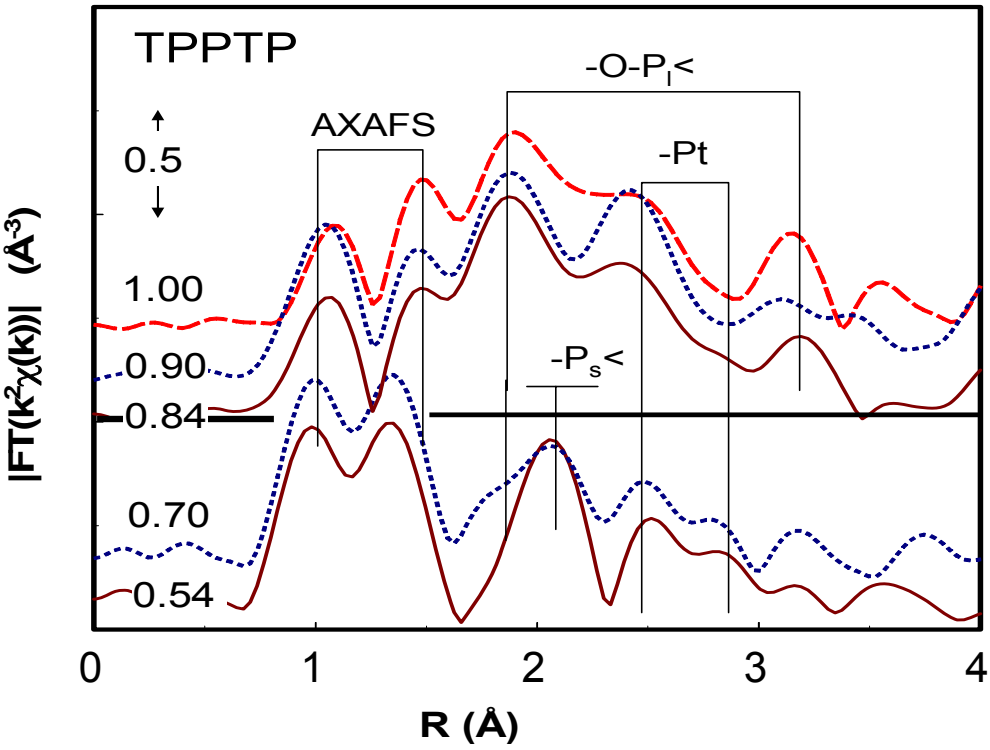

Figure 4.5 Variation of EXAFS spectra with potential for Pt/TPPTP, with the principle peaks identified as determined from the fits in Figure 4.2.

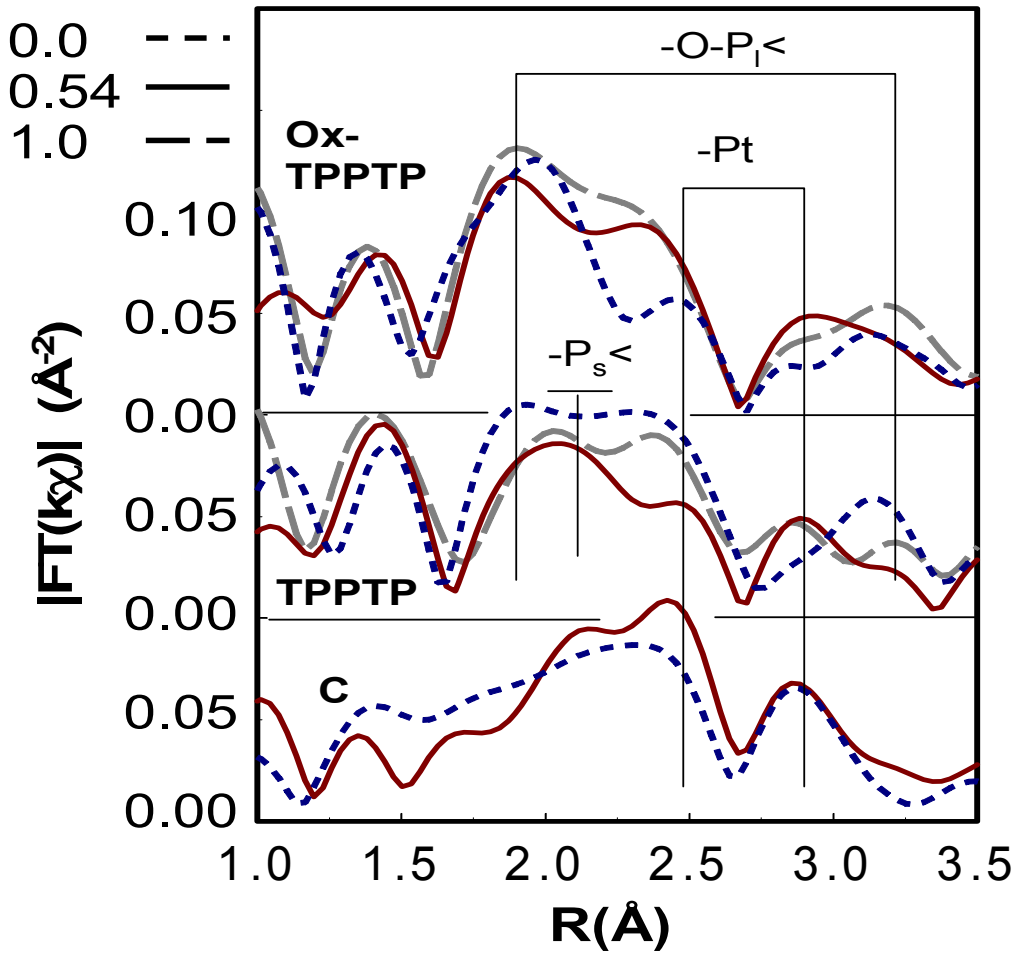

Figure 4.6 Comparison of the EXAFS spectra in the region between 1.0 and 3.5 Å to emphasize the Pt-P and Pt-O-P interaction for the potentials and catalysts indicated. The dominant peaks are identificed as determined in Figure 4.2.

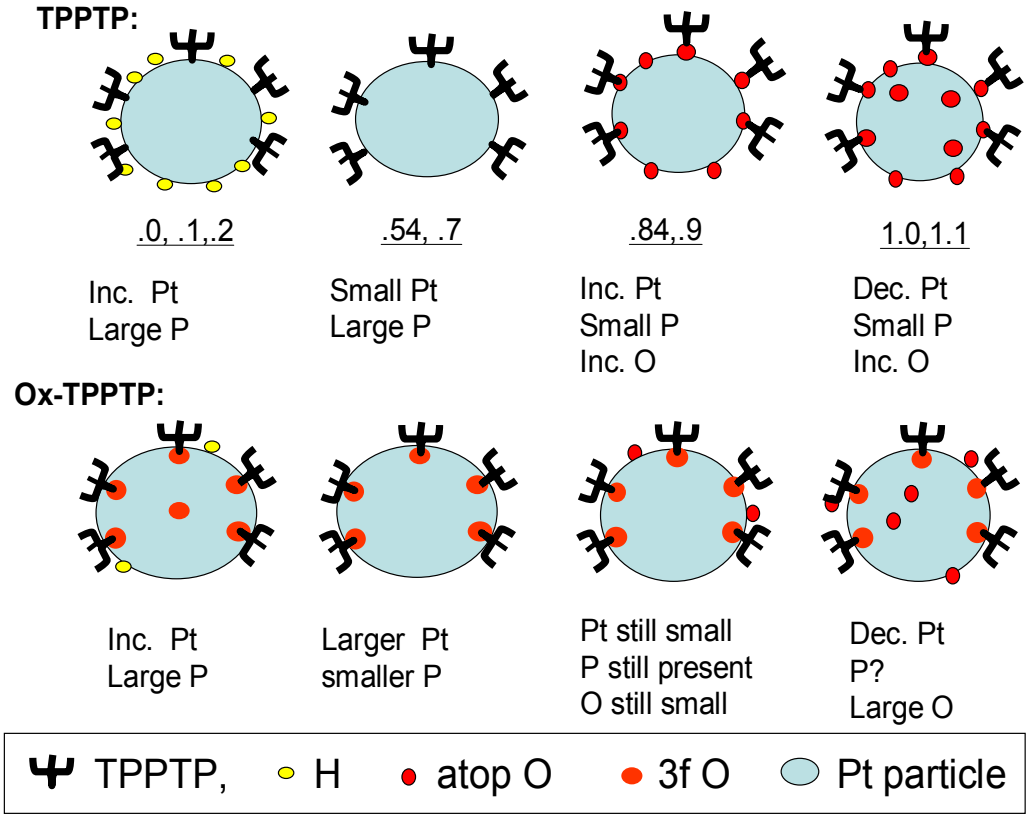

Figure 4.7 Summary of the changes seen in the EXAFS data with potential for the two different ligands, and the changes in the cluster ligand structure responsible for these EXAFS changes.

4.3.2 Δμ results

Figure 4.8 compares the background-subtracted and normalized XANES spectra, μ, for the Pt/TPPTP before subtraction. Note that the spectra are very similar beginning just 15 eV above the edge, but the differences in the region below 15 eV are well above the noise level. Figure 4.9 shows the $\Delta\mu_{cl}$ experimental spectra (eq 6) for the Pt/TPPTP and Pt/ox-TPPTP at 0.54 and 1.0 V with FEFF8 calculated $\Delta\mu_{theo}$ signatures obtained with various adsorbates on the Pt_6 Janin cluster[26] such as that illustrated in Figure 4.9. Since the experimental $\Delta\mu_{cl}$ spectra are shown here, the experimental signatures should reflect both the P<tp and O-P<tp adsorbates as well as O, where for brevity we use P<tp to represent bonding to the triphenyl groups. At 0.54V the experimental $\Delta\mu_{cl}$ spectra are nicely reproduced by $\Delta\mu_{theo}$ for –P<tp and ≡O-P<tp adsorbates, for the TPPTP and ox-TPPTP catalysts respectively. Here '-' represents atop and '≡' 3-fold fcc coordination on the Pt. These $\Delta\mu$ results very clearly reveal yet another difference between the two catalysts, and why in the latter case the ≡O-P<tp adsorbate appears to be fixed on the Pt surface at all potentials.

The relative magnitudes of the $\Delta\mu_{theo}$ and experimental $\Delta\mu_{cl}$ can be used to estimate adsorbate coverages, since the $\Delta\mu_{theo}$ were calculated with a single adsorbate molecule next to the Pt absorber atom. In Figure 4.9 the –P<tp signature was divided by 3 and the ≡O-P<tp by 2 as indicated, suggesting a coverage of about 0.3 monolayers (ML) in the TPPTP case. The 0.3 ML coverage for TPPTP is entirely consistent with that indicated by the EXAFS data and the MM model in Figure 4, with about 4 TPPTP ligands adsorbed on a 13 Pt atom cluster. The effective coverage in the 3-fold case is a bit more difficult to estimate. Each adsorbate molecule in a 3-fold site is coordinated to 3 Pt atoms (this would suggests a coverage (ox-TPPTP molecues/ Pt atom) of only 0.5/3 = 1.6 ML), but each ligand in a 3-fold may block 3 or more sites, so that half or

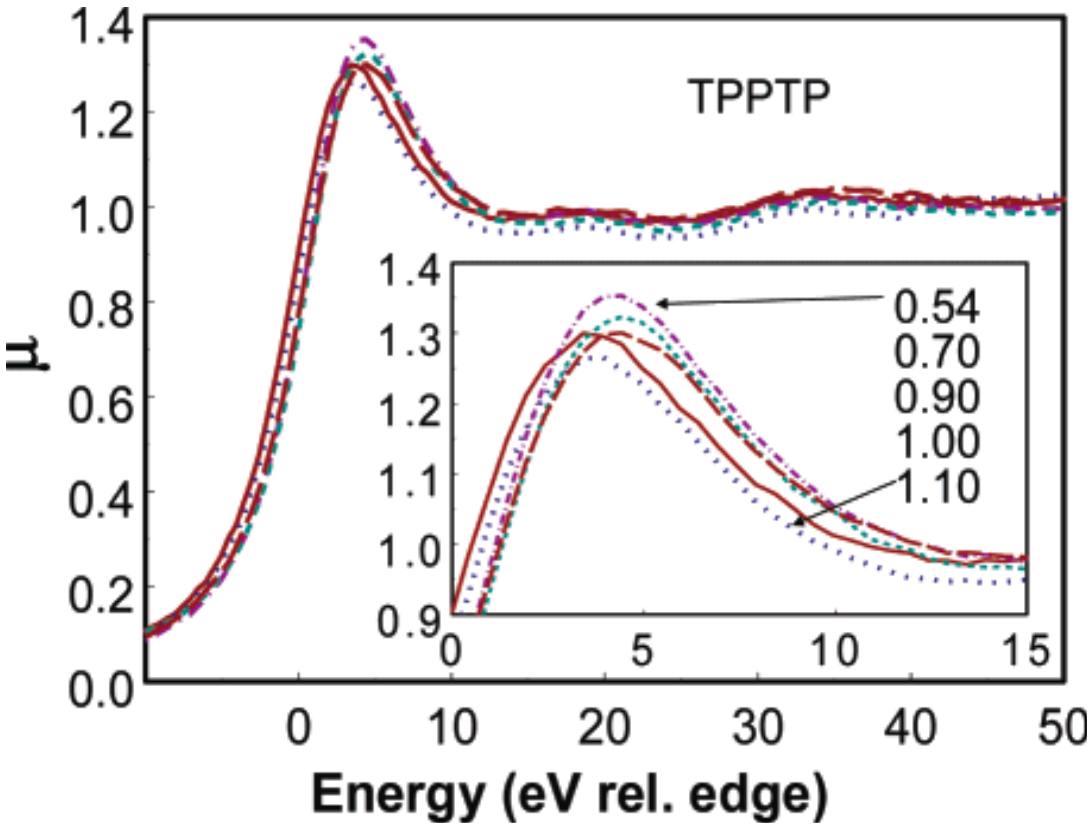

Figure 4.8 Comparison of background-subtracted and normalized XANES spectra, μ, for the Pt/TPPTP catalysts at the indicated potentials (V relative to RHE). Both expanded (insert) and full-scale spectra are shown for comparison (lines in the full scale are identical to those in the expanded scale).

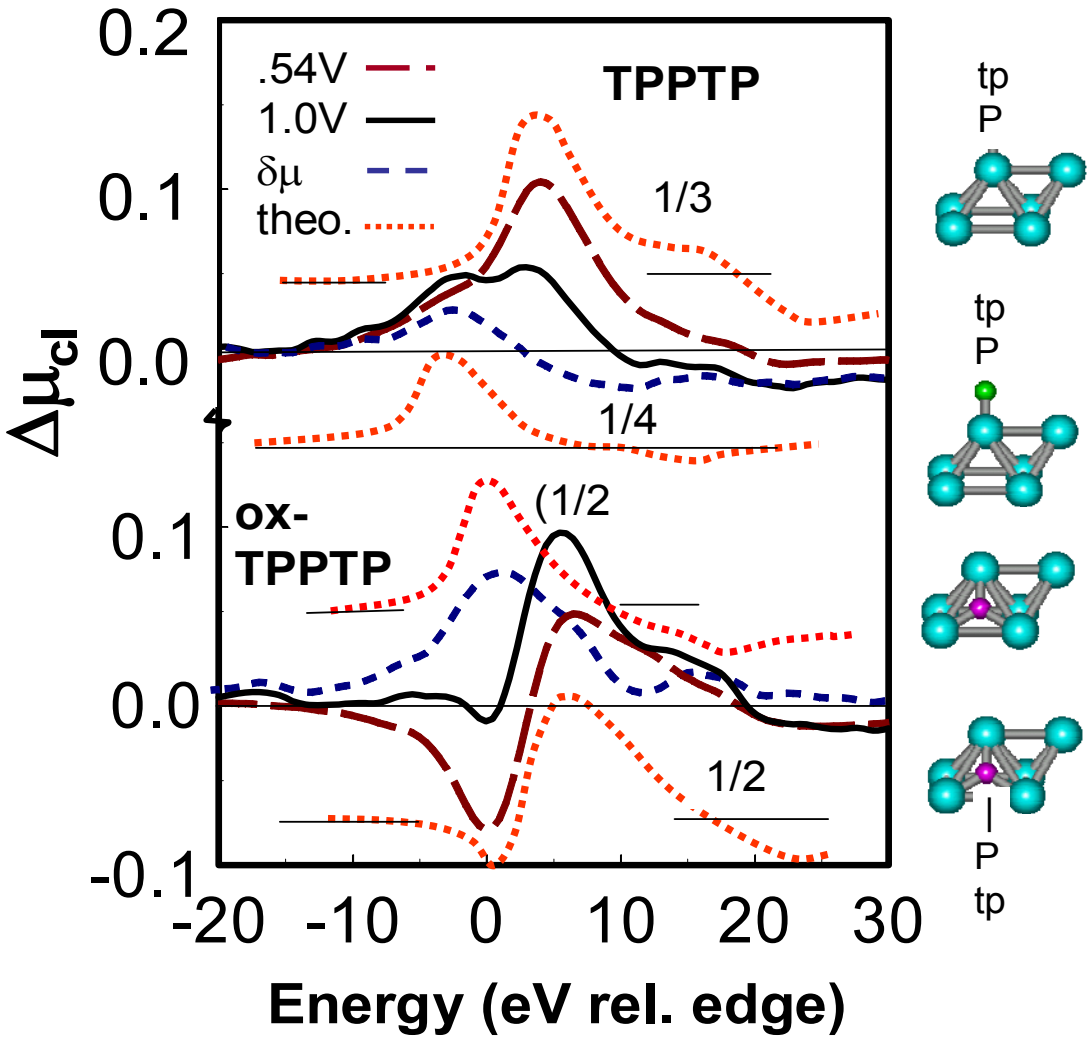

Figure 4.9 Comparison of experimental $\Delta\mu_{cl}$ (see Eq. 4.6) at 0.54 and 1.0 V for TPPTP and ox-TPPTP with FEFF8 calculated $\Delta\mu_{theo}$. The $\Delta\mu_{theo}$ were calculated using the Pt_6 cluster and the adsorbates as indicated in the figure and described in the text. Scaled factors applied to the $\Delta\mu_{theo}$ are also indicated. The $\delta\mu$ difference spectra are obtained as described in the text.

more of the Pt sites may be blocked by the ligand. Because of the bulky nature of the ox-TPPTP ligand, this is highly likely therefore an effective coverage of 0.5 ML or more is expected, consistent with what will be evident below.

Next we consider the experimental $\Delta\mu_{cl}$ signatures at 1.0V. That for TPPTP clearly shows about a 50% reduction in the –P<tp coverage, and then the addition of another component at lower energy. Obtaining the difference $\delta\mu = \Delta\mu_{cl}(1.0V) - 0.5\ \Delta\mu_{cl}(0.54\ V)$ isolates this component, and gives a signature very similar to $\Delta\mu_{theo}$ for –O-P<tp, suggesting now an atop –O-P<tp ligand coordination. The relative magnitudes between theory and experiment then suggest that about half of the existing –P<tp at 0.54 V (0.15 ML) is converted to –O-P<tp at 1.0 V (this is consistent with the EXAFS). In contrast, no reduction in the ≡O-P<tp component is seen for the ox-TPPTP, and the addition of a ≡O component appears. However the coverage is probably much less than 0.5 ML suggested by the relative magnitudes between $\Delta\mu_{cl}$ and $\Delta\mu_{theo}$ in this case (we will see below that it is much less).

Figure 4.10 illustrates a close-up of the geometry optimized O-P<tp model in the two different catalysts. Note that the Pt-P_l distance remains around 3.2 Å in both cases consistent with the EXAFS; however, the Pt-O MM optimized distance is around 2.2Å for the atop and < 2.0 Å for the 3-fold sites reflecting the stronger Pt-O bond in the latter case.

Figure 4.11 examines the H coverage at low potentials for the two catalysts. Since in general the ligand existing at 0.54 V in both catalysts is not expected to leave at low potentials, Fig. 11 utilizes $\Delta\mu_L$ to isolate the effect of the additional H adsorption. H can exist in both atop and 3-fold sites on Pt, and indeed this is evident for the Pt/TPPTP catalysts as shown by comparison with the $\Delta\mu_{theo}$ shown in the figure. Generally, the 3-fold sites are favored on the faces, and the atop H at the corners/edges of the clusters. In contrast, the Pt/ox-TPPTP catalysts shows only increasing atop H as the potential is lowered to 0.0 V. Generally the corner/edges fill with H first, followed by the 3-fold on the faces; indeed, the atop H existing at lower coverage

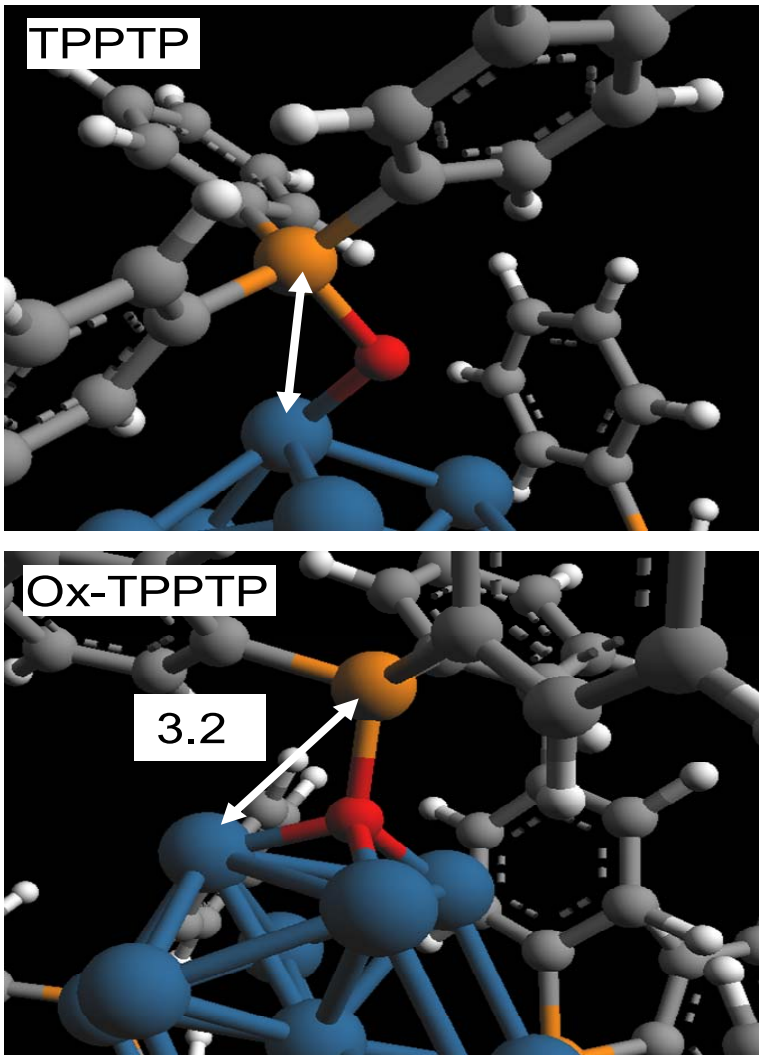

Figure 4.10 Molecular mechanics illustrations of the –O-P<tp and ≡O-P<tp ligand interactions obtained using Arguslab[31]. White arrows indicate Pt-P lengths which are similar in both cases.

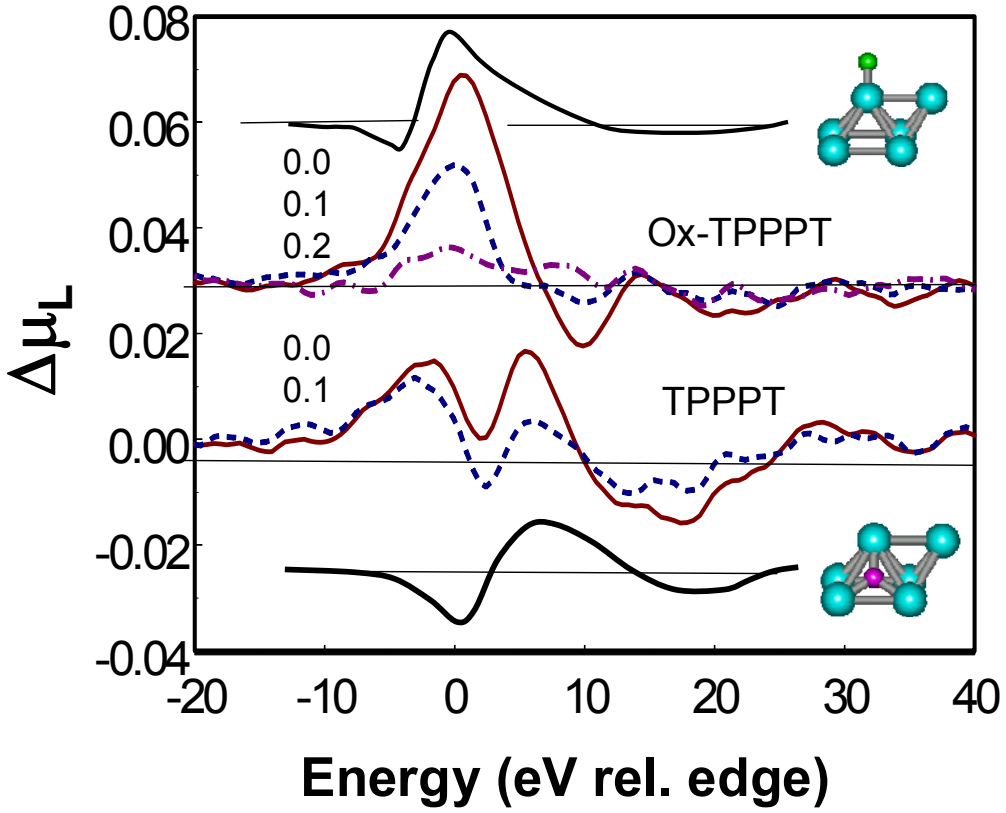

Figure 4.11 Comparison of $\Delta\mu_L$ (Eq. 4.5) in the H region at the indicated potentials for the two ligands. The $\Delta\mu_{theo}$ atop and 3-fold H/Pt signatures, obtained using the clusters illustrated, are shown.

often converts to 3-fold H at higher coverage. Thus, the existence of only atop H on the Pt/ox-TPPTP catalysts shows a very strong reduction in H adsorption in this case, suggesting that the 3-fold ≡O-P<tp ligands either severely block sites or exert a very strong ligand effect (this will be discussed further below).

The above results are consistent with the CV plots in Figure 4.12, where a dramatic reduction in H adsorption is revealed for ox-TPPTP and a normal H adsorption current appears for theTPPTP case. It appears that about one-third of the Pt sites are"blocked" even for the TPPTP case. This is consistent with about 0.3 ML of -P<tp existing on the surface, blocking these sites for H adsorption.

Finally, Figure 4.13 shows $\Delta\mu_L$ results to isolate the effects of O adsorption with potential for the two TPPTP catalysts and two Pt/C catalysts with different particle sizes. Those $\Delta\mu$ spectra in Figure 4.14 for TPPTP are just the difference between those at potential V and that at 0.54 V in Figure 4.9. From previous work[18] examining OH and O adsorption [18,32] on Pt, atop OH and *n*-fold O sites are occupied, and the $\Delta\mu_{theo}$ for three-fold O (shown in Figure 4.9) and atop -OH are similar except for an _5-7 eV energy shift as indicated in Figure 4.13 and 4.14. Note that the signature for *n*-fold O is seen in the ox-TPPTP case because the O-P<tp ligand is not leaving, and hence, its contribution is canceling out in the difference technique, but the OH signature for the TPPTP case has a large negative contribution between3 and 10 eV that is inconsistent with the OH theoretical signature. This arises because the -P<tp ligand is converting to -O-P<tp with potential, as shown in Figure 4.7. Nevertheless, we shall utilize the magnitude of the experimental $\Delta\mu_L$ signatures in both cases as representative of the relative amount of O(H) adsorption in Figure 4.15.

Figures 4.13 and 4.15 show the dramatic effects of particle size. Atop OH is preferred at the corners and edges, and since these sites dominate on very small particles, mostly OH exist on

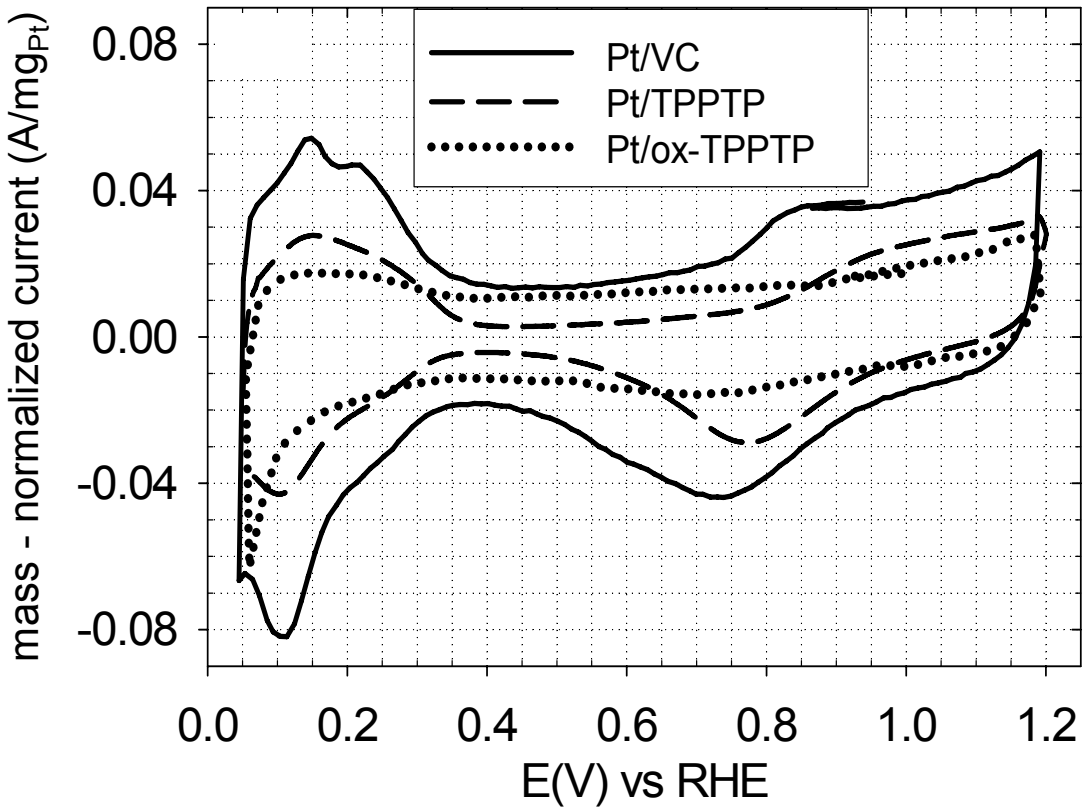

Figure 4.12 CV curves for the thin-film catalyst layers in 0.1 M $HClO_4$ at 25°C. Scan rate = 50mV/s

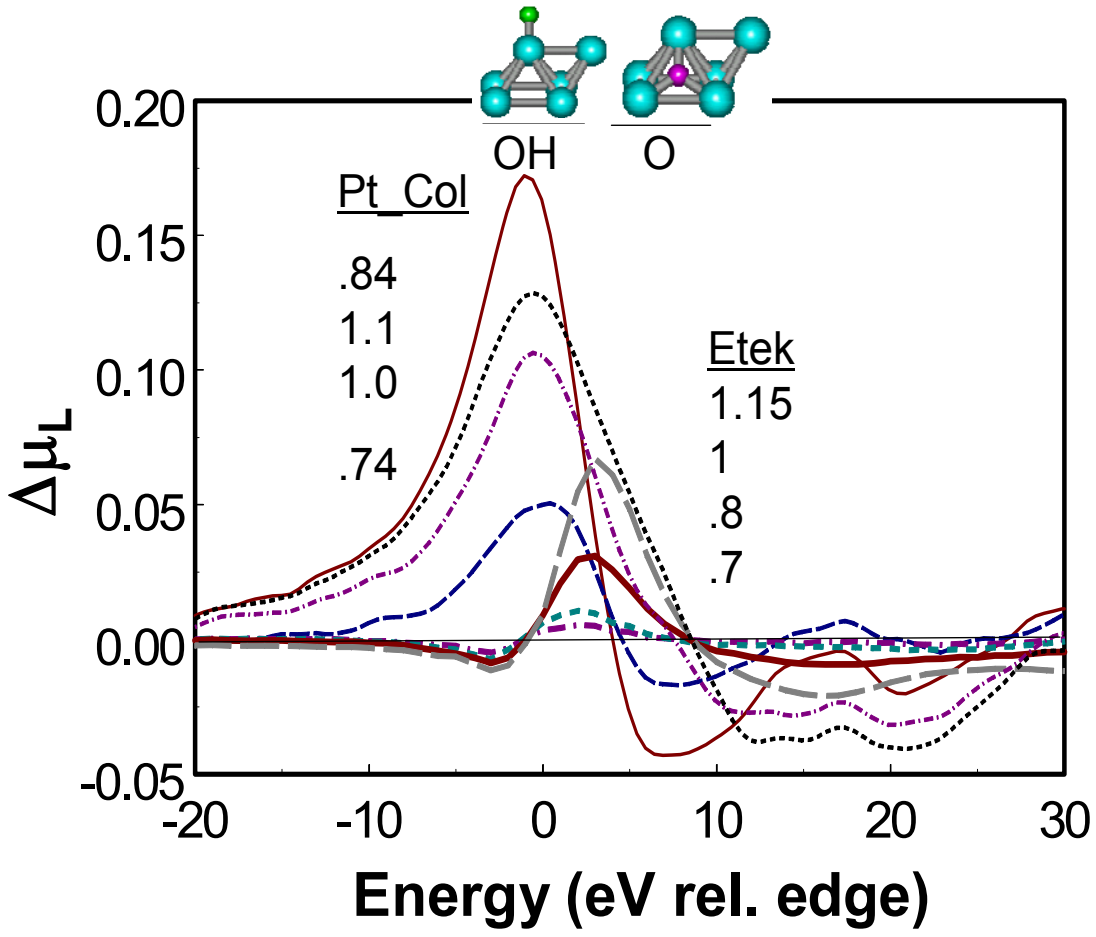

Figure 4.13 Comparison of the experimental $\Delta\mu_L$ (eq 5) at the potentials indicated for the Pt/C studied in this work (0.8 nm), and a Pt/C Etek catalysts (2 nm)[32] to compare the effects of bigger Pt particles.

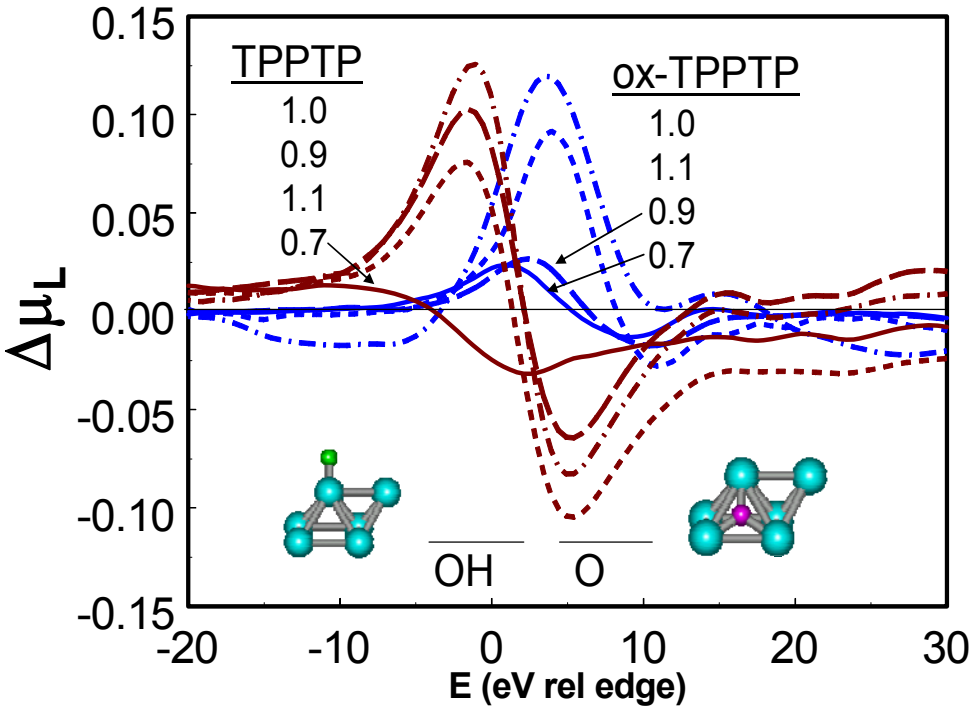

Figure 4.14 Same as Figure 4.13 but now comparing the effects of the two different ligands, the Pt/TPPTP and the Pt/ox-TPPTP catalysts, at the indicated potentials. The regions where the $\Delta\mu$ signatures should show maxima for OH and O on Pt are also indicated.

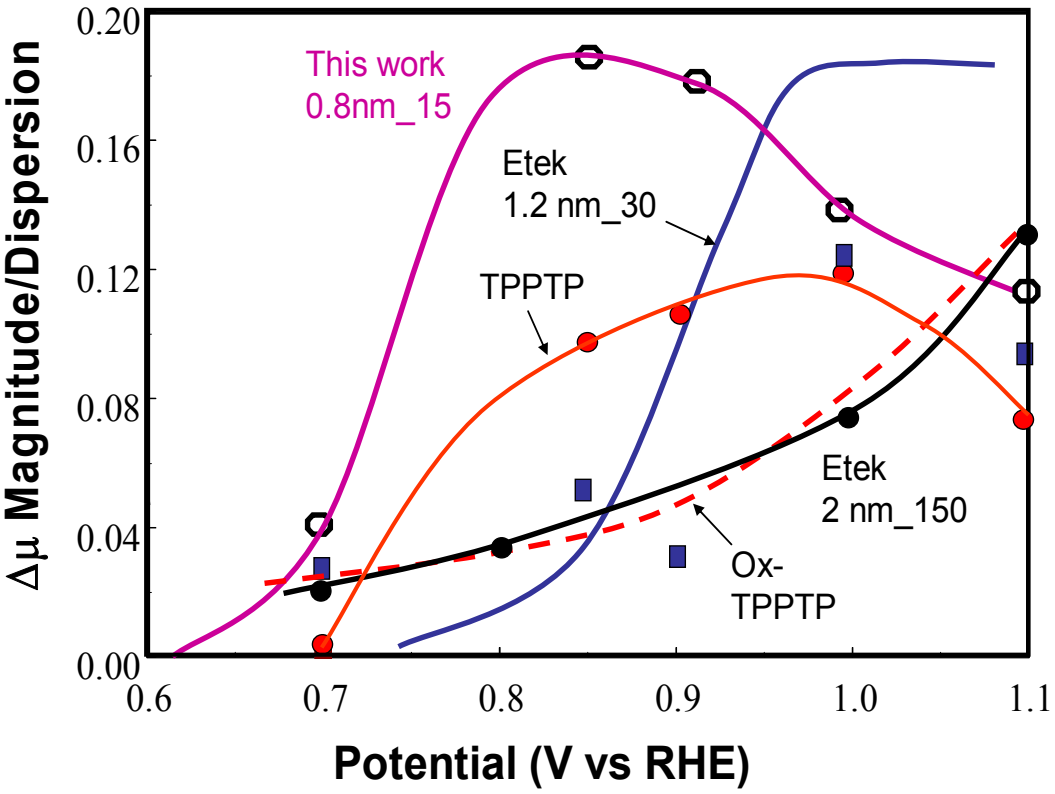

Figure 4.15 Plot of $\Delta\mu_L$ magnitudes corrected for the dispersion vs. potential for three [4] different Pt catalysts C, Etek, TPPTP, and ox-TPPTP studied in this work and another Pt Etek catalysts (1.2 nm_30) studied previously[18,32]. The notation xx nm_yy indicates the cluster diameter and number of Pt atoms for the Pt/C catalysts assuming the particles size obtain from EXAFS. The cluster sizes for the ligand stabilized catalysts are assumed to be the same as the 0.8nm 15.

small particles, while on the big Pt Etek particles a very small amount of OH at 0.7 V is quickly overwhelmed by *n*-fold O at higher potential. Figure 4.15 shows a similar domination of atop OH in the TPPTP case, but a surprising early transition to *n*-fold O above 0.9 V. Figure 4.15 shows that at least a 300 mV shift to lower potential occurs in O(H) adsorption as the particles get smaller. This shift has been noted previously by others, either by examining CV curves[33] or with a similar $\Delta\mu$ technique.[6] In Figure 4.15 reduction of the $\Delta\mu_L$ magnitudes at higher potential reflects the O going subsurface, since subsurface O has been shown previously[18] to have a slightly different $\Delta\mu$ spectral shape with a smaller magnitude between 0 and 5 eV.

Figures 4.13 and 15 also reveal the effects of the phosphine ligands. The Pt/ox-TPPTP shows a dramatic reduction in O(H)adsorption consistent with the CV curve in Figure 4.12. Clearly the O-P<tp ligand severely blocks both H and O(H) adsorption, but a very interesting difference is seen in the binding sites for this catalysts; H appears to adsorb mostly on the corner/edge sites and O (apparently) on the face sites. This will be discussed in light of a possible electronic effect in the next section. Furthermore, the Pt/TPPTP catalyst shows a significant shift of the OH adsorption to higher potential compared with the Pt/C catalysts, consistent with the CV curve in Figure 4.12. Note that the $\Delta\mu_L$ magnitude compared with $\Delta\mu_{theo}$ for the Pt/C (0.8 nm) catalysts (not shown) reveals a 1 ML coverage at 0.8 V, while we concluded above that the combined-O-P<tp and -P<tp coverages were only about 0.3 ML.Thus, the difference in O coverage is even larger than the relative difference in $\Delta\mu_L$ magnitudes shown in Figure 4.15.

4.4 Discussion

The results above reveal significant effects of both particle size and phosphine ligands on O(H) and H adsorption. OH adsorption is known to dramatically alter the oxygen reduction ORR, as OH poisons sites where the ORR might occur.[34] Although the particle size effect on ORR has been attributed to other effects such as geometric site dependencies for the ORR,[35] it is generally

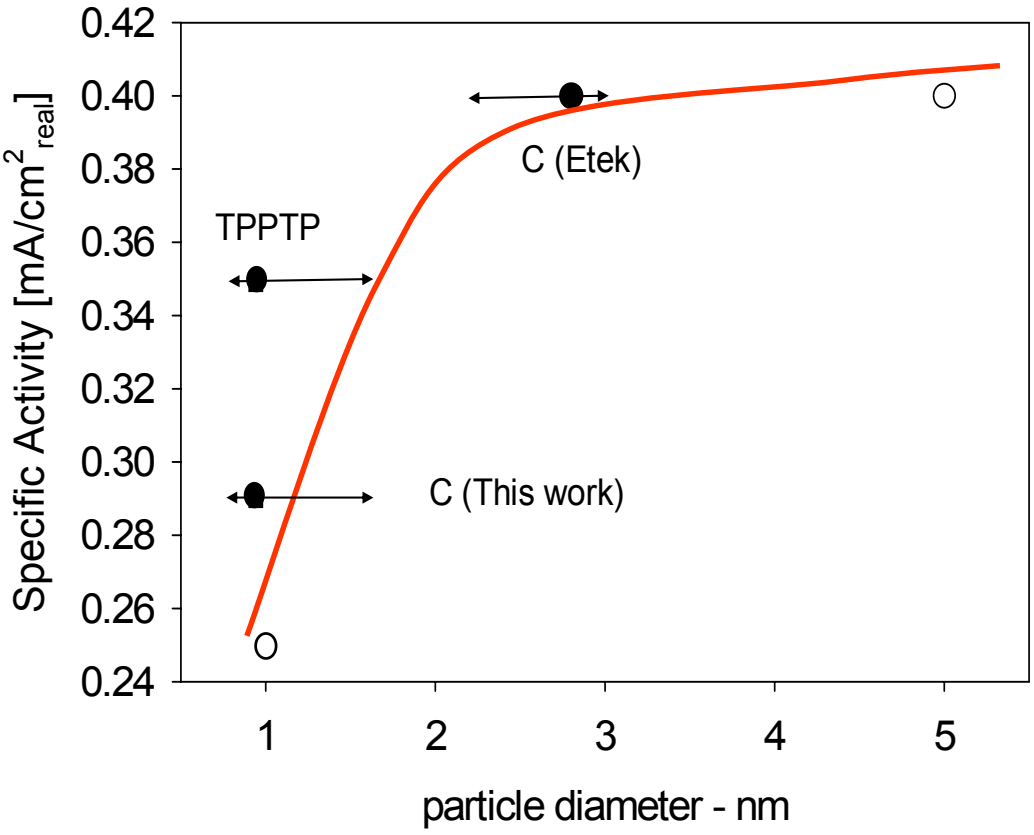

Figure 4.16 Previously reported[14,15] ORR specific activities for 4 catalysts studied in this work and for those reported by Mayrhofer et al[33] (open circles). The solid line is the optimal plot through the Pt/VC catalysts, and shows the sharp change with particle diameter similar to that reported previously by Kinoshita.[35] Uncertainty in particle diameters are indicated for the small particles discussed in this work with the lower limit given by the EXAFS analysis in this work, and the higher limit from the HRTEM[1415] as discussed above.

accepted now that OH adsorption is the critical factor. This can be made more evident here again by examining the specific ORR activity with particle size, as shown in Figure 4.16. Recent results for Pt/C are shown along with those for the catalysts examined in this work.[15] Factors of 5 and even larger differences in specific reactivity have been seen between very large particles (.5 nm) and small ones[33,35] even though the range shown in Figure 4.16 shows a factor of only 2.

We discuss here the role of site blocking and hydrophobic and electronic effects on O(H) adsorption due to water activation, the reaction studied in this work, as well as the ORR. To distinguish these effects more clearly, Figure 4.17 shows previously reported[36] $\Delta\mu$ results (reflecting relative O(H) coverage as above) on Pt/C clusters of around 1.2 nm in different electrolytes. Adsorption of O(H) in 0.1 M HClO4 and 1 M TFMSA is similar because anion adsorption does not occur in either case. The upward shift in O(H) adsorption in 0.1 M H_2SO_4 of course arises because of bisulfate adsorption, but the mechanism here may be either simple site blocking or an electronic effect because of the negative bisulfate anion. Wang et al.[37] separated these two effects on the ORR and concluded that between 500 and 900 mV detrimental electronic effects from the charged bisulfate anion dominate but that OH adsorption primarily acts through simple site blocking between 700 and 950 mV. Figure 4.17 shows that 6 M TFMSA impedes OH adsorption from water activation even more, but it has been shown that in 6 M TFMSA anion adsorption also occurs. In spite of the anion adsorption in 6 M TFMSA, the ORR rate is generally larger in 6 M TFMSA than in 1 M TFMSA.[38] Apparently in 6 M TFMSA, anion adsorption actually helps the ORR rate, and this occurs apparently because of the concentration and/or hydrophobic effects, which keep water away from the Pt surface and reduces OH poisoning. It follows that in 6 M TFMSA reduction of OH adsorption more than compensates for the sites which may be poisoned by the TFMSA anion adsorption. Indeed, a significant motivation for this work[14, 15] was that a neutral and hydrophobic ligand such as TPPTP might be ideal. It has the hydrophobic phenyl groups that may act similar to the hydrophobic F groups in TFMSA yet

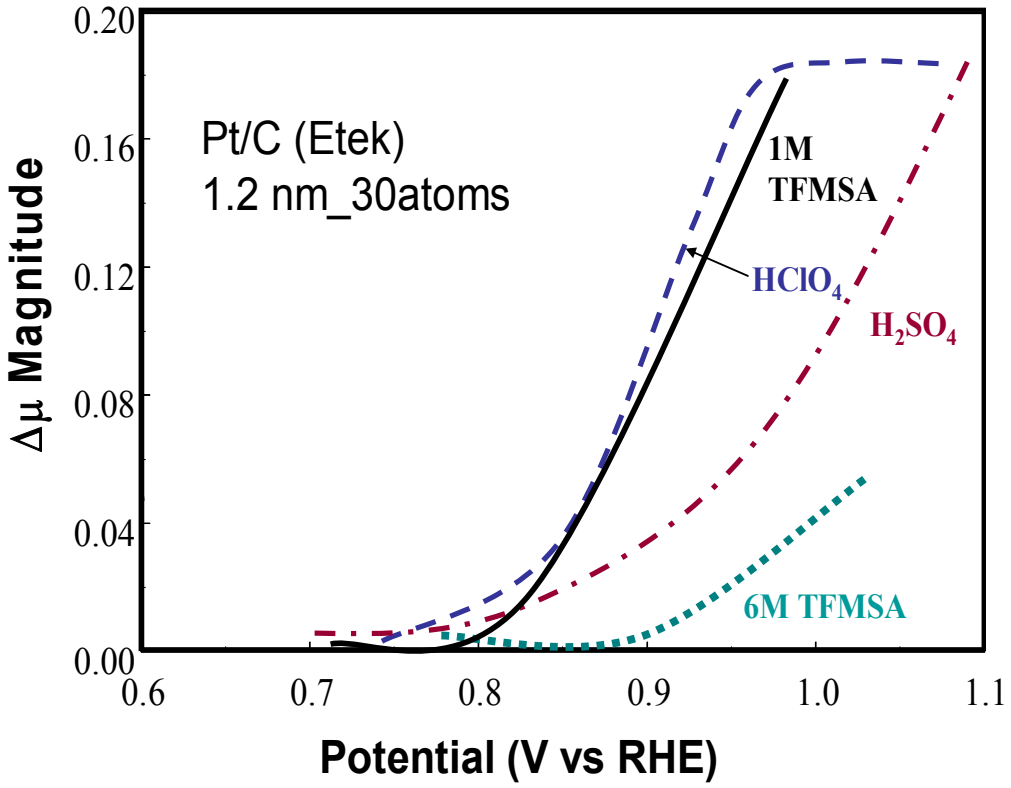

Figure 4.17 Previously reported[36] $\Delta\mu$ magnitudes indicating relative OH coverage as a result of water activation in the indicated electrolytes. Results are shown for 0.1 M $HClO_4$ and H_2SO4 as well as for 1 and 6 M TFMSA. The average cluster size is indicated for all results.

provides a neutral ligand, which hopefully will lower the detrimental electronic effects that are severe with bisulfate and probably also TFMSA on the ORR.

Figure 4.16 reveals that the TPPTP ligand does indeed improve the surface-specific ORR rate on small particles; the surface-specific ORR rate is larger in the Pt/TPPTP catalysts than for the similarly sized Pt particles in Pt/C (0.8 nm) catalysts. This arises no doubt because, in spite of the adsorbed phosphine ligands that block sites, the OH poisoning is reduced. This leaves the question, is the reduced OH adsorption due to the hydrophobic effect or an electronic effect? One would expect H adsorption to experience an electronic effect as well if it existed. However, Figure 4.11 shows a remarkable similarity between the CV curves in the H region for both Pt/C and Pt/TPPTP. This suggests that indeed the neutral TPPTP ligand may not be exhibiting much of an electronic effect as expected and that indeed the hydrophobic effect is dominating.

Finally, we consider the strange difference between the H and O(H) adsorption in the Pt/ox-TPPTP catalyst. The atop H adsorption seen at low potentials may in fact be on top H adsorption, i.e., adsorption on top of those Pt sites already involved in bonding to the ligands. On top H is known[16-18] to adsorb in the presence of 3-fold 'underpotential deposited" (UPD) H, so perhaps it can adsorb in the presence of the 3-fold phosphine ligands as well, in precisely the same potential range as normal. This would suggest that the 3-fold sites are mostly blocked by the O-P<tp ligands. However, the O(H) adsorption appears to behave similar to large particles, i.e., initially a small atop OH component followed early on by n-fold O (Figure 4.14), albeit at low overall coverage. This n-fold O adsorption may indeed be 2-fold bridged O, which is known to adsorb early on at step edges (the $\Delta\mu$ technique cannot distinguish between 2- and 3-fold bonded O). The transition from OH to O is dependent on the relative Pt-O bond strength. At normal corners and edges the Pt-O bond strength is very large, [39] so the OH tends to stay as it is rather than moving to a bridged or fcc site. If indeed most of the Pt atoms are already bonded to an adsorbed ligand, this will weaken the Pt-OH bond, enabling early transition to bridged O. Thus, the H and O adsorption sites (although different) may indeed simply be reflecting a weakened

adsorption bond due to prebonding with a ligand (i.e., a type of electronic effect) in the ox-TPPTP catalysts.

4.5 Conclusion

The following conclusions can be drawn from this X-ray absorption study of TPPTP stabilized Pt nanocatalysts: (1) The TPPTP ligands partially block Pt sites but reduce water activation, most likely due to the hydrophobic effect which reduces water concentrations near the surface and therefore enhances the Pt surface-specific ORR activity. Unfortunately the mass-specific ORR activity is not enhanced,[15] apparently because the ligand site blocking effect is larger than the reduction in OH poisoning. Thus, the primary motivation for this study, to enhance the ORR rate by utilizing the TPPTP ligands, has been only partially met. (2) The ox-TPPTP ligands appear to exert a large electronic effect but dramatically block sites (apparently because they lie in 3-fold fcc sites), making these catalysts inactive for ORR. (3) The combination of EXAFS with the $\Delta\mu$ technique provides significant details on cluster size, ligand coverages, binding sites, and change in ligands from P<tp to O-P<tp, which correlate with and significantly complement the CV data. This is the first application of the ΔXANES technique to such complex ligands, and the success here reveals again its enormous applicability to study and characterize catalysts in situ.

4.6 References

[1] Wang, J. X.; Markovic, N. M.; Adzic, R. R. *J. Phys. Chem. B* **2004**, *108*, 4127.
[2] Teliska, M.; Murthi, V. S.; Mukerjee, S.; Ramaker, D. E. *J.Electrochem. Soc.* **2005**, *152*, A2159.
[3] Anderson, A. B.; Albu, T. V. *J. Electrochem. Soc.* **2000**, *147*, 4229.
[4] Stamenkovic, V.; Mun, B. S.; Mayrhofer, K. J. J.; Ross, P. N.; Markovic, N. M.; Rossmeisl, J.; Greeley, J.; Nørskov, J. K. *Angew. Chem.,Int. Ed.* **2006**, *45*, 2897.
[5] Chan, K.-Y.; Ding, J.; Ren, J.; Cheng, S.; Tsang, K. Y. *J. Mater.Chem.* **2004**, *14*, 505.
[6] Scott, F. J.; Mukerjee, S.; Ramaker, D. E. *J. Electrochem. Soc.* **2007**, *154*, A396.
[7] Zhang, J.; Lima, F. H. B.; Shao, M. H.; Sasaki, K.; Wang, J. X.;Hanson, J.; Adzic, R. R. *J. Phys. Chem. B* **2005**, *109*, 22701.
[8] Bligaard, T.; Nørskov, J. K. *Electrochim. Acta* **2007**, *52*, 5512.
[9] Schmid, G.; Mailhack, V.; Lantermann, F.; Peschel, S. *J. Chem.Soc., Dalton Trans*. **1996**, 589.
[10] Ye, H.; Crooks, R. M. *J. Am. Chem. Soc.* **2005**, *127*, 4930.
[11] Markarian, M. Z.; Harakeh, M. E.; Halaoui, L. I. *J. Phys. Chem. B* **2005**, *109*, 11616.
[12] Cotton, F. A.; Wilkinson, G.; Murillo, C. A.; Bochmann, M.*Advanced Inorganic Chemistry*, 6th ed.; John Wiley & Sons: New York, 1999;Chapter 10.
[13] Examples: (a) Gold: Woehrle, G. H.; Brown, L. O.; Hutchison, J.E. *J. Am. Chem. Soc*. **2005**, *127*, 21723. (b) Platinum: Yang, J.; Lee, J. Y.; Too, H.-P.; Valiyaveettil, S. *J. Phys. Chem. B* **2006**, *110*, 125. (c)Palladium: Son, S. U.; Jang, Y.; Yooon, K. Y.; Kang, E.; Hyeon, T. *Nano Lett.* **2004**, 4, 1147. Rhodium: Glo¨cker, J.; Klu¨tzke, S.; Meyer-Zaika, W.; Reller, A.; Ga´rcia-Ga´rcia, F. J.; Strehblow, H.-H.; Keller, P.; Rentschler, E.; Kla¨ui, W. *Angew. Chem., Int. Ed.* **2007**, *46*, 1164.
[14] Kostelansky, C. N.; Pietron, J. J.; Chen, M.-S.; Dressick, W. J.; Swider-Lyons, K. E.; Ramaker, D. E.; Stroud, R. M.; Klug, C. A.;Zelakiewicz, B. S.; Schull, T. L. *J. Phys. Chem. B* **2006**, *110*, 21487.
[15] Pietron, J. J.; Garsany, Y.; Baturina, O.; Swider-Lyons, K. E.; Ramaker, D. E.; Schull, T. L. *Electrochem. Solid State Lett.,* submitted for publication.
[16] Koningsberger, D. C.; de Graaf, J.; Mojet, B. L.; Ramaker, D. E.; Miller, J. T. *Appl. Catal. A* **2000**, *191*, 205. Mojet, B. L.; Miller, J. T.; Ramaker, D. E.; Koningsberger, D. C. *J. Catal.* **1999**, *186*, 373. Ramaker, D. E.; Mojet, B. L.; Garriga Oostenbrink, M. T.; Miller, J. T.; Koningsberger, D. C. *Phys. Chem. Chem. Phys.*, **1999**, *1*, 2293. Koningsberger, D. C.; Oudenhuijzen, M. K.; Bitter, J. H.; Ramaker, D. E. *Top. Catal.* **2000**, *10*, 167. Mojet, B. L.; Ramaker, D. E.; Miller, J. T.; Koningsberger, D. C.
Catal. Lett. 1**999**, *62*, 15.
[17] Ramaker, D. E.; Koningsberger, D. C. *Phys. Re*V*. Lett.* **2002**, *89*,139701.
[18] Teliska, M.; O'Grady, W. E.; Ramaker, D. E. *J. Phys. Chem. B* **2004**, *108*, 2333. Teliska, M.; O'Grady, W. E.; Ramaker, D. E. *J. Phys. Chem. B* **2005**, *109*, 8076.
[19] Scott, F. J.; Roth, C.; Ramaker, D. E. *J. Phys. Chem. C* **2007**, *111*, 11403.
[20] Roth, C.; Benker, N.; Buhrmester, T.; Mazurek, M.; Loster, M.; Fuess, H.; Koningsberger, D. C.; Ramaker, D. E. *J. Am. Chem. Soc.* **2005**,*127*, 14607.
[21] Wang, Y.; Ren, J. W.; Deng, K.; Gui, L.; Tang, Y. *Chem. Mater.* **2000**, *12*, 1622.
[22] Gasteiger, H. A.; Kocha, S. S.; Sompalli, B.; Wagner, F. T. *Appl. Catal. B: Environ.* **2005**, *56*, 9.
[23] Sasaki, K.; Wang, J. X.; Balasubramanium, M.; McBreen, J.; Uribe, F.; Adzic, R. R. *Electrochim. Acta* **2004**, *49*, 3873.
[24] Ravel, B.; Newville, M. *J. Synchrotron Radiat.* **2005**, *12*, 537.
[25] Newville, M.; Livins, P.; Yacoby, Y.; Rehr, J. J.; Stern, E. A. *Phys.Rev. B*. **1993**, *47*, 14126.
[26] Janin, E.; von Schenck, H.; Gothelid, M.; Karlsson, U. O.; Svensson, M. *Phys. Rev. B*. **2000**, *61*, 13144.

[27] Oudenhuijzen, M. K.; van Bokhoeven, J. A.; Ramaker, D. E.; Koningsberger, D. C. *J. Phys. Chem. B* **2004**, *108*, 20247.
[28] Mojet, B. L.; Miller, J. T.; Ramaker, D. E.; Koningsberger, D. C. *J. Catal.* **1999**, *186*, 373. O'Grady, W. E.; Ramaker, D. E.; Qian, X. *J. Phys. Chem. B* **1997**, *101*, 5624.
[29] Ramaker, D. E.; Oudenhuijzen, M. K.; Koningsberger, D. C. *J.Phys. Chem. B* **2005**, *109*, 5608.
[30] Calvin, S.; Luo, X.; Caragianis-Broadbridge, C.; McGuinness, J.K.; Anderson, E.; Lehman, A.; Wee, K. H.; Morrison, S. A.; Kurihara, L. K. *Appl. Phys. Lett.* **2005**, *87*, 233102. Calvin, S.; Miller, M. M.; Goswami, R.; Cheng, S. F.; Mulvaney, S. P.; Whitman, L. J.; Harris, V. G. *J. Appl.Phys.* **2003**, *94*, 778. Calvin, S.; Riedel, C. J.; Carpenter, E. E.; Morrison, S. A.; Stroud, R. M.; Harris, V. G. *Phys. Scr.* **2005**, *T115*, 744.
[31] Thompson, M. A. ArgusLab 4.0; Planaria Software, LLC: Seattle, WA; http://www.arguslab.com.
[32] Arruda, T. M.; Shyam, B.; Ziegelbauer, J. M.; Ramaker, D.; Mukerjee, S. Manuscript in preparation.
[33] Mayrhofer, K. J.; Blizanac, B. B.; Arenz, M.; Stamenkovic, V. R.; Ross, P. N.; Markovic´, N. M. *J. Phys. Chem. B* **2005**, *109*, 14433.
[34] Markovic, N. M.; Gasteiger, H.; Ross, P. N. *J. Electrochem. Soc.***1997**, *144*, 1591.
[35] Kinoshita, K. *J. Electrochem. Soc.* **1990**, *137*, 845.
[36] Teliska, M.; Murthi, V. S.; Mukerjee, S.; Ramaker, D. E. *J. Phys.Chem. C* **2007**, *111*, 9267.
[37] Wang, J. X.; Markovic, N. M.; Adzic, R. R. *J. Phys. Chem. B* **2004**, *108*, 4127.
[38] Murthi, V. S.; Urian, R. C.; Mukerjee, S. *J. Phys. Chem. B* **2004**, *108*, 11011.
[39] Ramaker, D. E.; Teliska, M.; Zhang, Y.; Stakheev Yu, A.; Koningsberger, D. C. *Phys. Chem. Chem. Phys.* **2003**, *5*, 4492.

Chapter 5

In situ determination of Water Activation and Oxygen Reduction in Rhodium Sulfide based Chalcogenides using X-ray Absorption Spectroscopy

5.1 Introduction

Attempts at finding alternatives to Pt for catalysis of the oxygen reduction reaction (ORR) in acidic environments have included a wide variety of geometric structures, some fundamentally different from the conventional metal surfaces in highly dispersed Pt (i.e., with typical particle sizes in the range of 1.5-8 nm). Extensive studies have been previously conducted on metal alloys with and without enrichment of alloying elements on the surface.[1,2] These more conventional structures have been relatively easy to characterize. However, the more complex alternative structures, such as those involving inorganic complexes and organo-metallics,[3-5] have proven to be more difficult to characterize, particularly in terms of our understanding of the nature of the reaction centers and the electrocatalytic pathways as a function of overpotential.

Some of the most promising alternative systems for facilitating the ORR are based on transition metal chalcogenides.[6,7] Several of these systems exhibit reasonably high performances

(e.g. Ru_xSe_y/C $i_0 = 2.22x10^{-5}$ A m^{-2}, 0.5M H_2SO_4),[8,9] and many have been reported to be relatively unaffected by typical poisons of Pt electrocatalysts, such as methanol[10-12] and halides[13]. However a full characterization of the pertinent structure/property relationships that give rise to their performance and depolarization has proven to be difficult. This arises in part because the synthetic methods[14,15] typically involve mixing nanoparticles of unreduced metal or metal carbonyl complexes with the elemental chalcogen in an organic solvent, and tend to produce small, amorphous clusters.[16,17]

The limited crystallinity of these alternate catalysts almost immediately rules out powder X-ray diffraction as a characterization technique. In addition, many other techniques (e.g. XPS, HREELS, LEEDS, etc.) can provide detailed information regarding the structure of amorphous materials, but are limited by both their *ex situ* nature and ultra-high vacuum (UHV) requirements. FTIR techniques can be applied to study certain species on the catalyst surface (CO, CO_2, HCOOH, etc.) but cannot provide information regarding O and OH adsorption nor the specific adsorption sites of the active metal.[18,19] Additionally, specialized IR techniques, such as subtractively normalized interference FTIR (SNIFTIRS), have been employed to study compact adlayers of adsorbed CO on Pt and Pt-alloy catalysts.[20-22] Unfortunately, a surface with a mirror finish is required, and thus it is not yet possible to probe catalysts supported on porous carbon substrates with this technique.[23]

In light of these limitations, synchrotron X-ray absorption spectroscopy (XAS) is particularly promising. In addition to being a short range order technique, XAS is element specific, and, as a core level spectroscopy, inherently quantitative. The use of high-intensity synchrotron radiation eliminates the need for high vacuum conditions, and allows for the investigation of electrocatalysts *in operando*[24] via specially designed electrochemical cells.[25,26] XAS is, however, a bulk-averaging technique. Thus, while the morphologies of the examined catalysts could be ascertained from traditional EXAFS analysis (coordination number, Debye-Waller factor, and bond distances) the adsorbate species could not traditionally be resolved with

the exception of clusters where the surface-to-bulk atomic ratio is favorable. This is possible only in a narrow particle size range of up to 4 nm. This limitation was finally eliminated with the advent of the Δμ analysis technique.[27,28] By performing a careful normalization of X-ray absorption spectroscopy near-edge structure (XANES) spectra, and then subtracting successive signals from a reference spectrum (such as those on clean surfaces absent adsorbed moieties), the bulk information (traditional metal–metal and metal–oxide interactions) is effectively removed from the signal. The remaining data then reflect adsorbate (e.g. adsorbed O(H) and H) species on the catalyst surface. Prior to the advent of the Δμ technique, these interactions ($O(H)_{ads}$ and H_2O_{ads}) were only observable in small cluster sizes as noted above due to their weak scattering and non-specific adsorption on the electrocatalyst surface. This technique has been successfully applied to Pt and Pt-M electrocatalysts to study a variety of adsorbates under *in situ* conditions.[2,28-31]

The water activation pathway is of particular interest in elucidating the mechanisms for the ORR on an electrocatalyst surface. Adsorbed OH serves as a surface poison on Pt electrocatalysts by effectively blocking the active sites for molecular O adsorption.[2] Evidence of this effect has been gathered from both spectroscopic and electrochemical investigations.[28,32] Further, a recent body of work used density-functional theory in conjunction with experimental data to model various oxo-species as they relate to ORR and the apparent activation energies on Pt and Pt-alloys. These studies assisted in further elucidating the effects of alloyed transition metals in Pt electrocatalysts.[33,34] These alloyed metals were found to increase the activity of the electrocatalysts by either: (a) taking the brunt of the OH adsorption and because of OH-OH repulsions leaving the Pt sites more free to proceed with ORR, or (b) partially deactivating the Pt surface (hence increasing the partial valence of Pt) which shifts the onset of OH adsorption to higher potentials.[2,32,35]

Incorporating the information gathered from these previous studies on Pt-based electrocatalysts, we recently published the first ever communications regarding the spectroscopic

observation of the water activation process on a chalcogenide electrocatalyst (30wt% Rh_xS_y/C, commercially available from De Nora).[3,36] This material is the current state-of-the-art chalcogenide-based electrocatalyst, available as an oxygen depolarized cathode (ODC).[37] Recent reports provide insight into the inherent stability of this material in HCl-saturated ORR environments.[13,38] The De Nora Rh_xS_y/C electrocatalyst exhibits the highest ORR performance and stability of the sulfide-based chalcogenide electrocatalysts.[4] Further, this electrocatalyst does not contain selenium, which owing to its toxicity, likely will cause the higher-performing Ru_xSe_y-class of chalcogenide electrocatalysts[6,39] to be ruled untenable for consumer applications. The performance and structural characteristics of the Rh_xS_y/C electrocatalyst renders it an ideal model compound for investigation of the ORR pathway on a sulfur-based chalcogenide electrocatalysts.

Despite its high level of performance, it is unlikely that Rh_xS_y/C will ever be a viable alternative to Pt-based electrocatalysts in PEMFC or DMFC applications. While Pt is expensive, Rh is typically 5-10 times more costly.[40] In addition, Rh does not exhibit the high degree of methanol tolerance of Ru-based chalcogenide electrocatalysts.[41] Nevertheless, the Rh_xS_y/C electrocatalyst is well-accepted for applications in chlorine generation.[13] Here the traditional hydrogen evolution cathode is replaced with a oxygen reduction analog, thereby providing a 800 to 900 mV reduction in cell voltage and saving an equivalent of 700 kWh ton^{-1} of chlorine.[42,43]

The De Nora Rh_xS_y/C electrocatalyst is comprised of a balanced phase of Rh_2S_3, Rh_3S_4, and $Rh_{17}S_{15}$.[44-46] XRD studies of the commercially produced material only reveal a spectrum for the $Rh_{17}S_{15}$ phase. The lack of observable XRD patterns for the Rh_2S_3 and Rh_3S_4 phases does not indicate their absence, but rather that they exist as extremely small particles (small grain sizes) in comparison to the $Rh_{17}S_{15}$ phase. Thus the microcharacterization of this material by standard methods (e.g. XRD) is severely limited by the uncertainty regarding the fraction of these phases and their complex structure. In a prior communication, application of the $\Delta\mu$ technique to in situ XAS water activation studies in 1 M trifluoromethanesulfonic acid (TFMSA) coupled with

laboratory rotating disk electrode experiments suggested that the active phase in the Rh_xS_y/C electrocatalyst is Rh_3S_4.[3]

That initial work was conducted solely on the mixed-phase Rh_xS_y/C electrocatalyst, as the constituent phases were not available in any substantial quantity with sufficient purity. Here, we present water activation and ORR studies on thermally-grown carbon-supported Rh_2S_3 and Rh_3S_4 preferential phases in 1 M TFMSA. In addition, the Rh_xS_y/C catalyst was further probed in 6 M TFMSA electrolyte (i.e., water content is significantly lower).[32,47] These additional studies confirm the initial conclusions that Rh_3S_4 is the more active phase,[3,36] but also point out the instability of the Rh_xS_y catalyst in strong acid such as TFMSA. Further, high acid concentrations result in the formation of a Rh skin on the electrocatalyst particle surfaces, and this may in fact be the more active constituent. These results also serve to fully validate the $\Delta\mu$ technique as a powerful new tool for elucidating the active sites of mixed-phase inorganic complexes for ORR electrocatalysts. To the authors' knowledge, this is the first time the active site has been determined in a mixed inorganic complex to this high level of detail. Therefore, the present work constitutes a major advance in our understanding of electrocatalysis on systems very different from the conventional metal cluster surfaces. This work is expected to open new avenues for materials synthesis tailored for particular applications.

5.2. Experimental

5.2.1 Synthesis

30wt% Rh_xS_y/C (De Nora) and 30wt% Rh/C (8.3 nm grain size, E-TEK, Inc., now "BASF Fuel Cell, Inc.", Somerset, NJ) were used in as-received form. The carbon support was Vulcan XC-72 (Cabot Corporation). The properties and morphology of the 30wt% Rh/C electrocatalyst (i.e. 8.3 nm grain size) were reported in a prior publication.[13] The synthetic methodology for the Rh_xS_y/C electrocatalyst can be found in the patent literature.[48-50] The preferential phases, 40-45wt% Rh_2S_3/C (orthorhombic *Pbcn*)[46] and Rh_3S_4/C (monoclinic, space

group C*2/m*),[44] were prepared by heat treating the carbon-supported 30wt% Rh_xS_y precursor material (De Nora) under conditions outlined by Beck *et al*.[44] Briefly, this involved heating the samples under flowing argon (high purity, Medtech Gases, Inc.) in a quartz furnace tube for ~2 hours at 1220 and 1340 K for Rh_2S_3 and Rh_3S_4, respectively. Attempts to generate a preferential $Rh_{17}S_{15}$ phase from the precursor were unsuccessful, and resulted in a near complete breakdown of the Rh-S precursor into metallic Rh.

5.2.2 Catalyst Morphology (XRD and High-Resolution Transmission Electron Microscopy)

XRD data were obtained with high-resolution synchrotron radiation at beamline X-7B at the National Synchrotron Light Source (NSLS, Brookhaven National Laboratory, Upton, NY). The as-synthesized catalyst powders were packed into amorphous glass capillaries. The X-ray radiation, adjusted to a wavelength of 0.9177 Å via a Si(111) monochromator, was chosen as to prevent XAS signals from interfering with the XRD spectra. Data was acquired through a MAR345 image plate detector (marUSA, Evanston, IL). Owing to the high intensity of the X-ray beam (flux $\approx 6\times10^{11}$ photons sec^{-1}) it required less than 15 minutes per sample to collect a full XRD pattern.

All three samples were examined using a 300 kV FEI Tecnai F30 ST field-emission gun high-resolution transmission electron microscope. This instrument is equipped with a lithium-drifted silicon detector for X-ray energy dispersive spectrometry (XEDS). Specimens for high-resolution transmission electron microscopy (HRTEM) were prepared by dispersing each nanoscale electrocatalyst in methanol and ultrasonicating them (10 min) to reduce agglomeration. Subsequently, a single drop of each dispersion was either deposited onto a thin carbon film supported by a copper grid, or a carbon film was dipped into the dispersion.

5.2.3 Rotating Disk Electrode Studies

Rotating disk electrode (RDE) studies were conducted in $O_{2(g)}$-saturated (MedTech Gases, Inc.) 1 M TFMSA (3M Corporation). The as-received TFMSA electrolyte was distilled

and purified prior to use.[47,51] TFMSA was chosen as the supporting electrolyte because of its low anion adsorption.[31] The RDE setup was comprised of a glassy carbon (GC) RDE (5.6 mm diameter, Pine Instrument Co.) interfaced with a model AFASR rotator (Pine). Potentiostatic control (for both the RDE and in situ XAS studies) was obtained with a model PGSTAT30 potentiostat/galvanostat (Eco Chemie, Brinkmann Instruments). Prior to all RDE experiments, the GC was polished to a mirror-finish with 1 and 0.05 micron alumina slurry (Buehler, Inc.). The inks were comprised of a mixture of the relevant electrocatalyst and a small amount of 5wt% Nafion® as a binder (Sigma-Aldrich). The suspension was a 1:1 wt% mixture of 2-propanol (HPLC grade, Sigma-Aldrich) and de-ionized water (MegaPure, Millipore). The target geometric loading of the cast electrocatalyst films on the GC were 14 μg metal cm^{-2}. The final metal:Nafion® mass ratio in the dried film was < 1:50, and thus allowed for additional diffusion effects when analyzing the RDE data to be neglected.[32,52]

For all electrochemical experiments (RDE and in situ XAS), a Pt mesh (Alfa Aesar) served as the counter electrode with a sealed RHE as the reference electrode. The RHE was generated from the identical electrolyte to eliminate the possibility of junction potentials. All potentials are reported relative to RHE. The catalysts were activated (under $Ar_{(g)}$-saturated conditions) prior to RDE studies by collecting cyclic voltammograms at 50 mV s^{-1} until a steady state signal was achieved (typically 30 cycles). RDE data was obtained in room temperature electrolyte at 100, 400, 625, 900, 1225, and 1600 rpm (rotations per minute). Data were collected at each rotation rate for 5 scans (20 mV s^{-1}), and the final three scans averaged for analysis. To ensure reproducibility, each data set was collected at least three times with separately-cast RDE films. All electrochemical analysis[53] was performed on the cathodic sweeps.

5.2.4 XAS Data Collection and Analysis

Details on the experimental equipment and materials have been published recently.[3,4,36] One important difference in this report involves the utilization of 6 M TFMSA. To study the effect of water activity with the Rh_xS_y/C material, concentrated solid 9 M monohydrate was

diluted to 6 M. Special care was taken with the distillation and crystallization of the TFMSA in accordance with previously reported procedures.[32,47,51] To ensure that the total water content was kept as low as possible, both of the electrodes as well as the Nafion® 112 separator were soaked in de-aerated 6 M TFMSA for 2 hours prior to cell assembly.

Following an activation step (0.02 to 1.2 V vs. RHE at 20 mV s^{-1}), full Rh K edge (23,220 eV) EXAFS scans (-250 eV to 16k) were collected at different potentials by cycling the cell to the respective anodic potential and holding potentiostatically during the absorption measurements. All XAS signals were collected with a beam spot size of 0.3 x 1.5 mm. These measurements were collected in fluorescence mode via a 13-element fluorescence detector at beamline X18-B (National Synchrotron Light Source, Brookhaven National Labs, Upton, NY). During all the measurements, transmission data were collected in conjunction with a thin Rh foil to account for shifts in measured energy due to drifts in the Si(111) monochromator position. For alignment, background subtraction, and normalization of the XAS data, the IFEFFIT suite[54] was utilized.

The theory and normalization processes for the $\Delta\mu$ analysis are described in detail elsewhere.[3] Briefly, the collected spectra were aligned by using the signals from the reference foil in order to preserve any shifts in the absorption edge arising from oxidation of the Rh. The aligned spectra were then carefully normalized in a previously described manner.[27,28] It should be noted that the normalization range appropriate for $\Delta\mu$ analysis is significantly more constrained than for typical EXAFS analysis. In order to isolate adsorbate scattering, the normalization was applied in the range 40-200 eV past the edge.

The $\Delta\mu$ signals were generated according to the relationship:

$$\Delta\mu = \mu(V) - \mu(0.40\ V) \qquad (5.1)$$

where the signal at 0.40 V is considered the cleanest (e.g. double layer) region free of adsorbed H, O(H), and anions as determined via the electrochemical analysis and EXAFS fitting. All potentials correspond to a point on the anodic sweep. For signals at 0.50 and 0.60 V, a correction to account for both charging effects of the electrode and the Rh lifetime core width was performed.[27,55] Interpretation of the acquired spectra was accomplished by generating XANES spectra via the FEFF 8.0 code[56] utilizing models of the pertinent Rh-S clusters generated with CAChe® (version 6.1.12, Fujitsu Computer Systems Corporation) from published[44-46] and experimental[3,13,38] crystallographic parameters. The theoretical spectra were then treated to the same subtraction process as the experimental results: $\Delta\mu = \mu(Rh_xS_y\text{-}O_{ads}) - \mu(Rh_xS_y)$.

5.3 Results and Discussion

5.3.1 Morphology

5.3.1.1 X-ray diffraction

Figure 5.1 presents the high resolution synchrotron (λ = 0.9177 Å) powder X-ray powder diffraction results for the carbon-supported rhodium sulfide electrocatalysts. As discussed in prior publications,[3,13] the XRD spectrum for the Rh_xS_y/C electrocatalyst is very complex. It is well established[44] that this system is composed of a balanced phase mixture of cubic *Pm3m* $Rh_{17}S_{15}$,[45] orthorhombic *Pbcn* Rh_2S_3,[46] and monoclinic C*2/m* Rh_3S_4[44] (Table 5.1). Nonetheless, only the $Rh_{17}S_{15}$ phase could be accurately indexed to the Rh_xS_y/C spectrum. This suggests that the grain size of the $Rh_{17}S_{15}$ is much larger than that of the other Rh-S phases thereby limiting the utility of XRD for determination of the phase balance.

Utilizing the derived values reported by Beck *et al.*,[44] the carbon-supported Rh_xS_y precursor was heat-treated at 1220 K in an effort to skew the phase balance towards the Rh_2S_3 phase. The resulting XRD pattern (Figure 5.1, middle) is again dominated by the fingerprint of

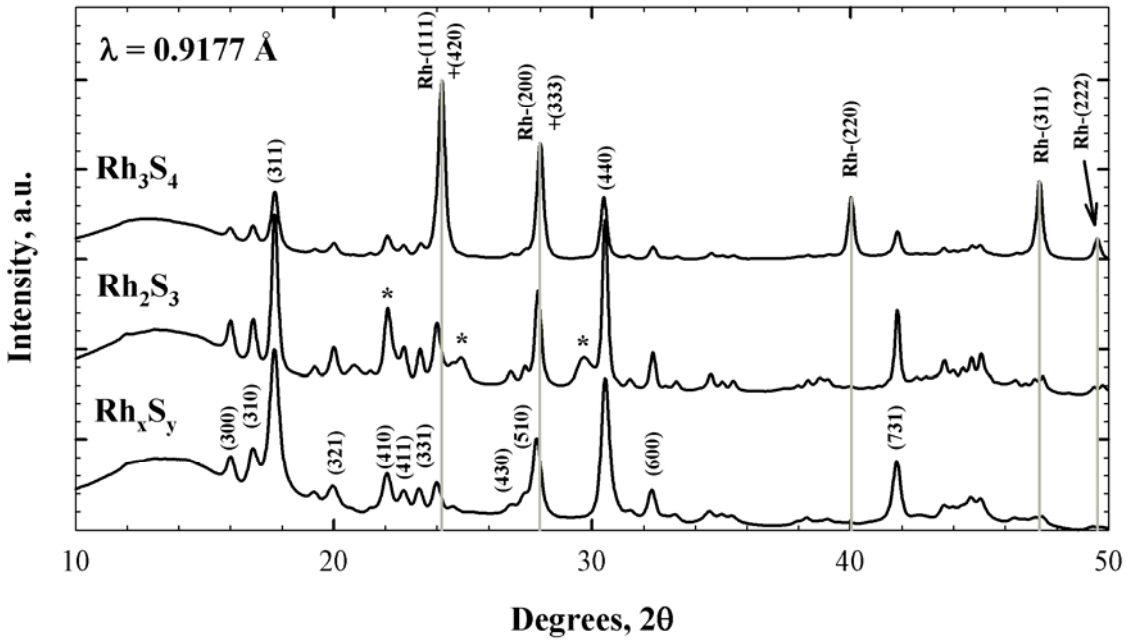

Figure 5.1. Capillary powder X-ray diffractograms for the Rh-S electrocatalysts from high-resolution (0.9177 Å) synchrotron radiation (NSLS beamline X-7B) studies. The Rh_xS_y diffractogram is indexed to *Pm3m* $Rh_{17}S_{15}$. The grey vertical lines denote the expected pattern for cubic *Fm3m* elemental rhodium . The asterisks denote possible reflections from the *Pbcn* Rh_2S_3 phase.

Table 5.1: Crystallography

	Symmetry	Space Group	Cell Parameters						$Rh\text{-}Rh_{avg}$, (Å)	$Rh\text{-}S_{avg}$ (Å)
			a/Å	b/Å	c/Å	α/°	β/°	γ/°		
Rh	cubic	*Fm3m*	3.803	-	-	90	-	-	2.69	
Rh_2S_3	ortho-rhombic	*Pbcn*	8.462	5.985	6.138	90	-	-	3.208	2.365
Rh_3S_4	monoclinic	C*2/m*	10.292	10.671	6.213	90	107.71	90	2.70/ 3.092	2.30
$Rh_{17}S_{15}$	cubic	*Pm3m*	9.911	-	-	90	-	-	2.59	2.33

References: Rh (JCPDF # 01-1214), Rh_2S_3 (Ref. 46), Rh_3S_4 (Ref. 44), $Rh_{17}S_{15}$ (JCPDF # 73-1443).

the $Rh_{17}S_{15}$ phase, although very small elemental Rh metal (*Fm3m*) could also be present. Despite the complexity of the X-ray diffractogram, several features (marked by asterisks) suggest that the thermal growth of Rh_2S_3 was successful. The peak at 22.1° could be representative of combined (311) and (212) reflections[46] from nanoscale Rh_2S_3 particles overlaid with the (410) reflection[45] of $Rh_{17}S_{15}$. If this is the case, then the peak at 24.9° can be considered the (022) and (400) reflections from Rh_2S_3. It is important to note that these reflections seen at 22.1 and 24.9° give the second and third most intense reflections for Rh_2S_3. Further evidence for the presence of nano-crystallites of Rh_2S_3 can be seen at 29.7 and 30.5°. Indexing the peak at 29.7° to the (213) reflection of Rh_2S_3 provides for an elegant explanation for the larger magnitude of the $Rh_{17}S_{15}$ (440) peak compared to the $Rh_{17}S_{15}$ (333) reflection in the Rh_2S_3 spectrum vs. the Rh_xS_y spectrum. At 30.5° the Rh_2S_3 should exhibit a high intensity peak composed of combined reflections from the (402), (231) and (420) facets. In combination with the (440) reflection from the omnipresent $Rh_{17}S_{15}$ phase, this peak should appear with greater intensity than in the Rh_xS_y spectrum.

In contrast to the other Rh-S spectra, the XRD pattern for the Rh_3S_4 preferential phase (Figure 5.1, top) exhibits a strong fingerprint from elemental Rh. These features are so dominant that the $Rh_{17}S_{15}$ reflections are quite muted with respect to the other Rh-S XRD spectra. The Rh_3S_4 preferential phase spectrum could not be indexed to either Rh_3S_4 or Rh_2S_3. Thus, if the Rh_3S_4 phase is present in this material, it is nominally crystalline in comparison to the $Rh_{17}S_{15}$ phase, and is therefore invisible to the powder XRD technique.

5.3.1.2 Transmission electron microscopy

XEDS confirmed that all three samples were composed of only carbon, rhodium, and sulfur. A montage of several typical TEM images of the three samples is presented in Figure 5.2. Figures 5.2a-c are low-magnification bright-field TEM images showing the size distribution of the particles for samples Rh_xS_y, Rh_2S_3, and Rh_3S_4, respectively. The catalyst particles generally had diameters of less than 20 nm, though it could vary significantly. The globular amorphous

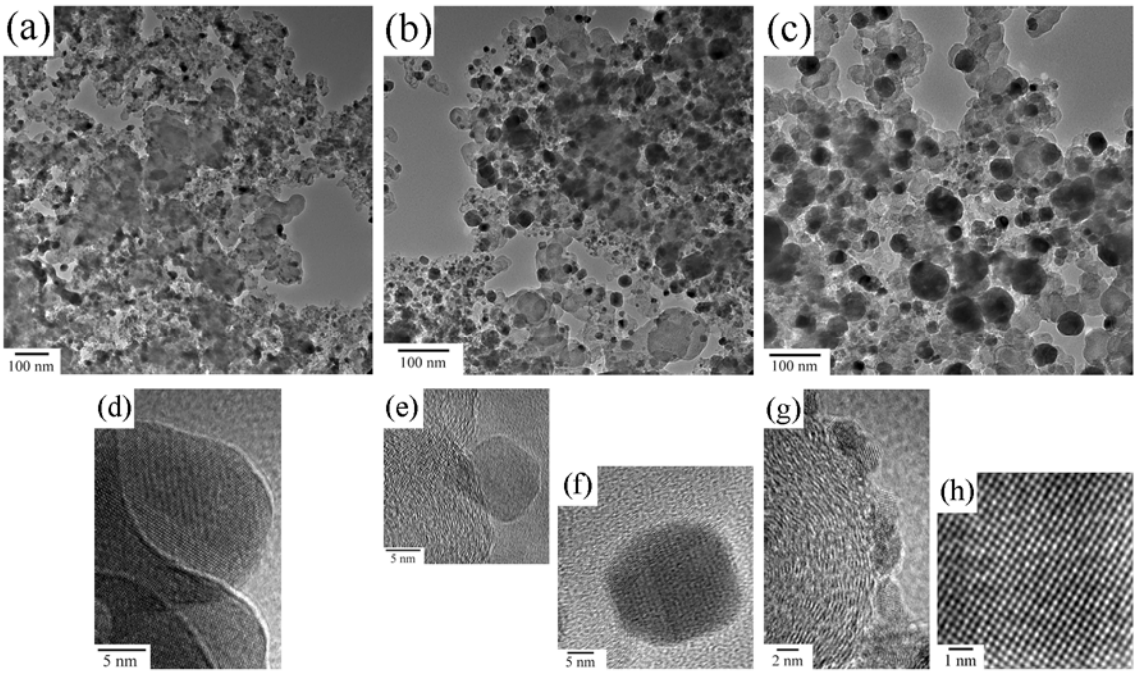

Figure 5.2. TEM images of Rh–S electrocatalysts. (a-c) Low magnification bright-field TEM images obtained from samples Rh_xS_y, Rh_2S_3 and Rh_3S_4, respectively. (d) A nanoparticle from the Rh_xS_y sample in contact with several others. (e, f) Two images of nanoparticles recorded from sample Rh_2S_3 in intimate contact with the amorphous globular carbon support. (g) Nanoparticles of the Rh_3S_4 sample, wetting the surface of the amorphous globular carbon support. (h) HRTEM image of a nanoparticle of the Rh_3S_4 sample, viewed in either the <521> or the <311> direction.

carbon support is omnipresent and generally interferes with TEM imaging and analysis. The larger darker particles (with diameters 10-25 nm in the Rh_2S_3 and up to 100 nm in the Rh_3S_4 samples) suggest the growth of Rh metal particles with heating to higher temperatures, which is in good agreement with the XRD data. Figures 5.2d-h are HRTEM images of the corresponding nanoparticles. The continuous amorphous carbon support film has the disadvantage of generating a speckled pattern in the background of the images. The bright contour around the edge of the particles, especially visible in image (d), suggests that a continuous "skin" is formed on the surface of these Rh_xS_y particles. This will be discussed further below. The catalyst nanoparticles of each of the three samples were found to form intimate contacts with the globular amorphous carbon support. Interestingly, it is sometimes found (e.g. Figure 5.2g) that these particles actually wet their amorphous carbon support.

Figure 5.2d was recorded from the Rh_xS_y sample and shows several agglomerated catalyst particles. The crystal structure of the most distinct particle seems to belong to the cubic system. The lattice planes apparent in the HRTEM image originate from *410* planes oriented along the directions from the top right to the bottom left, and from the top left to the bottom right, respectively.

Figures 5.2e and f were recorded from the Rh_2S_3 sample and illustrate the morphology of two different catalyst particles with diameters ≈12 and ≈25 nm, respectively. These particles exhibit faceting on crystallographic planes of a much greater extent than observed in Figures 5.2d and g. The Rh_3S_4 sample notably contained only small Rh-S phase particles with diameters of only a few nanometers (Figure 5.2g) in addition to the large Rh particles. The HRTEM image of Figure 5.2h shows a portion of a larger nanoparticle from the Rh_3S_4 sample. Likely, this particle is *Pm3m* $Rh_{17}S_{15}$ viewed in a <521> or <311> direction (which generate very similar fringe patterns). In this case, the dominant lattice fringes correspond to *311* or *310* planes.

5.3.2 Electrochemical Kinetics

5.3.2.1 Cyclic voltammetry

Figure 5.3 shows 50 mV s^{-1} cyclic voltammograms of the four electrocatalysts in $Ar_{(g)}$-saturated 1 M TFMSA. The standard 30wt% Rh/C electrocatalyst (Figure 5.3, top left) exhibits features correlated to the adsorption/desorption of H and oxo-species.[57,58] The large cathodic peak centered at ~0.48 V can be assigned to the reduction of adsorbed oxo-species on the rhodium surface. At potentials < 0.25 V, hydrogen adsorption/desorption features are apparent, and evidence of hydrogen evolution is observed at the lowest anodic potential (0.02 V). On the anodic sweep, a smooth double layer region is observed just past the hydrogen desorption region at ~0.25 - 0.45 V. Immediately following this a gradual increase in the anodic current begins. This is attributed to oxo-species adsorption on the electrocatalyst surface beginning with water activation. If the scan was continued to potentials greater than 1.25 V, it is expected that the onset of oxygen evolution would become apparent.

In contrast, the CV for Rh_xS_y/C is considerably muted. This material does not possess the broad cathodic feature seen with Rh/C, although a small peak is observable at ~0.24 V. Further, while a hydrogen evolution peak is discernable, the catalyst does not exhibit a significant H_{des} peak. Finally, the broad increase in the anodic current typically assigned to the progression of $OH/(H_2O) \rightarrow O_{ads}$ on Rh/C is arguably nonexistent until ~0.90 V, whereas this feature becomes noticeable on the standard Rh/C electrocatalyst a full ~450 mV earlier .

When compared to the Rh/C and Rh_xS_y/C electrocatalysts, the Rh_2S_3/C and Rh_3S_4/C preferential phases exhibit a mixture of features. For Rh_2S_3, the depth of the cathodic feature is still small, but has shifted to a higher potential in comparison to the Rh_xS_y/C electrocatalyst. Further, the Rh_2S_3 preferential phase exhibits a noticeable increase in anodic current at 0.75 V. The magnitudes of the cathodic and anodic features of the Rh_3S_4 preferential phase sit between the Rh_xS_y/C and Rh_2S_3/C electrocatalysts. Further, the CV for the Rh_3S_4 phase is differentiated by the well-defined (and considerably larger) H_{des} peak as opposed to Rh_2S_3/C; this however is

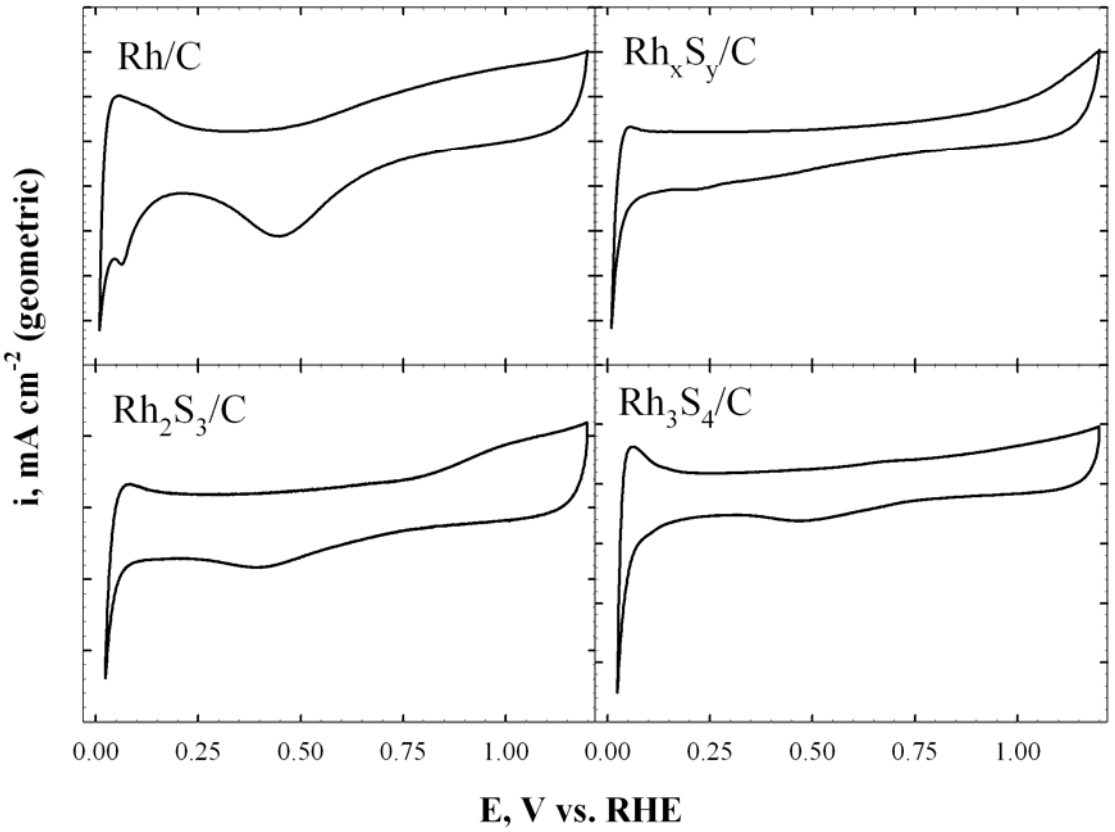

Figure 5.3. Room temperature 50 mV s^{-1} cyclic voltammograms of the denoted catalysts in de-aerated 1 M TFMSA.

still considerably smaller in magnitude compared to the corresponding peak in the case of Rh/C. Despite this similarity with Rh/C, the Rh_3S_4 preferential phase is comparably devoid of the anodic oxo-species adsorption features exhibited by Rh/C.

These CV curves will be more carefully correlated with the Δμ results and interpreted below.

5.3.2.2 RDE studies

The performance of the electrocatalysts in $O_{2(g)}$-saturated 1M TFMSA was determined via the RDE technique (Figure 5.4). The electrocatalysts reveal a single reduction wave suggesting single reaction sites. In terms of gross current density and ORR onset potential (Table 5.2), the Rh_2S_3 preferential phase significantly lags behind the other electrocatalysts. Unlike Rh/C, the Rh-S electrocatalysts do not exhibit clear, well-defined limiting currents. This property was previously reported for the Rh_xS_y/C electrocatalyst,[3,4] and the limiting currents were therefore approximated by utilizing the potential where the slope of the ORR curve became constant (~0.30 V determined by a first derivative analysis). Further, the Rh-S phases do not possess an H_{des} region that would allow for proper determination of the electrochemical surface areas.[52] As a result, all current densities (also for Rh/C) are reported with respect to the mass-normalized (14 μg total Rh) geometric surface areas.

Approximation of the limiting currents allowed for extraction of the mass transfer-corrected Tafel slopes (Figure 5.4, right) and relevant kinetic parameters (Table 5.2). Both Rh/C and Rh_xS_y/C exhibit Tafel slopes of ~120 mV dec^{-1} in the kinetic/diffusion-controlled region, and a lower slope of ~60 mV dec^{-1} at very low overpotential. The well-established interpretation for these values is that the -120 mV dec^{-1} slope is indicative of $4e^-$ electron transfer whereas the lower slope can be attributed to oxo-species adsorption on an oxide-covered surface.[32,59-61] These results indicate that both Rh/C and Rh_xS_y/C effectively accomplish ORR via a kinetic pathway similar to Pt/C. In particular, these results bolster the determined apparent activation energies for Rh_xS_y/C in prior publications,[3,4] which were found to trend downwards with respect to increasing

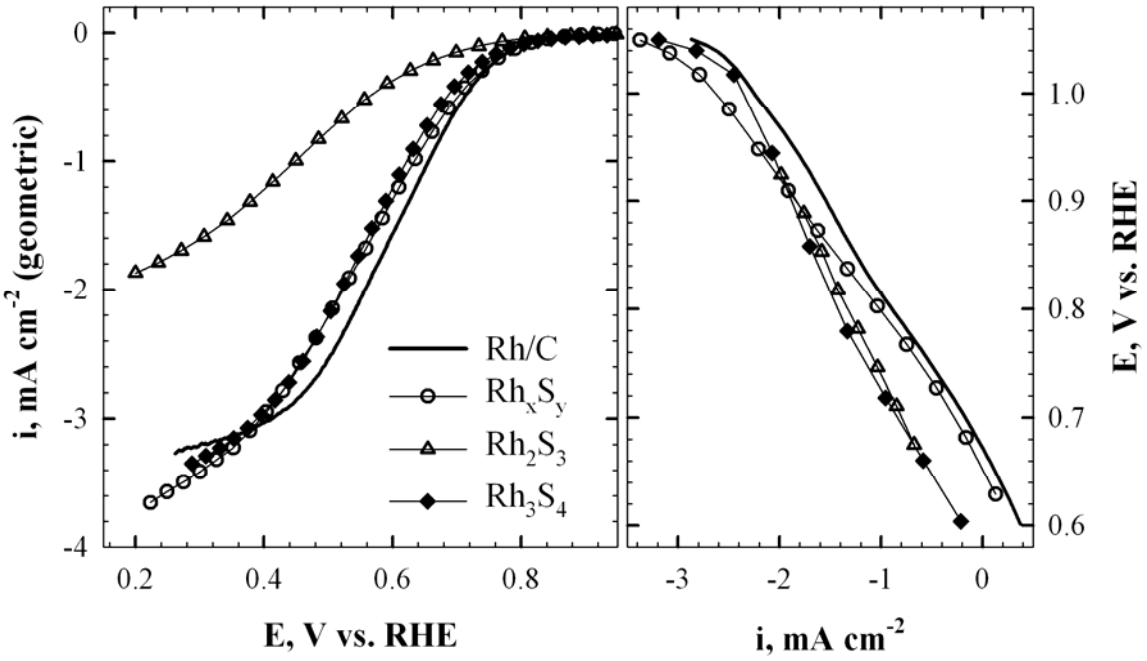

Figure 5.4. 900 rpm RDE results for the standard 30wt% Rh/C, 30wt% Rh_xS_y/C (De Nora), and the thermally grown Rh_2S_3/C and Rh_3S_4/C preferential phases. Cathodic scans in room temperature O_2-saturated 1M TFMSA, 20 mV s^{-1} scan rate.

Table 5.2. Electrochemical Kinetics

Catalyst	E_{onset}[b], V vs. RHE	-b, mV dec^{-1}	i at 0.9/0.8/0.7 V[c], 10^3 mA cm^{-2}	i_k at 0.85 V[b], 10^3 mA cm^{-2}
Rh	1.05	140	21.4 94.5 591	58
Rh_xS_y	1.05	124	16.1 103 507	36
Rh_2S_3	0.93	190	14.4 45.0 150	26
Rh_3S_4	1.05	196	24.8 90.6 404	29

[a]Room temperature 1 M TFMSA, 900 rpm, 20 mV s^{-1} scan rate

[b]Determined by 1st derivative analysis of the cathodic ORR sweep

[c]Geometric area

overpotential. An identical trend has been reported for Pt and Pt-alloy electrocatalysts.[32] Subsequent experimental and theoretical studies[34] have shown that the pre-exponential factor is influenced by the surface oxide/oxo-species coverage. Considering the similarity of Rh_xS_y/C to the results reported for Pt and Pt-alloy electrocatalysts, it is reasonable to expect that the water activation and ORR processes on Rh_xS_y/C proceed similarly to that on the active sites of Pt.

In contrast to Rh/C and Rh_xS_y/C, the preferential phases show significantly higher Tafel slopes of ~190 mV dec^{-1}. This trend could be indicative of a larger cathodic transfer coefficient for the preferential phases, differences in diffusion at the electrocatalyst surfaces, an increase in the number of active sites with decreasing potential, or just a larger resistance in these preferential phases. A proper determination of these parameters would require true, single phases, but such materials were unavailable for this study. Indeed, the aforementioned XRD and HRTEM analyses show that the preferential phases still contain a substantial number of large $Rh_{17}S_{15}$ particles, and increasing amounts of elemental Rh metal with heating. Considering the nanocrystalline nature (i.e., high surface areas) of the Rh_2S_3 and Rh_3S_4 particles, however, the majority of the exhibited activity of the preferential phases can be attributed to the target phases. While it was not unexpected that the Rh_3S_4 preferential phase would show ORR activity, the results for the Rh_2S_3 preferential phase are somewhat surprising and will be explained below.

5.3.3 XAS Analysis

5.3.3.1 *In situ* XANES

Figure 5.5 presents normalized in situ (0.40 V) Rh K edge (23,220 eV) absorption spectra for the Rh-S electrocatalysts in addition to the standard 30wt% Rh/C. The Rh/C electrocatalyst exhibits the signature of Rh metal in the oscillatory features. The nanoscale nature of the Rh particles is reflected in the low magnitudes of these oscillations. In contrast to the metallic Rh/C spectrum, the Rh_xS_y/C signal possesses a more intense white line at 5-50 eV past the edge. The white line in an XAS μ(E) spectrum is attributed to excitation into the electron vacancies in the d-type valence orbital.[24,62,63] Typically, this feature will grow as the extent of ligation around the

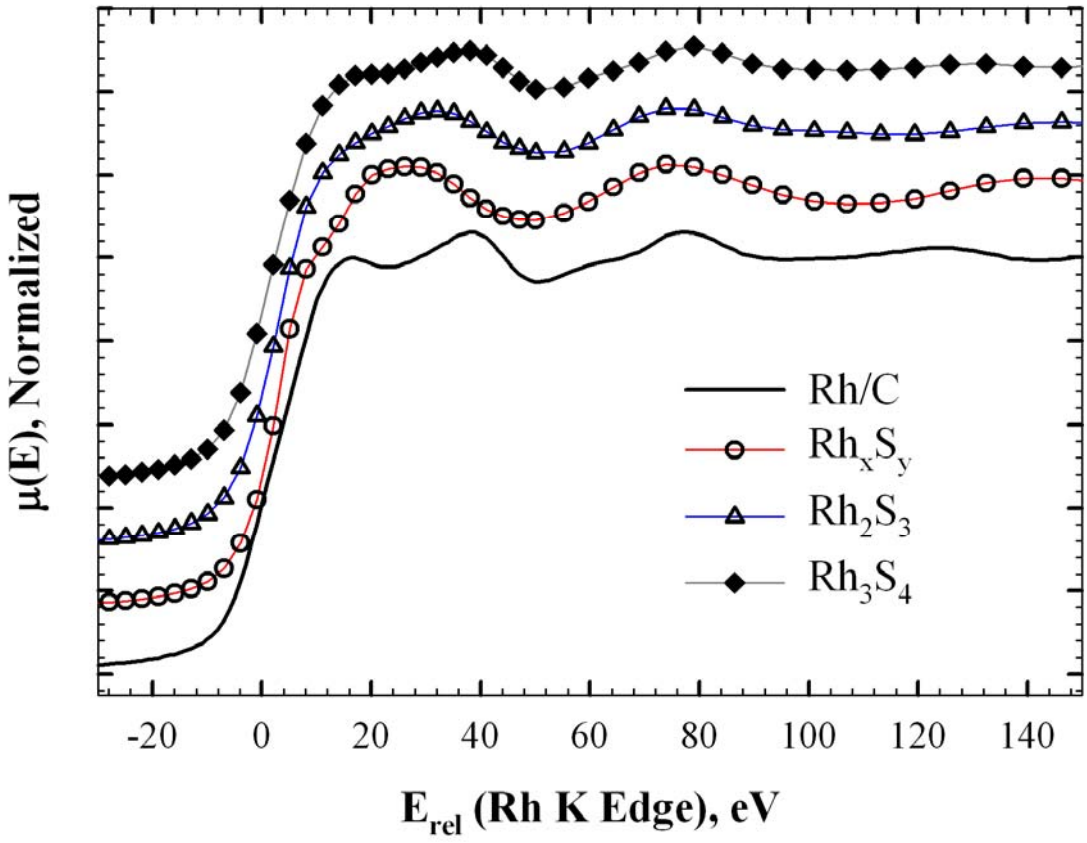

Figure 5.5. *In situ* (0.40 V) Rh K edge (23220 eV) XANES signals for the electrocatalysts in de-aerated 1 M TFMSA.

absorbing atom increases thus increasing the electron vacancy. As expected, the Rh_xS_y/C electrocatalyst (consisting of sulfided Rh species) exhibits a substantial increase in this feature compared to the Rh/C electrocatalyst. With heating to higher temperature to prepare the Rh_2S_3 and Rh_3S_4 preferential phases, the spectra increasingly revert back to the Rh/C signature reflecting the Rh particles being formed as indicated above by the XRD and TEM data.

5.3.3.2 *In situ* Rh K edge EXAFS

Figure 5.6 presents the $\chi(k)$ (k^2-weighted) spectra derived from spectra similar to that in Figure 5.5. With the exception of the Rh_2S_3 preferential phase, the materials exhibit oscillations to 14 k reflecting the quality of the collected data. These spectra again reveal the transformation of the Rh_xS_y spectrum to that more resembling the Rh/C spectrum with heating to higher temperature to form the preferential phases.

The non-phase-corrected Fourier transforms (FT) of these data are presented in Figure 5.7. These FT spectra reflect the inter-atomic distance (in units of Å, ±0.02 Å) between the absorbing Rh atom and its neighbors, either S or another Rh atom with the intensity reflecting the product of the coordination number (N_{Rh-X}) and Debye-Waller factor (σ^2).[62] The Rh/C standard exhibits a large peak at the expected position for Rh-Rh (average R_{Rh-Rh} = 2.69 Å) interactions in Rh. The Rh-S electrocatalysts all show features at lower R which are attributed to Rh-S interactions. Note that the ratio of intensities I_{Rh-Rh}/I_{Rh-S} increases in the order xy < 23< 34, reflecting the formation of Rh particles with heating during the preparation of the preferential phases as evident already in the XANES and raw EXAFS data discussed above. As outlined in Table 1, Rh_2S_3 is an orthorhombic (ABAB stacking) crystal with the space group *Pbcn* and is essentially comprised of canted rows of RhS_6 clusters. As shown in the model of Figure 5.8, it does not possess direct Rh-Rh bonds, yet Figure 5.7 clearly shows an Rh-Rh peak reflecting the Rh particles formed from heating.

A representation of the monoclinic C*2/m* Rh_3S_4 cluster is shown in the top right of Figure 5.8. It is in this view that the intimate interrelationship of the Rh-S phases becomes apparent.

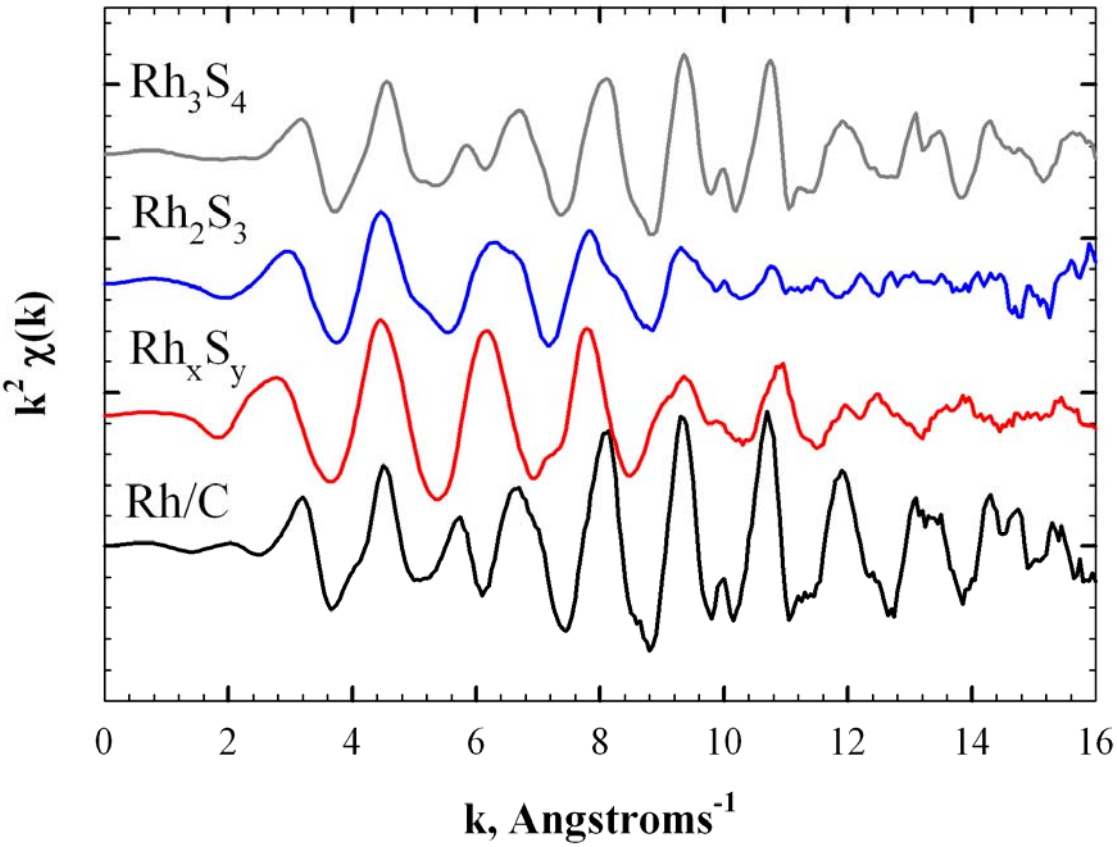

Figure 5.6. (k) spectra for the electrocatalysts in de-aerated 1 M TFMSA i*n situ* (0.40 V) Rh K edge (23220 eV). k^2-weighted χ

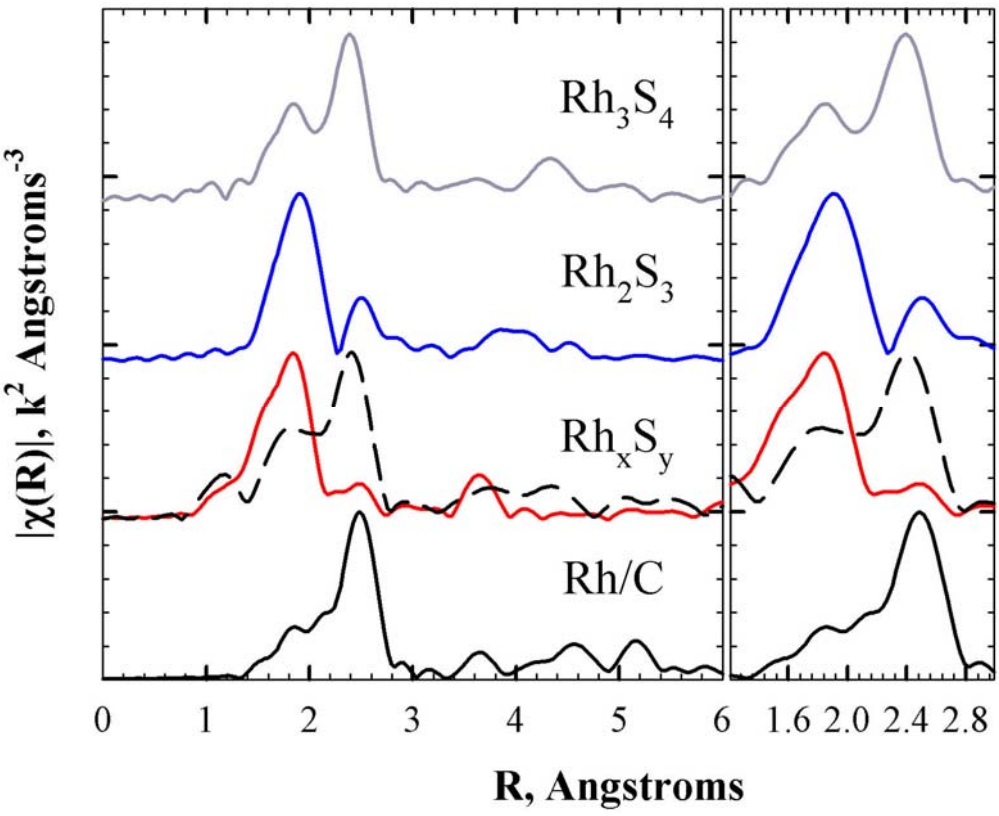

Figure 5.7. *In situ* (0.40 V), non phase-corrected, Rh K edge (23220 eV) k^2-weighted $|\chi(R)|$ spectra for the electrocatalysts in de-aerated 1 M TFMSA. The spectrum for Rh_xS_y at 0.40 V in de-aerated 6 M TFMSA is represented by the overlaid dashed line on the 1 M spectrum.

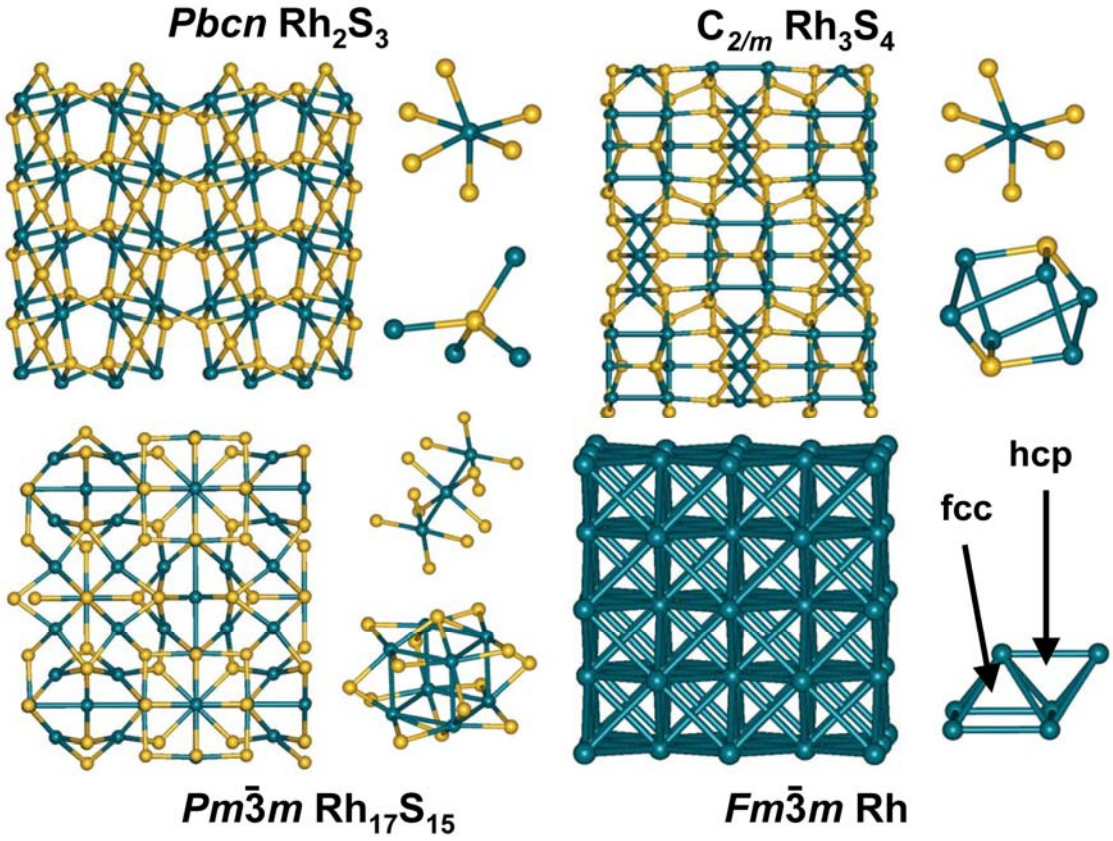

Figure 5.8. Three dimensional representations of the Rh-S phases and Rh metal: Rh (dark), sulfur (yellow). Clusters: (Top left) Rh_2S_3, RhS_6, and Rh_4S, (Top right) Rh_3S_4, RhS_6, and Rh_6S_2, (Bottom right) Rh, Rh_6 Janin cluster, (Bottom left) $Rh_{17}S_{15}$, RhS_4 chains, sulfided Rh_8 cube.

Indeed, the RhS_6 clusters that fully comprise the Rh_2S_3 crystal, are present as a sulfur-rich backbone in the Rh_3S_4 phase. To either side of the Rh_2S_3 backbone in the Rh_3S_4 material are canted metallic Rh_6 "octahedra". Thus, the extent of Rh-Rh bonding is much higher in this component than in the Rh_2S_3 backbone. The primitive cubic $Rh_{17}S_{15}$ (*Pm3m*) system is shown at the bottom right of Figure 5.8. This phase is comprised of two unique Rh-S domains: a series of RhS_4 "chains" and heavily sulfided cubes of Rh_8. Nevertheless, the magnitude of the Rh-Rh peak is much larger than expected for a pure Rh_3S_4 sample, and it too reflects the large Rh clusters existing in this sample. While $Rh_{17}S_{15}$ has been reported to act like a superconductor,[45,64] its metallic character is considerably lacking, no doubt in part to the magnitude of Rh-S interactions. Finally, a representation of face centered cubic Rh (*Fm3m*) is given at the bottom right of Figure 5.8, with an Rh_6 Janin-type[65] cluster showing fcc and hcp adsorption sites.[27,66]

The XRD (Rh metal peaks), TEM (visible black clusters), XANES (spectral signature) and EXAFS (Rh-Rh peaks in FT) data all show that the Rh_xS_y sample undergoes Rh metal particle growth with respect to increasing temperature, so that the Rh particle size increases in the order: $Rh_xS_y < Rh_2S_3 < Rh_3S_4$. This explains the Rh-Rh peak in the FT-EXAFS for the Rh_2S_3 (Rh-Rh distances do not exist in the pure crystalline Rh_2S_3 phase), and the very large Rh-Rh peak for in Rh_3S_4 (much larger than expected from the inherent Rh-Rh "coordination" in the pure Rh_3S_4 phase). Nevertheless it is instructive to fit the Rh-Rh and Rh-S peaks and Figure 5.9 presents a graphical representation of the high quality of these fits. Tables 5.3-5 present the fitting results over the entirety of the experimental electrochemical range for Rh_2S_3, Rh_3S_4, and Rh/C, respectively, and Figure 5.10 plots the change in $N_{Rh\text{-}Rh}$ ($\delta N = N(x\ V)-N(0.3V)$) for the Rh_3S_4 and Rh/C catalysts.

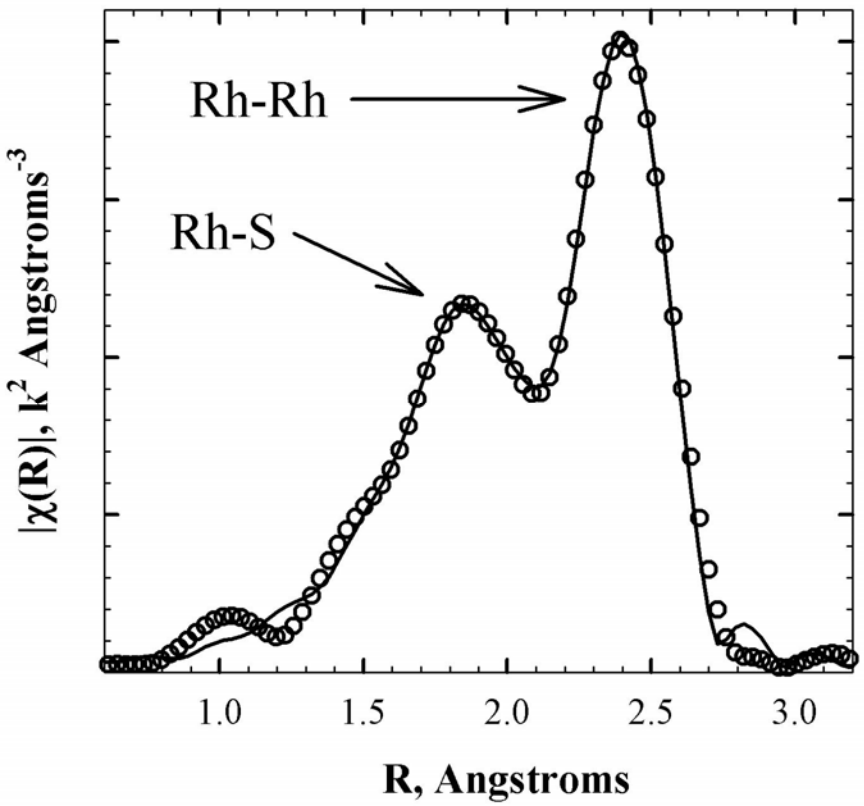

Figure 5.9. Comparison of the non phase-corrected k^2-weighted Fourier transform data for the Rh_3S_4/C preferential phase at 0.40 V in de-aerated 1 M TFMSA (○) and a two-shell (Rh-S and Rh-Rh) fit (-).

Table 5.3. First shell EXAFS fit results for Rh_2S_3/C

E, V vs. RHE	$N_{Rh\text{-}S}$[a], Å	$R_{Rh\text{-}S}$[a], Å	E_0, eV
0.30	2.52	2.320	-0.397
0.40	2.51	2.323	7.231
0.50	2.43	2.316	4.295
0.60	2.57	2.319	1.999
0.70	2.43	2.320	5.935
0.80	2.20	2.319	3.499
0.90	2.28	2.314	6.565
1.00	2.32	2.316	3.334

S_0^2 fixed at 0.921 as calculated via FEFF8.0, k range: 2.5-15.5 $Å^{-1}$ (k^2), R range: 1.8-3.3 Å. Gross errors: N ±20%, R ±0.02 Å.

[a]σ^2 fixed at 0.004 $Å^2$ f**rom Ref. 46.**

Table 5.4. First shell EXAFS fit results for Rh_3S_4/C

E, V vs. RHE	N_{Rh-Rh}[a]	R_{Rh-Rh}[a], Å	E_0, eV	N_{Rh-S}[b]	R_{Rh-S}[b], Å	E_0, eV
0.30	3.63	2.687	-1.642	1.82	2.331	-4.368
0.40	3.66	2.683	8.316	1.78	2.318	6.492
0.50	3.48	2.690	1.254	1.84	2.310	-1.305
0.60	3.64	2.686	2.114	1.85	2.318	0.683
0.70	3.45	2.690	1.415	1.81	2.307	-1.443
0.80	3.50	2.686	5.254	1.79	2.311	3.921
0.90	3.60	2.692	3.403	1.69	2.306	0.560
1.00	3.29	2.680	0.654	1.82	2.321	2.087

S_0^2 fixed at 0.921 as calculated via FEFF8.0, k range: 2.5-15 $Å^{-1}$ (k^2), R range: 1.8-3.4 Å. Gross errors: N ±20%, R ±0.02 Å.

[a]σ^2 fixed at 0.004 $Å^2$ from Ref. 44.

Table 5.5. First shell EXAFS fit results for Rh/C

E, V vs. RHE	N_{Rh-Rh}	R_{Rh-Rh}, Å	E_0, eV
0.30	7.75	2.683	-5.01
.040	7.77	2.682	-5.06
0.50	7.63	2.681	-2.98
0.60	8.27	2.682	-3.26
0.70	8.23	2.682	-4.77
0.80	7.92	2.683	-5.56
0.90	7.63	2.683	-4.31
1.00	7.40	2.682	-4.62
1.10	7.24	2.684	-4.04
1.20	7.00	2.684	-3.97

S_0^2 fixed at 0.921 as calculated via FEFF8.0, k range: 2.5-15 $Å^{-1}$ (k^2), R range: 1.8-3.0 Å. Gross errors: N ±20%, R ±0.02 Å. σ^2 fixed at 0.005 $Å^2$ from reported crystallographic data (JCPDF #01-1214).

The results for both the Rh_3S_4 and Rh/C catalysts in Figure 5.10 show a similar trend, an initial decrease, followed by an increase, and then a final decrease in δN. This strongly suggests that both results reflect the behavior of metallic particles, and hence that the EXAFS results for the Rh_3S_4 sample are dominated by the comparably large 100 nm Rh particles seen in the HRTEM and not that from the RhS phases. The initial decrease is due to water desorption (which we will confirm from the Δμ data below). In the absence of adsorbates we have noted many times previously that metallic particles (such as Pt and Ru) tend to flatten out to increase there interaction with the support, and thereby decrease the average $N_{Rh\text{-}Rh}$. Upon adsorption of atop OH, the Rh particles again become more round and the $N_{Rh\text{-}Rh}$ again increases. The final decrease is due to atop OH moving to 3-fold O (with loss of H) and even subsurface O which decreases the Rh-Rh scattering. We have seen the exact same trend with Pt many times previously.[2,28,31] The shift to higher potentials for the Rh_3S_4 sample suggests that the large 100 nm Rh particles in this case are much less reactive than the smaller particles in the Rh/C sample; the peak maximum due $O(H)/O_{sub}$ adsorption shifted from 0.65 to 0.9 V. This 250 mV shift on Rh is similar to a nearly 350 mV shift with Pt when going from small Pt particles to single crystal Pt(111).[67,68]

Finally the dramatic increase in the magnitude of the $N_{Rh\text{-}Rh}$ peak for the Rh_xS_y catalysts in 6 M TFMSA compared to in 1 M TFMSA (see Figure 5.7) suggests a substantial change in the Rh_xS_y catalyst in the presence of strong acid. Since large Rh particles are not visible in the TEM, but rather an over layer of some type is apparent on the Rh_xS_y sample even in 1M TFMSA, we suggest that S dissolution is occurring with the formation of an Rh skin. Analysis of the Δμ data below will confirm this.

The Rh_xS_y/C electrocatalyst was designed and optimized as an oxygen depolarized cathode (ODC) for electrolytic generation of chlorine gas from HCl feedstocks.[13,38] In this application, the cathode serves as a counter electrode to the important chlorine gas generating anode.[42,43] Reducing oxygen at the cathode lowers the overall cost of the process (by circa 700

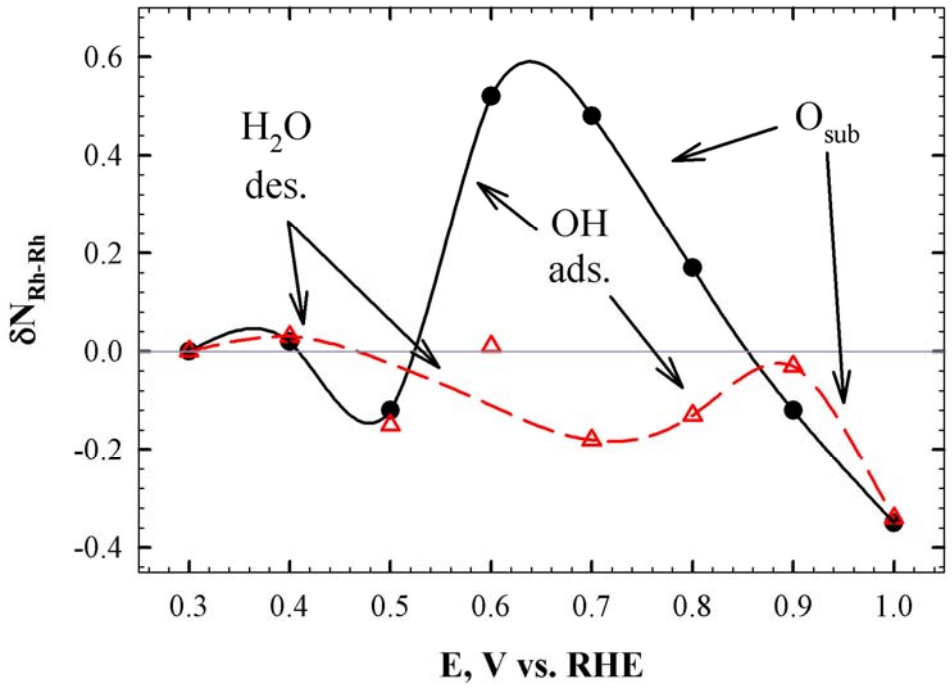

Figure 5.10. Plot of $\delta N_{Rh\text{-}Rh} = N_{Rh\text{-}Rh}(V) - N_{Rh\text{-}Rh}(0.30\ V)$ for Rh/C (●) and Rh_3S_4/C (Δ) in de-aerated 1 M TFMSA. The processes responsible for the variations in δN are indicated and discussed in the text.

Wh kg^{-1} chlorine gas), and presents a safe alternative to the dangerous production of hydrogen gas. To perform ORR in O_2-saturated 5 M HCl at temperatures of 80°C requires a material of exceptional stability. In a recent publication,[13] we evaluated Pt/C, Rh/C and traditional $M_xRu_yS_z$/C (M = Co, Mo, Rh, or Re) chalcogenide electrocatalysts produced by the traditional nonaqueous method[15] for ODC applications. These materials immediately suffered irreversible dissolution under these harsh environments. For the traditional chalcogenides, the sulfur essentially forms loose adlayers on the surfaces of nanoscopic metal particles which can be easily stripped from the particle surfaces.[4,13,17,39] In contrast, the De Nora Rh_xS_y/C electrocatalyst apparently forms a metallic layer in strong acid; albeit this layer is passivated with a layer of O(H) at nearly all potentials as we will see in the Δμ data. In the presence of HCl it is entirely possible that the metallic layer is covered with Cl ions in addition to the O(H) layer at some potentials, as is typical of Pt metal in the presence of Cl.[69] XAS studies of both Pt[70] and Rh_xS_y[71] catalysts in HCl are currently underway.

5.3.4 Δμ Analysis

5.3.4.1 Theoretical signatures

A proper interpretation of the experimental Δμ data below requires both an understanding of the change in magnitude and line shape with increase in electrochemical potential.[27,28,66] To understand the changes in lineshape, the FEFF8.0 program[56] was utilized to produce theoretical XANES spectra from crystallographic models of the electrocatalyst. Based on the crystallographic properties of the three Rh-S phases in the balanced phase Rh_xS_y/C electrocatalyst (Table 5.1), our initial communications[3,36] centered on the metallic C*2/m* Rh_3S_4 phase. The clusters, and their corresponding FEFF8.0-calculated Δμ spectra, are presented in Figure 5.11. The left side of this Figure provides another elegant example of the crystallographic interrelationship of the Rh_2S_3 and Rh_3S_4 phase. As described above, Rh_3S_4 is essentially comprised of an Rh_2S_3 backbone of RhS_6 pseudo-octahedra. These octahedra are connected by a disulfide bridge with canted metallic Rh_6 octahedra to either side.[44] Both chemical intuition and

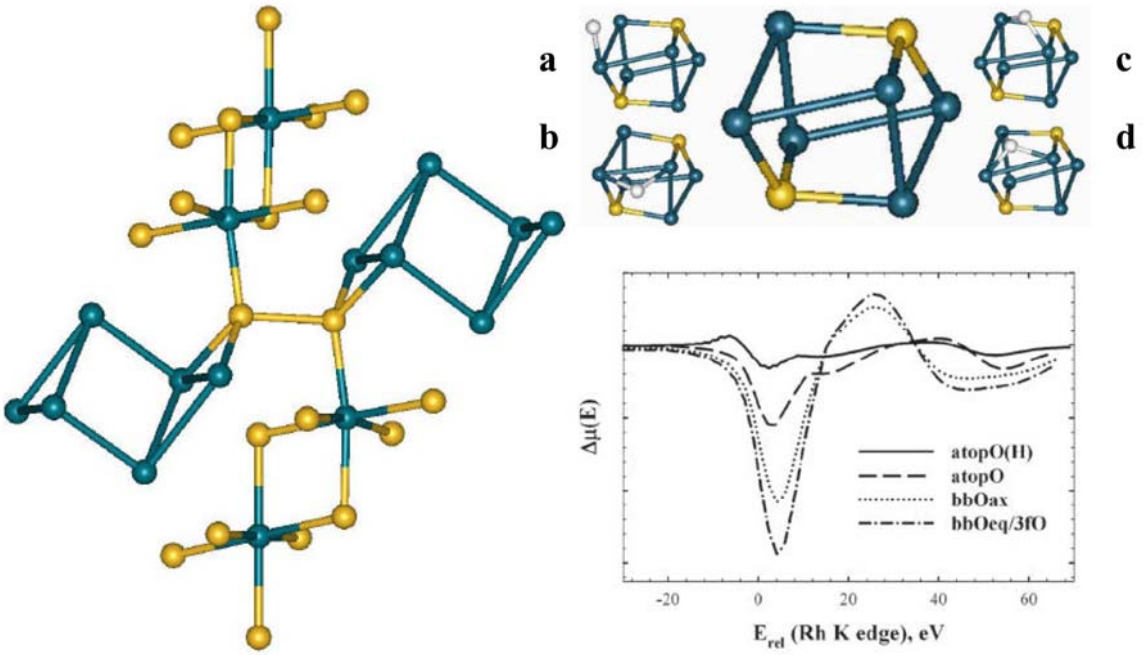

Figure 5.11. FEFF8.0-calculated $\Delta\mu = \mu(Rh_6S_2\text{-}O_{ads}) - \mu(Rh_6S_2)$ theory curves for C*2/m* Rh_3S_4 and the corresponding models. The Rhodium and sulfur atoms are colored dark and light, respectively, with oxygen appearing as the white orb in the FEFF cluster fragments. LEFT: Rh_3S_4 fragment displaying the metallic Rh_6 octahedra to either side of the (Rh_2S_3) backbone. TOP RIGHT: Rh_6S_2 pseudo-octahedral clusters: a) atopO, b) axial bridge-bonded O (bbOax), c) equatorial bridge-bonded O (bbOeq), d) 3-fold O (3fO), center: clean cluster. BOTTOM RIGHT: Rh K edge $\Delta\mu = \mu(Rh_6S_2\text{-}O_{ads}) - \mu(Rh_6S_2)$ signatures calculated with the FEFF8.0 code from the above clusters.

the reported density of states determinations[44] designate these metallic Rh_6 clusters as the most likely active site for $O(H)_{ads}$.

Figures 5.11a-d show the Rh_6 octahedra models utilized (with a "clean" cluster in the center) to generate the theoretical $\Delta\mu = \mu(Rh_6\text{-}O_{ads}) - \mu(Rh_6)$ curves at the bottom right. Figure 5.11a provides an example of 1-fold (i.e. "atop") O_{ads} on the Rh_6 cluster. Teliska *et al*., via density functional theory calculations,[28] showed that it is highly unlikely that molecular oxygen adsorption will occur via atop geometry, and this model therefore reflects the likely mode of either OH_{ads} resulting from water activation on the electrocatalyst surface or even of weakly chemisorbed H_2O.[32,34] Figures 5.11b-d show modes of n-fold O_{ads} (bridge-bonded and 3-fold, respectively). Comparison of the FEFF8.0-calculated $\Delta\mu$ spectra to the experimentally-derived spectra in the figures below will provide for an interpretation of the water activation process upon the different catalysts discussed in this work.

5.3.4.2 $\Delta\mu$ spectra for Rh_xS_y/C

Figure 5.12 shows the XANES spectra (μ) before subtraction and the resultant differences, $\Delta\mu = \mu(V)\text{-}\mu(0.40V)$, for the Rh_xS_y/C electrocatalyst in de-aerated 1 M TFMSA.. The sensitivity of the $\Delta\mu$ difference technique is clearly indicated here. It is not until a potential of 1.00 V is reached that the Rh K edge XANES (Figure 5.12, left) exhibits a clearly visible increase in the white line (at least to the naked eye), but the $\Delta\mu$ show systematic differences and lineshapes similar to the theory in Figure 5.11. Note that the noise levels in these difference spectra (smoothed with a 3 point (1.5 eV wide) Savitsky-Golay smoothing function) are still remarkably low. While it is impossible to state that the surface of the Rh_xS_y/C electrocatalyst is completely devoid of adsorbed species at 0.40 V, this potential represents the "cleanest" region between H_2O_{ads} and $O(H)_{ads}$ as we will show below. The surface sensitivity of the $\Delta\mu$ technique arises from the elimination of bulk, un-reacting species from the XANES signals through normalized subtraction.

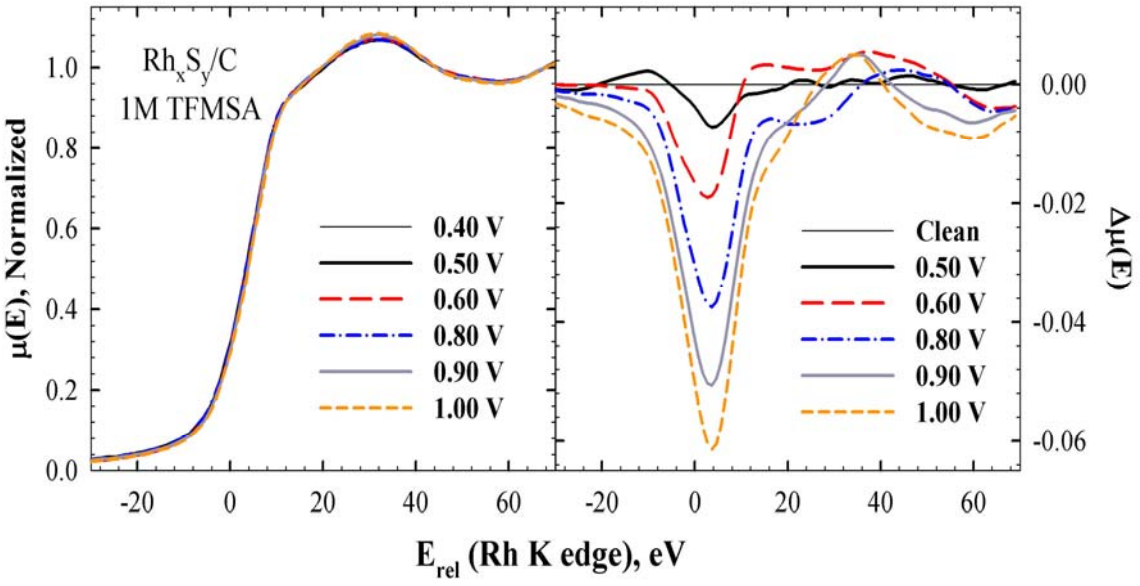

Figure 5.12. *In situ* Rh K edge XANES (left) and $\Delta\mu = \mu(V) - \mu(0.40\ V)$ (right) spectra for the De Nora 30wt% Rh_xS_y/C electrocatalyst in de-aerated 1 M TFMSA.

The Δμ results in Figure 5.12 for Rh_xS_y in 1 M TFMSA were the basis of our initial communications.[3,36] Below (Figures 5.13-15) we also present Δμ results for the Rh_2S_3, Rh_3S_4, Rh/C catalysts in 1 M TFMSA (and Rh_xS_y in 6 M TFMSA), to more fully understand the changes in the Δμ lineshapes. We also plot in Figure 5.16 the absolute magnitudes of the Δμ spectra around 0-3 eV to reflect the relative amount of O(H) on the surface. These magnitudes only qualitatively reflect the coverage because, as the coverage goes from atop OH to 3-fold O, the magnitudes of the Δμ signals per O adsorbate will change since the Rh-O coordination has changed. Further, the magnitudes of the Δμ will reflect the dispersion of the Rh in the various Rh clusters, and/or the extent of surface Rh atoms in the different RhS phases. Nevertheless; such a plot nicely summarizes the large amount of data (5 catalysts at several potentials) making it possible to see the trends, and the qualitative fits given in Figure 5.16 enable a qualitative understanding of why these magnitudes vary as they do.

5.3.4.3 Interpretation of the Δμ signatures

a. Rh/C: Comparison of the theoretical signatures and data in Figure 5.15 suggest predominantly atop OH below 0.7V and n-fold O well above. The EXAFS in Figure 5.10 gives some evidence also for subsurface O above 1.0 V as discussed above.

b. Rh_3S_4: Comparison of the theoretical signatures and data in Figure 5.14 (right) suggests atop O at all potentials. We suggest that below 0.7 V the magnitudes in Figure 5.16 reflect H_2O adsorption. This is strongly suggested by the lack of significant current below 0.7 V in the CV data shown on the curves other than "Rh", yet a significant Δμ intensity appears (current arises from oxidation, and chemisorbed water is not oxidized). Apparently a weakly bonded water double layer forms and then this double layer is disrupted prior to the adsorption of OH. We have seen this water double layer also on Pt in the potential range between 0.65 and 0.75 V with similar behavior (i.e. disruption before the onset of O(H)).[2,28] At 0.7 V all H_2O has desorbed and OH adsorbs above 0.7 V (see Figure 5.16).

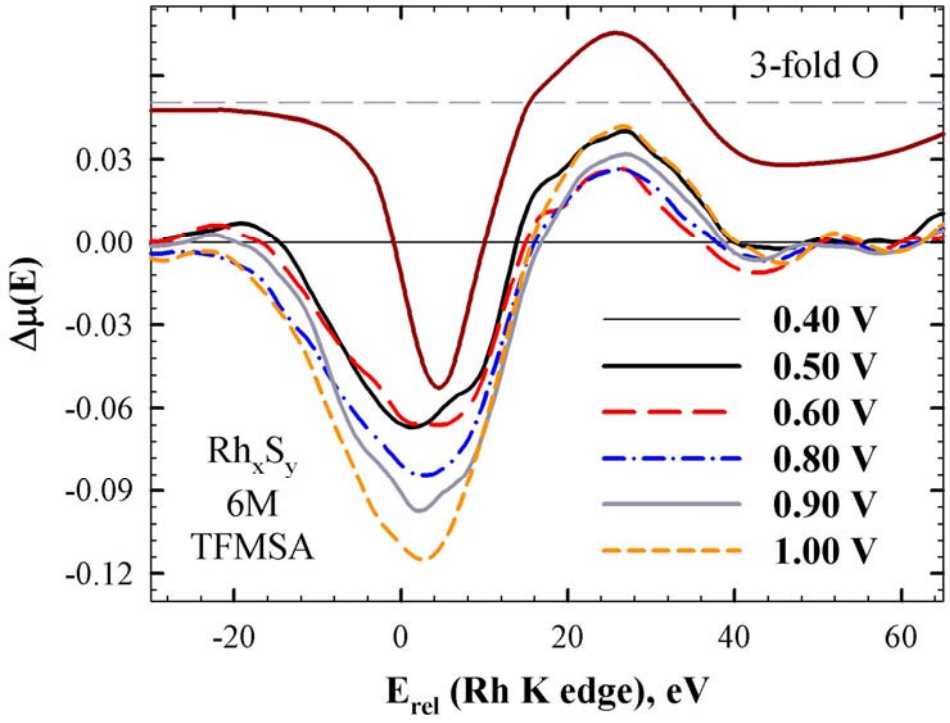

Figure 5.13. Experimental Rh K edge Δμ = μ(V) - μ(0.40 V) spectra for Rh_xS_y/C in de-aerated 6 M TFMSA (bottom) and comparison with theoretical n-fold O signature (top) from Figure 5.11.

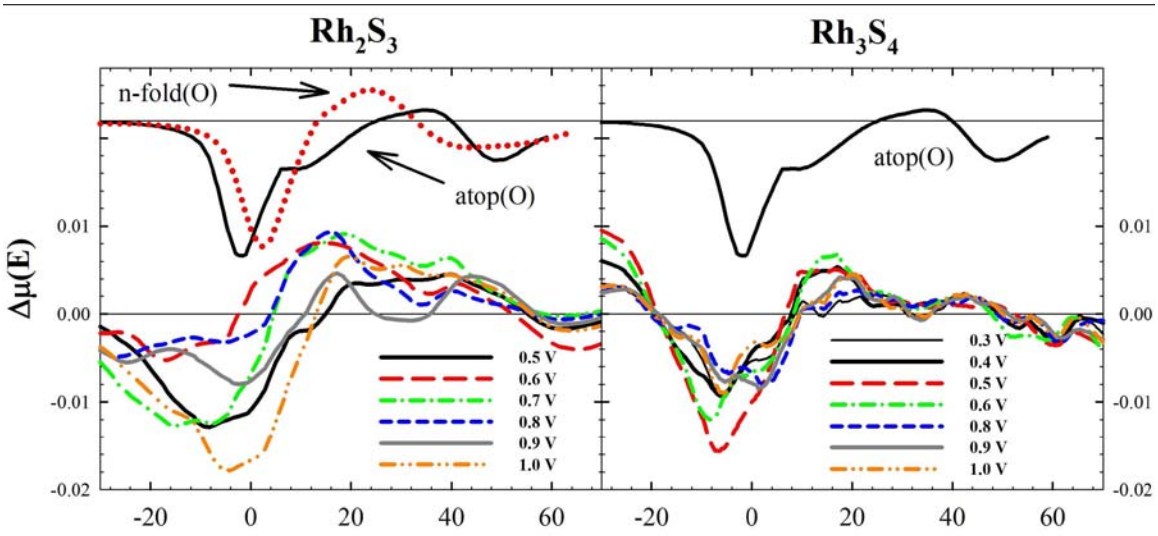

Figure 5.14 Rh K edge $\Delta\mu = \mu(V) - \mu(0.40\ V)$ signatures for the Rh_2S_3/C (left) and $\Delta\mu = \mu(V) - \mu(0.70V)$ for Rh_3S_4/C (right) preferential phases in de-aerated 1 M TFMSA. The theoretical signatures for the indicated 3-fold O and atop O(H) moieties from Figure 5.11 are also indicated.

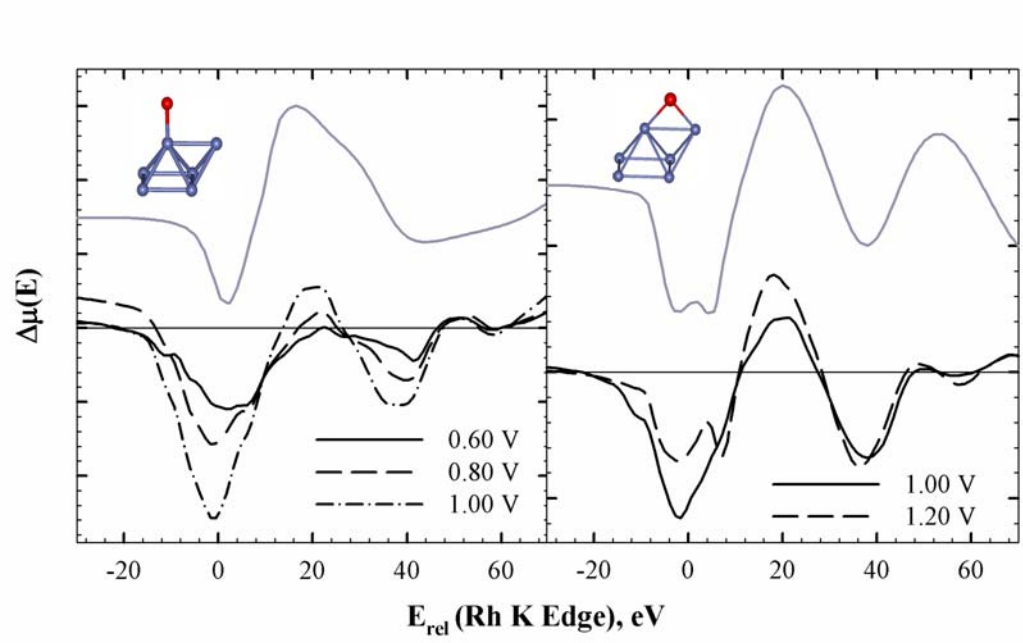

Figure 5.15. FEFF8.0-calculated $\Delta\mu = \mu(Rh_6\text{-}O_{ads}) - \mu(Rh_6)$ signals (grey) compared with experimental Rh/C $\Delta\mu$ spectra collected *in situ* in de-aerated 1 M TFMSA: (left) atop O(H), (right) n-fold (bbO) signals.

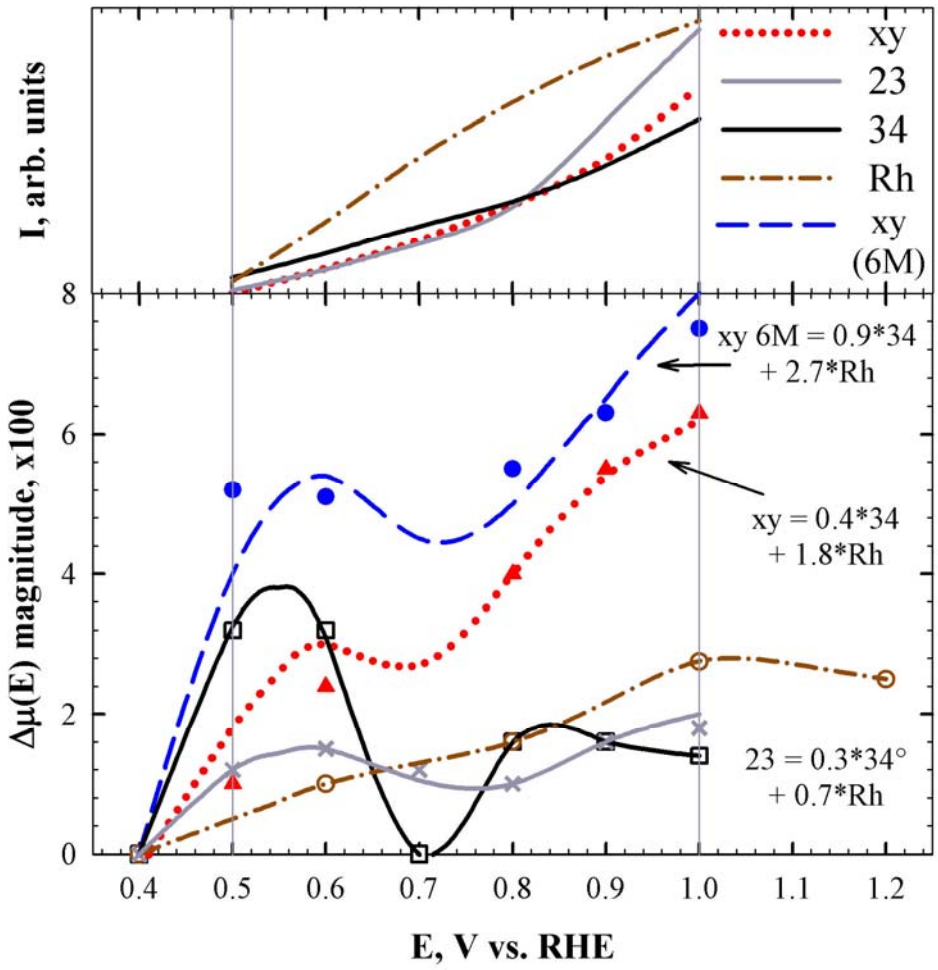

Figure 5.16. Plot of the Δμ amplitudes (between 0-3 eV) as a function of potential (denoted by the points) for the indicated Rh_nS_m catalysts (all in de-aerated 1 M TFMSA except for that indicated in 6 M TFMSA) and the corresponding CV curves from Figure 5.3 (top). Lines through the points are the optimal linear fits of the indicated components with coefficients as discussed in the text. Lines for Rh/C and Rh_3S_4 are simply drawn through the points.

c. Rh_2S_3: Again comparison with the theoretical signatures shown in Figure 5.14 suggests adsorption of atop O but which appears to convert to more n-fold O above 0.7 V. The evidence from the XRD, TEM and EXAFS analyses above, indicates that some Rh_2S_3 exists along with some small Rh metal particles, the Δμ is reflecting O(H)/Rh metal and some water on the Rh_2S_3 phase below 0.7 V. We estimate the magnitude of each of these components of each in Figure 5.16 by taking linear a combination of the Δμ water component on Rh_3S_4 (labeled 34° because it is only that part below 0.7 V) and the full O(H)/Rh metal Δμ amplitude, and determine the optimal linear fit. This fit is given in Figure 5.16 and denoted as 23 =.3*34°+.7*Rh, where we give only the nm indices to indicate the Δμ amplitude dependence for Rh_nS_m for brevity, and the numbers in front of the nm indicate the optimal coefficients. We believe the n-fold O comes from adsorption on Rh metal particles, as the Rh_2S_3 sample cannot dissociate water and only gives H_2O/Rh_2S_3 below 0.7 V.

d. Rh_xS_y in 1M TFMSA: The experimental signatures in Figure 5.12 for Rh_xS_y indicate atop O below 0.7 V and then an increasing component of n-fold O above 0.7 V. The amplitude trend shown in Figure 5.16 is remarkably similar to that for Rh/C except a bit larger. The latter suggest we are just seeing O(H)/Rh, but that is not consistent with the Δμ signatures (i.e., the Δμ's for Rh_2S_3 and Rh/C are quite different). Therefore we suggest we are seeing H_2O/Rh_xS_y and O(H)/Rh metal. A fit of the components suggest xy = 0.4*34+1.8*Rh. Note we do not use 34° here but 34 since we now used the amplitude over the entire range, below and above 0.7 V. We believe that some Rh_3S_4 phase is present in the Rh_xS_y sample so we use the entire amplitude trend to fit the Rh_xS_y trend in this case.

e. Rh_xS_y in 6M TFMSA: Finally the Δμ signatures for Rh_xS_y in 6 M TFMSA in Figure 5.13 suggests n-fold O at all potentials. We use the exact same components as for the Rh_xS_y in 1 M TFMSA and obtain the fit xy 6M/2 = .9*34° + 2.7*Rh. (Note we write xy 6M/2 because the experimental amplitudes in Figure 5.16 have been divided by 2 to place it on the same curve in the figure; it is not clear why the amplitudes are so large for the xy 6M). The very large

component of Rh metal now explains why the signature reflects n-fold O at all potentials (i.e. the Rh skin is more complete and thicker) and this layer is very reactive with n-fold O at all potentials.

5.3.4.4 Correlation of the Δμ spectra with the cyclic voltammetry results

Figure 5.16 also shows the magnitude of the CV curves from Figure 5.3 expanded in the range between 0.5 and 1.0 V. Above 0.7 V, the CV curves correlate with the component of Rh metal as found in the amplitude fits, that is the current follows the trend Rh > 23 > xy > 34. Recall that above 0.7 V, the Δμ amplitudes for the Rh_2S_3 preferential sample is dominated by the Rh metal component as the Rh_2S_3 phase above 0.7 V is actually inactive. The Rh_3S_4 phase has no O(H) present, except that occurring from the large Rh metal particles that have a relatively smaller surface area, so the CV curve reflects the Rh_3S_4 phase with little oxidation. The Rh_xS_y sample has the Rh partial skin, so it shows an appreciable current.

Not shown in Figure 5.16, but evident in Figure 5.3, the onset of the lowest slope at low potentials begins at 0.4 V for all but the Rh_3S_4 sample, consistent with the Δμ amplitudes. The onset Rh_3S_4 begins already at 0.25 consistent with the Δμ (we set it to zero at 0.4 in order to fit the other curves). Therefore the CV data is completely consistent with the Δμ amplitudes, where the current comes primarily from water oxidation to OH and O, not chemisorbed water; however, the thresholds and low currents at the lowest potentials probably does come from some charge transfer between the chemisorbed H_2O and the Rh.

5.4. Summary and Conclusions

5.4.1 Water Activation and Stability in TFMSA

The water activation behavior can be summarized as follows:

a. OH adsorption occurs well below 0.75 V on Rh/C. This is not surprising because pure Rh is very reactive and can dissociate water well below 0.75 V. However the huge 100 nm particles are much less reactive.

b. Water dissociation does not occur at all on the Rh_2S_3 and only above 0.75 V on the Rh_3S_4. The small amount of n-fold O(H) seen well above 0.75 V in the Rh_2S_3 case, we believe occurs due to the smaller Rh particles resulting from the heating.

c. The Δμ amplitude trends for the Rh_2S_3 and Rh_3S_4 are very different from that for Rh. This suggests strongly that the Rh_2S_3 and Rh_3S_4 are stable to the 1M TFMSA. In contrast, the Δμ amplitude trend for the Rh_xS_y is remarkably similar to that for Rh/C, except for the larger overall magnitude (although the signatures for Rh and Rh_xS_y are quite different). This suggests that a very thin layer of Rh lies over the Rh_xS_y sample (i.e. S dissolution also occurred in the 1 M but less so). Its presence is not visible in the N_{Rh-Rh} EXAFS because of the very thin layer, but is indeed visible in the data for Rh_xS_y in the 6M TFMSA as discussed above.

5.4.2 ORR Reactivity

The ORR reactivity can be summarized as below:

a. The ORR reactivity on all samples takes off only below 0.75 V. This is where all Δμ data and the CV's show a second onset (Figure 5.16), and this onset arises from O(H) adsorption. Therefore O(H) adsorption (oxidation) clearly poisons ORR on RhS and O oxide formation on Rh.

b. OH adsorption occurs well below 0.75 V on Rh as stated above, because Rh is very reactive. Indeed this OH is now needed to "tame" the reactivity of Rh so that ORR can occur. In this regard, the ORR on Rh is not that different from ORR on the RhS samples, except now the Rh is "tamed" by the O(H) rather than by the S. It would appear partial coverage of the Rh surface by the OH is needed, but when it goes subsurface to form the oxide, the reactivity ceases (hence its onset at 0.75 V).

c. The ORR reactivity of the Rh_3S_4 sample apparently is occurring on the small Rh_6 moieties present in the crystalline Rh_3S_4 sample.

d. The ORR reactivity on the Rh_xS_y could be occurring either because of the presence of the Rh_3S_4 phase or Rh metal on the surface or both. The Δμ data suggest a Rh layer at the surface

as described above, but certainly the Rh_3S_4 phase can also contribute. The component fits to the amplitude curve reflect water activation on both, and ORR on both is clearly occurring (the Rh_3S_4 sample is equally ORR reactive).

e. The apparent greater Tafel slope for the Rh_2S_3 and Rh_3S_4 samples could arise from a number of factors: 1) increasing coverage of water seen directly in the $\Delta\mu$ as the potential decreases, 2) larger resistance in the cell, or 3) a different charge transfer mechanism (i.e. a different charge transfer coefficient). In the first mechanism chemisorbed water slows the exchange rate of the rds in the ORR. The fact that the slope for the Rh and Rh_xS_y is similar gives more evidence for the importance of the Rh surface layer on the Rh_xS_y clusters and that it could be dominating the ORR. In mechanism 2, the Rh-S phases have larger resistance than the Rh metal (Rh/C or the Rh skin on the Rh_xS_y sample). Finally, it is possible that the charge transfer coefficient is simply a bit larger for the Rh_2S_3 and Rh_3S_4 samples, reflecting a slightly different point where the electron transfer occurs.

5.4.3 Summary

Finally the following general conclusions can be drawn:

a. Heating causes Rh segregation and the formation of Rh metal particles. TFMSA causes S dissolution and the formation of a Rh skin on the Rh_xS_y samples, but not on the Rh_2S_3 and Rh_3S_4 preferential samples (the prior heating process has made them stable to TFMSA).

b. At least some Rh-Rh interaction is needed to carry out the ORR. This is present in the Rh_3S_4 sample on the Rh_6 moieties in the sample, and Rh_3S_4 is present in the Rh_xS_y sample, but the Rh skin resulting from dissolution of S in the TFMSA may be (probably is dominating) in this case. However, the Rh_3S_4 preferential sample is nearly equally reactive for the ORR.

5.5 Conclusion

This report builds on the initial XANES $\Delta\mu$ studies[3,36] of the mixed-phase Rh_xS_y/C (De Nora) chalcogenide electrocatalyst system, which yielded preliminary information regarding the

water activation pathway via theoretical investigations of the metallic Rh_3S_4 phase. In the present report, a more comprehensive picture is presented using preferential phases Rh_2S_3 and Rh_3S_4. These results indicate that our previous conclusions were correct, and that Rh_3S_4 serves as the active phase in the Rh_xS_y electrocatalyst system. As indicated earlier, the metallic Rh_6 octahedra in the Rh_3S_4 serve as an active site for ORR. However, the results of the 6M TFMSA study indicate that Rh_3S_4 has an additional active site: a metallic self-generating Rh layer. While both phases are active for ORR, the results indicate that the brunt of the reactivity is attributable to the metallic Rh layer. Direct spectroscopic observation of these dual sites was accomplished through the application of the Δμ technique of XANES analysis to *in operando* catalyst systems.

5.6 References

[1]Ross, P. N. The Science of Electrocatalysis on Bimetallic Surfaces. In *Electrocatalysis*; Lipkowski, J., Ross, P. N., Eds.; Wiley-VCH: New York, 1998; pp 43.

[2]Teliska, M.; Murthi, V. S.; Mukerjee, S.; Ramaker, D. E. *J. Electrochem. Soc.* **2005**, *152*, A2159.
[3]Ziegelbauer, J. M.; Gatewood, D.; Gullá, A. F.; Ramaker, D. E.; Mukerjee, S. *Electrochem. Solid-State Lett.* **2006**, *9*, A430.
[4]Ziegelbauer, J. M.; Murthi, V. S.; O'Laoire, C.; Gullá, A. F.; Mukerjee, S. *Electrochim. Acta* **2008**, *53*, 5587.
[5]Ziegelbauer, J. M.; Olson, T. S.; Pylypenko, S.; Alamgir, F.; Jaye, C.; Atanassov, P.; Mukerjee, S. *J. Phys. Chem. C* **2008**, *112*, 8839.
[6]Alonso-Vante, N. Novel nanostructured material based on transition-metal compounds for electrocatalysis. In *Catalysis and Electrocatalysis at Nanoparticle Surfaces*; Wieckowski, A., Savinova, E. R., Vayenas, C. G., Eds.; Marcel Dekker: New York, 2003; pp 931.
[7]Vante, N. A.; Tributsch, H. *Nature* **1986**, *323*, 431.
[8]González-Huerta, R. G.; Chávez-Carvayar, J. A.; Solorza-Feria, O. *J. Power Sources* **2006**, *153*, 11.
[9]Shukla, A. K.; Raman, R. K. *Annu. Rev. Mater. Res.* **2003**, *33*, 155.
[10]Reeve, R. W.; Christensen, P. A.; Dickinson, A. J.; Hamnett, A.; Scott, K. *Electrochim. Acta* **2000**, *45*, 4237.
[11]Reeve, R. W.; Christensen, P. A.; Hamnett, A.; Haydock, S. A.; Roy, S. C. *J. Electrochem. Soc.* **1998**, *145*, 3463.
[12]Tributsch, H.; Bron, M.; Hilgendorff, M.; Schulenburg, H.; Dorbandt, I.; Eyert, V.; Bogdanoff, P.; Fiechter, S. *J. Appl. Electrochem.* **2001**, *31*, 739.
[13]Ziegelbauer, J. M.; Gullá, A. F.; O'Laoire, C.; Urgeghe, C.; Allen, R. J.; Mukerjee, S. *Electrochim. Acta* **2007**, *52*, 6282.
[14]Schulenburg, H.; Hilgendorff, M.; Dorbandt, I.; Radnick, J.; Bogdanoff, P.; Fiechter, S.; Bron, M.; Tributsch, H. *J. Power Sources* **2005**, *155*, 47.
[15]Solorza-Feria, O.; Ellmer, K.; Giersig, M.; Alonso-Vante, N. *Electrochim. Acta* **1994**, *39*, 1647.
[16]Bastide, S.; Levy-Clement, C.; Albu-Yaron, A.; Boucher, A. C.; Alonso-Vante, N. *Electrochem. Solid-State Lett.* **2000**, *3*, 450.
[17]Dassenoy, F.; Vogel, W.; Alonso-Vante, N. *J. Phys. Chem. B* **2002**, *106*, 12152.
[18]Fan, Q.; Pu, C.; Ley, K. L.; Smotkin, E. S. *J. Electrochem. Soc.* **1996**, *143*, L21.
[19]Fan, Q.; Pu, C.; Smotkin, E. S. *J. Electrochem. Soc.* **1996**, *143*, 3053.
[20]Marković, N. M.; Lucas, C. A.; Rodes, A.; Stamenković, V.; Ross, P. N. *Surf. Sci.* **2002**, *499*, L149.
[21]Stamenković, V. C.; Arenz, M.; Lucas, C. A.; Gallagher, M. E.; Ross, P. N.; Marković, N. M. *J. Am. Chem. Soc.* **2003**, *125*, 2736.
[22]Villegas, I.; Weaver, M. J. *J. Chem. Phys.* **1994**, *101*, 1648.
[23]Christensen, P. A.; Hamnett, A.; Weeks, S. A. *J. Electroanal. Chem.* **1998**, *250*, 127.
[24]Mukerjee, S. In-Situ X-Ray Absorption Spectroscopy of Carbon-Supported Pt and Pt-Alloy Electrocatalysts: Correlation of Electrocatalytic Activity with Particle Size and Alloying. In *Catalysis and Electrocatalysis at Nanoparticle Surfaces*; Wieckowski, A., Savinova, E. R., Vayenas, C. G., Eds.; Marcel Dekker: New York, 2003; pp 501.
[25]McBreen, J.; O'Grady, W. E.; Pandya, K. I.; Hoffman, R. W.; Sayers, D. E. *Langmuir* **1987**, *3*, 428.
[26]Russell, A. E.; Maniquet, S.; Mathew, R. J.; Yao, H.; Roers, M. A.; Thompsett, D. *J. Power Sources* **2001**, *96*, 226.
[27]Teliska, M.; O'Grady, W. E.; Ramaker, D. E. *J. Phys. Chem. B* **2004**, *108*, 2333.

[28]Teliska, M.; O'Grady, W. E.; Ramaker, D. E. *J. Phys. Chem. B* **2005**, *109*, 8076.
[29]Roth, C.; Benker, N.; Buhrmester, T.; Mazurek, M.; Loster, M.; Fuess, H.; Koningsberger, D. C.; Ramaker, D. E. *J. Am. Chem. Soc.* **2005**, *127*, 14607.
[30]Scott, F. J.; Mukerjee, S.; Ramaker, D. E. *J. Electrochem. Soc.* **2007**, *154*, A396.
[31]Teliska, M.; Murthi, V. S.; Mukerjee, S.; Ramaker, D. E. *J. Phys. Chem. C* **2007**, *111*, 9267.
[32]Murthi, V. S.; Urian, R. C.; Mukerjee, S. *J. Phys. Chem. B* **2004**, *108*, 11011.
[33]Anderson, A. B.; Neshev, N. M.; Sidik, R. A.; Shiller, P. *Electrochim. Acta* **2002**, *47*, 2999.
[34]Anderson, A. B.; Roques, J.; Mukerjee, S.; Murthi, V. S.; Markovic, N. M.; Stamenkovic, V. *J. Phys. Chem. B* **2005**, *109*, 1198.
[35]Mukerjee, S.; Urian, R. C. *Electrochim. Acta* **2002**, *47*, 3219.
[36]Ziegelbauer, J. M.; Gatewood, D.; Ramaker, D. E.; Mukerjee, S. *ECS Trans.* **2006**, *1*, 119.
[37]ChemicalProcessing.com. Bayer charges ahead with novel cathode; ChemicalProcessing.com, 2006.
[38]Gullá, A. F.; Gancs, L.; Allen, R. J.; Mukerjee, S. *Appl. Catal. A: General* **2007**, *326*, 227.
[39]Cao, D.; Wieckowski, A.; Inukai, J.; Alonso-Vante, N. *J. Electrochem. Soc.* **2006**, *153*, A869.
[40]Johnson-Matthey. The Platinum Metals Report: May 2008. In *The Platinum Metals Report*; www.platinum.matthey.com, 2008; Vol. 2008.
[41]Papageorgopoulos, D. C.; Liu, F.; Conrad, O. *Electrochim. Acta* **2007**, *52*, 4982.
[42]Gestermann, F. "Oxygen Depolarized Cathodes in the Chlor Alkali Electrolysis - on the Way to Industrial Application"; Electrolysis in the Chemical Industry, 1998, Clearwater Beach, FL.
[43]Gestermann, F.; Ottaviani, A. *Mod. Chlor-Alkali Tech.* **2001**, *8*, 49.
[44]Beck, J.; Hilbert, T. *Z. Anorg. Allg. Chem.* **2000**, *626*, 72.
[45]Geller, S. *Acta Cryst.* **1962**, *15*, 1198.
[46]Parthe, E.; Hohnke, D. K.; Hulliger, F. *Acta Cryst.* **1967**, *23*, 832.
[47]Enayetullah, M. A. The Role of Electrolyte in Oxygen Electroreduction Catalysis. Ph.D., Case Western Reserve University, 1986.
[48]Allen, R. J.; Giallombardo, J. R.; Czerwiec, D.; De Castro, E. S.; Shaikh, K. Rhodium electrocatalyst and method of preparation; De Nora S.p.A: US, 2000; pp 14.
[49]Allen, R. J.; Giallombardo, J. R.; Czerwiec, D.; De Castro, E. S.; Shaikh, K. Rhodium electrocatalyst and method of preparation; De Nora S.p.A.: US, 2002.
[50]Allen, R. J.; Gullá, A. F. Synthesis of noble metal sulfide catalysts in a sulfide ion-free aqueous environment; De Nora Elettrodi S.p.A.: US, 2005; pp 15.
[51]Enayetullah, M. A.; DeVilbiss, T. D.; Bockris, J. O. M. *J. Electrochem. Soc.* **1989**, *136*, 3369.
[52]Paulus, U. A.; Schmidt, T. J.; Gasteiger, H. A.; Behm, R. J. *J. Electroanal. Chem.* **2001**, *495*, 134.
[53]Bard, A. J.; Faulkner, L. F. *Electrochemical Methods: Fundamentals and Applications*, 2 ed.; Wiley: New York, 2001.
[54]Newville, M. *J. Synchrotron. Radiat.* **2001**, *8*, 322.
[55]Chen, M. H.; Crasemann, B.; Mark, H. *Phys. Rev. A* **1981**, *24*, 177.
[56]Ankudinov, A. L.; Ravel, B.; Rehr, J. J.; Conradson, S. D. *Phys. Rev. B* **1998**, *58*, 7565.
[57]Horanyi, G.; Rizmayer, E. M. *J. Electroanal. Chem.* **1986**, *198*, 379.
[58]Hourani, M.; Weickowski, A. *J. Electroanal. Chem.* **1988**, *244*, 147.
[59]Marković, N. M.; Ross, P. N. *Surf. Sci. Rep.* **2002**, *45*, 117.
[60]Damjanovic, A.; Brusic, V. *Electrochim. Acta* **1967**, *12*, 615.
[61]Damjanovic, A.; Grenshaw, M. A.; Bockris, J. O. M. *J. Phys. Chem.* **1966**, *70*, 3761.
[62]Koningsberger, D. C.; Mojet, B. L.; van Dorssen, G. E.; Ramaker, D. E. *Top. Catal.* **2000**, *10*, 143.
[63]Mukerjee, S.; Srinivasan, S.; Soriaga, M. P.; McBreen, J. *J. Phys. Chem.* **1995**, *99*, 4577.
[64]Nagata, S.; Atake, T. *J. Therm. Anal. Calor.* **1999**, *57*, 807.
[65]Janin, E.; von Schenck, H.; Göthelid, M.; Karlsson, U. O. *Phys. Rev. B* **2000**, *61*, 13144.
[66]Ramaker, D. E.; Koningsberger, D. C. *Phys. Rev. Lett.* **2002**, *89*, 139701.

[67]Garsany, Y.; Baturina, O. A.; Swider-Lyons, K. *J. Electrochem. Soc.* **2007**, *154*, B670.
[68]Gatewood, D. S.; Schull, T. L.; Baturina, O. A.; Pietron, J. J.; Garsany, Y.; Swider-Lyons, K.; Ramaker, D. E. *J. Phys. Chem. B* **2008**, *112*, 4961.
[69]Schmidt, T. J.; Paulus, U. A.; Gasteiger, H. A.; Behm, R. J. *J. Electroanal. Chem.* **2001**, *508*, 41.
[70]Arruda, T. M.; Shyam, B.; Ziegelbauer, J. M.; Mukerjee, S.; Ramaker, D. E. *J. Phys. Chem. C* **2008**, *accepted*.
[71]Korovina, A.; Ziegelbauer, J. M.; Mukerjee, S.; Ramaker, D. E. *(in preparation)*.

Chapter 6

Elucidation of the Mechanism for Sulfur Oxidation on Pt and Pt_3Co Electrocatalysts using *in situ* X-ray Absorption Spectroscopy

6.1 Introduction

Fuel cells utilized in practical applications are often required to maintain successful operation for long periods of time, sometimes months and even years. One drawback of proton exchange membrane fuel cells (PEMFCs) containing Pt is that they can be easily poisoned. Specifically, they passivate, and a drop in power occurs in the presence of certain materials. Most often this concern has been concentrated on the poisoning of the anode due to CO poisoning from parts per million (ppm) CO in the hydrogen fuel such as in reformate[1], or in a direct methanol fuel cell[2]. However, other poisons can exist in hydrocarbon fuels, and the cathode catalyst fed oxygen from the air can easily be poisoned from typical air-borne species. Air-borne poisons such as sulfur dioxide (SO_2), nitrogen dioxide (NO_2), and various organic contaminants can poison Pt-containing cathodes in fuel cells, and thereby dramatically decrease their efficiency.[3,4,5]

6.1.1 S poisoning

This work will concentrate on S poisoning and how to remove it. Sulfur containing species are a

common poison of Pt electrodes both in fuel hydrocarbons and air.[6] When platinum is exposed to any form of sulfur, active sites on the metal surface are blocked, which therefore hinders both the hydrogen oxidation reaction (HOR) at the anode and oxygen reduction reaction (ORR) at the cathode resulting in lower fuel cell current densities.[7,8]

In an effort to understand the complex behavior sulfur exhibits when poisoning a Pt surface, many S poisoning studies have been conducted. A good review of these early electrochemical studies has been given by Quijada et al. [9] It has been found that sulfur can be removed from Pt via electro-oxidation at high potentials presumably to sulfate (SO_4^{2-}) or bisulfate (HSO_4^{2-}) in solution.[9,10,11] These studies are typically done in an electrochemical environment without spectroscopic support, and thus speciation of the SO_x (x = 0 to 4) adsorption on the Pt surface is not clear. While these electrochemical cyclic voltammetry studies can determine the total charge density of adsorbed species resulting from S, and can therefore suggest something about the S coverage assuming some oxidation state, they do not allow clear determination of the coverages of different adsorbed anions (e.g., S^0, SO_2, SO_3^{2-}, and SO_4^{2-})[12,13], and even the S coverage may be in error. For example, Loučka[14], when studying S oxidation on Pt with cyclic voltammetry, indicated an oxidation product can be formed that is poorly reducible. He further concluded that the poorly reducible oxide can become reducible in the H region, while an easily reducible oxide leaves the electrode, and suggested that the poorly reduced oxide involved an oxide of Pt. Our results will confirm that the poorly reducible oxide is adsorbed and/or sub-surface OH and O on Pt, and the easily reducible oxide is $SO_{3/4}$, and these will be separately monitored as a function of potential using the $\Delta\mu$ XANES technique in this work.

Using electrochemical studies along with spectroscopic techniques still leaves the SO_x adsorbate speciation unclear. Quijada et. al., utilizing *in situ* Fourier transform infrared spectroscopy (FTIR), suggested that in the potential range from 0.55 to 1.50 V, SO_4^{2-} and SO_2 are the only S containing species on polycrystalline Pt[41]. Others have used coloumetric coverage analysis[15,16] and competing anion adsorption[17] to specify some type of sulfate or bisulfate

chemisorption; however, no direct molecular speciation or exact adsorption site has been determined from these studies.

Not only the speciation of S, but even the binding of SO_4 on Pt has been controversial. *In situ* FTIR and infrared reflection spectroscopy have both been incorporated to study adsorption of sulfate or bisulfate (referred to here as (bi)sulfate since it is not clear which) on Pt surfaces[18,19,20,21]. These studies have shown that the degree of sulfur adsorption is very much dependent on the structural characteristics of the Pt surface. Most studies have agreed that (bi)sulfate adsorbs onto a Pt (111) surface via three oxygen atoms, this site producing a single band at around 1270 cm^{-1}.[22] Another study concluded that (bi)sulfate prefers a two-fold bridged coordination with its oxygen atoms on a Pt (110) surface[23]. Still other FTIR studies suggested either an "upright" three oxygen atom binding to Pt or an "inverted" SO_4 with one O atom binding in the double layer region, and even SO_4 on top of OH (i.e. Pt-OH-O-SO_3) in the oxygen region[24]. Finally Thomas et al[25], using FTIR, suggested upright bisulfate in the double layer region (0.4-0.8V) and an inverted orientation with the OH down when above 0.8 V. However, these sites are not conclusive due to controversy over the assignment of the IR bands. One study proposed that the band at 1270 cm^{-1} was not due to (bi)sulfate but from of an H_3O^+-SO_3 complex[26, 27]. Another study concluded that the band appears to be due to an S-O stretch arising from a non-coordinated SO bond of adsorbed (bi)sulfate[28].

Radiotracer studies by Wieckowski[29,30] have shown more detailed proof of (bi)sulfate coverage with potential, but no information on the binding site. A radioactive isotope of S was used to label the (bi)sulfate and the resulting magnitude of radioactivity coming off the surface was measured. It was found that (bi)sulfate adsorption coverage was higher on Pt (111)[31] and Pt (100)[32] surfaces than Pt (110) faces[33]. Polycrystalline Pt showed a decrease in the amount of adsorbed (bi)sulfate compared to single crystals[34]. These studies have shown that the magnitude of adsorption is dependent on potential for both single and polycrystalline structures, and they show an increase in regions where H, O, and OH species are usually not found to adsorb. For

example, a radiotracer study showed that the maximum coverage occurred at 0.60V vs. RHE[35]. In contrast, a study using Auger electron spectroscopy (AES) in UHV (i.e. in the absence of O and OH) showed that adsorption falls off only beyond 0.92V vs. RHE, independent of sulfur concentration,[36] confirming the apparent displacement of bi(sulfate) by the more strongly bonding OH or O above 0.7 V. A study using *in situ* (i.e. in water*)* scanning tunneling microscopy (STM)[37]confirmed that the maximum adsorption occurs between 0.50-0.70V vs. RHE, however surprisingly *in situ* (i.e. in water) FTIR showed it increased all the way up to 1.40V vs. RHE. New interpretations of Electrochemical Quartz Crystal Nanobalance (EQCN) data[38] confirm that (bi)sulfate leaves the surface upon monolayer adsorption of O or OH. Recent XAS data indicate that (bi)sulfate does not bind in a specific site sufficient to be seen by the electron scattering that provides the signal in XAS, but upon a small adsorption of OH, the (bi)sulfate is apparently forced into a specific site making it visible[39]. Thus the (bi)sulfate is still clearly on the surface upon initial adsorption of OH, but upon monolayer OH(O) adsorption, it is apparently forced off.

All of these latter studies involved (bi)sulfate species adsorbing on a Pt surface. This is mainly due to the fact that the (bi)sulfate was obtained from the electrolyte being used, mainly H_2SO_4 or TFMSA, i.e., from S already in an oxidized SO_4-like state. But there are less details on what types of sulfur species are formed with respect to potential when the S is deposited in a reduced state such as S^o or SO_2. The studies, as summarized above, have provided much information dependent on potential, but they have not provided much explanation on the specific SO_x ($x < 4$) speciation and adsorption sites.

Theoretical calculations have been of some help in this regard. Lin et al.[40, 41, 42] have recently performed theoretical calculations using density functional theory (DFT) on S and SO_x ($x = 2$ and 3) adsorption on Pt (111) surfaces. Using DFT, they were able to determine the most thermodynamically stable orientation and geometric binding site for the S species. Their results show that S prefers to bind to Pt(111) at relatively low coverage (1/4 ML where 1 ML equal 1 S

per Pt atom) in an 3-fold fcc site; however, above 1/3 ML the S prefers the atop site. At ¼ ML, SO_2 bonds in an $\eta^2S_bO_a$ site, SO_3 in an $\eta^3S_aO_aO_a$ site, and SO_4 in $\eta^3O_aO_aO_a$ site where η refers to the number of atoms bound to the Pt surface and the subscripts and 'a', 'b' and 'f' refer to atop, bridged and 3-fold fcc sites, respectively. The binding energies obtained by Lin et al are shown in Fig. 1. The binding energy is greater than 100 kJ/mol for each of the oxidized S species shown, which might leave one to wonder how SO_x can ever leave the surface. However, the binding energies are generally much less then those in Fig. 1 because of very strong lateral interactions existing between adsorbed species even at ¼ ML as calculated by Lin et al[41]In the presence of high OH and O coverage, which usually exist from water activation in an electrochemical or fuel cell environment at the potential where SO_2 is oxidized, lateral interactions, are expected to be even stronger. Finally DFT calculations for S/Pt and Pt_3Ni [43] have recently been reported which show that S binds covalently to Pt, with the binding energy decreasing in the order S > H > OH, and that all species bind more tightly on Pt(111) than on $Pt_3Ni(111)$. Although these DFT results are quite helpful in sorting out the preferred binding sites and SO_x speciation on clean Pt, the presence of adsorbed O and OH at the potentials where SO_2 is oxidized makes the situation complex. Very few calculations have been given under these conditions.

6.1.2 S Removal

Not only is the SO_x speciation and adsorption sites on Pt or on OH/Pt a bit controversial, but the best way to clean the surface of adsorbed S species is not clear. Perhaps the most basic questions arising are; Why can't all of the S species be removed by one voltammetric oxidization cycle? What does the amount of S removed in each cycle depend on?

Recently, rotating disk electrode (RDE) cyclic voltammetry studies showed that the ORR activity on a Pt electrode decreased by 95% for S coverages of just 14%[44]. Figure 6.2 shows that it takes nearly 8 voltammetric cycles to fully oxidize this sulfur off the Pt surface. Large

coverage of sulfur on Pt causes the 4-electron ORR (eq. 6.1) pathway to convert to a 2-electron

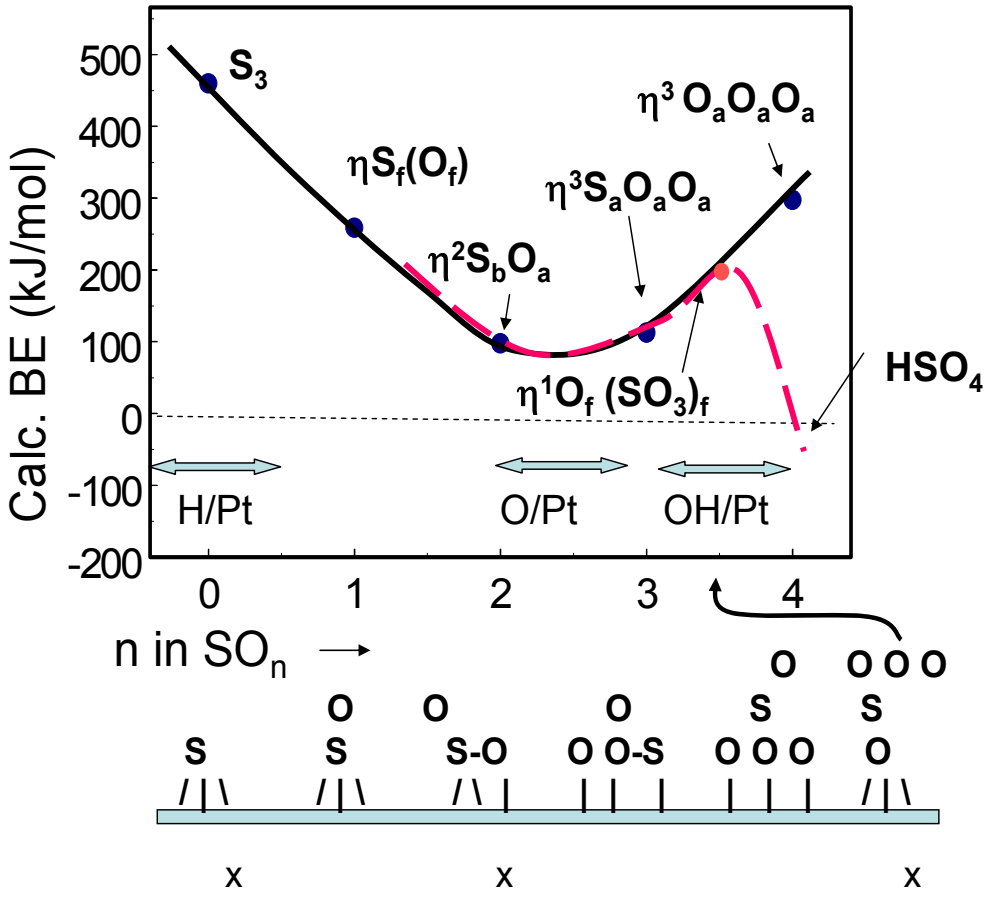

Figure 6.1 Calculated SO_n binding energies and binding sites of SO_n species on Pt(111) at ¼ ML coverage as determined by DFT calculations reported by Lin et al[43] (black solid line). Here ηm indicates m atoms directly bound to the Pt surface and the subscripts a, b, and f indicate atop, bridged, and fcc sites, respectively. Red dashed line gives binding energy of $SO_{3/4}$ as discussed in text for an oxygen covered surface with apparent removal as bisulfate (see eqs. 6.5 and 6). Shaded double arrows show regions that H, OH and O exist co-adsorbed with SO_x in the potential region where these species exist on the surface in water electrolyte. Bottom: Schematic binding of SO_x species on Pt surface with $SO_{3/4}$ added as discussed in text

(only those marked by x are evident in this work).

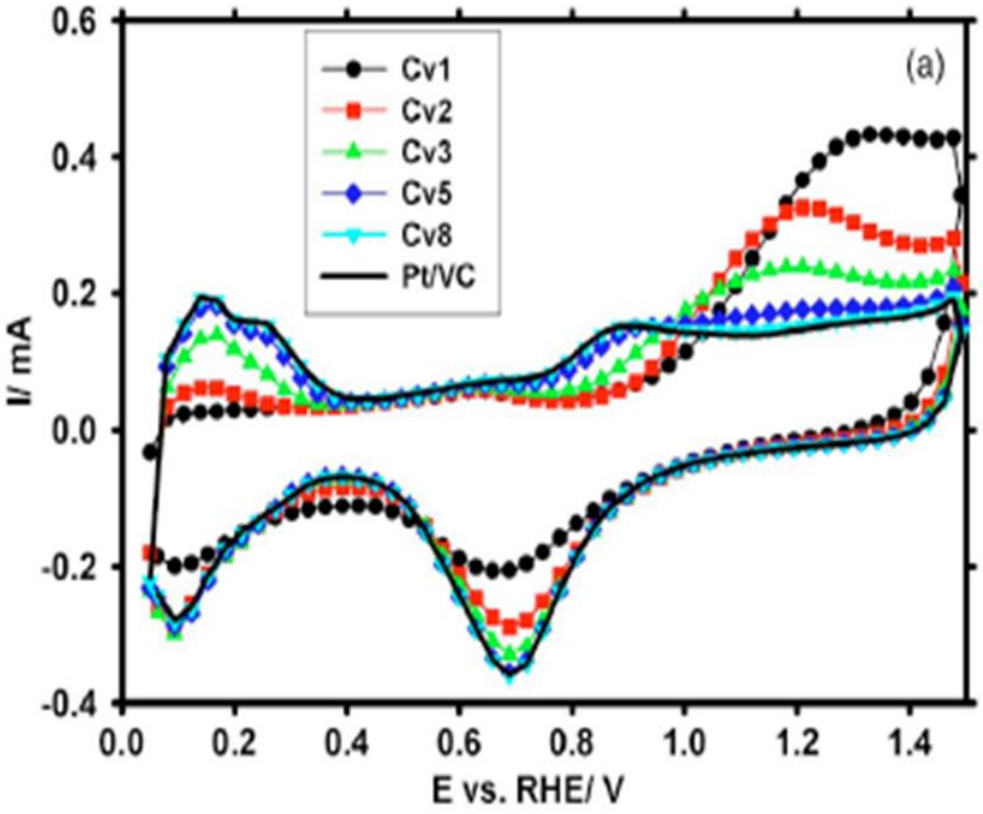

Figure 6.2 Cyclic voltammogram of Pt/VC compared to poisoned Pt/VC. Catalysts were cycled as follows: 0.05V

permission).

pathway which produces peroxide (eq. 6.2). This not only decreases fuel cell performance, but the peroxide can attack and destroy the Nafion in the fuel cell membrane. The overall sulfur oxidation equation is shown in equation 6.3, but of course this 6 e^- oxidation may occur in several steps with several intermediate species adsorbed on the Pt.

$$O_2 + 4H^+ + 4e^- \rightarrow 2H_2O \qquad (6.1)$$

$$O_2 + 2H^+ + 2e^- \rightarrow H_2O_2 \qquad (6.2)$$

$$S^0 + 4H_2O \rightarrow SO_4^{2-} + 8H^+ + 6e^- \qquad (6.3)$$

It should be noted that decreasing the voltammetric cycling rate (e.g., cycles per sec) does not appreciably increase the oxidation rate (i.e. S removed per cycle), so that the S removal is apparently not kinetically driven, but rather coverage driven. Thus it is important to further understand the mechanism for the S removal and SO_x speciation on the surface in order to find better ways to clean the catalyst surface of S containing species.

Some new perspectives on S removal have been suggested by recent studies on Pt-M alloys (M usually being a first row transition metal such as Co). Pt alloys have been shown to produce nearly 2-10 times more catalytic activity for the ORR as compared to pure Pt[45,46,47,48]. This has been attributed to a numbers of possible changes, such as a decreased Pt-Pt bond distance, which may result in a better O_2 adsorption site, lower number of surrounding Pt atoms, escalation of Pt 5d orbital vacancies, and a decrease in coverage of surface oxide layers.[49,50,51,52] Recent results by Garsany et al. [53], showed that only 3 cyclic scans were necessary to remove the sulfur species from Pt_3Co compared to 8 for Pt/VC, even though initially more S appears to adsorb on the surface. This suggests that Pt_3Co/VC may be more susceptible to sulfur poisoning than Pt/VC, but it is easier to be removed. The reason for this is not clear at all, but the results presented here will provide new insight as to why this is true.

6.1.3 This work

In this study, X-ray absorption spectroscopy (XAS) is used to further understand sulfur oxidation on Pt/VC and Pt_3Co electrocatalysts. *In situ* XAS can be used to provide detailed

information on metal-adsorbate surface interactions as indicated by previous work on Pt and Pt alloys[1,2,38,39,54,55,56,57]. X-ray absorption near edge spectroscopy (XANES) analysis cannot only be used for determination of adsorbate oxidation state but also for obtaining coverage information for H, O, OH, Cl and CO adsorbates on Pt. Adsorbate binding site geometries, i.e., atop, bridged, face-centered cubic (fcc), or hexagonal close packed (hcp) sites can also be determined for most atomic and small molecular adsorption using the novel Δμ XANES technique[54, 55, 56].

In this work, we primarily look at the binding of various sulfur SO_x species combined with O(H) adsorption utilizing the Δμ technique. This technique incorporates taking the difference between two spectra, μ. The difference $\Delta\mu = \mu(V) - \mu(V_{ref})$ is obtained by subtracting out a suitable reference spectrum, $\mu(V_{ref})$ taken at a potential V_{ref} when the surface is relatively free of adsorbates. The resulting difference produces a spectral signature which is sensitive to binding site (Figure 6.3). Theoretical calculations using the FEFF 8.0 code[58] are then incorporated to interpret the Δμ difference curve. Extended X-ray absorption fine structure (EXAFS) analysis (also shown in Figure 6.3) can provide information regarding the particle morphology and cluster size.

6.2 Experiment Details

6.2.1 Sample preparation

Commercially made 40% Pt, Pt/VC and 3:1 Pt:Co (Pt_3Co) from Johnson-Mathey were used for the *in situ* XAS measurements. Two separate studies were conducted for both samples, with the first study being on non-poisoned Pt and Pt_3Co and the second when both catalysts were poisoned. For the clean study, the Pt sample was mixed with enough 1M $HClO_4$ electrolyte to make a paste. Poisoning the Pt began with first making a stock solution of sulfur contaminated electrolyte by dissolving anhydrous Na_2SO_3 (Fisher Scientific, ACS Grade) in 1M $HClO_4$. Once the contaminant was dissolved in the electrolyte, the Pt sample was allowed to mix into the solution for around an hour to ensure substantial sulfur adsorption. The catalysts was centrifuged

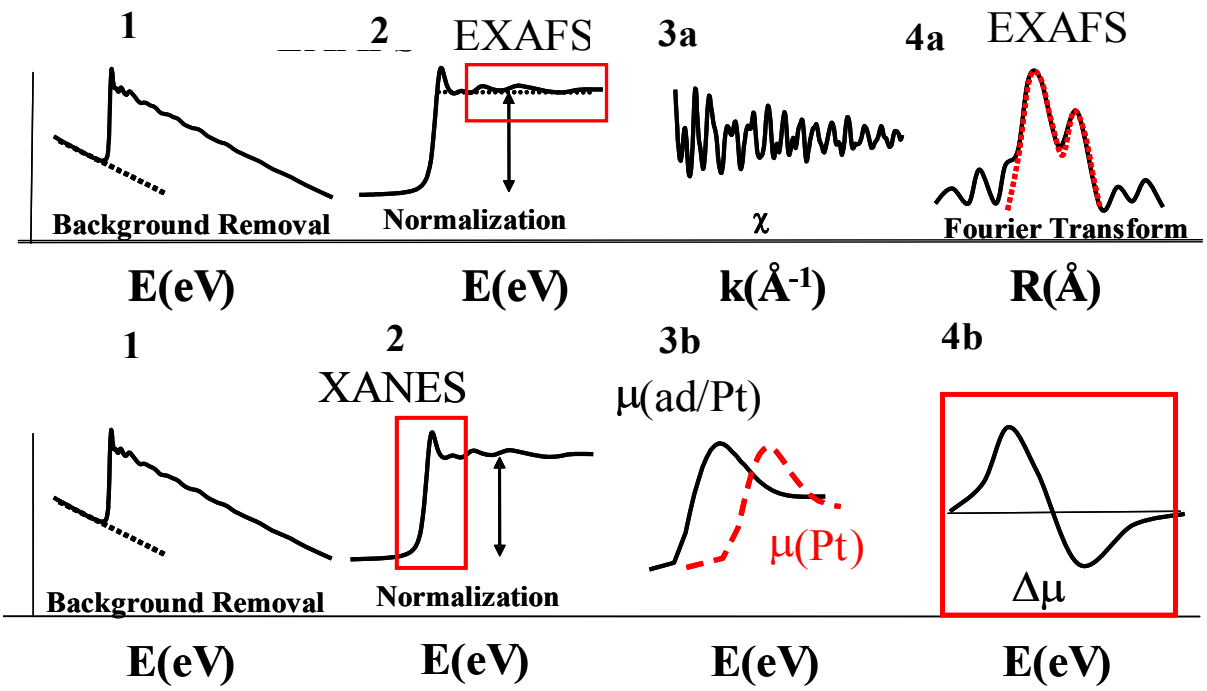

Figure 6.3 Isolation of (a) EXAFS and (b) XANES features. (1) Pre-edge background removal. (2) Normalization. (3a) Post-edge background removal and k-space conversion. (4a) Fourier transform and fit using FEFF 8.0 calculated scattering paths. (3b) Pt L_3 lineshapes prior to subtraction. (4b) $\Delta\mu$ adsorption signature

5-6 times for approximately 20 minutes and rinsed with clean $HClO_4$.

The measurements were taken in an electrochemical half cell, which was designed by the Adzic research group at Brookhaven National Lab[59]. Both poisoned and non-poisoned Pt samples were made into thick film electrodes on carbon gas diffusion layers (E-Tek) with high platinum loadings (7 mg Pt/cm^2). The electrochemical cell was then flooded with 1M $HClO_4$ and placed in front of the beam between two detectors that collected incident (I_0) and sample (I) beam intensity in transmission mode. The potential in the cell was controlled by an Eco Chemie Autolab PGSTAT-30 potentiostat, and all the data presented are with respect to the reversible hydrogen electrode (RHE). The potentials studied were sequenced in time similar to that experienced in an electrochemical cyclic voltammogram. First, a scan of the open circuit potential (OCP) of the catalyst was conducted and then scans were done at descending potentials in 0.1V increments until 0.05V was reached. Then the potentials were increased again, 0.1V increments to 1.4V, then eventually back down to around 0.6V to observe any sulfur coming off.

6.2.2 X-ray Absorption Experiments

In situ XAS experiments were conducted at room temperature in transmission mode on beamline X-11A of the National Synchrotron Light Source (NSLS) at Brookhaven National Laboratory. The NSLS storage ring operated at 2.80 GeV with ring currents between 40 and 200mA. Three gas flow ionization detectors were used to observe the intensities of the incident (I_0) and transmitted x-rays (I) through the sample. A simultaneous Pt reference foil was used for alignment (I_{ref}). The Si (111) double crystal monochromator was detuned by 30% at 200 eV above the Pt L_3 edge (11.564 keV) to minimize the presence of higher harmonics in the beam. The energy calibration was made by recording the XAS of a 7μm Pt foil concurrently with the sample.

6.2.3 XANES Analysis

The absorption coefficient, μ, was obtained from the raw XAS data using the ATHENA

code of Ravel and Newville[60]. The pre-edge background was removed using the AUTOBK function which is detailed more fully elsewhere[61]. A normalization procedure was conducted over a range of 40-100 eV (relative to the Pt L_3 edge) for XANES analysis. This was done for both the foil and sample in transmission.

All XANES spectra are carefully energy calibrated before taking the energy differences, Δμ. This is done by carefully aligning the reference foil data and then transferring any shifts to the sample data.[2,62] This is done because slight shifts in the data arising from photon beam drift and other possible energy uncertainties arising from the monochromator must be removed. This energy calibration is critical for the success of the $\Delta\mu$ technique to guarantee full cancellation of the atomic contribution in the XANES regions; the atomic contribution dominates the spectrum so that Δμ is typically only 1-5% of the total μ signal.

The difference $\Delta\mu = \mu(V) - \mu(V_{ref})$ is generally utilized by subtracting μ taken at an appropriate reference potential. V_{ref} was set to 0.54V (e.g. the double layer water region) in this work as in previous work, since Pt is generally clear of any adsorbates such as adsorbed hydrogen, OH, O or perchlorate anions in this region. In order to observe the effects of sulfur poisoning, a similar difference technique was employed as displayed in equation 6.4.

$$\Delta\mu_p = \mu_p(V) - \mu_c(0.54V) \qquad (6.4)$$

In this equation, 'p' represents an x-ray spectrum of a "poisoned" catalyst while 'c' is for an unpoisoned ("clean") catalyst. This difference method was applied to both the Pt/VC and Pt_3Co studies.

6.2.4 EXAFS Analysis

The EXAFS analysis was carried out by using the ATHENA and ARTEMIS codes from the IFEFFIT software package[63]. The linear absorption coefficient, μ, was obtained from the ATHENA program and the post-edge background was taken out using normal spline techniques. A smoothing procedure was performed to leave the atomic XAFS in the χ function instead of in

the background, a procedure previously described in the literature[64,65,66,67]. The data were then transported into ARTEMIS for analysis. Theoretical analysis (i.e. reference phase and amplitude functions) was incorporated using the FEFF 8.0 code on a Pt_6 Janin cluster[68] to fit Pt-Pt scattering as discussed below.

6.2.5 FEFF 8.0 Calculations

FEFF 8.0 calculations were completed to interpret both the EXAFS region and the Δμ spectra from XANES region. The model cluster that was used was the Pt_6 Janin cluster mentioned previously and used in previous research reported on Pt catalysts[54, 55, 56, 69]. The structure of the Janin cluster is preferred mainly because it has both fcc and hcp sites and has lower symmetry, which is preferred over an octahedral cluster that can produce a state near the Fermi level in the unoccupied density. Such a state is problematical for obtaining an accurate Δμ signature generated by FEFF 8.0. In this work, the Pt_6 Janin cluster was used with the Pt-Pt distance set at 2.77Å. The model clusters used are shown in Figure 6.4. It is important to note that even though Pt_3Co was a catalyst studied in this work, a model cluster of it was not needed due to the finding that Co was not present at the particle surface (i.e. a Pt skin existed) and had no real effect on interpreting the Δμ. Various sulfur species were used in the calculations in specific binding sites as calculated by DFT calculations discussed above.[41] A more detailed explanation of this will be presented below.

6.3 Results

6.3.1 FEFF 8.0 Calculations

Figure 6.4 displays the three models used for calculating Δμ signatures for S, SO_2, and SO_4 adsorption in FEFF 8.0. Figures 6.3a and 6.3b display the S and SO_2 thermodynamically favored binding sites as indicated by previous DFT calculations[40-42] for 0.25 ML coverage of SO_x species in vacuum. However, the correct geometric model to be used in FEFF 8.0 to calculate the Δμ signature for the oxidized SO_4 adsorbate is not clear.

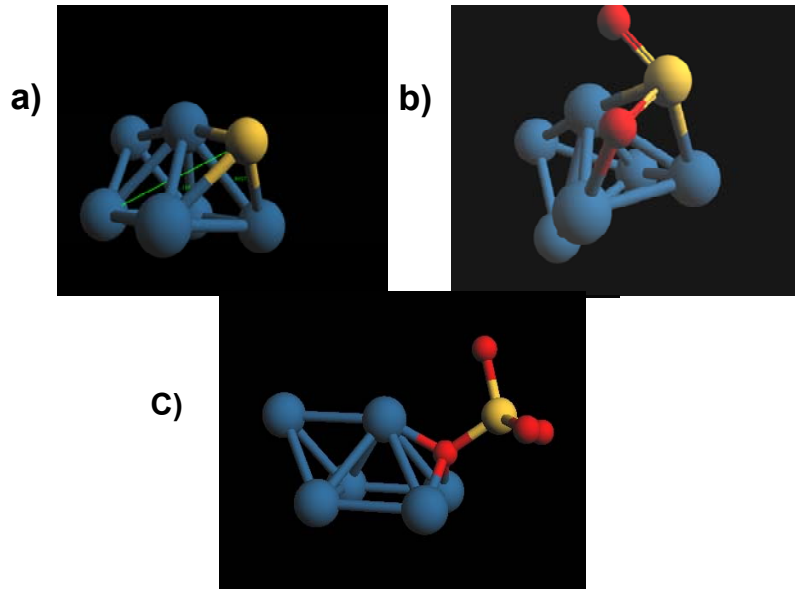

Figure 6.4 Illustration of Pt_6 clusters used for modeling the various sulfur species. a) S/Pt: η^1S_f. b) SO_2/Pt: $\eta^2S_bO_a/Pt_6$. c) $SO_{3/4}$/Pt: η^1O_f. η indicates m atoms bound to Pt surface, f= fcc 3-fold, b = bridged, and a=atop.

Two questions arise concerning the oxidized adsorbate:

a. Is the oxidized adsorbate SO_3, SO_4, or HSO_4? b. What is the preferred geometric binding orientation of SO_4 if it is the oxidized adsorbate?

It would appear that the best answer to question 'a' is SO_4 or HSO_4. As noted above, Quijada et al using FTIR data did not find peaks attributable SO_3 above 0.9 V RHE. Further, recent DFT calculations by Pillay et al[70] show that SO_3 in the presence of other adsorbed O goes directly to SO_4 without an activation barrier, and this has been noted previously[71]. Finally DFT calculations by Lin et al[41] also show that SO_4 is more stable than SO_3 in the presence of chemisorbed O. Thus is seems clear that the oxidized SO_2 species is SO_4.

The answer to question 'b' is more difficult. The theoretical $\Delta\mu$ signature obtained for SO_4 in the favored DFT orientation of Fig. 6.1 ($\Delta\mu$ not shown in Fig. 6.5 below) produce a |NEG| that is smaller than that for SO_2, but experiment clearly shows that |NEG| increases upon oxidation of SO_2 (e.g., see Fig. 6.12 below). An increase in |NEG| implies some occupation of the 3-fold fcc site upon oxidation of the SO_2 because all previous work shows that a negative amplitude appears only when n-fold sites are occupied[1,2, 38,39,54]. Thus an orientation in an electrochemical environment other than that preferred (i.e. the SO_4 η^3 $O_aO_aO_a$) by DFT calculations for a 1/4 ML coverage of SO_4 on Pt(111) in vacuum appears to be indicated by the experimental $\Delta\mu$ results. The adsorption of OH and O on Pt in aqueous electrolyte at potentials above 0.8V, the possibility for un-oxidized SO_2 still present on the surface, and even the possibility for higher coverages of SO_4 than 1/4 ML, all apparently force the SO_4 to take an orientation that limits its 'footprint' on the surface.

This orientation could be the stable alternate η^1 $O_f(SO_3)_f$ orientation found by Lin et al[41], but with a binding energy of only about half that of the η^3 $O_aO_aO_a$ orientation found in vacuum (see Fig. 6.1). They find the S-O bond lengths to be 2.79 Å and 1.46(3) Å with the Pt-O bond to be 2.08Å in this $\eta^1O_f(SO_3)_f$ configuration. Lin et al further suggest that this might be considered

an SO_3 –like entity on top of an O covered Pt(111) surface, but they considered this an SO_4 species since the S is indeed bonded to 4 oxygen atoms. Such an "inverted" orientation, particularly in the oxygen region, has also been indicated as summarized above by the FTIR studies[24,25].

Indeed the η^1 $O_f(SO_3)_f$ orientation for SO_4 shown in Fig. 6.4c does give the desired increased |NEG| and much increased |POS|, both indicated by the experimental results to be discussed below. For the remainder of this work we will use the notation $SO_{3/4}$ to indicate the oxidized adsorbate, leaving it unspecified as to whether it is better to consider it SO_3/O or SO_4.. In any event, the $SO_{3/4}$ notation denotes that the S-O bond involved in the bond to the Pt surface is much longer than the others, and has a binding to Pt(111) half way between SO_3 and SO_4. This notation also highlights that this SO_4 is apparently not in the most stable η^3 $O_aO_aO_a$ configuration found at 1/4 ML in vacuum on Pt(111), but rather in the η^1 O_f configuration under aqueous electrolyte on Pt cubooctahedral particles consistent with that suggested by FTIR studies. This difference may arise from the different faces existing on multifaceted Pt particles, or more likely because it provides a lower footprint on the surface due to the high coverage of O(H) at these potentials.

DFT calculations to be reported by Pillay et al will consider these binding orientations, how protonation of SO_4 (i.e. to HSO_4^- and H_2SO_4) significantly weakens the binding to the Pt surface so that it can leave as shown in Fig 1 as it reaches a full SO_4 (or HSO_4) -like structure, and finally how a nearby OH/Pt can carryout this protonation.

The theoretical $\Delta\mu$ signatures obtained from FEFF 8.0 for some of the indicated adsorbates in Fig. 6.4 are shown in Figure 6.5. Due to the remarkable similarity between the different S and SO_2 signatures above 3 eV, and the large amplitude of the signature for OH above 0 eV, the changes in S oxidation level are best watched by plotting the absolute magnitude of the

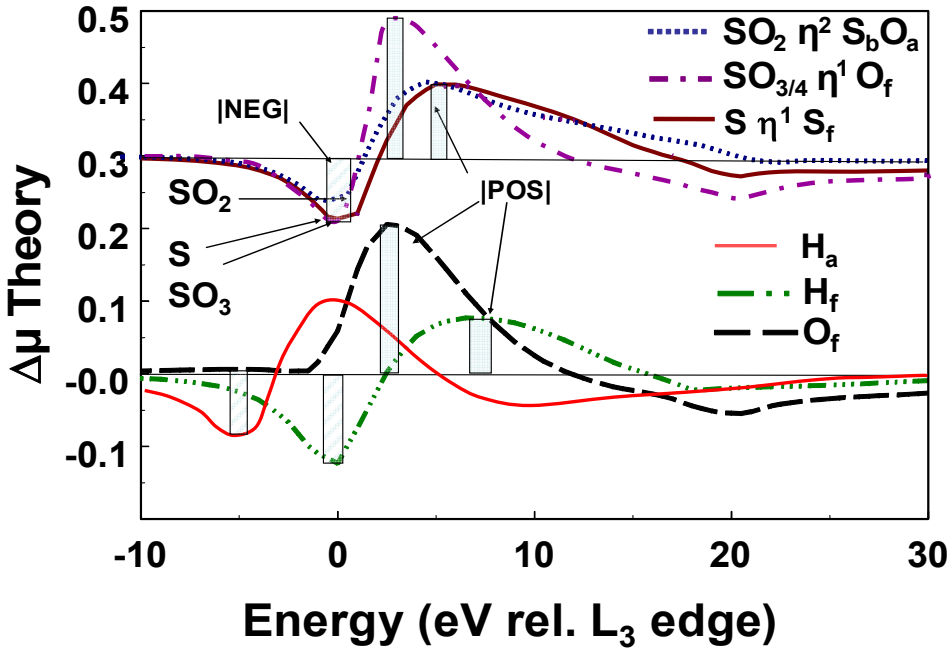

Figure 6.5 FEFF 8.0 calculated line shapes for S, SO_2, and $SO_{3/4}$ (moved up by 0.3) compared to calculated line shapes for 3-fold O and atop and 3-fold H. The (|NEG|) and |POS| magnitudes of all the signatures are highlighted with the stripped or shaded boxes. Subscripts a, b, and f indicate atop, bridged, and fcc 3-fold sites, respectively.

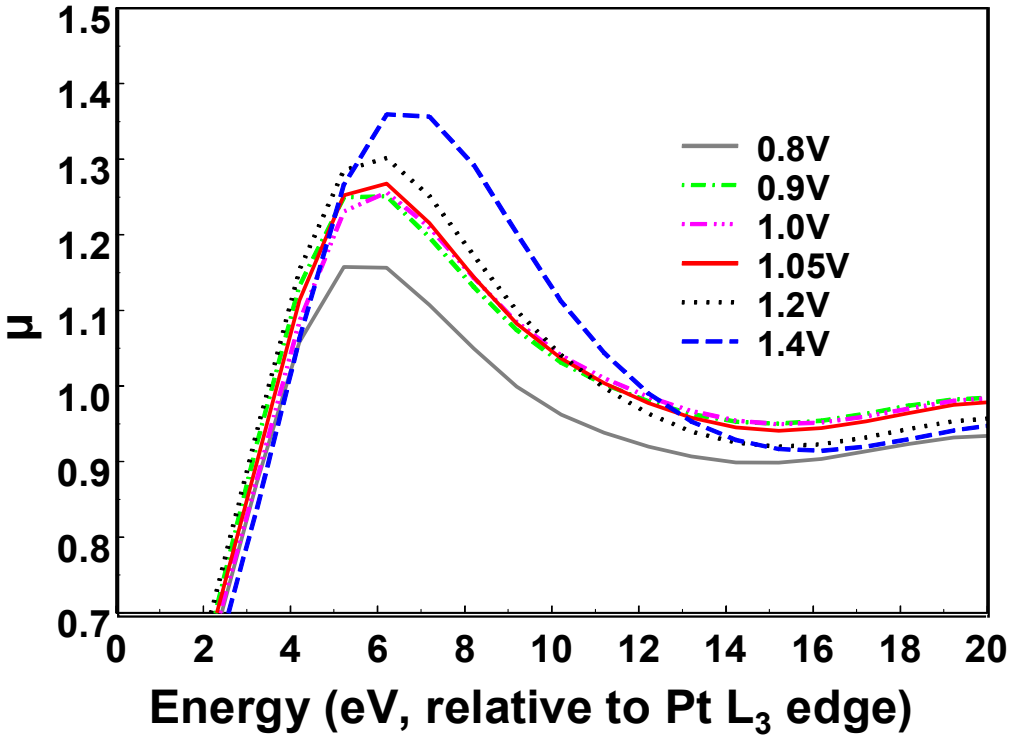

Figure 6.6 Experimental XANES data (μ) taken on sulfur-poisoned Pt/VC electrode in 1M HClO4 at the potentials indicated.

Δμ (which is negative) just below 0 eV. We label this magnitude |NEG|. Note that O/Pt does not contribute in this region, but H does significantly. Fortunately, we need only examine the oxidation of S above 0.5 V (RHE), when H is not expected to be present; although watching the reduction of SO_2 below 0.5 V using |NEG| will be affected by the presence of H . In contrast O has large positive amplitude around 5 eV which we label |POS|. Hence, by watching |NEG| with potential we can watch the adsorption or change of oxidation state of SO_x and by watching |POS| with potential we can watch the adsorption of OH and O.

6.3.2 XANES Analysis

Figure 6.6 shows the Pt L_3 absorption spectrum, μ, at different potentials for Pt/VC poisoned by sulfur. Data for non-poisoned Pt/VC and Pt_3Co as well as sulfur-poisoned Pt_3Co were also collected in a similar process and showed similar changes. It can be observed that there are visible changes in μ that are well above the noise level as a function of potential. Figure 6.7 shows the Δμ difference spectra for non-poisoned Pt/VC using 0.54V as the reference potential. A systematic trend is observed from 1.2 to 1.4V where maximum amplitude, |POS| increases substantially with only a small change in |NEG|. This is indicative of OH adsorption followed by O adsorption and even eventual subsurface oxide (hcp O or 4-fold O) formation which has been seen in previous research. Returning back to 1.2V and eventually to OCP, the amplitudes then decrease indicating most of the OH has left with perhaps only a small amount of subsurface oxide behind. Figure 6.8 illustrates the Δμ difference spectra for sulfur-poisoned Pt/VC once again using 0.54V in the absence of S ("clean') as the reference potential. In this case, the the |NEG| increased by a factor of 6 over the non-posioned case (in non-poisoned Pt/VC, the |NEG| of only 0.02 is seen in Figure 6.7). A plot of these magnitudes as a function of potential, and comparison with the theoretical magnitudes obtained from FEFF 8.0, will assist in determining the sulfur speciation at various potentials below.

6.3.3 EXAFS Analysis

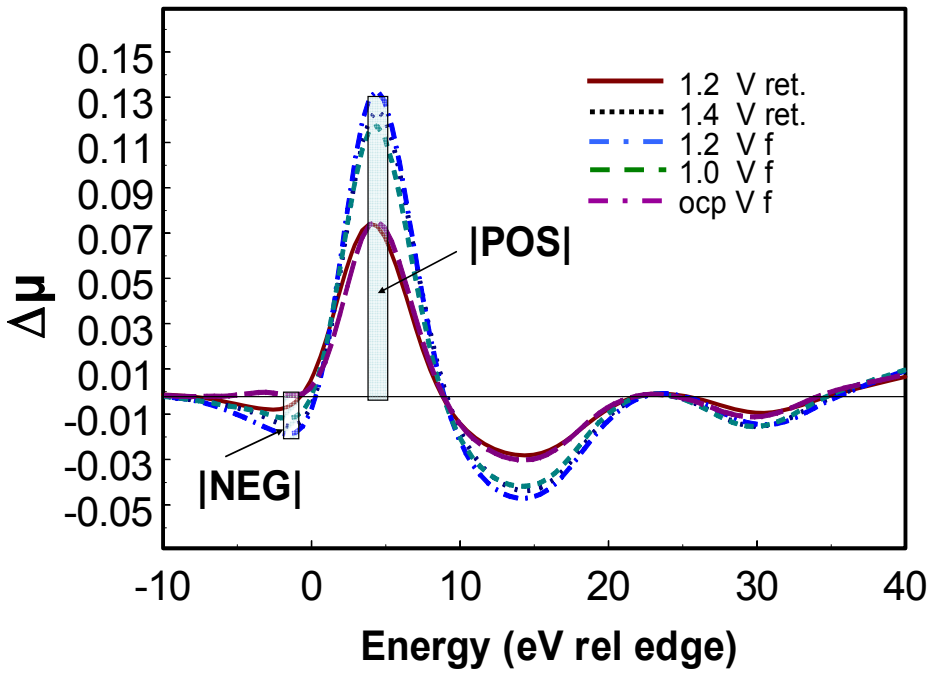

Figure 6.7 The experimental Δμ non-poisoned Pt/VC in 1M $HClO_4$ at the potentials indicated (ret. indicates on the "return" and f indicates "final" as defined in text). The maximum and minimum amplitudes (|POS| and |NEG|) at 5 and – 3 eV respectively, are also highlighted.

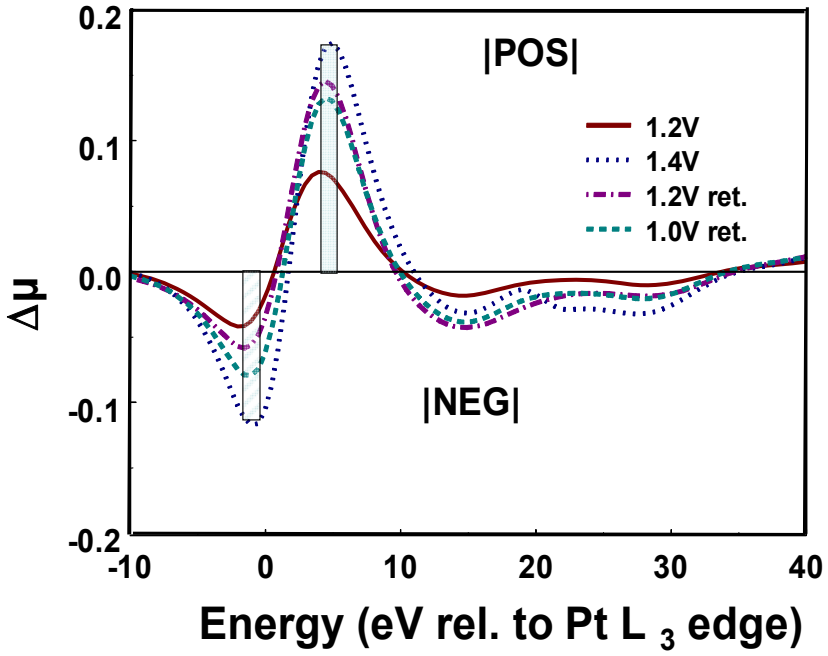

Figure 6.8 The experimental Δμ difference spectra of sulfur-poisoned Pt/VC in 1M $HClO_4$ at the potentials indicated. Note the much larger |NEG| here compared to the clean case in Fig. 6.7.

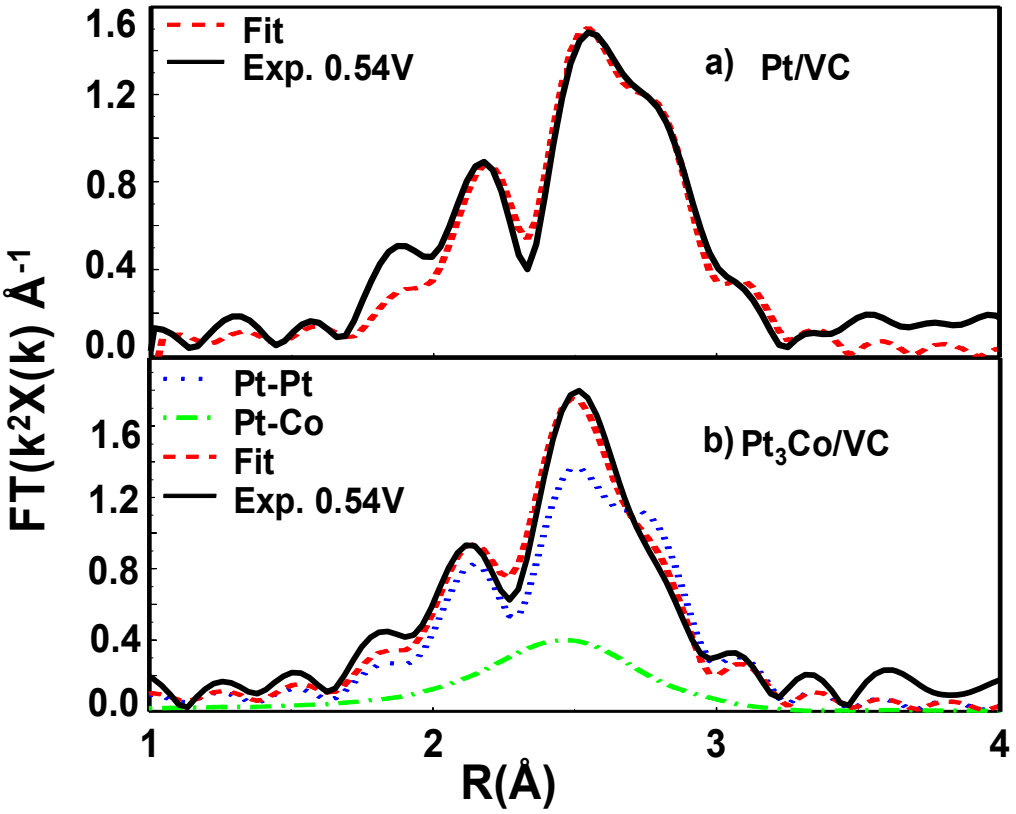

Figure 6.9 The Fourier transform (2<k<15.5, k2) of the χ function obtained for **a)** Pt/VC and **b)** Pt_3Co/VC both in sulfur-poisoned 1M $HClO_4$.

Figures 6.9 shows a comparison between the Fourier transform of the experimental EXAFS data for both poisoned Pt/VC and Pt_3Co/VC in 1M $HClO_4$ at 0.54V using a Pt-Pt fit in both cases and a Pt-Co fit for Pt_3Co. As can be seen, an excellent fit can be achieved over the R region indicated. EXAFS parameters such as N, R, E_0, and the Debye-Waller factor, σ^2, are not reported here due to the extensive number of data points. However, plots of the coordination number (N) of Pt as a function of potential for both non-poisoned Pt and sulfur-poisoned Pt are shown in Fig. 6.10 along with a CV of the non-poisoned Pt.

Most visible in Fig. 6.10, above 1.0V a sharp decrease of N_{Pt-Pt} is observed for both clean and poisoned Pt. This arises due to O adsorption in 3-fold fcc sites as well as eventually undergoing place exchange with the Pt and hence going beneath the surface. We have noted the sharp drop in N_{PtPt} many times before upon oxidation of Pt[38,54]. Note the slight increase in N_{PtPt} between 0.6-0.8 and again between 0.8-1.0. This is attributed to the chemisorption of H_2O and OH in atop sites. We have observed the increase in N_{PtPt} previously upon adsorption in atop sites,[38,39,62] this is believed to occur because the Pt particles "relax" and become more spherical upon atop adsorption, which increases the Pt-Pt coordination. The adsorption of H_2O is only slightly visible in the CV because no real oxidation and resultant current flow is occurring, as opposed to when OH and O adsorption occurs. Note also the increase of N_{Pt-Pt} below 0.2 V, when atop H comes on the clean surface. H adsorption in either a 3-fold or atop sites has been shown to increase N_{Pt-Pt} previously.

Below 0.6 V, the S-poisoned Pt has a larger N_{Pt-Pt} than the clean. This of course must be due to the presence of the S^0, but we are a bit surprised by the increase. We would expect S^0 in a 3-fold site, like O fcc, to decrease N_{Pt-Pt}. However at low potentials fcc H also increases N_{Pt-Pt} as noted above, so S may act more similar to H in this potential region. Lin et al[41] have indicated that at high coverage of S, lateral interactions force the S to move into the atop site, so perhaps this may also be playing a role. The very different behavior of N_{PtPt} above 1.2 V for the clean and S-poisoned Pt must be due to the adsorbed $SO_{3/4}$. The presence of $SO_{3/4}$

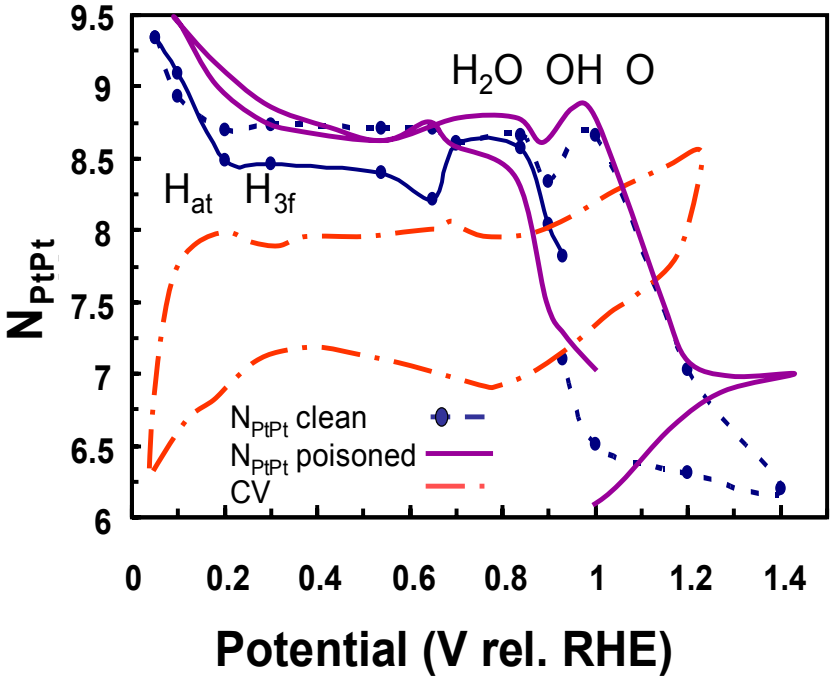

Figure 6.10 Plot of Pt-Pt EXAFS coordination number (N_{Pt-Pt}) as a function of potential obtained from analysis for non-poisoned (dashed line with measured points) and S-poisoned Pt/VC (solid line with points at same potentials as for clean but not shown). Also shown is a current-voltage plot for the non-poisoned sample with current in arbitrary units. The adsorbates as described in the text are indicated.

certainly decreases the amount of O going subsurface, so this explains the smaller "drop" of N_{Pt-Pt} in this region. Plots of N_{Pt-Pt} as a function of potential for Pt_3Co are not shown due the interference between the Pt-Pt and Pt-Co scattering and hence difficulty with obtaining reliable results Nevertheless, Tables 6.1a and b show all EXAFS parameters for each catalyst, Pt/VC and Pt_3Co/VC, both sulfur-poisoned and non-poisoned, at 0.54V. This potential is the double-water layer region where surface adsorbates are not usually found, except of course for SO_x. The potential is chosen only to give an idea of the actual cluster sizes of the two catalysts. These EXAFS results in Tables 6.1a and b were determined by keeping the Debye-Waller factor, σ^2, parameter at an optimum value for all potentials to make the resultant N_{Pt-Pt} more significant (a large linear dependence exist between N and σ^2). The EXAFS data in Tables 6.1a and b show that both catalysts are around 3-5 nm in size.

6.4 Discussion

6.4.1Reaction mechanisms of sulfur species revealed through Δμ amplitudes

6.4.1.1 Sulfur oxidation on Pt/VC

Figure 6.11 shows a plot of both the |NEG| and |POS| amplitudes for clean Pt/VC obtained from the experimental Δμ signatures, some of which are shown in Fig. 6.7. The theoretical Δμ signatures for atop and fcc H, and fcc O are shown in Fig. 6.5. The Δμ signature for OH is similar to fcc O only the peak at 3 eV is shifted down by a few electron volts. That for sub-surface O is also similar to fcc O, except a negative component appears around -3 eV[1,2,54,62] Thus the |POS| amplitude in Fig. 6.12 primarily reflects atop H adsorption (below 0.3 V), atop chemisorbed H_2O adsorption (0.6-0.8 V) and O (above 0.8 V) in the indicated regions. The |NEG| amplitude primarily reflects 3-fold H adsorption (below 0.5 V), H_2O adsorption (0.6-0.8 V) and subsurface O (Pt-O above 0.8 V). Fig. 6.11 indicates that as one proceeds to lower potential, first 3-fold fcc H adsorbs, followed by atop H consistent with previous observations.

Table 6.1: Summary of EXAFS results for:

a) Pt/VC at Pt L_3 edge: 2<k<15 $Å^{-1}$, 1.6<R<3.0 Å

	Potential, V	N_{Pt-Pt} [b]	R(Å)	E_0 (eV) ± 1eV	σ^2 ($Å^2$)
Pt/VC clean	0.54V	8.404	2.761	8.380	0.006
Pt/VC sulfur	0.54V	8.715	2.758	7.405	0.006

b) Pt_3Co at Pt L_3 edge: 2<k<15 $Å^{-1}$, 1.34<R<3.0 Å

	Potential, V	N_{Pt-Pt} [b]	N_{Pt-Co} [c]	R(Å) ± 0.01	E_0(eV) ± 1eV	σ^2 ($Å^2$) $_{Pt-Pt}$	σ^2 ($Å^2$) $_{Pt-O}$
Pt_3Co/VC clean	0.54V	7.023	0.765	2.727	2.707	0.006	0.009
Pt_3Co/VC sulfur	0.54V	7.289	1.084	2.73	2.692	0.006	0.009

[a] S_0^2 fixed at 0.933 as calculated by FEFF 8.0

[b,c] Absolute errors are usually of the order of 20%, the differences with potential are expected to be meaningful to 0.1 due to fixed σ^2

.

In the O region, OH comes on above 0.8 V and some subsurface O appears only above 1.2 V (as observed with the N_{PtPt} plot in Fig. 6.10), the latter occurring by place exchange with Pt atoms at the surface. Note the relative reversibility of the H adsorption compared to the O adsorption, consistent with that previously observed in many CV curves (e.g. see Fig. 6.10). It is important to note the feature seen in both |POS| and |NEG| between 0.65 and 0.8V. This feature is particularly striking since both |POS| and |NEG| indicate a rise and then a fall in magnitude **before** the adsorption of O(H) above 0.8 V. We suggest that this is due to atop O in adsorbed H_2O. In this region, it is surmised that the formation of a weakly bonded water layer develops and then it is disrupted as the adsorption of O(H) begins. This adsorbed H_2O was also visible in the N_{PtPt} plots of Fig. 6.10, but was less visible. CV data reported by Ross et al[72] for Pt(111) in 0.1M $HCLO_4$ report a feature at similar potentials and suggest it arises from an overlayer of H_2O with ClO_4^- anions, which we cannot rule out.

As mentioned above, variation in sulfur speciation and coverage is best watched with |NEG| because the |POS| is so dominated by O adsorption above 0.7 V. The theoretical signatures for S, SO_2, and SO_3 in Figure 6.5 each show a negative amplitude with SO_3 displaying the largest and SO_2 the lowest magnitude (i.e. $|NEG|_{SO2} < |NEG|_S \approx |NEG|_{SO3/4}$). Figure 6.12 gives a plot of |NEG| with potential for the sulfur-poisoned Pt/VC. The increase of |NEG| seen upon comparing the clean (Fig. 6.11) and sulfur-poisoned Pt clearly arises due to the presence of S, and comparison with the theoretical signature suggests that roughly about 0.2 to 0.4 ML of SO_2 is adsorbed onto the Pt surface in the S-poisoned case (conversion of $\Delta\mu$ magnitudes to absolute coverage is difficult because of many factors). The large |NEG| amplitudes at low and high potential with a minimum around 0.7 V reflects the relative |NEG| magnitudes of the different S species, i.e. mostly S at low potentials, SO_2 around 0.7 V, and $SO_{3/4}$ at high potentials.

Assignment of the individual features in |NEG| in Fig. 6.12 to specific processes is best determined by comparison with previous CV data reported by Quijada et al. CV data reported by them are included for reduction of surface SO_2 (i.e. after exposure to SO_2 and then the CV taken

in SO_2 free electrolyte) in the region from 0.6 down to 0.05 V and oxidation of bulk SO_2 (i.e. CV taken in the presence of SO_2 containing electrolyte) in the region 0.30 or 0.6V to 1.5 V. We include these different CV's because they most clearly resemble and hence reveal the source of the features in |NEG|.

The reduction of SO_2 is indicated to occur irreversibly below 0.6 V giving two ill-defined waves at 0.45 and 0.2 V. Indeed the |NEG| reveals the same two waves with the one at 0.2 V clearly now dominant. The reason for the two waves is not given by Quijada et al, but we suspect they have to do with the adsorption of 3-fold H beginning around 0.45 V, and atop H beginning around 0.2 V as one proceeds down to 0.0 V. The oxidation of surface SO_2 occurs primarily at 1.2 V as revealed in a CV given by Ouijada et al not shown in here. Rather the CV data in the presence of electrolyte containing SO_2 is shown because it remarkably reproduces the features in |NEG|. Ouijada et al assign the features as indicated in Fig. 6.6; namely oxidation of either S or SO_2 to $SO_{3/4}$ in the potential regions indicated. In all cases, peaks in the CV's do not exactly align with peaks in |NEG| because the CV reflects current (i.e. rate of oxidation or reduction) and |NEG| reflects coverage of product on the surface. Thus the CV's generally peak when the coverage is changing the fastest. The difference between the solid and dotted CV's in the oxidation region is just the starting potential, i.e., 0.3 V or 0.65 volts. The former reflects more S to $SO_{3/4}$ oxidation because more S is on the surface when beginning at 0.3 V.

It is not clear why the |NEG| data more closely reflect the CV for oxidation of "bulk" SO_2 than surface SO_2, since the SO_2 contaminated electrolyte was removed before the XAS data were obtained. Perhaps sufficient SO_2 was still adsorbed on the VC support which could migrate onto the Pt so that the |NEG| data mimic more closely the "bulk" CV. Organically bound S species are known to absorb strongly on VC, and removal by migration to or contact with Pt at raised potentials is known to be quite effective in removing this sulfur.[10,11] Whatever the reason, a comparison of the change in experimental amplitudes with potential, and using information from previous CV studies on S oxidation as discussed above, suggest the following:

a) SO_2 is on the surface of Pt at OCP, the start of the cycle, and gradually gets reduced irreversibly to zero-valent S in two waves when the potential is lowered to 0.05V (recall $|NEG|_{SO2} < |NEG|_S$).

b) The peak arising in the region between 0.8 to 1.0V in the forward scan is believed to result from zero-valent S being oxidized to $SO_{3/4}$.

c) Above 1.2V, some SO_2 is oxidized to $SO_{3/4}$.

d) The largest removal of $SO_{3/4}$ appears to occur below 1.0 V in the reverse scan.

Point d) is not all evident from the CV data of Quijada et al, as electrochemical data can give no evidence of this. How do we understand most of the $SO_{3/4}$ removal below 1.2 V? It would appear that adsorbed O is needed to oxidize SO_2, but adsorbed OH is needed to remove the $SO_{3/4}$, because as noted above and indicated in Fig. 6.12, OH exist primarily on the surface below 1.0 V and O above. This would suggest that the potential must be raised above 1.0 V to initiate the oxidation reaction:

$$SO_2/Pt + 2\ O/Pt \rightarrow SO_{3/4} \qquad (6.5)$$

but back below 1.0 V to carry out the protonation and desorption reaction:

$$SO_{3/4}/Pt + nOH/Pt \rightarrow H_nSO4\ (n = 1 \text{ or } 2) + Pt + O/Pt \qquad (6.6)$$

Lin et al[41] have presented DFT calculations highlighting details of the SO_2 to SO_3 reaction as well as reactions similar to reaction 6.5 and Pillay et al of reaction 6.6, so we do not further discuss these here. Calculations show that addition of H to the $SO_{3/4}$ indeed significantly weakens the binding to the Pt, so apparently protonation is required for removal from the surface. This is consistent with the discussion in the Introduction above that bisulfate (HSO_4^-) is apparently easily removed as OH and O adsorb and displace the bisulfate, but SO_4 is not as shown by Lin et al[41]. It would appear that the necessity to cycle back down below 1.0 V to protonate and remove the oxidized $SO_{3/4}$ explains in part why several CV cycles must be carried out to remove most of the SO_x, and why just holding the electrode at 1.2 V will not remove all of the sulfur. What determines the amount of S that can be

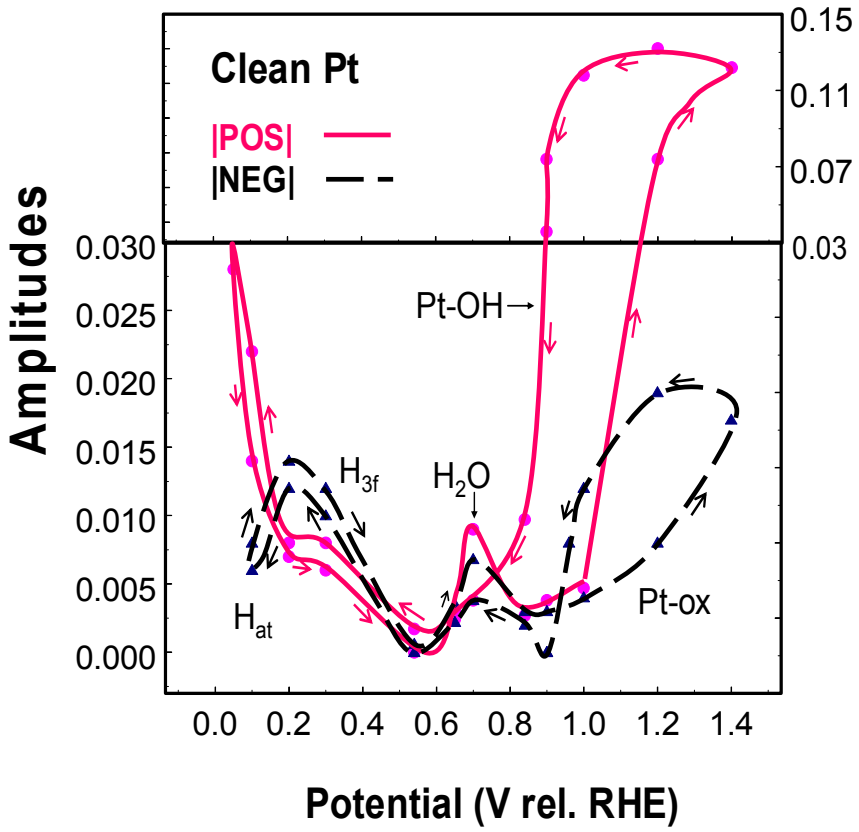

Figure 6.11 Plot of |POS| and |NEG| from the experimental Δμ as a function of potential for clean Pt/VC. Note different scales for magnitudes below and above 0.03 to increase clarity. Arrows indicate direction of scan beginning and ending at OCP (around 0.95 V).

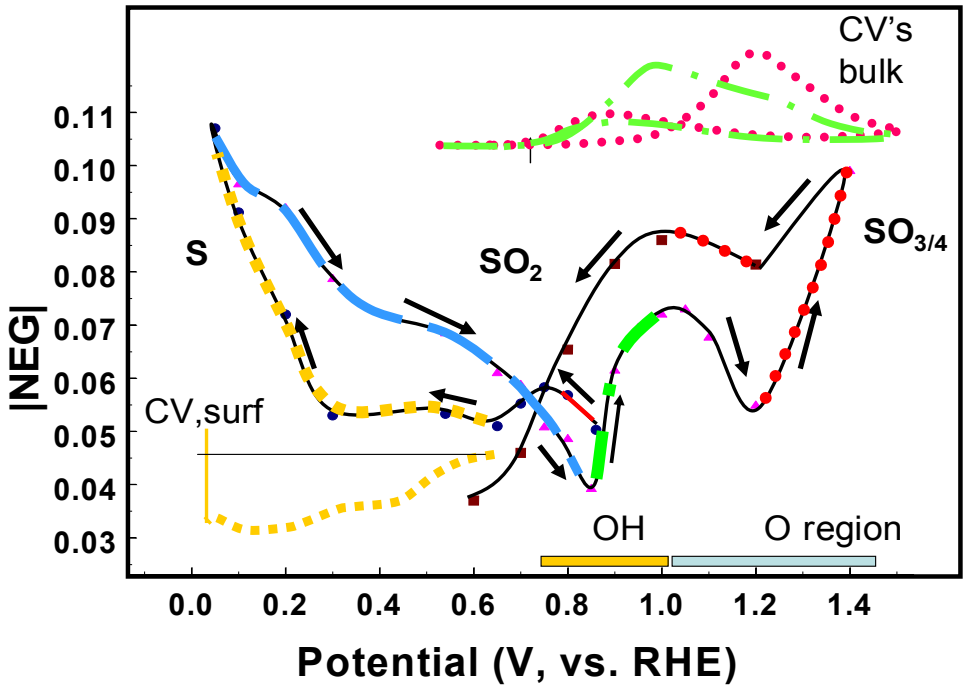

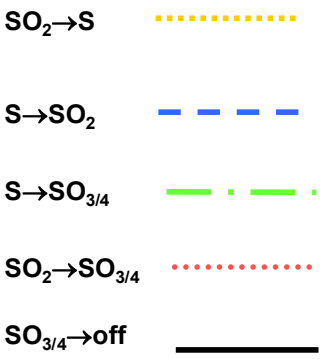

Figure 6.12 |NEG| vs. potential for S poisoned Pt/VC. Note that $|NEG|_{SO_{3/4}} \approx |NEG|_S > |NEG|_{SO_2}$ as shown in Fig. 6.5. Potential regions where various oxidation/reduction reactions occur and regions where OH and O are co-adsorbed on the Pt surface are indicated. CV data from Quijada et al[9] are discussed in the text.

removed with each cycle? Perhaps the $SO_{3/4}$ species has a larger footprint on the surface, so that only a fraction of the SO_2 species can be oxidized to $SO_{3/4}$, and this must be removed before further $SO_{3/4}$ can be produced.One might question the reproducibility of the |NEG| curve in Fig. 6.12, even though the features are remarkably parallel to previously reported CV features. Fig. 6.13 presents a second set of data using a similar sample but at a different beam time at NSLS. The data for set 1 have been moved down by 0.007 to provide better comparison with the second set of data (i.e. less S is present on the surface in the second set compared to the first). The agreement between the two sets is remarkable, with all features reproduced and appearing at nearly the exact same potential to within reasonable determination of the features (the XAS data were taken at fewer points in data set 2). The difference between sets 1 and 2 below 0.5 V suggests that the SO_2 reduction and re-oxidation in set 2, with the initially lower S coverage, is more reversible and the so-called 3-fold and atop H waves mentioned above less well defined. Both 3-fold H and S^0 are contributing to the total |NEG| plotted in this region, and the H adsorption/desorption process is much more reversible than the S redox process. Therefore Run 2 with less S and therefore more H shows the more reversible |NEG| curve as expected.

Finally, Fig. 6.12 includes a plot of |POS| for S-poisoned Pt (run 2). Note that the features in |POS| between 0.7-0.8 and between 0.9-1.0 correspond to features in |NEG|. This confirms that the |POS| of $SO_{3/4}$ is indeed larger than that for SO_2 consistent with the theoretical signatures in Fig. 6.5. The plots of |POS| for the S-poisoned Pt can be compared to the clean in Fig. 6.11. Note that the maximum magnitude of 0.14 between 1.1 and 1.4 V for the S-poisoned Pt corresponds to 0.13 in the same region for the clean Pt in Fig. 6.11. This further confirms that the |POS| of both 3-fold O and $SO_{3/4}$ are comparable as shown by the theoretical signatures in Fig. 6.5, so that regardless of the amount of O vs. $SO_{3/4}$, the maximum |POS| will be about the same at full coverage.

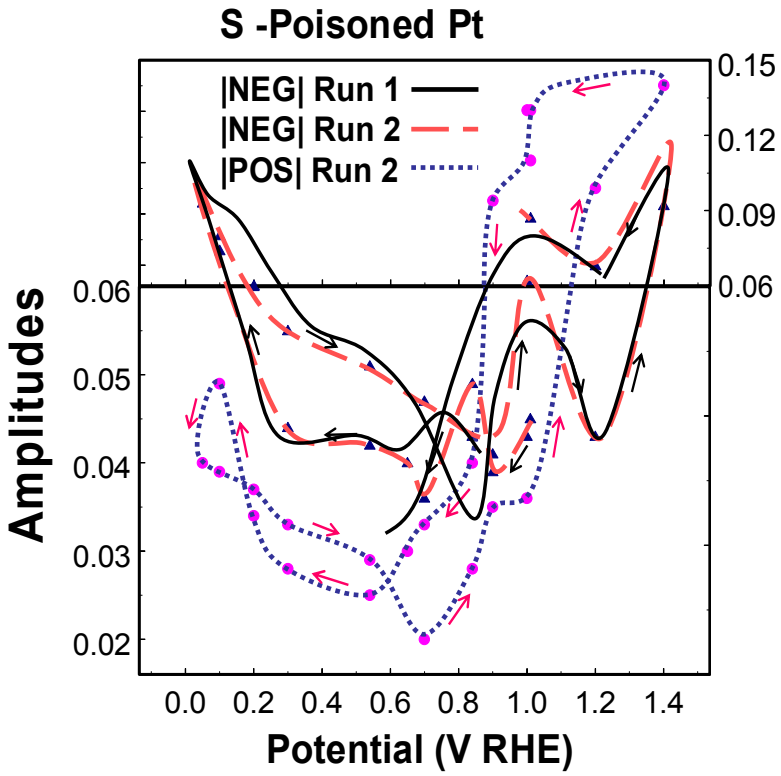

Figure 6.13 Comparison of |NEG| data from two different S-poisoned Pt/VC Runs. Data of Run 1 have been shifted downward by 0.007 to provide clearer comparison, and indicates slightly more S was present on the Pt surface in Run 1. Points where XAS data were taken are not indicated for Run 1 (they are indicated in Fig. 6.12), but fewer points were taken in the region between 0.6 and 1.2 V in Run 2. Note change of scale at 0.06 to provide more clarity for the |NEG| below 0.06.

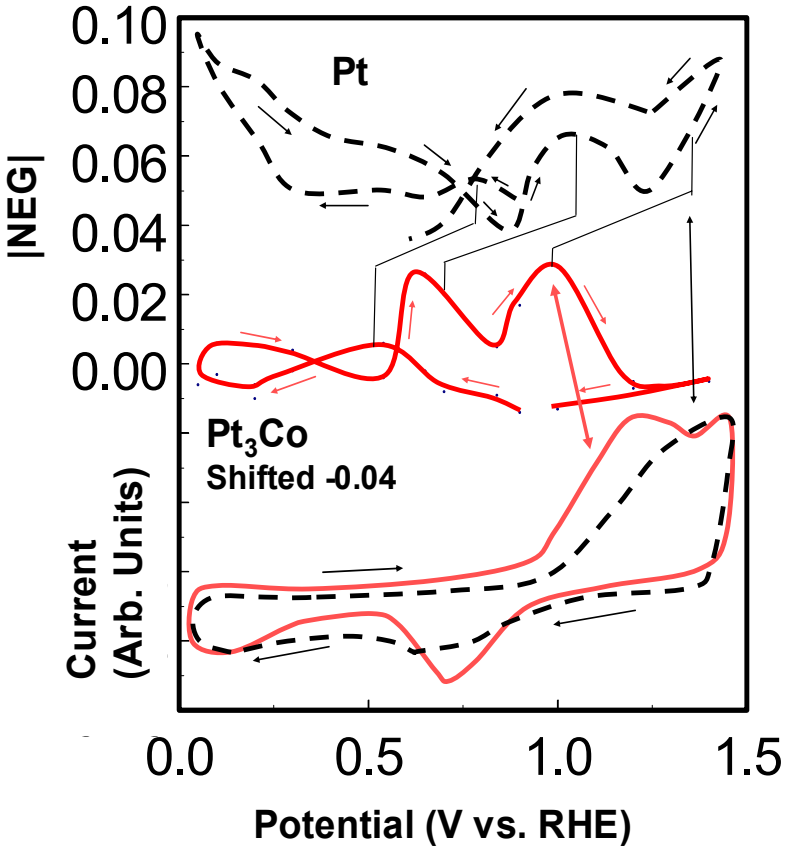

Figure 6.14 Comparison of |NEG| and CV plots for S-poisoned Pt and Pt_3Co with small arrows indicating direction of scans. The |NEG| data for Pt_3Co have been shifted downward by 0.04 for clarity. Corresponding peaks in |NEG| for Pt and Pt_3Co are indicated, and arrows to the CV data point to corresponding features coming from the dominant SO_2 to $SO_{3/4}$ oxidation reaction.

6.4.1.2 Sulfur oxidation on Pt_3Co/VC and the benefits of the ligand effect

Figure 6.14 compares |NEG| $\Delta\mu$ results obtained for Pt_3Co (solid line) and Pt (dashed line). Although the data appear to be quite different, the same features are seen in both, only they are shifted down by about 0.2 V in the Pt_3Co case as highlighted by the lines correlating features coming from the same three different S redox processes. Thus it appears the ligand effect of the Co enables the SO_2 to be oxidized to $SO_{3/4}$ (eq. 6.5) at significantly reduced potentials. To confirm that this is indeed occurring, we also show the CV plots for S-poisoned Pt and Pt_3Co in Fig. 6.14. Note the drop in the onset for S oxidation in the Pt_3Co case. Comparing the CV and |NEG| plots clearly reveals that the dominant current in the CV comes from the SO_2 to $SO_{3/4}$ oxidation step between 1.0 and 1.2 V, which is the case when only previously adsorbed S species are present (i.e. no S from the electrolyte or carbon surface). Figure 6.15 shows in detail the sulfur speciation on Pt_3Co occurring during the cycle, similar to Fig. 6.12 for Pt. Another striking feature of Figs. 6.12 and 6.15 (also shown in Fig. 6.14) occurs between 0.6 and 1.4V, where it appears the two catalysts "turn" in opposite directions. The |NEG| plot for Pt goes up and around counterclockwise, while that for Pt_3Co turns down clockwise. Clearly the $SO_{3/4}$ removal process is very different in these two cases. What can be the cause of this dramatic difference? An examination of the different onsets for H_2O and OH adsorption induced by the Co ligand effect can shed some light. Fig. 6.16 compares the |POS| curve for the two clean catalysts. Note that both the onset for H adsorption and H_2O and OH adsorption are pushed out (i.e. H to lower and H_2O and OH to higher potentials) as indicated by the arrows. This reveals that the Co ligand effect weakens the Pt-H and Pt-O bonds, a point noted and observed previously. However while the onset for Pt-OH adsorption is pushed upward in Pt_3Co compared to Pt, as noted above the onset for S oxidation is pushed downward by the same ligand effect. This means that for Pt_3Co, the OH adsorption region and S oxidation region overlap considerably enabling the $SO_{3/4}$ desorption process (eq. 6.6) to occur nearly simultaneously with the oxidation (eq. 6.5). We attribute the much greater removal of $SO_{3/4}$ per

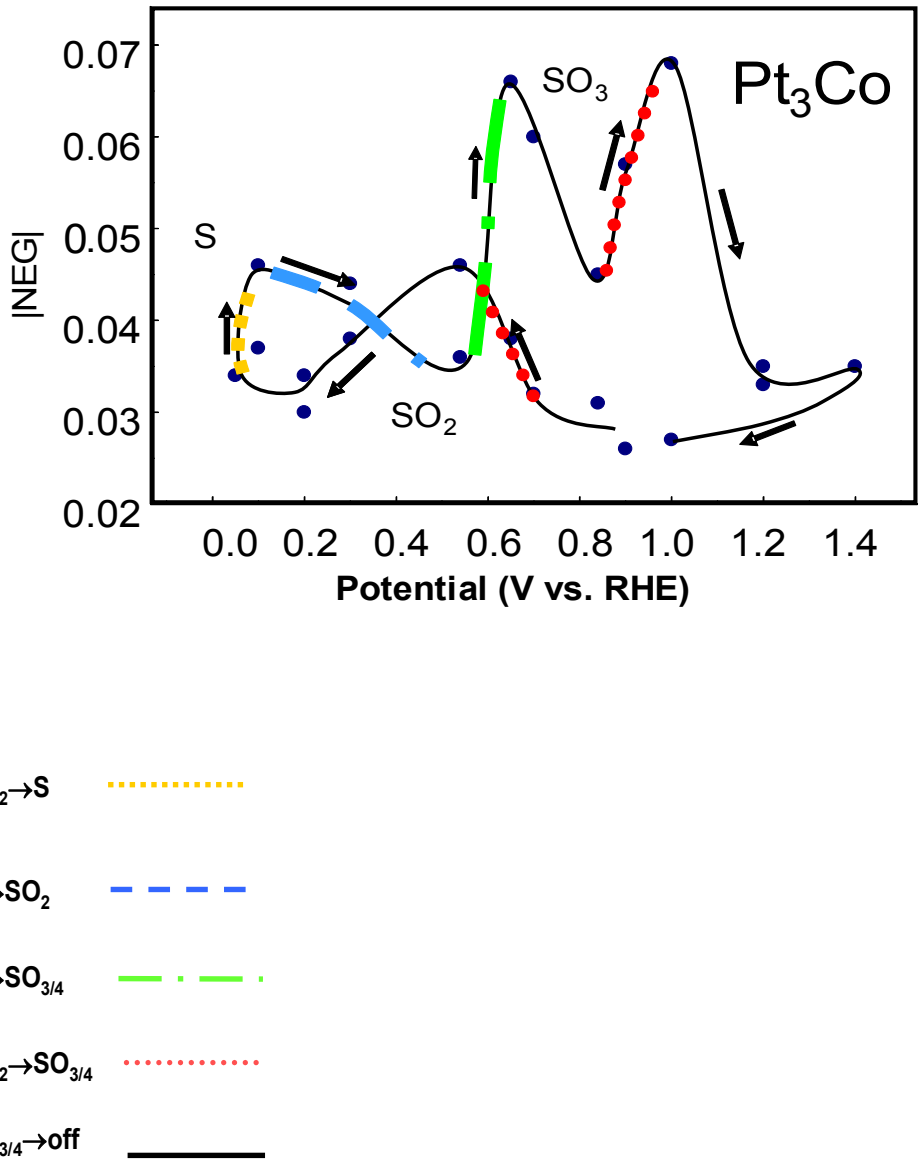

Figure 6.15 |NEG| vs. potential for sulfur-poisoned Pt_3Co/VC. Regions where the indicated S oxidation and reduction reactions occur are indicated.

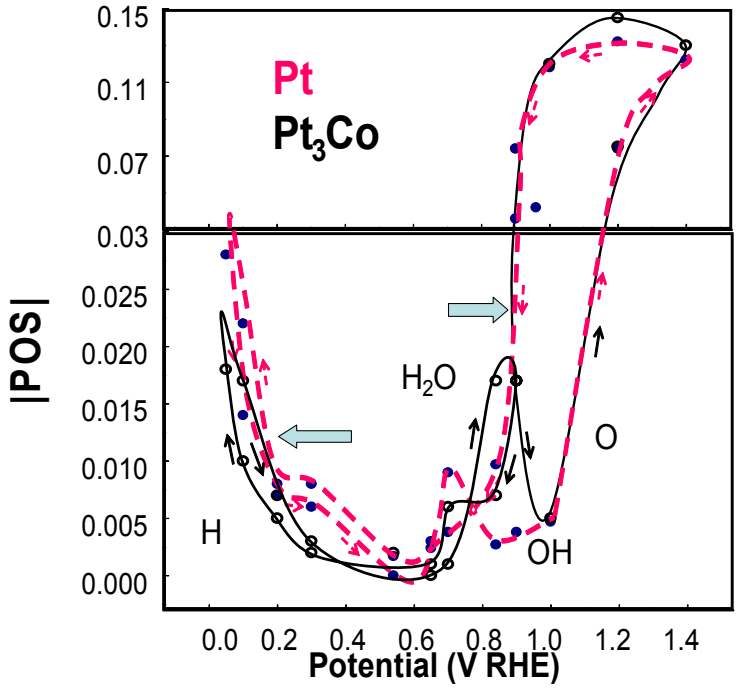

Figure 6.16 Comparison of |POS| for clean Pt/VC (dashed) and Pt_3Co/VC (solid) as a function of potential with small arrows indicating scan direction. Note different scales for magnitudes below and above 0.03 to increase clarity. Shaded arrows highlight shift of H and OH features in the Pt_3Co scan.

cycle for the Pt_3Co catalysts to the concurrent presence of OH, O and $SO_{3/4}$ on the Pt_3Co surface.

Figure 6.16 further reveals that the maxima in |POS| for both Pt and Pt_3Co are remarkably similar in the region 1.2-1.4 V. This suggests that the sum of the $\Delta\mu$'s for $SO_{3/4}$ and O is the same in the two catalysts, and suggest that the Co does not block many active Pt sites. This suggests that the Co is mostly below the surface, so that a Pt skin exists. This is consistent with the $\Delta\mu$ lineshape in the O adsorption region, which does not show a second feature to lower photon energy. We have shown previously that when M islands (M = Ru, Fe, Co, Cr, Co) exists on a Pt surface and OH adsorption occurs near this M island, a chemical shift in the Pt core level caused by the strong ligand effect from the M island, shifts the OH adsorption feature to lower energy[1,2,39]. This causes two separate features to appear, an OH feature from OH adsorption near and far from the M islands. But this does not occur for Pt_2Co consistent with the Co existing below the surface.

6.5 Conclusions

This study incorporated the use of X-ray absorption spectroscopy to study the mechanism for sulfur oxidation and removal from Pt/VC and Pt_3Co/VC. The adsorption of sulfur can deplete the ORR by blocking active sites on Pt where the ORR can occur. From this work we can conclude the following:

a) Both the |NEG| and |POS| amplitude variations with potential support the correctness of the theoretical $\Delta\mu$ signatures and that the $SO_{3/4}$ oxidation product is bonded in a 3-fold fcc site through one of the O atoms consistent with FTIR data, but in contrast to that indicated by DFT calculations for SO_4 in vacuum at ¼ ML coverages.

b) The requirement to cycle the potential to remove S from Pt catalysts apparently arises from the requirement for adsorbed O to oxidize the SO_2, but for adsorbed OH to protonate the $SO_{3/4}$ which occurs at lower potential. Since these two species don't appear concurrently on the surface, cycling is required.

c) Pt_3Co/VC may be more susceptible to sulfur adsorption but it is easier to oxidize it off than on Pt. This apparently arises because, on this surface, OH and O exist concurrently with $SO_{3/4}$ on the surface, so that much more S can be removed per cycle.

d) The concurrent existence of $SO_{3/4}$ and OH on Pt_3Co arises because the Co ligand effect weakens the Pt-OH bond thus pushing the presence of OH to higher potentials, but the oxidation of SO_2 to $SO_{3/4}$ occurs at lower potentials. The reason for the latter is not entirely understood, but most likely the ligand effect weakens not only the Pt-O bond, but also the Pt-S bond between Pt and SO_2making its lift off the Pt surface to go ontop of the O adlayer in the $SO_{3/4}$ configuration easier.

These results show that *in situ* XANES can provide detailed information on sulfur speciation and coverage on Pt and Pt alloy electrocatalysts. Sulfur poisoning (among many poisons) dramatically affects the performance of a fuel cell. Although additional experiments should be performed *in situ* on an operating fuel cell along with additional theoretical calculations to provide more detailed information on the S poisoning and cleaning mechanisms, a much clearer understanding of the S removal mechanism was obtained in this work.

6.6 References

[1] Scott, F.J.; Roth, C.; Ramaker, D.E., *J. Phys. Chem. C.,***2007**, *111*, 11403
[2] Scott, F.J.; Mukerjee, S.; Ramaker, D.E., *J. Electrochem. Soc.,* **2007,** *154*, A396
[3] Moore, J.M.; Adcock, P.L.; Lakeman J.B.; Mepsted, G.O. *J. Power Sources*, **2000**, *85*, 254
[4] Chin, D.T.; Howard, P.D. *J. Electrochem. Soc.*, **1986**, *133*, 2447
[5] Mohtadi, R.; Lee, W.-k.; Van Zee, J.W. *J. Power Sources*, **2004**, *138*, 216
[6] Chin, D-T.; Howard, P.D., *ibid*., **1986**, *133*, 845
[7] Biswas, J.; Bickle, P.G.; Gray, D., Do, D.; Barbier, J. *Catal. Rev.-Sci. Eng.,***1988**, *30*, 161
[8] Zolfaghari, A.; Jerkiewica, G. *J. Electroanal. Chem.* **1999**, *467*, 177
[9] Quijada, C.; Rodes, A.; Vazquez, J.L.; Perez, J.M.; Aldaz, A., *J. Electroanal. Chem.***1995**, *394*, 217
[10] Swider, K.E.; Rolison, D.R.; *J. Electrochem. Soc.***1996**, *15*, 813
[11] Swider, K.E.; Rolisin, D.R.; *Langmuir*, **1999**, *15,* 3302
[12] Gomez, R.; Climent, V.; Feliu, J.M.; Weaver, M.J., *J. Phys. Chem. B.,* **2000**, *104*, 597
[13] Herrero, E.; Mostany, J.; Feliu, J.M.; Lipowski, J. *J. Electroanal. Chem.*, **2002**, *534*, 79
[14] Loučka, T., *J.Electroanal. Chem.,***1971**, *31*, 319
[15] Adzic, R.R.; Feddrix, R.R.; Nikolic, F.; Yeager, E. *J. Electroanal. Chem.*, **1992**, *341*, 233
[16] Matveeva, E.S.; Shepelin, V.A.; Kasathin, E.V. *Sov. Electrochem.,***1982**, *18*, 634
[17] Savich, W.; Sun, S.; Lipowski, J. *J. Electroanal. Chem.,***1995**, *338,* 233
[18] Nart, F.C.; Iwasitea, T.; Weber, M.,*Electrochim. Acta.,***1994**, *39*, 961
[19] Iwasita, T.; Nart, F.C., *J. Electroanal. Chem.,* **1990**, *295*, 215
[20] Iwasita, T.; Nart, F.C.; Rodes, A.; Pastor, E.; Weber, M., *Electrochim. Acta.***1995**, *388,*233
[21] Faguy, P.W.; Markovic, N.; Adzic, R.R.; Fierro, C.A.; Yeager, E.B. *J. Electroanal. Chem.* **1990**, *289*, 245
[22] Nart, F.C.; Iwasita, T.; Weber, M. *Electrochim. Acta*. **1994**, *39*, 961
[23] Iwasita, T.; Nart, F.C.; Rodes, A.; Pastor, E.; Weber, M. *Electrochim. Acta.***1995**, *40*, 53
[24] Kunimatsu, K.;Samant, M.G.;Seki, H., *J. Electroanal. Chem.* **1989**, 258, 163; *ibid.* **1989**, 272,185; Samant, M.G.; Kunimatsu, K.; Seki, H.; Philpott, M.R. *J. Electroanal. Chem.* **1988**, 243, 203; ibid. **1990**, 280, 391.
[25] Thomas S.; Sung Y.-E.;Kim H.S.;Wieckowski A., *J. Phys. Chem.* **1996**, 100, 11726.
[26] Faguy, P.W.; Marinkovic, N.S.; Adzic, R.R., *J. Electroanal. Chem.,***1996**, *407*, 209
[27] Faguy, P.W.; Marinkovic, N.S.; Adzic, R.R., *Langmuir,***1996**, *12*, 243
[28] Nart, F.C.; Iwasita, T.; Weber, M. *Electrochim. Acta.***1994**, *12*, 243
[29] Weickowski, A.I.; Bockris, J.O'M.; Conway, D.E.; White, R.E.; eds. *Modern Aspects of Electrochemistry*, **1990**, *65*, 21, Plenum Press, New York
[30] Zelanay, P.; Wieckowski, A.In.; Abruna, H.D., ed *Electrochemical Interfaces: Modern Techniques for In Situ Surface Characterization*, **1991**, 479, VCH Publishers, New York
[31] Gamboa-Aldeco, M.E.; Franaszczuk, K.; Wieckowski, A. In.; Hubbard, A.T., ed., *The Handbook of Surface Imaging and Visualization*, **1995**, 479, VCH Publishers, New York
[32] Sung, Y.E.; Thomas, A.; Gamboa-Aldeco, M.; Franaszczuk, K.; Wieckowski, A. *J. Electroanal. Chem.,***1994**, *378*, 131
[33] Wieckowski, A.; Zelanay, P.; Varga, K., *J. Chem. Phys.* **1991**, *88*, 1247
[34] Gamboa-Aldeco, M.E.; Herreo, E.; Zelanay, P.S.; Wieckowski, A. *J. Electroanal. Chem.* **1993**, *348*, 451
[35] Gamboa-Aldeco, M.E.; Herrero, E.; Zelanay, P.S.; Wieckowski, A., *J. Electroanal. Chem.***1993**, *348*, 458
[36] Thomas, S.; Sung, Y.E.; Kim, H.S. Wieckowski, A. *J. Phys. Chem.***1996**, *100*, 11726
[37] Funtikov, A.M.; Stimming, U.; Vogel, R. *J. Electroanal. Chem.* **1997**, *428*, 147
[38] Arruda,T; Shyam,B.; Ziegelbauer, J.; Mukerjee, S; Ramaker, D.E., *J. Phys. Chem.* **B 2008,** *112***,**

18087.
[39] Teliska, M.; Murthi, V.S.; Mukerjee, S.; Ramaker, D.E., *J. Phys. Chem. C,* **2008,***111*, 9267.
[40] Lin,X.; Ramer, N.; Rappe, A.;Hass, K.; Schneider, W.; Trout, B. *J. Phys. Chem. B*, **2001**, *105*, 7739
[41] Lin,X.; Ramer, N.; Rappe, A.;Hass, K.; Schneider, W.; Trout, B. *J. Phys. Chem. B*, **2002**, *106*, 12575
[42] Lin, X.; Schneider, W.F.; Trout, B.L. *J. Phys. Chem. B.,***2004**, *108*, 13329
[43]Pillay, D.; Johannes, M. D.; *J. Phys. Chem. C.*, **2008**, *112*, 1544.
[44] Garsany, Y.; Baturina, O.A.; Swider-Lyons, K.E. *J. Electrochem. Soc.,***2007**, *154*, B670
[45] Luczak, F.J.; Landsman, D.A., U.S. Pat. 4,447,506, **1984**
[46] Luczak, F.J.; Douglas, A., U.S. Pat. 4,711,829, **1987**
[47] Luczak, F.J.; D.A. Landsman, U.S. Pat. 4,677,092, **1987**
[48] Paffet, M.T.; Beery, G.J.; Landsman, D.A., *J. Electrochem. Soc.,***1987**, *143*, 58
[49] Min, M.-K.; Cho, J.; Cho, K.; Kim, H., *Electrochim. Acta.,***2000**, *135*, 1431
[50] Mukerjee, S; Srinivasa, S., *J. Electroanal. Chem.,* **1993**, *357*, 201
[51] Toda, T., Igarashi, H.; Uchida, H; Watanabe, M., *J. Electrochem. Soc.,***1999**, *146*, 3750
[52] Mukerjee, S.; Srinivasan, S.; Soriaga, M.P., *J. Electrochem. Soc.,***1995**, *142*, 1409
[53] Garsany, Y.; Baturina, O.A.; Swider-Lyons, K.E., *J. Electrochem. Soc.,*to be submitted
[54] Teliska, M.; O'Grady, W.E.; Ramaker, D.E., *J. Phys. Chem. B.,***2005**, *109*, 8076
[55] Ramaker, D.E.; Koningsberger, D.C., *Phys. Rev. Lett.,***2002**, *89*, 139701
[56] Teliska, M.; Murthi, V.S.; Mukerjee, S.; Ramaker, D.E., *J. Electrochem. Soc.,***2005**, *152*, A2159
[57] Bae, I.T.; Scherson, D.A.; *J. Phys. Chem. C.,***1996**, *100*, 19215; *J. Phys. Chem. C.,* **1998**, *145*, 80
[58] Ankudinov, A.L.; Rehr, J.J.; Low, J.; Bare, S.R., *Phys. Rev. Lett.,* **2001**, *86(8)*, 1642
[59] Sasaki, K; Wang, J.X.; Balasubramanium, M.; McBreen, J.; Uribe, F.; Adzic, R.R. *Electrochim. Acta.***2004**, *49*, 3873.
[60] Ravel, B; Newville, M. *Sycnhrotron Radiat.,* **2005**, *12*, 537.
[61] Newville, M.; Livins, P.; Yacoby, Y.; Rehr, J.J.; Stern, E.A.; *Phys. Rev. B.* **1993**, *47*, 14126
[62] Teliska, M.; O'Grady, W.E.; Ramaker, D.E., *J. Phys. Chem. B.,* **2004**, *108*, 2333
[63] Newville, M., *J. Synchrotron Radiat.,* **2001**, *8*, 322
[64] Ramaker, D.E.; Mojet, B.L.; Koningsberger, D.C.; O'Grady, W.E., *J. Phys.: Condens. Matter,* **1998**, *10*, 8753
[65] van Dorssen, G.E.; Koningsberger, D.C.; Ramaker, D.E., *J. Phys.: Condens. Matter,* **2002**, *14*, 13529
[66] Ramaker, D.E.; Mojet, B.L.; Millter, J.T.; Koningsberger, D.C., *Top. Catal.,* **2000**, *10*, 157
[67] Koningsberger, D.C.; Mojet, B.L.; Ramaker, D.E., *J. Synchrotron Radiat.,* **1999**, *6*, 135
[68] Janin, E.; von Schenk, M.; Gothelid, M.; Karlsson, U.O.; Svensson, M., *Phys. Rev. B.,***2000**, *61*, 13144
[69] Gatewood, D.; Schull, T.; Baturina, O.; Garsany, Y.; Pietron, J.J.; Swider-Lyons, K.; Ramaker, D.E., *J. Phys. Chem. C*, **2008**, *112*, 4961
[70] Pillay, D.; Johannes, M. D.; Gatewood, D.; Ramaker, D.E.; *in prep*.
[71] Nekrasov, B., *Textbook of General Chemistry*, Mir, Moscow, **1965**.
[72] Markovic, N,N,; Schmidt, T.J.; Grgur, B.N.;Gastieger, H.A.;Ross, P.N.;Behm. R.J.;*J. Phys. Chem. B* **1999,** *103*, 8568

Chapter 7

Summary and Future Work

7.1 Summary of Current Work

This work utilized the Δμ technique, which was combined with the traditional EXAFS analysis technique and theoretical modeling, to obtain a more detailed understanding of the oxygen reduction reaction mechanisms on platinic and non-platinic electrocatalysts. These XAS data were taken *in situ* in an electrochemical cell. The Δμ technique has been developed by the Ramaker group and has since been incorporated by several other scientists and collaborators in their work. As originally developed, the technique was primarily limited to H, O, OH, and anionic adsorption on Pt and Pt alloy electrocatalysts in an electrochemical cell (i.e., *in situ* but not *operando*). However, this early work provided a pathway to gradually more complicated systems. The Δμ technique was then advanced to study CO adsorption for the first time in real working fuel cells running on reformate or methanol (i.e., *operando* systems). In the work reported in this dissertation, Δμ was applied to more complex systems on Pt nanoparticles as well as other catalysts. Here, for the first time, the technique was advanced to reveal more phenomena such as complicated organic TPPTP ligand orientations on Pt, as well as different

sulfur oxidation states on Pt and Pt_3Co electrocatalysts. Also, non-platinic electrodes were studied, such Au nanoparticles on a metal oxide support, as well as the novel Rh-based chalcogenides. In these studies, significant new understanding about the dioxygen reduction mechanisms occurring at the Au-metal oxide interface and on the novel Rh sulfide catalysts, as well as in the sulfur-oxidation process was gained, even though these complicated reactions have been studied for many years.

7.1.1 Oxygen Reduction on Tin-Oxide Supported Au Electrocatalysts

As shown previously via electrochemical analysis, Au supported on Vulcan carbon (VC) is not active for the 4-electron reduction of oxygen to water but and mainly generates peroxides in a 2-electron reduction. Hence, Au/VC shows no promise of being a good fuel cell catalyst for the ORR reaction. However, Au nanoparticles incorporated on a tin-oxide support showed enhanced ORR activity. Using Au L_3 and Sn K edge *in situ* XANES data, along with detailed analysis and FEFF 8.0 calculations, the coverage of OH and O on Au/VC and Au-SnO_x/VC could be observed. It was found that O(H) does not adsorb on Au/VC until >1.4V. This indicates that the Au-O bond is very weak compared to the Pt-O bond when O(H) adsorbs onto the surface already above 0.8V. In contrast to Au/VC however, Au-SnO_x/VC showed nearly an order of magnitude greater O(H) coverage at 1.4V, indicating that the Au-O bond strength was increased by a metal-support interaction between the Au and the SnO_x. EXAFS analysis of the Sn K edge showed an increase in the Sn-Sn coordination betweeen 0.3-0.5V indicating the support was getting reduced at these potentials. However, above 0.5V, oxidation of the SnO_x support occurred again. The correlation of this SnO_2 oxidation state change with the onset for the ORR revealed in RDE results, clearly suggests that the SnO_2 is directly involved in the dioxygen reduction. In this "bifunctional" mechanism, SnO_x apparently dissociates the O_2 that is normally the slow rate-determining step on Au. Charge transfer from the Au then finishes the process by reducing the adsorbed O(H) at the Au-SnO_2 interface to water.

7.1.2 Oxygen Reduction on Ligand-Stabilized Pt nanoparticles.

Similar Δμ analysis of experimental Pt L_3 XANES data of triphenyl phosphine triphosphonate (TPPTP) stabilized Pt nanoparticles has revealed interesting information on oxygen adsorption: it has been shown that on Pt-TPPTP, a dramatic reduction in the coverage of OH that poisons the Pt surface occurs. Δμ analysis of Pt L_3 edge XAS data showed that about 0.3ML (1 ML = 1 TPPTP per Pt atom) of TPPTP lies on the Pt surface via a Pt-P<tp linkage at 0.54V, converting to Pt-O-P<tp linkage at 1.0V (tp indicates triphenyl groups). The reduction in OH coverage enhances the surface specific oxygen reduction reaction (ORR) rate relative to the same sized Pt particles on carbon, but not sufficiently to increase the mass specific ORR rate. On the other hand, the Pt-ox-TPPTP linkage occurs via a 3-fold coordinated Pt≡O-P<tp, which severely blocks sites and makes the electrocatalysts almost inactive to water activation and the ORR. The different linkage to the Pt, i.e. atop TPPTP ligands vs. 3-fold bonded O-TPPTP ligands, and the dramatically different effect this has on the ORR rate, emphasizes the importance of knowing the Pt-ligand linkage when studying these materials. The Δμ technique was able to provide this information.

7.1.3 Oxygen Reduction on Rh based Chalcogenides

A broader range of experimental tools was used to study the Rh sulfide catalysts: namely Rh_xS_y/C, the thermally grown Rh_2S_3/C and Rh_3S_4/C preferential phases, and a standard 30 wt% Rh/C electrocatalyst. The tools included X-ray diffraction (XRD), high-resolution transmission electron microscopy (TEM), micro-analysis and electrochemical investigations, along with XAS. The specific adsorption of water, OH, and O as a function of overpotential is reported. Heating of the Rh_xS_y catalysts to prepare the two preferential phases causes Rh segregation and the formation of Rh metal particles; while immersion in TFMSA causes S dissolution and the formation of a Rh skin on the Rh_xS_y samples. It is shown that some Rh-Rh interactions are

needed to carry out the ORR; these are present in both the Rh_3S_4 and Rh_xS_y catalysts, but a partial Rh over layer (formed by dissolution and redeposition of Rh in acid solution) is also contributing to the ORR observed on Rh_xS_y. In this work, the Δμ technique was used to investigate the geometric binding sites of oxygen on each catalyst studied. This information was then helpful in interpreting the ORR activity these samples exhibited, with the XRD and TEM data providing the structural information on these more complex but novel chalcogenide catalysts.

7.1.4 Sulfur Oxidation on Pt and Pt_3Co

Pt L_3 edge XAS data from S-poisoned Pt and Pt_3Co catalysts were compared to similar non-poisoned catalysts. Direct contact adsorption of sulfur hinders the kinetics of the ORR by blocking active adsorption sites and altering the electronic properties of the Pt clusters. In this study, data were taken at many potentials beginning at OCP, after cycling down to 0.05V, up to 1.4V and finally back down to 0.6V. This was done in order to observe the effect of one full oxidation/reduction cycle. Δμ signatures were isolated at each potential to determine sulfur speciation, but because adsorbed O and OH have Δμ signatures that are similar to that for SO_x, this required a modification to the normal plotting of Δμ amplitudes with potential. This modification involved a plot of the negative Δμ amplitude at -3 eV to map SO_x speciation, and the positive Δμ amplitude at +5 eV to map the O adsorption. In this way both the coverage of O(H) and SO_x could be separately followed with potential. FEFF8 theoretical calculations confirmed previous DFT and FTIR results suggesting that in the presence of O, SO_4 prefers a peculiar inverted binding; i.e. with one oxygen down in a 3-fold site and the SO_3 pointing away from the surface. The Δμ derived results indicate that oxidation of SO_2 requires adsorbed O on the Pt surface, and removal of this $SO_{3/4}$ species then requires adsorbed O(H) that exists at lower potential. This accounts for the required potential cycling to remove S from a Pt surface. CV results show that complete sulfur removal on Pt requires 8 cycles while on Pt_3Co only 4 are

needed. The ligand effect deriving from the Co in Pt_3Co is found to shift the SO_2 to $SO_{3/4}$ oxidization about 0.2 V to lower potential compared with Pt The same ligand effect pushes the water activation process about 0.2 V to higher potential. The net result is that SO_2 to $SO_{3/4}$ oxidation occurs concurrently with OH and O adsorption on Pt_3Co, while on Pt the potential apparently has to be cycled to higher potential to oxidize the SO_2 in the presence of O/Pt, and then back down to lower potential to remove the $SO_{3/4}$ in the presence of OH/Pt. Again, the Δμ XANES derived *in situ* coverage and S speciation information obtained in this work allows this complex S removal process to be understood.

7.2 Future Directions

The objective of the work reported in this thesis was to apply the Δμ technique to more complex electrocatalytic systems and different samples other than Pt/VC. These studies were all conducted in an electrochemical cell, so the next logical step would be to take these findings and apply the *in situ* technique to gain more information in an operating fuel cell.

Further studies on non-platinic fuel cell catalysts need to be conducted. Though Au/SnO_x showed enhanced ORR activity, it still does not show ORR activity comparable to Pt. However, it should also be noted that O(H) did not poison the catalyst surface until very high potentials that are outside the fuel cell operating range. Further work on using different supports for Au should be conducted, such as incorporating tin polyanions to increase the potential of the redox couple seen in the case of Sn. This may be helpful in increasing the ORR.

Currently the Ramaker group is examining more biological applications to fuel cell catalysis. Cu-based Laccase is currently under study as a catalyst to replace the need for Pt althogether[1]. Preliminary findings using the Δμ technique have shown Cu being oxidized with increasing potential, showing for the first time changes in the Laccase enzyme during catalytic

operation. Further studies are on the way to observe the reduction of oxygen to water via enzyme activity.

The ultimate goal in fuel cell catalysis is to "fine tune" the catalysts: the anode for optimal performance in reformates, and methanol fed fuel cells and the cathode for better oxygen reduction kinetics. The oxygen reduction reaction causes most of the potential loss in a working hydrogen PEMFC. In a reformate fed fuel cell, even when transport losses have been minimized, the electrode potential is still 400 mV below theory.[1] In direct methanol fuel cells, the potential drop can be even larger, due to methanol crossover to the cathode. A variety of steps and intermediates, are involved in the 4 electron ORR mechanism, and a better understanding of these mechanisms through the use of the techniques utilized in this thesis could lead to similar detailed understanding required for better tuning of cathode materials. The research described in this thesis we explored novel ways of counteracting some of these problems, such as resorting to non-platinic catalysts (Au and Rh_xS_y), as well as attempting to modify the Pt by either attaching the TPPTP ligands, or alloying with Co to reduce the problem of S and OH poisoning.

The power of our novel $\Delta\mu$ XANES technique has been clearly demonstrated in this work. However, the biggest limitation of some of this work is probably in the determination of the particle size and morphology. The EXAFS modeling performed in this work provides only an average cluster morphology. Unfortunately very few techniques enable such a characterization *in situ*, where it must be done, since these small particles are heavily oxidized in air. Furthermore, better catalyst preparation procedures, ones that give a more monodisperse particle size and uniform particle morphology are required. The EXAFS analysis gives only an average particle size and morphology, and one never knows what component of the particle distribution is doing "the work". Major improvements in catalysts preparation techniques and catalysts morphology characterization would dramatically increase the power of the $\Delta\mu$ XANES technique, which already provide critical adsorbate coverages and binding site information.

7.3 References

[1] Shyam, B.; Arruda, T.; Mukerjee, S.; Ramaker, D.E.; in preparation